

ABSTRACT

LONG, YUN. Pressure Tensor of Adsorbate in Nanoporous Materials: Molecular Simulation Studies. (Under the direction of Dr. Keith E. Gubbins).

Abundant experimental evidence suggests that adsorbates confined in nanoporous materials can exhibit high pressures, even if the systems are in equilibrium with a bulk phase of 1 bar pressure. Examples include the occurrence in the confined nanophase of high pressure chemical reactions, high pressure solid phases, high pressure effects in solid-liquid equilibria, effects on spectral properties, and the deformation of the solid materials.

With the aim of providing fundamental understanding of the high pressure effects in confined nanophases, we report Monte Carlo simulation studies of the pressure tensor of adsorbates confined in microporous materials. The pressure tensor components are calculated by both the mechanical and thermodynamic routes with the Irving-Kirkwood and Harasima definitions. We calculate the microscopic pressures as functions of spatial position. Although they cannot be measured experimentally, these local pressures contain the information of maximum value, and can be readily used to calculate various average pressures that are appropriate for different applications.

We find that the in-pore pressure is either enhanced or reduced depending on the nature of the interaction between adsorbate and wall atoms. For a well adsorbate-wall system, the in-pore tangential pressure, the pressure tensor component which is parallel to the wall, is significantly enhanced (e.g., by a factor of $10^4 \sim 10^6$). This enhancement effect arises from the strong attraction from the wall, which compresses the adsorbate phase in the direction

parallel to the wall, leading to repulsive forces between the molecules. On the contrary, for a non-wetting system this enhancement is much weaker; in some cases the tangential pressure is reduced. This is because the attraction from the wall is weak (even weaker than the attraction between the adsorbate molecules), and thus the wall does not help to compress the adsorbate phase. A very large bulk pressure is needed (e.g., ~ 4000 bar for mercury into a carbon pore) to push the adsorbate into the pore. For a wetting system with a cylindrical or spherical pore, the surface curvature strengthens the adsorbate-wall interaction, so that the tangential pressure is more enhanced than that in a slit pore. Moreover, the in-pore tangential pressure is very sensitive to small changes in the bulk pressure, indicating a way to experimentally control the in-pore pressure. Studies for silica pores show similar pressure enhancement effects, but these are smaller by about one order of magnitude due to the roughness of the pore wall surfaces, which causes a looser structure of the adsorbate molecules in contact with the wall surface. The normal pressure of adsorbate, the pressure tensor component which is perpendicular to the wall, is also enhanced (by a factor of $\sim 10^3$), but the value can be positive or negative depending on the pore size. This large normal pressure causes deformation of the porous material: a positive normal pressure (strong repulsive force) expands the pore, while a negative normal pressure (strong attractive force) contracts the pore.

Pressure Tensor of Adsorbate in Nanoporous Materials: Molecular Simulation Studies

by
Yun Long

A dissertation submitted to the Graduate Faculty of
North Carolina State University
in partial fulfillment of the
requirements for the degree of
Doctor of Philosophy

Chemical Engineering

Raleigh, North Carolina

2012

APPROVED BY:

Keith E. Gubbins
Committee Chair

Donald W. Brenner

Carol K. Hall

Phillip R. Westmoreland

BIOGRAPHY

Yun Long was born in 1983 in Nanjing, a beautiful city with splendid history in the southeast part of China. Yun received his B.S. degree in Chemical Engineering from Zhejiang University (China) in 2005, and a joint master's degree in Materials Science and Engineering from Lulea Tekniska Universitet (Sweden) and Institut National Polytechnique de Lorraine (France) in 2007. With strong interests in applied mathematics and computer programming, Yun was doing process modeling, process design and simulations as well as materials modeling during his undergraduate and master's programs. Then Yun joined Dr. Gubbins Group as a Ph. D student in the Department of Chemical and Biomolecular Engineering at North Carolina State University (NCSU, USA). There, his research focuses on the molecular simulation of fluids confined in nanoporous materials, particularly studying the pressure enhancement effects in nanopores. Yun is also passionate in teaching and pedagogical research, and he has co-taught ChE graduate and undergraduate core courses many times during his Ph. D study at NCSU. Yun will be working as a teaching-track faculty member in the Department of Chemical and Biomolecular Engineering at the National University of Singapore after a Ph. D. degree is conferred by NCSU.

ACKNOWLEDGMENTS

In the first place, I would like to cordially appreciate Dr. Keith E. Gubbins for his supervision and support (technical, mental and economical). He is always nice and encouraging every time when I meet him to discuss our research, no matter whether I have exciting results to report or not. Although it is quite often that I have been stuck by some difficulties and cannot show any appreciable progress on my research, Keith is patient, allowing me more time to work it out on my own before pushing or providing suggestions. He also likes giving me resources (e.g., scientific papers, textbooks, lab mates, past group members, active researchers in other institutions) to learn rather than directly telling me the solution, which is very helpful for my growth. What is more, I enjoyed travelling with him. Yes, Keith is not only an excellent professor, but also a professional tourist. He likes all kinds of animals, especially birds. What I have learned from him is not only the way of research, but also an attitude of enjoying life. I feel lucky that I have been Keith's student.

I would also like to express my appreciation to all of my group members, who are really great. We get along with each other like a family, and everyone is very supportive. Dr. Thomas Roussel encouraged me to build my first modeling code. Dr. Jeremy C. Palmer, currently a postdoctoral researcher at Princeton, helped me to grow from a Mr. Know-Nothing to an independent researcher. Dr. Liangliang Huang and Katherine A. Phillips are always ready to answer my questions even if the problem is not of their areas of interests. Cody K. Addington is continuing my work, and we enjoy discussing the projects.

Also importantly, I would like to thank the administrative staff (including Sandra Bailey, Diane Harper, Shirley Kow, and especially June McKoy) in our department, without whom everything would be impossible (e.g., academic information, travelling for conference, reimbursement, stipend, processing administrative documents, etc.).

By the way, I would take this opportunity to thank the faculty members and staff in our department and also in the College of Education and the Graduate School who are very helpful for my growth in teaching and supportive for my application for a teaching-track faculty position. So I would thank Dr. Peter S. Fedkiw for taking me as his teaching assistant and guest lecturer for 4 years, Dr. Carol K. Hall for meeting with her about teaching thermodynamics, Dr. Michael D. Dickey, Dr. Barbi T. Honeycutt and Dr. Elizabeth L. Overman for working together for the Mentoring and Teaching Practicum, Dr. Lisa G. Bullard and Dr. Richard M. Felder for talking about pedagogical research, and finally Dr. Gerald A. Ponder and Dr. Betsy E. Brown for learning teaching from their course “Teaching in College” and always tracking my growth as a teacher.

In the final place, I would thank my wife Xiaozhen Liu, my parents, Xianli Long and Chao Zhong, and my parents-in-law, Qian Liu and Shuhong Zhang, who support me to finish my PhD unconditionally in all aspects, and my lovely son Junlun, who is my strong motivation to do anything.

TABLE OF CONTENTS

LIST OF TABLES	viii
LIST OF FIGURES	ix
CHAPTER 1	1
Introduction and Background	1
CHAPTER 2	4
Experimental Evidence of High Pressure in Nanopores and Simulation Work	4
2.1 High Pressure Phases in Pores	4
2.2 Chemical Reaction in Pores	6
2.3 Surface Force Apparatus Studies	8
2.4 Adsorption and Structure Deformation	10
2.5 Simulation Work on Pressure Tensor of Fluids	12
CHAPTER 3	16
Pressure Tensor of Inhomogeneous Fluids in Porous Materials	16
3.1 Pressure Tensor and Hydrostatic Equilibrium	16
3.2 Mechanical Route	19
3.2.1 <i>Irving-Kirkwood Choice</i>	22
3.2.2 <i>Harasima Choice for the Planar Surface</i>	28
3.3 Thermodynamic Route	29
3.3.1 <i>Slit Pore</i>	32
3.3.2 <i>Cylindrical and Spherical Pores</i>	34
3.4 Spatial Averaging of the Pressure Tensor	46
CHAPTER 4	50
Molecular Simulation Methods	50
4.1 Statistical Thermodynamics and Molecular simulation	50
4.2 Monte Carlo Method and Simulation of Adsorption	51
4.3 Semi-Grand Canonical Monte Carlo for System with Flexible Walls	55
CHAPTER 5	57
Pressure Enhancement in Slit Pores of Various Models	57
5.1 Introduction	57
5.2 Modeling Details	58
5.3 Simulation Details	62
5.4 Results and Discussion	63
5.4.1 <i>Argon in Steele (10,4,3) structureless rigid infinite walls</i>	63
5.4.2 <i>Argon in realistic carbon slit pores with LJ interactive potential model</i>	69
5.4.3 <i>Argon in realistic carbon slit pores with WCA interactive potential model</i> ..	80
5.5 Conclusions	82
CHAPTER 6	83
Effects of the Wetting Parameter on Adsorption and Pressure	83
6.1 Introduction	83

6.2 Nano-Scale Wetting and the Microscopic Wetting Parameter	84
6.3 Corresponding States Analysis	87
6.4 Effects of the Wetting Parameter α_w on Capillary Condensation	89
6.4.1 <i>Modeling and Simulation Details</i>	89
6.4.2 <i>Results and Discussion</i>	90
6.5 Effects of Wetting Parameter α_w on In-Pore Pressure	92
6.5.1 <i>Modeling and Simulation Details</i>	92
6.5.2 <i>Results and Discussion</i>	93
6.6 An Example of a Non-Wetting Fluid: Mercury Intrusion in a Carbon Slit Pore	98
6.6.1 <i>Introduction</i>	98
6.6.2 <i>Modeling and Simulation Details</i>	98
6.6.3 <i>Results and Discussion</i>	99
6.7 Conclusions	104
CHAPTER 7	106
Pressure of Fluids Confined in Spherical and Cylindrical Pores	106
7.1 Introduction	106
7.2 Modeling and Simulation Details	106
7.2.1 <i>Cylindrical Carbon Pore Model</i>	106
7.2.2 <i>Spherical Carbon Pore Model</i>	108
7.2.3 <i>Simulation Details</i>	109
7.3 Results and Discussion	110
7.3.1 <i>Pressures in Spherical Pores</i>	110
7.3.2 <i>Comparison of Pressures in Slit, Cylindrical and Spherical Pores</i>	115
7.3.3 <i>Effects of Bulk Pressure for Various Pore geometries</i>	119
7.4 Conclusions	121
CHAPTER 8	122
Normal Pressure Acting on the Wall and Pore Deformation	122
8.1 Introduction	122
8.2 Argon Adsorbed in Carbon Slit Pore and Pore Deformation	122
8.2.1 <i>Modeling Details</i>	122
8.2.2 <i>Simulation Details</i>	125
8.2.3 <i>Results and Discussion</i>	126
8.3 Carbon Tetrachloride and Water Adsorbed in Activated Carbon Fibers	128
8.3.1 <i>Experimental</i>	128
8.3.2 <i>Modeling Details</i>	129
8.3.3 <i>Simulation Details</i>	131
8.3.4 <i>Results and Discussion</i>	132
8.4 Argon Adsorbed in Cylindrical and Spherical Pores	135
8.4.1 <i>Modeling and Simulation Details</i>	135
8.4.2 <i>Results and Discussion</i>	136
8.5 Conclusions	138
CHAPTER 9	139
Effects of Wall Roughness on Pressure in Slit Pore	139

9.1 Introduction	139
9.2 Reduced Pressure Enhancement in the Silica Slit Pore	139
9.3 Effects of Wall Roughness on Adsorption Isotherm and In-Pore Pressure	145
<i>9.3.1 Models and Simulation Details</i>	145
<i>9.3.2 Results and Discussion</i>	148
9.4 Conclusions	158
CHAPTER 10	160
Conclusions and Perspectives	160
10.1 Conclusions	160
10.2 Recommendations for Future Studies	164
REFERENCES	167
APPENDICES	179
Appendix A.....	180
Derivations for Hydrostatic Equilibrium in Slit, Cylindrical and Spherical Pores ..	180
Appendix B.....	189
Volume Balance Examinations for the Volume Perturbation Method	189
Appendix C.....	192
Solution of Ordinary Differential Equations Arising from Volume Perturbation	
Method	192
Appendix D.....	198
Calculations of Wetting Parameters for Various Adsorbate-Substrate Systems	198
Appendix E.....	202
List of Important Symbols	202

LIST OF TABLES

Table 2.1 Surface force apparatus results showing the melting points of substances in pores.	4
Table 2.2 Comparison of experimental product mole fraction in bulk phase and in porous carbons for the NO dimerization reaction	7
Table 5.1 The BFW parameters for argon [96].....	59
Table 6.1 The wetting parameter and experimental contact angles of various liquids on graphite, silica and mica surfaces. The potential model parameters used to calculate the wetting parameters are taken from [8, 97, 110-112], and the detailed calculation can be found in Appendix D.	86
Table 7.1 The diameter of the carbon nanotube, D , as a function of the parameter (m,n) , and the length of the tube $L_{z,\text{wall}}$ as a function of the number of unit cells (N_{uc}).	107
Table 8.1 The interlayer spacings (d_{002}) of graphene sheets in ACF samples with the pores empty and loaded with adsorbates.....	134
Table 9.1 Model parameters for PN-TrAZ potential (in atomic units, $E_h = 3.1578 \times 10^5$ K, $a_0 = 0.529177$ Å) [126].	141
Table 9.2 The model parameters for pores of various roughnesses.....	147

LIST OF FIGURES

Figure 2.1 Phase diagram for bulk water [12].	5
Figure 2.2 The normal forces acting on the mica surfaces of SFAs by the confined fluids (a) OMCTS (recreated by using the data from Fig. 1B of [4]) and (b) conductivity water (pH = 6.0~6.2) (recreated by using the data from Fig. 2 of [42]) as functions of the separation distance between the mica surfaces.	10
Figure 3.1 Pressure tensor components for (a) planar, (b) cylindrical and (c) spherical surfaces.....	17
Figure 3.2 Schematic representations of two pressure tensor definition: (a) Irving-Kirkwood choice and (b) Harasima choice of the integral contour C_{ij} between particles i and j . Here dS is an element of area in some infinite plane S	23
Figure 3.3 Illustrations of test-area method: Choice (1): “Harasima-like”, $1/2 u(r_{ij})$ contribute to bin z_{k1} and another $1/2 u(r_{ij})$, will contribute to bin z_{k5} ; Choice (2): “IK-like”, $u(r_{ij})$ linearly contributes to the bins between them, e.g., $\delta z / z_{ij} u(r_{ij})$ contributes to $z_{k1}, z_{k2}, z_{k3}, z_{k4},$ and z_{k5} , respectively.	33
Figure 3.4 The illustration of the perturbation in ρ -direction and its consequence for cylindrical and spherical pores.....	36
Figure 3.5 A plane at constant φ , normal to the φ direction and to the xy -plane. Left part: looking down on the xy -plane, the constant φ plane is seen end on as the solid black line. Right part: the plane of constant φ , showing bin k as the solid black circle; the tangential pressure $P_{T\varphi}$ acts normal to this plane.	41
Figure 3.6 The shaded annuluses of the lower two parts show the surface area normal to the θ -direction ($dS_{\theta k}$) for different θ positions.	43
Figure 5.1 Intermolecular interaction potentials for argon for LJ and BFW models.	59
Figure 5.2 The simulation cells of (a) carbon slit pore with structureless wall and (b) carbon slit pore with atomistic wall. The green circles represent adsorbate argon molecules, and the blue circles and slabs represent wall atoms and carbon structureless walls, respectively. Carbon atoms are shown at reduced scale for clarity.	60
Figure 5.3 In a structureless rigid infinite pore of $H_e^* = 3.0$, at 87.3 K: (a) the density and pressure profiles at 1 bar bulk pressure; (b) the tangential pressure profiles from the mechanical and thermodynamic routes at 1 bar bulk pressure; (c) the average in-pore density and pressures of argon as a function of bulk pressure.....	66
Figure 5.4 The normal pressures calculated by the thermodynamic route in a structureless rigid infinite pore at 87.3 K and 1 bar bulk pressure: (a) with various values of the perturbation parameter ζ , for $H_e^* = 3.0$, and (b) compared with those calculated from the mechanical route for various pore widths.	67
Figure 5.5 The density and pressure profiles and snapshots of argon adsorbed in the flexible finite atomistic carbon slit pore model at 87.3 K and 1 bar bulk pressure for pores of reduced widths of (a) 2.0, (b) 3.0, (c) 4.5 and (d) 7.0, respectively. Carbon atoms are shown at reduced scale for clarity.....	71

Figure 5.6 Decomposition of the (a) tangential and (b) normal pressure tensor profiles into the kinetic contribution and the argon-argon and argon-carbon configurational contributions for $H_e^* = 3.0$ at 87.3K and 1 bar bulk pressure in the flexible finite atomistic carbon slit pore.	72
Figure 5.7 (a) Radial distribution function in the xy -plane for confined argon at 300 K and 3,990 bar bulk pressure (A, dashed line) and at 87.3 K and 1 bar bulk pressure (B, dotted line), and the isotropic radial distribution function for bulk argon at the boiling point, 87.3 K (C, solid line). (b) The intermolecular force between two argon molecules, F , with the most probable nearest neighbor separation distances shown for the three cases illustrated in (a).	74
Figure 5.8 The average in-pore density and pressures of argon as a function of bulk pressure at (a) 87.3 K, (b) 135 K and (c) 300 K, respectively, for $H_e^* = 3.0$	77
Figure 5.9 The pressure tensor components of LJ argon along the pore length at 87.3 K and 1 bar bulk pressure in an atomistic flexible finite pore of $H_e^* = 3.0$	78
Figure 5.10 The density and pressure profiles of (a) LJ argon and (b) BFW argon in an atomistic flexible finite pore of $H_e^* = 4.5$, at 87.3 K and 1 bar bulk pressure.	80
Figure 5.11 The density and pressure profiles of LJ argon in the atomistic flexible finite pore with a WCA-repulsive potential, at 87.3 K and bulk pressures of (a) 5 bar, and (b) 200 bar.	81
Figure 6.1 Wetting of a solid surface by a liquid at the macro-scale, for strongly wetting (left) and weakly wetting (right) adsorbates. Arrows indicate the forces due to surface tensions for the solid (S), gas (G) and liquid (L) phases.	84
Figure 6.2 A schematic illustration of wetting on a molecular scale.	85
Figure 6.3 Experimental contact angles as a function of wetting parameters of various fluids on different substrates. The curves are a guide to the eye.	87
Figure 6.4 The capillary condensation pressure of argon as a function of wetting parameter in slit pores with various pore widths at 87.3 K. The three parts shows the same results but on different scales.	91
Figure 6.5 The in-pore density, the normal pressure and the peak value of the tangential pressure of argon as functions of the wetting parameter at 87.3 K and 1 bar bulk pressure for the reduced pore widths of (a) 2.0, (b) 3.0, (c) 4.5 and (d) 7.0. Part (e) shows the effects of wetting parameter on the normal pressure in an expanded scale.	94
Figure 6.6 The in-pore density, the normal pressure and the peak value of the tangential pressure of argon in a carbon slit pore of $H^* = 7.0$ at 87.3 K as functions of bulk pressure for different wetting parameters of (a) 1.2554 (as argon-silica system), (b) 2.137 (as argon-carbon system), and (c) 2.434 (as argon-mica system).	97
Figure 6.7 The snapshot of Hg intrusion in model carbon slit pore.	99
Figure 6.8 The pressure tensor profiles of Hg confined in the carbon slit pores of (a) $H^* = 3.0$, (b) $H^* = 4.0$, and (c) $H^* = 6.5$ at 300 K and 4,080 bar bulk pressure. The average tangential pressures (dashed lines) are calculated for the accessible pore width, and the values are (a) 1,010 bar, (b) 3,140 bar, and (c) 3,700 bar, respectively. The normal pressures are (a) 2,503 bar, (b) 1,195 bar, and (c) 3,039 bar, respectively.	102

Figure 6.9	The normal pressure and peak value of tangential pressure of Hg confined in carbon slit pore as functions of pore width, at 300 K and 4,080 bar bulk pressure. .	104
Figure 7.1	Snapshots of model carbon pores: (a) cylindrical carbon pore constructed from a multi-walled carbon nanotube, and (b) spherical carbon pores with a small opening. Carbon atoms are shown at reduced scale for clarity.....	108
Figure 7.2	The density and pressure profiles (calculated by the mechanical route using the IK definition) of argon adsorbed in spherical carbon pores with various pore diameters of (a) 2.4 nm, (b) 3.2 nm, (c) 4.0 nm, and (d) 4.8 nm. The thick solid lines on the right vertical axes represent the positions of the pore walls. (e) The normal pressure is shown for the four pore diameters with an expanded vertical scale.	113
Figure 7.3	The (a) tangential and (b) normal pressure profiles (calculated by the mechanical and thermodynamic routes using the IK definition) of argon adsorbed in a spherical carbon pore ($D^* = 8.0$), at 87.3 K and 1 bar bulk pressure. The thick solid lines on the right vertical axes represent the positions of the pore walls.	115
Figure 7.4	The density and pressure profiles (calculated by using the IK definition) of argon adsorbed in (a) slit ($H^* = 8.0$), (b) cylindrical ($D^* = 8.0$) and (c) spherical ($D^* = 8.0$) carbon pores, at 87.3 K and 1 bar bulk pressure. The thick solid lines on the vertical axes represent the positions of the pore walls.	117
Figure 7.5	(a) Radial distribution function for the contact layer of argon at 87.3 K and 1 bar bulk pressure confined in the slit (A, solid line, $H^* = 8.0$), cylindrical (B, dotted line, $D^* = 8.0$), and spherical (C, dashed line, $D^* = 8.0$) carbon pores. (b) The intermolecular pair force between two argon atoms, F , with the most probable nearest neighbor separation distances shown for the three cases illustrated in (a). The most probable separation distance for bulk argon at 87 K and 1 bar bulk pressure is also shown.	118
Figure 7.6	(a) The adsorption isotherms of argon in slit ($H^* = 8.0$), cylindrical ($D^* = 8.0$) and spherical ($D^* = 8.0$) carbon pores at 87.3 K. (b) The peak value of the tangential pressure and the average normal pressure as functions of bulk pressure for argon confined in a spherical carbon pore ($D^* = 8.0$) at 87.3 K.....	120
Figure 8.1	The simulation cell of our flexible model for the carbon slit pore. The dark (green in color) circles represent adsorbate argon molecules, and the light (blue in color) circles represent carbon atoms. Dashed circles represent the equilibrium position of carbons atoms. Carbon atoms are shown at reduced scale for clarity.....	124
Figure 8.2	The normal pressures of argon adsorbed in carbon slit pores and the corresponding pore deformation for various pore widths at (a) 87.3 K and 1 bar bulk pressure and (b) 300.0 K and 3990 bar bulk pressure.....	127
Figure 8.3	The schetimatic illustration of (a) ACFs and (b) an ACF model for molecular simulation.....	129
Figure 8.4	The normal pressure of (a) carbon tetrachloride and (b) water as a function of the pore widths of carbon slit pores at 300 K and 1 bar bulk pressure. The experimental data are included for carbon tetrachloride and water adsorbed in ACF ($H = 0.85$ nm and 1.4 nm).	133

Figure 8.5 The normal pressure of adsorbed LJ argon acting on the wall of (a) cylindrical and (b) spherical carbon pores, at 87.3 K and 1 bar bulk pressure, for various pore widths.	137
Figure 9.1 Simulation cell of silica slit pore. The green circles represent adsorbate argon molecules. Atoms in silica are covalently bonded and less dense than those in carbon wall.	140
Figure 9.2 (a) The density and pressure profiles of argon in the atomistic fixed silica pore model with finite length ($H^* = 3.0$) at 87.3 K and 1 bar bulk pressure, (b) the individual contributions of tangential pressure, and (c) the radial distribution function of the different argon layers.	143
Figure 9.3 Schematic representations of adsorbate molecules accommodated on (a) a rough surface (e.g. surface of a silica pore) and (b) a smooth surface or an atomistic surface with high atomic density (e.g. graphene surface). Dark circles (green in color) represent adsorbate molecules, and light circles or slab (light blue in color) represent wall surfaces.	144
Figure 9.4 The schematic model of a rough pore. The thick solid lines represent the planar layer of graphene, and the red solid curves represent the rough wall surface, while the dotted lines show the average z -position of the rough wall layer.	146
Figure 9.5 A functionalized graphene with 30% coverage of defects including hydroxyl, epoxy, carboxyl, vacancies, and Stone-Wales, obtained by the DFT calculation: (a) the snapshots and (b) fitted by a sine wave curve. [129]	147
Figure 9.6 The adsorption isotherms of argon in carbon slit pore models with various roughness at 87.3 K (a) on a full pressure scale and (b) for low pressures.	149
Figure 9.7 The density and pressure profiles (left) and snapshots (right) of argon adsorbed in carbon pore models with various roughness at 87.3 K and 1 bar bulk pressure.	152
Figure 9.8 The peak value of tangential pressure of argon along the isotherm in carbon slit pore models with varying wall roughness at 87.3 K (a) on a full pressure scale and (b) with expanded vertical scale.	154
Figure 9.9 The average normal pressure of argon along the isotherm in carbon slit pore models with varying roughness at 87.3 K (a) on a log scale and (b) on a linear scale for the bulk pressure (horizontal axis).	156
Figure 9.10 The density and pressure profiles of argon confined in carbon slit pores with rough walls of (a) $\lambda_w = 3.0$ nm and (b) $\lambda_w = 4.0$ nm. The comparisons for the (c) tangential and (d) normal pressure components with those in the pore with smooth wall are also shown.	158

CHAPTER 1

Introduction and Background

Nanophases confined within solids with pores of nanometer dimensions often exhibit physical and chemical properties that are dramatically different from those of the bulk material [1]. Such confinement effects are of fundamental interest across many fields, and result from reduced dimensionality and the strong intermolecular forces between the molecules in the confined phase and the porous material. They find practical applications in areas as diverse as purification of water and air streams, heterogeneous catalysis, drug delivery, sensors, energy storage, as electrodes for fuel cells and supercapacitors, insulators in microcircuits, and in fabrication of nanomaterials such as nanowires.

Phenomena that occur only at very high pressures (e.g. thousands or tens of thousands of bars) in the bulk phase material are often observed to occur in the confined phase at pressures (the pressure of the bulk phase in equilibrium with the confined phase) that are orders of magnitude lower [2]. Examples of such phenomena include high pressure chemical reactions, high pressure solid phases, high pressure effects in solid-liquid equilibria and effects on spectral properties. These examples will be extensively discussed in Chapter 2.

With the aim of providing fundamental understanding of the high pressure effects in confined nanophases, we conduct molecular simulation studies of the pressure tensor of adsorbate confined in microporous materials. Using Semi-Grand Canonical Monte Carlo (SGCMC)

simulations, we examine the effects of the extent of confinement (pore width, pore shapes), temperature, and bulk phase pressure on the density and pressure profiles, and on the radial distribution functions. We find that the in-pore pressure is either enhanced or reduced depending on the nature of interaction between adsorbate and wall atoms. For a wetting adsorbate-wall system, the in-pore pressure is significantly enhanced, while for a non-wetting system this enhancement is much weaker; in some cases the pressure is reduced (e.g. mercury confined in microporous carbons). The enhanced normal pressure, the pressure tensor component which is perpendicular to the wall, leads to changes in the pore width and, for carbons, to changes in graphene interlayer spacing during adsorption, as has been observed experimentally [3].

The dissertation is arranged as follows. In Chapter 2, examples of experimental evidence showing high pressure phenomena in nanopores and some previous relevant simulation works are reviewed. In Chapter 3, the theory of pressure tensor for inhomogeneous fluids and materials (adsorbate) confined in pores is introduced and various ways of calculating pressure tensor components are discussed. In this chapter, a new scheme of calculating pressure tensor in cylindrical and spherical pores by the thermodynamic route is developed. We also present various ways of averaging the pressures in this chapter which correspond to different physical situations and are appropriate for different applications. In Chapter 4, molecular simulation methods, especially the techniques related to the adsorption and implementation of a flexible pore wall model, are discussed. From Chapter 5 to Chapter 9, the results are presented and discussed. In Chapter 5, as a starting point, the study of pressure

enhancement of argon adsorbed in carbon slit pores is presented. The reason for pressure enhancement is also investigated. In Chapter 6, the effects of the wetting parameter (a measure of the ratio of the adsorbate-wall interaction to the adsorbate-adsorbate interaction) on the capillary condensation and the in-pore pressure of the adsorbate are discussed. Specifically, mercury confined in a carbon slit pore, a highly non-wetting system, is studied. In Chapter 7, the pressures of a simple adsorbate (Lennard-Jones argon) confined in nanopores of other simple geometries (cylinder and sphere) are studied. The results show that the curvature of the pore walls causes the effects of pressure increase to be further enhanced. In Chapter 8, the normal pressure of the adsorbate acting on the wall and the resulting pore deformation are studied, and compared with the experimental results. In Chapter 9, the effects of roughness of the pore wall on the confined structure and the resulting pressure are studied, which provides an estimation of the pressure in a more realistic pore. Finally, in Chapter 10 our findings are summarized and recommendations are presented for future work.

CHAPTER 2

Experimental Evidence of High Pressure in Nanopores and Simulation Work

2.1 High Pressure Phases in Pores

Numerous studies observe high pressure phases in nanopores. Liquid-solid transitions in nanopores confined between atomically smooth mica surfaces in surface force apparatus (SFA) experiments have been observed for several substances at temperatures well above their normal melting temperatures, T_{mp} . Examples are shown in Table 2.1. These include cyclohexane [4-6] ($T_{mp} = 279$ K) at 296 K (bulk phase freezes at ~ 440 bar at 296 K) and *n*-dodecane [7] ($T_{mp} = 263.4$ K) at 300 K (bulk phase freezes at $\sim 1,860$ bar at 300 K). Molecular simulations [8] for dodecane between mica surfaces are in agreement with the experimental data.

Table 2.1 Surface force apparatus results showing the melting points of substances in pores.

Substance	Pore width / nm	T_{mp} / K	T_{exp} / K	$P_{freezing}$ at T_{exp} / bar
Cyclohexane [4-6]	1 ~ 7	279	296	~ 440
<i>n</i> -dodecane [7]	2.5 ~ 10	263.4	300	$\sim 1,860$

Another example for high pressure phases is confined water. The structure of confined ice has been studied in carbon nanotubes using molecular simulation [9] and experiment [10], and provides convincing evidence for the formation of different kinds of ice nanocrystals,

including ice VIII and ice IX, phases that only occur at pressures of $> 10^5$ bar for bulk water (Figure 2.1). Similar phenomena were also observed by Sliwinska-Bartkowiak et al. [11]: evidence of the formation of ice VII, VIII and IX, which only occur at pressures above 10^5 bar for bulk water, were observed in porous carbons at temperature about 250 K and atmospheric pressure.

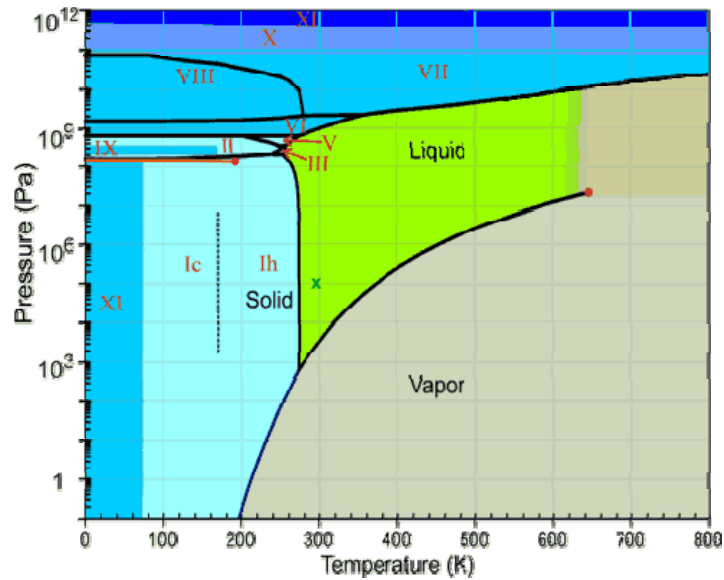


Figure 2.1 Phase diagram for bulk water [12].

Kaneko et al. also observed a high pressure structure for KI in porous materials [13]. They used high-resolution transmission electron microscopy and synchrotron X-ray diffraction experiments to provide evidence that a phase transition occurred in single-walled carbon nanohorns (~ 2 nm) at a pressure lower than 1 bar, for doped KI nanocrystals from the fcc (NaCl type) structure (also named B1 structure) to modified bcc (CsCl type) super-high-

pressure structure (also named B2 structure), which is induced at pressure above 19,000 bar for bulk KI crystals [14].

Other experimental examples of the occurrence of high-pressure phase in pores include: an anomalous rigid assembly structure of methane (characterized by infrared spectroscopy) adsorbed in single-walled carbon nanohorns at 105 ~ 140 K [15], and an increase in the crystallization temperature of carbon tetrachloride from 250 K in the bulk to 303 K in activated carbon fibers (ACFs) of 1 nm pore size [16]. Molecular simulation work also found that the phase diagrams for fluids confined in nanopores are shifted from those for the fluids in the bulk (e.g., freezing at higher temperatures or lower bulk pressures) [17-22]. These findings suggest that the nanopores enhance the in-pore pressure of confined fluids, so that the latter exhibit phase behaviors as if they are under high pressure in the bulk, even though the pressure of the bulk phase in equilibrium with the pore phase is as low as the ambient pressure (~ 1 bar).

2.2 Chemical Reaction in Pores

The well-studied dimerization of nitric oxide, $2\text{NO} \rightleftharpoons (\text{NO})_2$, provides an illustration of the high pressure effect on chemical reaction in pores. In the bulk gas phase, it has a yield of less than 1 mole% dimer at 300 K and 1 bar pressure, but in ACFs having an average pore width of 0.8 nm the yield of dimers is 99%, as measured by magnetic susceptibility [23]. Fourier transform infrared spectroscopy experiments on this reaction in single-walled carbon nanotubes (SWCNTs) with a diameter of 1.35 nm similarly show 100% yield of dimers [24].

These experimental results are summarized in Table 2.2. The molecular simulation results [25] for NO dimerization in slit-shaped carbon pores and carbon nanotubes are in qualitative agreement with these experiments. A simple thermodynamic calculation shows that dimer yields of 98 ~ 99 mole% would only be reached in the bulk phase at pressures between 12,000 and 15,000 bar at these temperatures.

Table 2.2 Comparison of experimental product mole fraction in bulk phase and in porous carbons for the NO dimerization reaction

Porous material	Pore size / nm	T / K	$(NO)_2$ mole fraction	
			Bulk	In Pore
ACF [23]	0.8	298 ~ 423	< 0.01	0.98 ~ 1.0
SWCNT [24]	1.35	103 ~ 136	≤ 0.01	1.0

Another example is the slit pore induced disproportionation reaction of dimerized nitric oxide, $3(NO)_2 \rightleftharpoons 2NO_2 + 2N_2O$ [26]. The reaction was performed in an ACF with an average slit pore width of 0.9 nm at the $(NO)_2$ pressure of < 0.24 bar and at the temperature of 273 ~ 373 K. Infrared spectroscopy was used to determine the gas concentrations. The conversion of $(NO)_2$ in this reaction system was > 50%, but for the bulk gas phase this reaction requires a high $(NO)_2$ pressure of at least 200 bar [27, 28]. The electrochemical reduction of carbon dioxide in micropores of ACFs at ambient bulk pressure (~ 1 bar) is also a good example [29]. The ACFs contained slit-shaped micropores of 2 nm, where the reaction occurred and showed a much higher activity compared with other metal catalyst (iron, nickel, and palladium) supported on non-ACFs. It was found that for these metal catalysts supported on

non-ACFs, the activity for CO₂ reduction is very low at ~ 1 bar [30-32], and is very high at high pressures (30 ~ 60 bar) [33-35]. It suggests that the use of the microporous catalyst materials mimics the effect of high pressure. Similar examples of high pressure reaction in pores include experiments on the ambient temperature reduction of NO to N₂ in Ru-Tailored carbon subnanospace at 0.1 bar bulk pressure; this reduction requires a high pressure of 200 bar for the bulk phase reaction [36]. A simulation study of the ammonia synthesis reaction found that a similar yield of ammonia can be achieved at 300 bar for the bulk phase, but only 50 bar in a pore of 1 nm [25]. All these examples suggest that the microporous materials provide the high pressure required for the bulk phase reactions.

2.3 Surface Force Apparatus Studies

The surface force apparatus is of great interest for studying the effects of confinement, because it provides a model system of a single slit pore with continuously adjustable dimension [37]. Anomalous phase transitions were observed for the fluids confined in SFAs. Besides the increase in melting temperatures of cyclohexane and *n*-dodecane between the mica surfaces whose separation distances are smaller than 10 nm (see Sec. 2.1), Christenson observed two relevant and interesting phase behaviors in confinement studied with the SFA (separation distance ranging from 10 to 20 nm) [38]. The first example is a phase separation in confinement of a binary mixture of perfluoro-*n*-hexane and *n*-hexane, which forms an incompletely miscible system with an upper consolute temperature of 296 K at a volume fraction of ~ 0.5. As the mica surfaces were brought together (after both components were in the condensate form), the volume fractions of the two phases varied from experiment to

experiment, indicating that a phase that is stable in bulk (e.g. in the reservoir) is not necessarily stable in confinement, which may suggest an enhanced effective pressure. The second example concerns the freezing and melting of *n*-octadecane confined in mica surfaces. This system showed an increase of 2 K in melting point of *n*-octadecane, and greater difficulty in being supercooled compared with that in bulk.

SFA can also be used for measuring the force of confined fluid acting on the surfaces. By using SFAs, J. Klein et al. [4] measured the normal force of octamethylcyclotetrasiloxane (OMCTS) confined between two mica surfaces (a slit pore) acting on the mica surfaces. This normal force oscillates between positive and negative values depending on the separation distance between the mica surfaces, ranging from 2 ~ 7 nm (see Figure 2.2a). The oscillation arises from the discretely increased capacity of accommodating fluid layers as the pore width increases. This oscillating behavior of the normal force and the proposed explanation agree with the simulation study of the solvation pressure (which is the pressure normal to the wall minus the bulk pressure) [39]. Similar experimental results were also found for tetrakis(trimethyl)siloxysilane (TMSS) confined between mica surfaces (pore width ranging from 2 ~ 4 nm) [40], and aqueous solutions (e.g., KNO_3 , BaCl_2 , or $\text{Ca}(\text{NO}_3)_2$) confined between mica surfaces [41, 42] (see Figure 2.2b).

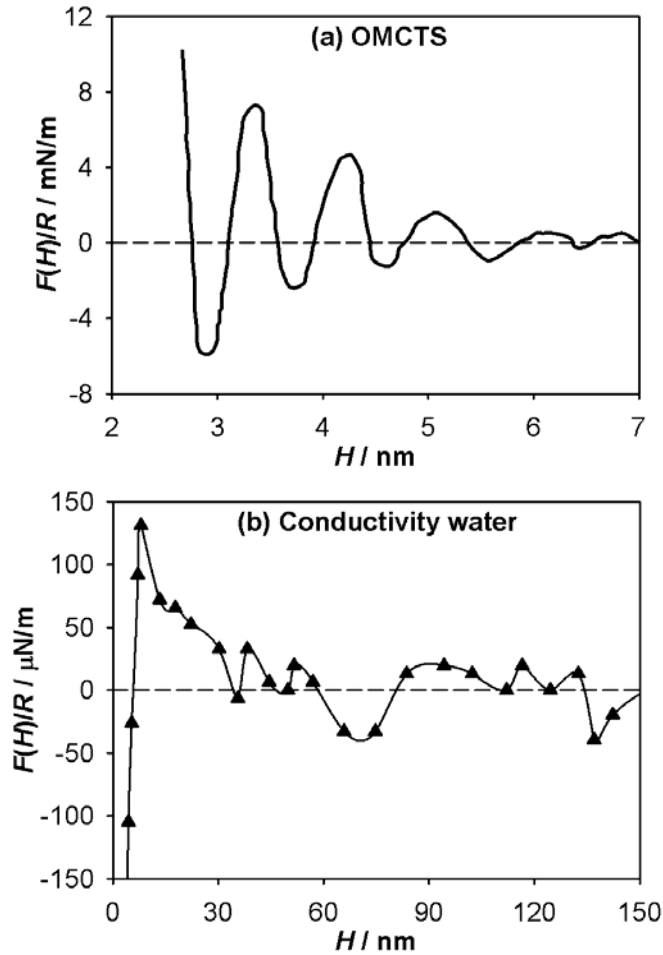


Figure 2.2 The normal forces acting on the mica surfaces of SFAs by the confined fluids (a) OMCTS (recreated by using the data from Fig. 1B of [4]) and (b) conductivity water (pH = 6.0~6.2) (recreated by using the data from Fig. 2 of [42]) as functions of the separation distance between the mica surfaces.

2.4 Adsorption and Structure Deformation

Several experimental studies show significant effects of the adsorption of a confined nanophase on the pore width and interlayer atomic spacing, indicating a strong positive or negative pressure normal to the pore walls. For example, by small-angle X-ray scattering

(SAXS) measurements, Professor Kaneko's group (Chiba University, Japan) found that the pore size of the activated carbon fiber (ACF) changes apparently with the relative humidity (the adsorption of water) [3, 43]. In one study, they found that the pore size of an ACF increased first with increasing relative humidity until $P/P_o \sim 0.5$ and then decreased, and the pore size change could be as large as 25% [3]. In another study, the interlayer spacing (d_{002}) of graphene sheets in ACF was found to change up to 0.06 nm with the loading of water, and the pore width was found to swell from 0.8 nm to 0.9 nm. The water adsorption also compresses and reorients the micrographitic layers [43]. Similar phenomena were also observed in other experiments: McBain et al. observed a linear expansion of an activated carbon block due to the adsorption of water, benzene and heptane by measuring the dimensions of the charcoal rod of ~ 65 mm [44]; Dacey et al. observed a contraction ($\sim 0.1\%$ in volume) of activated carbons followed by a large expansion during the adsorptions of water, methanol and benzene [45]. Micrographitic structure changes of ACFs have been observed by *in situ* X-ray diffraction [46], as well as the swelling of the micropores by *in situ* SAXS [47] during adsorption of water.

It is reported that due to their exceptional flexibility, metal-organic frameworks (MOFs) show an obvious stimulus-responsive behavior to the adsorption of guest molecules by undergoing structural changes. For example, by a combined computational and powder diffraction study, Mellot-Draznieks et al. found that MIL-88 swells by about 85% of its cell volume (atomic displacement larger than 0.4 nm) while fully retaining its topology upon exposure to water and various alcohols [48]. In another example, there is a transition between

two stable structures during the adsorption of water and carbon dioxide in the MIL-53 family of MOFs, determined by powder X-ray diffraction [49, 50]. The MIL-53 is a framework made of parallel one-dimensional $M(OH)$ chains ($M = Al^{3+}, Cr^{3+}$), connected by 1,4-benzenedicarboxylate ligands to form linear diamond-shaped channels, wide enough to accommodate small adsorbate molecules. This structure can oscillate between two conformations (“breathing”), one of which is the “large-pore phase” and the other is the “narrow-pore phase”, with a $\sim 40\%$ difference in the pore volume [51]. A stress-based model was proposed for this breathing by Neimark et al. and their simulation work showed results similar to the experimental observations of MIL-53 breathing due to the adsorption [52]. All of these structural changes in MOFs suggest a high pressure for the adsorbate confined in the micropores.

Because of these observations on pore deformation due to the adsorption, Professor Schoen’s group (Technical University Berlin, Germany) has proposed to apply flexibility to the pore wall atoms in molecular simulations to include these effects, rather than traditionally treating the wall atoms as fixed in the space [53]. Moreover, Kowalczyk et al. applied flexibility to a smooth Steele’s (10,4,3) wall [54], and a similar study was done by Do et al. [55]. We will discuss the flexible model and the related molecular simulation method in Sec. 4.3.

2.5 Simulation Work on Pressure Tensor of Fluids

Although abundant experimental observations, including the examples discussed in this chapter, suggest that the confined fluids are under a very large effective pressure enhanced

by the microporous materials, current experimental techniques are not able to directly measure all components of the in-pore pressure tensor. We note that the normal force acting on the pore wall can be measured by SFAs (Sec. 2.3), but due to layering effects in the pore, the confined fluids are inhomogeneous, and thus the pressure acting parallel to the wall (tangential pressure) is different from the pressure acting normal to the wall (normal pressure). Many of the high-pressure phenomena occur due to the very high tangential pressure. For example, phase transitions to the high-pressure phases or the high-pressure chemical reactions occur mainly for the fluid layers in contact with the pore wall, because of the very high planar pressure in those layers (tangential pressure).

Via molecular simulation methods, the pressures of fluids acting in all directions can be calculated directly (for an extensive discussion, see Chapter 3). Walton et al., 1983 [56] calculated the normal and tangential pressure profiles of a gas-liquid interface system of a pure Lennard-Jones (LJ) fluid, using molecular dynamics (see a brief introduction in Sec. 4.2). They found that the normal pressure is almost a constant across the interface and is equal to the bulk fluid pressure, while the tangential pressure shows a strong negative peak, indicating a strong attraction between molecules, at the interface. This agrees with the surface tension phenomenon of a gas-liquid equilibrium system, i.e., the attraction tends to minimize the surface area. Following this, Lee et al., 1984, calculated the pressure tensor components for a similar gas-liquid system, where the fluid was LJ argon-krypton mixtures, and obtained similar results [57]. The in-pore pressure studies by molecular simulations started in the 1990's. Balbuena et al., 1993 [39], studied the solvation pressure in slit pores,

and found the oscillating behavior of the normal pressure with increasing pore width, which agreed with experimental results found by SFA (see Sec. 4.3). Similar simulation work by Lei and Leng, 2010 [58], found that for argon confined in a slit of two simulated SFA surfaces the normal pressure oscillated with an amplitude of 1,000 ~ 8,000 bar, decreasing with increasing pore width. Hamada et al., 2009 [59], calculated the normal and tangential pressures for simple fluids confined in slit and cylindrical nanopores. They found that the tangential pressure was large and positive, which resulted in a negative surface tension, indicating that the fluid molecules were more likely to be located on the wall-fluid interface, rather than staying in the fluid phase. However, the tangential pressure they calculated was an average over the whole pore, and they did not calculate the local tangential pressure as a function of the distance from the pore wall. For the cylindrical case, they only calculated the average tangential pressure acting on the axial direction (there is another tangential pressure in the azimuthal direction). Van Workum and de Pablo, 2003 [60], calculated the local stress tensor (equal to minus the pressure tensor) of LJ fcc crystal film confined in hard walls. They observed the layering effect, and the tangential stress peaked at the position where the density of crystal peaked, suggesting that the tangential pressure depends on how close-packed the adsorbate molecule is in the layer. Pellenq et al., 1997 [61], calculated the pressure of a colloidal suspension of charged particles confined between two charged surfaces by canonical Monte Carlo simulations, and found the normal pressure (the swelling pressure of water) oscillation with pore width. Similar results of the normal pressure of water in pores were observed by Giovambattista et al., 2009 [62], who also found the in-pore

tangential pressure of water was $\sim 3,000$ bar. But again, this tangential pressure was averaged over the pore width, rather than the local tangential pressure for a specific layer.

In summary, there is not a systematic molecular simulation study of the local pressure tensor components for the confined system so far, but it is important to obtain a fundamental understanding of local pressure, especially the tangential pressure, of a certain layer, since the very high local tangential pressure could be the reason for high-pressure phenomena in porous materials. In this dissertation, we present a systematic study of the pressure tensor of various fluids confined in pores with different geometric and energetic properties.

CHAPTER 3

Pressure Tensor of Inhomogeneous Fluids in Porous Materials

3.1 Pressure Tensor and Hydrostatic Equilibrium

Pressure is the force per unit area acting on a surface element and is the sum of a kinetic contribution which arises from the convective momentum transport of molecules and a configurational contribution which arises from interactions among molecules. For the homogeneous fluids, such as the air in a room, or water in a glass, the pressure can be regarded as a scalar. However, for inhomogeneous fluids, for example, the fluids confined in nanopores, pressure is a second-order tensor, \mathbf{P} , whose component $P_{\alpha\beta}$ gives the force per unit area in the β -direction on a surface pointing in the α -direction. Because of the geometrical symmetry and system orthogonality, the off-diagonal components of the pressure tensor of the adsorbate confined in planar, cylindrical and spherical pores are zero, provided that the system is not under strain, while the non-trivial diagonal components are only functions of the distance between a position in space and the wall surface [63]. For example, for the fluids confined in the slit pore, the tangential pressure (parallel to the walls, which lie in the xy -plane) $P_{xx} = P_{yy} = P_T$ and the normal pressure (pointing to the wall) $P_{zz} = P_N$ only depend on z , the distance from the pore wall. Similarly, in the cylindrical pore, using cylindrical polar coordinates (ρ, φ, z) , the tangential pressure in the φ -direction $P_{\varphi\varphi} = P_{T\varphi}$, the tangential pressure in the z -direction $P_{zz} = P_{Tz}$, and the normal pressure $P_{\rho\rho} = P_N$ are only functions of the radial coordinate ρ . In spherical pores, the tangential pressure in the φ - and

θ -directions $P_{\varphi\varphi} = P_{\theta\theta} = P_T$ and the normal pressure $P_{\rho\rho} = P_N$ are only functions of the radial coordinate ρ [63]. Pressure tensor components for planar, cylindrical and spherical surfaces are illustrated in Figure 3.1, and can be expressed mathematically in Eqn. (3.1):

$$\mathbf{P} = \mathbf{P}_{kin} + \mathbf{P}_{conf} = \begin{cases} \begin{bmatrix} P_T(z) & 0 & 0 \\ 0 & P_T(z) & 0 \\ 0 & 0 & P_N(z) \end{bmatrix} & \text{(slit)} \\ \begin{bmatrix} P_N(\rho) & 0 & 0 \\ 0 & P_{T\varphi}(\rho) & 0 \\ 0 & 0 & P_{Tz}(\rho) \end{bmatrix} & \text{(cylinder)} \\ \begin{bmatrix} P_N(\rho) & 0 & 0 \\ 0 & P_T(\rho) & 0 \\ 0 & 0 & P_T(\rho) \end{bmatrix} & \text{(sphere)} \end{cases} \quad (3.1)$$

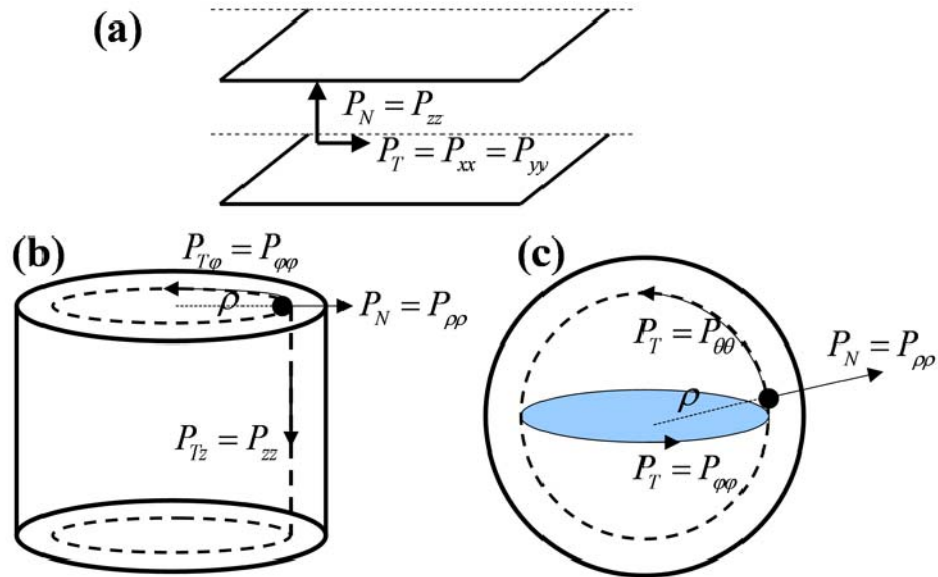


Figure 3.1 Pressure tensor components for (a) planar, (b) cylindrical and (c) spherical surfaces.

Equilibrium between the confined and bulk phases requires, in addition to the usual thermodynamic conditions (equality of temperatures and chemical potentials), hydrostatic equilibrium (i.e. no net momentum transfer between the two phases, also called mechanical equilibrium):

$$\nabla \cdot \mathbf{P} = -\rho_{ad}(\mathbf{r})\nabla v(\mathbf{r}), \quad (3.2)$$

where ρ_{ad} is the number density of the fluid (interchangeable with adsorbate in this dissertation) molecules, and v is the external force field, both of which are functions of the position \mathbf{r} where the pressure tensor is evaluated. Specifically, in the absence of external fields (or alternatively, when the external force field is negligible compared to the strong internal interaction), the hydrostatic equilibrium condition can be expressed as [63, 64]:

$$\nabla \cdot \mathbf{P} = 0. \quad (3.3)$$

In molecular simulations, for this condition to be satisfied, in general, the confined phase must be in physical contact with the bulk phase. However, if the wall atoms are fixed in space the condition is satisfied in grand canonical Monte Carlo simulations without the necessity of such physical contact [64]. The hydrostatic equilibrium condition (Eqn. (3.3)) leads to useful results and relations for the pressure components (see Appendix A for more details):

$$\text{Slit: } P_N = \text{constant (independent of } z) \quad (3.4)$$

$$\text{Cylinder: } P_{T\phi}(\rho) = P_N(\rho) + \rho \frac{dP_N(\rho)}{d\rho} \quad (3.5)$$

$$\text{Sphere: } P_T(\rho) = P_N(\rho) + \frac{\rho}{2} \frac{dP_N(\rho)}{d\rho} \quad (3.6)$$

To calculate the pressure tensor \mathbf{P} or its component as functions of the position in space in Eqn. (3.1), the kinetic contribution \mathbf{P}_{kin} is well-defined as the ideal gas pressure:

$$\mathbf{P}_{kin} = \rho_{ad}(\mathbf{r}) k_B T \mathbf{1}, \quad (3.7)$$

where k_B is Boltzmann constant, T is the temperature and $\mathbf{1}$ is the second-order unit tensor. Eqn. (3.7) is true for any coordinate system (Cartesian, cylindrical and spherical). On the other hand, the configurational contribution \mathbf{P}_{conf} is not uniquely defined, but can be operationally defined and calculated by various ways as discussed below.

3.2 Mechanical Route

The expression of microscopic stress tensor $\boldsymbol{\sigma}(\mathbf{r}, t)$ in a fluid can be obtained from the microscopic law of momentum conservation at some point \mathbf{r} in the fluid at time t . The pressure tensor $\mathbf{P}(\mathbf{r})$ is then given by the ensemble average of minus the stress tensor:

$$\mathbf{P}(\mathbf{r}) = -\langle \boldsymbol{\sigma}(\mathbf{r}, t) \rangle. \quad (3.8)$$

The microscopic conservation law for linear momentum is derived in [63]:

$$j^\alpha(\mathbf{r}, t) = -\frac{\partial}{\partial r^\beta} \sum_i \frac{p_i^\alpha p_i^\beta}{m_i} \delta(\mathbf{r} - \mathbf{r}_i) + \sum_i \dot{p}_i^\alpha \delta(\mathbf{r} - \mathbf{r}_i), \quad (3.9)$$

where J^α is the rate of change of the α component of the linear momentum density, p_i is the momentum of molecule i , and $\delta(x)$ is the Dirac Delta function. The second term on the right

hand side in Eqn. (3.9) can be expressed in a more explicit form by considering the relationship between force and momentum:

$$\sum_i \dot{p}_i^\alpha \delta(\mathbf{r} - \mathbf{r}_i) = - \sum_i \left[\frac{\partial}{\partial r_i^\alpha} U(\mathbf{r}^N, \boldsymbol{\omega}^N) + \frac{\partial}{\partial r_i^\alpha} V(\mathbf{r}^N) \right] \delta(\mathbf{r} - \mathbf{r}_i), \quad (3.10)$$

where U and V are the internal potential energy and external force field, respectively.

After mathematical manipulations (and considering that Newton's third law requires that $\sum_i -\nabla_i U$ vanishes) for Eqn. (3.10), and we obtain:

$$\begin{aligned} \sum_i \dot{p}_i^\alpha \delta(\mathbf{r} - \mathbf{r}_i) &= - \sum_i \left[\frac{\partial}{\partial r_i^\alpha} U(\mathbf{r}^N, \boldsymbol{\omega}^N) + \frac{\partial}{\partial r_i^\alpha} V(\mathbf{r}^N) \right] \delta(\mathbf{r} - \mathbf{r}_i) \\ &= - \sum_i \frac{\partial}{\partial r_i^\alpha} U(\mathbf{r}^N, \boldsymbol{\omega}^N) \delta(\mathbf{r} - \mathbf{r}_i) - \sum_i \frac{\partial}{\partial r_i^\alpha} V(\mathbf{r}^N) \delta(\mathbf{r} - \mathbf{r}_i) \\ &= - \sum_i \frac{\partial U(\mathbf{r}^N, \boldsymbol{\omega}^N)}{\partial r_i^\alpha} [\delta(\mathbf{r} - \mathbf{r}_i) - \delta(\mathbf{r} - \mathbf{r}_0)] - \rho_{ad}(\mathbf{r}, t) \frac{\partial v(\mathbf{r})}{\partial r^\alpha}, \quad (3.11) \\ &= - \sum_i \frac{\partial U(\mathbf{r}^N, \boldsymbol{\omega}^N)}{\partial r_i^\alpha} \left[- \frac{\partial}{\partial r^\beta} \int_{C_{0i}} d\tilde{l}^\beta \delta(\mathbf{r} - \tilde{l}^\beta) \right] - \rho_{ad}(\mathbf{r}, t) \frac{\partial v(\mathbf{r})}{\partial r^\alpha} \\ &= \frac{\partial}{\partial r^\beta} \sum_i \left[\frac{\partial U(\mathbf{r}^N, \boldsymbol{\omega}^N)}{\partial r_i^\alpha} \right] \int_{C_{0i}} d\tilde{l}^\beta \delta(\mathbf{r} - \tilde{l}^\beta) - \rho_{ad}(\mathbf{r}, t) \frac{\partial v(\mathbf{r})}{\partial r^\alpha} \end{aligned}$$

where C_{0i} is an arbitrary contour from the center of mass position of particle i , to an arbitrary point \mathbf{r}_0 in the fluid.

By substituting Eqn. (3.11) into Eqn. (3.9), we get

$$\begin{aligned}
j^\alpha(\mathbf{r}, t) &= -\frac{\partial}{\partial r^\beta} \sum_i \frac{p_i^\alpha p_i^\beta}{m_i} \delta(\mathbf{r} - \mathbf{r}_i) + \sum_i \dot{p}_i^\alpha \delta(\mathbf{r} - \mathbf{r}_i) \\
&= \frac{\partial}{\partial r^\beta} \left\{ -\rho_{ad}(\mathbf{r}, t) k_B T + \sum_i \frac{\partial U(\mathbf{r}^N \omega^N)}{\partial r_i^\alpha} \int_{C_{0i}} d\tilde{l}^\beta \delta(\mathbf{r} - \tilde{l}) \right\} - \rho_{ad}(\mathbf{r}, t) \frac{\partial v(\mathbf{r})}{\partial r^\alpha}. \quad (3.12)
\end{aligned}$$

If we define

$$\begin{aligned}
j^\alpha(\mathbf{r}, t) &= \frac{\partial}{\partial r^\beta} \sigma^{\alpha\beta}(\mathbf{r}, t) - \rho_{ad}(\mathbf{r}, t) \frac{\partial v(\mathbf{r})}{\partial r^\alpha} \\
&= \frac{\partial}{\partial r^\beta} \left[\sigma_{kin}^{\alpha\beta}(\mathbf{r}, t) + \sigma_{conf}^{\alpha\beta}(\mathbf{r}, t) \right] - \rho_{ad}(\mathbf{r}, t) \frac{\partial v(\mathbf{r})}{\partial r^\alpha}, \quad (3.13)
\end{aligned}$$

and considering the relationship between the stress tensor and pressure tensor (Eqn. (3.8)), we get the expressions for the kinetic and configurational contributions and the total pressure tensor from the mechanical route [63]:

$$\mathbf{P}(\mathbf{r}) = \rho_{ad}(\mathbf{r}) k_B T \mathbf{1} - \left\langle \sum_i \frac{\partial U(\mathbf{r}^N \omega^N)}{\partial \mathbf{r}_i} \int_{C_{0i}} d\tilde{l} \delta(\mathbf{r} - \tilde{l}) \right\rangle, \quad (3.14)$$

$$\mathbf{P}_{kin} = \rho_{ad}(\mathbf{r}) k_B T \mathbf{1}, \quad (3.15)$$

$$\mathbf{P}_{conf} = - \left\langle \sum_i \frac{\partial U(\mathbf{r}^N \omega^N)}{\partial \mathbf{r}_i} \int_{C_{0i}} d\tilde{l} \delta(\mathbf{r} - \tilde{l}) \right\rangle. \quad (3.16)$$

In the case that the spherical particles interact in a purely pair-wise fashion, the configurational contribution can be simplified as:

$$\mathbf{P}_{conf} = -\frac{1}{2} \left\langle \sum_{i \neq j}^N \frac{du(\mathbf{r}_{ij})}{d\mathbf{r}_{ij}} \int_{C_{ij}} \delta(\mathbf{r} - \tilde{\ell}) d\tilde{\ell} \right\rangle, \quad (3.17)$$

where C_{ij} is an arbitrary contour from the center of mass position of particle i , \mathbf{r}_i , to the center of mass position of particle j , \mathbf{r}_j , $\mathbf{r}_{ij} = \mathbf{r}_j - \mathbf{r}_i$, and $\langle \dots \rangle$ indicates an ensemble average of the quantity inside.

The kinetic contribution to the pressure tensor, as shown in Eqn. (3.15), is well defined, and easy to obtain from simulation. However, the configurational contribution is not uniquely defined because of the arbitrary nature of the integral contour C_{ij} in Eqn. (3.17). Physically this means that there is no unique way of determining how interactive forces between particles should be assigned to surface elements of the local pressure tensor. This is a consequence of the momentum flux being defined with respect to the gradient of the pressure tensor and not the pressure tensor itself [63, 65]. For a homogeneous or bulk system, the choice of the integral contour has negligible effects on the pressure tensor [57], but for inhomogeneous fluids, e.g., the fluids confined in nanopores, the choice matters. Two simple but widely-used choices are the Irving-Kirkwood choice (interchangeable with “IK definition” in this dissertation) and Harasima choice (interchangeable with “Harasima definition” in this dissertation).

3.2.1 Irving-Kirkwood Choice

The most natural choice was proposed by Irving and Kirkwood [66], who chose the integration path to be a straight line connecting particles i and j , along the vector \mathbf{r}_{ij} (as illustrated in Figure 3.2a):

$$\tilde{\ell}(\mathbf{r}_i, \mathbf{r}_j) = \lambda \mathbf{r}_{ij} + \mathbf{r}_i; \quad 0 \leq \lambda \leq 1. \quad (3.18)$$

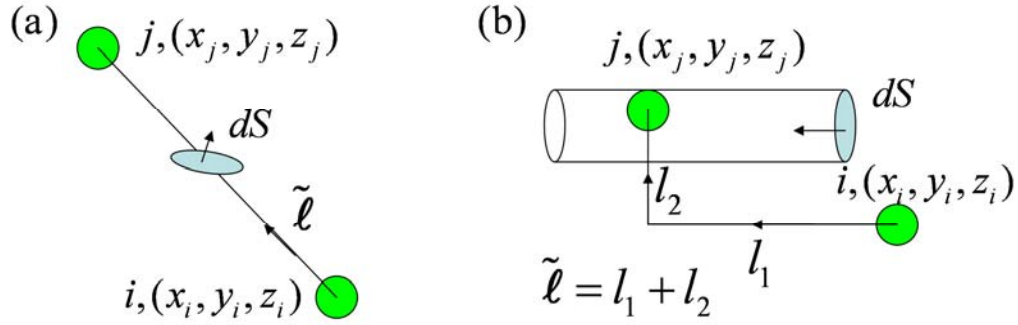


Figure 3.2 Schematic representations of two pressure tensor definition: (a) Irving-Kirkwood choice and (b) Harasima choice of the integral contour C_{ij} between particles i and j . Here dS is an element of area in some infinite plane S .

With this choice substituted into Eqn. (3.17), the configurational contribution of the pressure tensor by IK definition can be expressed as [66]:

$$\mathbf{P}_{conf}^{IK}(\mathbf{r}) = -\frac{1}{2} \left\langle \sum_{i \neq j}^N \frac{\mathbf{r}_i \mathbf{r}_j}{r_{ij}} \frac{du(\mathbf{r}_{ij})}{dr_{ij}} \int_0^1 d\lambda \delta(\mathbf{r}_i - \mathbf{r} + \lambda \mathbf{r}_{ij}) \right\rangle. \quad (3.19)$$

The Dirac Delta function in Eqn. (3.19) and the visualization of Figure 3.2a indicate a physical meaning of IK definition that the interactive force between particles i and j contributes to the pressure tensor at a surface element dS if the joining straight line between particles i and j passes through dS . The above derivations and arguments hold true for all the orthogonal coordinate systems (e.g., Cartesian, cylindrical and spherical coordinate systems).

Specifically, the expressions of pressure tensor components (the tangential pressure P_T and the normal pressure P_N) for a planar surface were derived by Walton et al. [56] for an infinite interface in the xy -plane and evaluated at a certain z -position:

$$P_{T,IK}(z) = \rho(z)k_B T - \frac{1}{4A} \left\langle \sum_{i \neq j} \frac{x_{ij}^2 + y_{ij}^2}{r_{ij}} \frac{1}{|z_{ij}|} \frac{du(r_{ij})}{dr_{ij}} \theta\left(\frac{z-z_i}{z_{ij}}\right) \theta\left(\frac{z_j-z}{z_{ij}}\right) \right\rangle, \quad (3.20)$$

$$P_{N,IK}(z) = \rho(z)k_B T - \frac{1}{2A} \left\langle \sum_{i \neq j} \frac{z_{ij}^2}{r_{ij}} \frac{1}{|z_{ij}|} \frac{du(r_{ij})}{dr_{ij}} \theta\left(\frac{z-z_i}{z_{ij}}\right) \theta\left(\frac{z_j-z}{z_{ij}}\right) \right\rangle. \quad (3.21)$$

where $\theta(x)$ is the Heaviside unit step function, A is the area of the surface, and x_{ij} , y_{ij} , and z_{ij} are components of the intermolecular separation vector \mathbf{r}_{ij} . The expression in Eqn. (3.20) results from averaging the two in-plane components, $P_{T,IK}(z) = (P_{xx}(z) + P_{yy}(z))/2$, while $P_{N,IK}(z) = P_{zz}(z)$, as discussed in Sec. 3.1 (also Eqn. (3.1)).

For a spherical surface, Tjatjopoulos and Mann published detailed derivations for the pressure tensor components by the IK definition [67]. A summarized derivation is presented here, and only the configurational contribution is discussed, because the kinetic part is well-defined.

Considering the identity of Dirac Delta function in spherical coordinates [68]:

$$\delta(\mathbf{a} - \mathbf{b}) = \frac{1}{a_\rho^2 \sin a_\theta} \delta(a_\rho - b_\rho) \delta(a_\phi - b_\phi) \delta(a_\theta - b_\theta), \quad (3.22)$$

the general equation for the configurational pressure tensor (Eqn. (3.17)) can be written as

$$\mathbf{P}_{conf,IK}(\mathbf{r}) = -\frac{1}{2} \left\langle \sum_{i \neq j}^N \frac{du(\mathbf{r}_{ij})}{d\mathbf{r}_{ij}} \frac{\mathbf{r}_{ij}}{\rho^2 \sin \theta} \int_0^1 \delta(\rho-l) \delta(\varphi-l_\varphi) \delta(\theta-l_\theta) d\lambda \right\rangle \quad (3.23)$$

where $\mathbf{r} = \rho \mathbf{e}_\rho + \theta \mathbf{e}_\theta + \varphi \mathbf{e}_\varphi$ is the position where the pressure tensor is evaluated, and $\tilde{\ell} = l \mathbf{e}_\rho + l_\theta \mathbf{e}_\theta + l_\varphi \mathbf{e}_\varphi = \lambda \mathbf{r}_{ij} + \mathbf{r}_i$ ($0 \leq \lambda \leq 1$) is the integral contour, where \mathbf{e}_ρ , \mathbf{e}_θ , and \mathbf{e}_φ are unit vectors at evaluated positions (not constants as in the Cartesian system).

As discussed previously, for a spherically symmetric system, the pressure tensor depends only on the radius coordinate, ρ . The configurational normal pressure can be obtained by averaging over the ρ -surface, where $A_\rho = 4\pi\rho^2$:

$$P_{conf,N}(\rho) = \frac{1}{4\pi} \int_0^{2\pi} d\varphi \int_0^\pi d\theta \sin\theta [\mathbf{e}_\rho(\theta, \varphi) \cdot \mathbf{P}_{conf}(\mathbf{r}) \cdot \mathbf{e}_\rho(\theta, \varphi)]. \quad (3.24)$$

By substituting Eqn. (3.23) into Eqn. (3.24) and considering the following identity:

$$\int_0^1 f(\lambda) d\lambda = \int_{-\infty}^{+\infty} f(\lambda) \theta(\lambda) \theta(1-\lambda) d\lambda, \quad (3.25)$$

the configurational normal pressure by IK definition, after appropriate mathematical manipulation, can be rewritten as:

$$P_{conf,N,IK}(\rho) = -\frac{1}{8\pi\rho^2} \left\langle \sum_{i \neq j}^N \int_{-\infty}^{+\infty} (d\lambda) \left[\mathbf{e}_l \cdot \frac{du(\mathbf{r}_{ij})}{d\mathbf{r}_{ij}} \right] [\mathbf{r}_{ij} \cdot \mathbf{e}_l] \delta(\rho-l) \theta(\lambda) \theta(1-\lambda) \right\rangle, \quad (3.26)$$

where $\mathbf{e}_l = \mathbf{e}_\rho$ evaluated at $\tilde{\ell}$ is the unit radial vector in the direction of the vector $\tilde{\ell}$. Also note that, in Eqn. (3.26), the scalar l is a function of λ .

A necessary condition that a particular pair ij will contribute to the stresses acting on the ρ -surface is that the argument of the Dirac Delta function in Eqn. (3.26) is zero:

$$f(\lambda) = \rho - l(\lambda) = \rho - \|\lambda \mathbf{r}_{ij} + \mathbf{r}_i\| = 0. \quad (3.27)$$

The roots of Eqn. (3.27) can be obtained by solving the quadratic equation:

$$r_{ij}^2 \lambda^2 + 2\lambda \mathbf{r}_{ij} \cdot \mathbf{r}_i + \rho_i^2 - \rho^2 = 0. \quad (3.28)$$

Mathematically, there would be 0, 1 or 2 real roots for Eqn. (3.28), depending on its discriminant. Furthermore, considering the Heaviside unit step functions in Eqn. (3.28), only the roots lying between 0 and 1 will contribute. Geometrically, if the straight joining line between the particles i and j crosses the ρ -surface (a spherical shell) n times ($n = 0, 1$ or 2), the intermolecular force will contribute to the pressure tensor evaluated at the ρ -surface n times. In Figure 1 of [67], six different cases are illustrated schematically.

If the real roots of Eqn. (3.28) are repeating (or sometimes regarded as a single real root), a trivial value of $(\mathbf{r}_{ij} \cdot \mathbf{e}_l)$ will result, and thus only the case of non-repeating real roots needs to be considered. We denote these two distinct real roots of Eqn. (3.28) as $\alpha_{k(ij)}$, and the normal pressure by IK definition in a spherical surface can be derived as (after appropriate mathematical manipulations):

$$P_{conf,N,IK}(\rho) = -\frac{1}{8\pi\rho^2} \left\langle \sum_{i \neq j} \sum_{k=1}^2 \frac{|\mathbf{r}_{ij} \cdot \mathbf{e}_l(\alpha_{k(ij)})|}{r_{ij}} \frac{du(r_{ij})}{dr_{ij}} \theta(\alpha_{k(ij)}) \theta(1 - \alpha_{k(ij)}) \right\rangle, \quad (3.29)$$

where $\mathbf{e}_l(\alpha_{k(ij)}) = \tilde{\ell}(\alpha_{k(ij)}) / \|\tilde{\ell}(\alpha_{k(ij)})\|$.

The configurational tangential pressure of a spherical surface (P_T or $P_{\varphi\varphi}$) can be derived similarly by spatially averaging over the appropriate surfaces. The detailed derivation is also discussed in [67], and a brief outlined derivation is presented here. Consider a φ -surface defined by $\rho \in [\rho - \Delta, \rho + \Delta]$, $\theta \in [0, \pi]$, and $\varphi = \text{constant}$, and ρ is the radial position where the pressure tensor is evaluated, and Δ is a tiny radial increment (small compared to the molecule diameter). Then the configurational tangential pressure can be averaged as:

$$P_{conf,T}(\rho) = \frac{1}{2\pi\rho\Delta} \int_0^\pi (d\theta) \int_{\rho-\Delta}^{\rho+\Delta} (d\rho) \rho [\mathbf{e}_\varphi(\varphi) \cdot \mathbf{P}_{conf}(\mathbf{r}) \cdot \mathbf{e}_\varphi(\varphi)]. \quad (3.30)$$

By substituting Eqn. (3.23) into Eqn. (3.30) and after appropriate mathematical manipulations, the configurational tangential pressure can be written as:

$$P_{conf,T,IK}(\rho) = -\frac{1}{4\pi\rho\Delta} \left\langle \sum_{i \neq j} \int_{-\infty}^{+\infty} d\lambda \left[\mathbf{e}_\varphi(\varphi) \cdot \frac{d\mathbf{u}(\mathbf{r}_{ij})}{d\mathbf{r}_{ij}} \right] \left[\mathbf{r}_{ij} \cdot \mathbf{e}_\varphi(\varphi) \right] \frac{1}{l \sin l_\theta} \right. \\ \left. \times \theta(\rho + \Delta - l) \theta(l - \rho + \Delta) \theta(\lambda) \theta(1 - \lambda) \delta(\varphi - l_\varphi) \right\rangle \quad (3.31)$$

The interaction of the ij pair contributes to the configurational tangential pressure if the argument of the Dirac Delta function in Eqn. (3.31) is zero, i.e., the root of the following equation provides a single value of λ (which should also be between 0 and 1):

$$f(\lambda) = \varphi - l_\varphi(\lambda) = \varphi - \arctan \frac{y_i + \lambda y_{ij}}{x_i + \lambda x_{ij}} = 0. \quad (3.32)$$

By solving for Eqn. (3.32), a single root is obtained:

$$\lambda_{ij} = \frac{y_i - x_i \tan \varphi}{x_{ij} \tan \varphi - y_{ij}}. \quad (3.33)$$

The final expression for the configurational tangential pressure is then given by:

$$P_{conf,T,IK}(\rho) = \frac{-1}{4\pi\rho\Delta} \left\langle \sum_{i \neq j} |\mathbf{r}_{ij} \cdot \mathbf{e}_\varphi| \frac{u'(r_{ij})}{r_{ij}} \theta(\rho + \Delta - l(\lambda_{ij})) \theta(l(\lambda_{ij}) - \rho + \Delta) \theta(\lambda_{ij}) \theta(1 - \lambda_{ij}) \right\rangle \quad (3.34)$$

where the unit vector $\mathbf{e}_\varphi = -\mathbf{e}_x \sin \varphi + \mathbf{e}_y \cos \varphi$.

3.2.2 Harasima Choice for the Planar Surface

Another famous choice of the contour C_{ij} in Eqn. (3.17) is the Harasima choice [69], where for the planar surface the path is composed of two straight segments: from (x_i, y_i, z_i) to (x_j, y_j, z_i) and then from (x_j, y_j, z_i) to (x_j, y_j, z_j) . Geometrically, that means the interaction of the ij pair contributes to the surface dS if one of the particles lies in the cylinder (or prism) whose base is dS , and another particle is located on the other side of the plane of dS , as shown in Figure 3.2b.

For the planar case, the Harasima normal component of pressure tensor is the same as that for the IK definition (Eqn. (3.21)), and the tangential component can be derived as [56]:

$$P_{T,H}(z) = \rho(z) k_B T - \frac{1}{4A} \left\langle \sum_{i \neq j} \frac{x_{ij}^2 + y_{ij}^2}{r_{ij}} \frac{du(r_{ij})}{dr_{ij}} \delta(z - z_i) \right\rangle. \quad (3.35)$$

The physical meaning of the Dirac Delta function in Eqn. (3.35) is that the tangential pressure is zero at the plane where there is no molecule. Thus, in a layering system, the Harasima tangential pressure is “concentrated” in the planes where the molecular layers are located, whereas the IK tangential pressure is “distributed” also in the space between the molecular layers.

Both the IK and Harasima definitions yield the same result for the surface tension at planar interfaces [65]. However, in addition to being the most widely used and natural choice, only the IK definition has been shown to yield expressions for the pressure difference, surface tension and Tolman length that are consistent with those obtained using microscopic sum rules [70]. More seriously, the Harasima contour has been found to yield inconsistent and unphysical results when calculated using different coordinate systems [71]. For these reasons, in most cases, the IK definition is used for the pressure tensor calculations presented in this dissertation.

3.3 Thermodynamic Route

As suggested by Professors Jackson and Müller (Imperial College, London, UK), the pressure tensor can also be calculated from the thermodynamic route: in the canonical ensemble (constant- NVT ensemble), the pressure is given by the change in the Helmholtz free energy for an infinitesimal increase in the volume. This is called the volume perturbation method of pressure calculation. If the volume change is isotropic, the pressure averaging over the system can be obtained by [72, 73]:

$$P^V = -\left(\frac{\partial F}{\partial V}\right)_{N,T} = -\lim_{\Delta V \rightarrow 0} \left(\frac{\Delta F}{\Delta V}\right) = P_{kin} + P_{conf}^V, \quad (3.36)$$

where F is the Helmholtz free energy, V is the volume of the system, N is the total number of particles, P_{kin} is the kinetic contribution and $P_{conf}^V = -(\partial F_c / \partial V)_{N,T}$ is the configurational contribution due to the intermolecular interaction. The configurational Helmholtz free energy is defined in statistical mechanics as:

$$F_c = -k_B T \ln \int_0^V \int_0^V \dots \int_0^V dx_1 dx_2 \dots dx_N \exp(-U(x^N) / k_B T), \quad (3.37)$$

where x_1, x_2, \dots, x_N are the spatial and orientational coordinates needed to specify the location and configuration of molecules 1, 2, \dots , N .

For a small change in volume, ΔV , the change in the configurational Helmholtz free energy is

$$\begin{aligned} \Delta F_c &= F_c(V + \Delta V) - F_c(V) \\ &= -k_B T \ln \left[\frac{\int_0^{V+\Delta V} \int_0^{V+\Delta V} \dots \int_0^{V+\Delta V} e^{-U_0/k_B T} e^{-\Delta U/k_B T} dx^N}{\int_0^V \int_0^V \dots \int_0^V e^{-U_0/k_B T} dx^N} \right] = -k_B T \ln \langle e^{-\Delta U/k_B T} \rangle_0, \end{aligned} \quad (3.38)$$

where ΔU is the change in the intermolecular potential energy due to the volume change, the subscript 0 means the value for an unperturbed system of volume V , and $\langle \dots \rangle_0$ indicates an ensemble average over the unperturbed system. Eqn. (3.38) is a general result for the effect of a volume change ΔV on F_c . From Eqns. (3.36) and (3.38) we can derive the equation for the configurational contribution of the pressure:

$$P_{conf}^V = k_B T \lim_{\Delta V \rightarrow 0} \left(\frac{\ln \langle e^{-\Delta U/k_B T} \rangle_0}{\Delta V} \right). \quad (3.39)$$

It is instructive to expand the right hand side of Eqn. (3.39) in a standard perturbation treatment. We first expand the exponential for small x : $e^x = 1 + x + x^2/2 + x^3/6 + \dots$, where $x = -\Delta U / k_B T$. Then, $\ln(1+y)$ is expanded for small y : $\ln(1+y) = y - y^2/2 + y^3/3 - \dots$, where $y = \langle x \rangle + \langle x^2 \rangle/2 + \langle x^3 \rangle/6 + \dots$. This gives

$$\begin{aligned}
P_{conf}^V &= - \lim_{\Delta V \rightarrow 0} \left(\frac{\Delta F_c}{\Delta V} \right) \quad (\text{if define } \Delta F_c = \Delta F_{c1} + \Delta F_{c2} + \Delta F_{c3} + \dots) \\
&= - \lim_{\Delta V \rightarrow 0} \left(\frac{\Delta F_{c1}}{\Delta V} \right) - \lim_{\Delta V \rightarrow 0} \left(\frac{\Delta F_{c2}}{\Delta V} \right) - \lim_{\Delta V \rightarrow 0} \left(\frac{\Delta F_{c3}}{\Delta V} \right), \tag{3.40}
\end{aligned}$$

where

$$\Delta F_{c1} = \langle \Delta U \rangle_0, \tag{3.41}$$

$$\Delta F_{c2} = -\frac{1}{2k_B T} \left(\langle (\Delta U)^2 \rangle_0 - \langle \Delta U \rangle_0^2 \right), \tag{3.42}$$

$$\Delta F_{c3} = \frac{1}{6(k_B T)^3} \left(\langle (\Delta U)^3 \rangle_0 - 3 \langle (\Delta U)^2 \rangle_0 \langle \Delta U \rangle_0 + 2 \langle \Delta U \rangle_0^3 \right). \tag{3.43}$$

It is possible to show that the first order term, ΔF_{c1} , is the mechanical (virial) route result, while the higher order terms account for the fluctuations (capillary waves). Jackson, Müller and coworkers have shown that these fluctuations contribute a large amount to the free energy for curved interfaces, in the case of spherical liquid drops [73].

If the volume is changed by perturbing in the α -direction only, the pressure tensor component $P_{\alpha\alpha}$ can be obtained [74]:

$$P_{conf,\alpha\alpha}^V = k_B T \lim_{\Delta V \rightarrow 0} \frac{1}{\Delta V} \ln \left\langle \exp \left(\frac{-\Delta U}{k_B T} \right) \right\rangle_{0,N,T,L_{\beta \neq \alpha}} \quad (3.44)$$

Operationally, in molecular simulations this perturbation is achieved by rescaling the α -coordinates of all the particles by a factor of $(1 + \zeta)$, where $\zeta \ll 1$. A series of ζ (e.g. $\pm 10^{-4}$, $\pm 10^{-5}$, $\pm 10^{-6}$...) is used to help get the limit value as ζ goes to zero.

3.3.1 Slit Pore

In the slit pore, the normal pressure is a constant due to the hydrostatic equilibrium and Eqn. (3.44) can be applied directly for $\alpha = z$ to get the normal pressure:

$$P_{conf,N}^V = P_{conf,zz}^V = \lim_{\Delta L_z \rightarrow 0} \frac{k_B T}{L_x L_y \Delta L_z} \ln \left\langle \exp \left(\frac{-\Delta U}{k_B T} \right) \right\rangle_{0,N,T,L_x,L_y} \quad (3.45)$$

On the other hand, the tangential pressure, which depends on the z -coordinate, should be calculated locally. In order to apply Eqn. (3.45) to calculate local tangential pressure, one should divide the system into many thin slabs in the z -direction, whose center location and thickness are z_k and δz , respectively. Thus, the local tangential pressure is:

$$P_{conf,T}^V(z_k) = \lim_{\Delta A_{xy} \rightarrow 0} \frac{k_B T}{L_z \Delta A_{xy}} \ln \left\langle \exp \left(\frac{-\Delta U(z_k)}{k_B T} \right) \right\rangle_{0,N,T,L_z} \quad (3.46)$$

where ΔA_{xy} is the change in the xy -surface area due to the perturbation in the x and/or y dimensions, and the $\Delta U(z_k)$ is the configurational energy change at slab k . Here there is much ambiguity regarding how to calculate the energy for a given slab k [75]. Different choices

will lead to different tangential pressure profiles, but their integrals over the pore width should be the same for all choices. Two choices are (1) if particle i is located in bin k_i , and particle j is located in bin k_j , then half of the interactive energy between them, $1/2 u(r_{ij})$, contributes to bin k_i , and another half, $1/2 u(r_{ij})$, contributes to bin k_j ; and (2) the interactive energy $u(r_{ij})$ linearly contributes to the bins between them (each bin takes a fraction of $\delta z / |z_{ij}| u(r_{ij})$), as illustrated in Figure 3.3. By both choices, the energy summation over all the bins is equal to the total energy of the pore system.

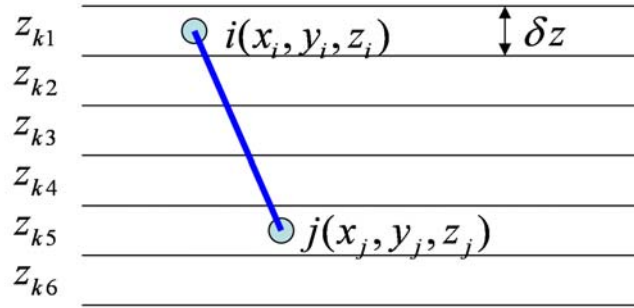


Figure 3.3 Illustrations of test-area method: Choice (1): “Harasima-like”, $1/2 u(r_{ij})$ contribute to bin z_{k1} and another $1/2 u(r_{ij})$, will contribute to bin z_{k5} ; Choice (2): “IK-like”, $u(r_{ij})$ linearly contributes to the bins between them, e.g., $\delta z / |z_{ij}| u(r_{ij})$ contributes to $z_{k1}, z_{k2}, z_{k3}, z_{k4},$ and z_{k5} , respectively.

The first choice was mathematically defined by Ladd and Woodcock [76]:

$$U(z_k) = \frac{1}{2} \sum_{i \neq j} H_k(z_i) u(r_{ij}), \quad \text{where } H_k(z_i) = \begin{cases} 1, & \text{for } |z_i - z_k| < \delta z / 2 \\ 0, & \text{otherwise} \end{cases} \quad (3.47)$$

where the top-hat function H_k in Eqn. (3.47) corresponds to the Dirac delta function in Eqn. (3.35) of the Harasima definition of the mechanical route. Thus, the local tangential pressure

calculated by this definition (Eqn. (3.47)) of energy assignment should be similar to the Harasima pressure by the mechanical route. This definition was adopted by Ghoufi et al. to calculate surface tension of water in slit pores [72].

We develop the mathematical expression for the second choice:

$$U(z_k) = \frac{1}{2} \sum_{i=1}^N \sum_{j \neq i}^N \frac{\delta z}{|z_{ij}|} u(r_{ij}) \theta\left(\frac{z_k - z_i}{z_{ij}}\right) \theta\left(\frac{z_j - z_k}{z_{ij}}\right) \quad (3.48)$$

where $\theta(x)$ is the Heaviside unit step function. Similar to the mechanical route, the product of two θ functions ensures that the pair-wise interactive energy only contributes to the bins sitting “between” the two molecules, and corresponds to the similar Heaviside functions in Eqns. (3.20) and (3.21). Thus, the local tangential pressure calculated by this definition (Eqn. (3.48)) of energy assignment should be similar to the IK pressure calculated by the mechanical route.

3.3.2 Cylindrical and Spherical Pores

It is straightforward to apply Eqn. (3.44) to get the tangential pressure in the z -direction (P_{zz} or P_{Tz}) for a cylindrical pore by setting $\alpha = z$ and in a local sense if we rescale the z -coordinates of all the particles in the system and keep the ρ - and φ -coordinates (and their dimensions) fixed:

$$P_{conf, Tz}^V(\rho_k) = k_B T \lim_{\Delta L_z \rightarrow 0} \frac{1}{\pi \rho_k^2 \Delta L_z} \ln \left\langle \exp\left(\frac{-\Delta U(\rho_k)}{k_B T}\right) \right\rangle_{0, N, T, \rho, \varphi} \quad (3.49)$$

It is more complex to get the ρ - and φ -components of the pressure tensor in cylindrical and spherical pores, because, for example, rescaling the ρ -coordinates will also result in a perturbation in the φ -dimension (a larger radial dimension means a larger circumference of a circle as well) for both spherical and cylindrical pores. We propose here a framework to get these components by taking advantage of the hydrostatic equilibrium condition, which provides relationships between the tangential and normal pressure components (Eqns. (3.5) and (3.6)).

We use as variables the usual cylindrical polar coordinates, (ρ, φ, z) , and divide the cylinder into annular cylindrical bins of radial width $\Delta\rho$, so that bin k has radii of $(\rho_k - \Delta\rho/2)$ for the inner wall of the annulus, and $(\rho_k + \Delta\rho/2)$ for the outer wall before the perturbation, where k is the index of the bin. We now perturb the volume by changing the pore radius from R to $(R + dR)$, keeping z and φ fixed. Operationally the radial coordinate of the system is scaled by a factor of $(1 + \zeta)$ where $\zeta = dR/R$. This causes the radius of bin k to change from ρ_k to $\rho_k(1 + \zeta)$, and the bin width changes from $\Delta\rho$ to $(\Delta\rho + d(\Delta\rho)) = \Delta\rho(1 + \zeta)$ where $d(\Delta\rho) = \zeta\Delta\rho$. The length of the arc in the φ -direction will increase from l_k to $(l_k + dl_k)$ (see Figure 3.4), where $dl_k = 2\pi d\rho_k = 2\pi\rho_k\zeta$.

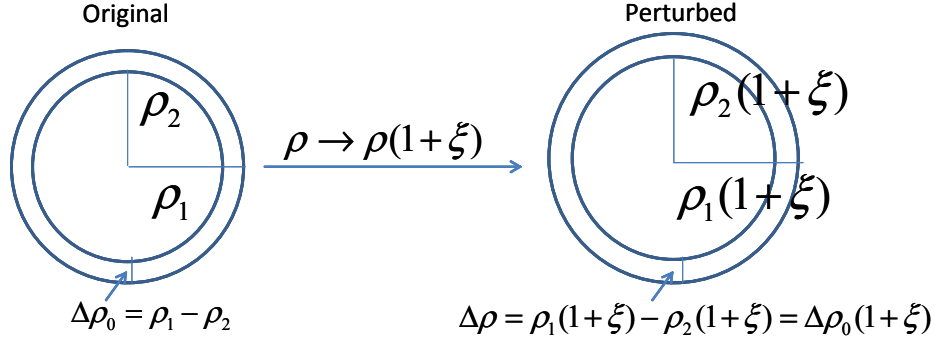


Figure 3.4 The illustration of the perturbation in ρ -direction and its consequence for cylindrical and spherical pores.

The change in the configurational Helmholtz energy of bin k , $F_{c,k}$, due to the volume perturbation will be the reversible work done in moving boundaries against the normal and tangential pressures:

$$dF_{c,k} = -P_{conf,Nk}^V \mathcal{S}_{Nk} d(\Delta\rho) - P_{conf,T\varphi k}^V \mathcal{S}_{\varphi k} dl_k, \quad (3.50)$$

where the areas on which the normal and tangential pressures act are:

$$\mathcal{S}_{Nk} = 2\pi\rho_k L_z \quad \mathcal{S}_{\varphi k} = L_z \Delta\rho. \quad (3.51)$$

Substituting Eqn. (3.51) into Eqn. (3.50) and using $dl_k = 2\pi d\rho_k = 2\pi\rho_k \xi$ and $d(\Delta\rho) = \xi\Delta\rho$ gives:

$$\begin{aligned} dF_{c,k} &= -P_{conf,Nk}^V (2\pi\rho_k L_z) d(\Delta\rho \xi) - P_{conf,T\varphi k}^V (L_z \Delta\rho) (2\pi\xi\rho_k) \\ &= -P_{conf,Nk}^V dV_{\rho k} - P_{conf,T\varphi k}^V dV_{\varphi k} \quad (\text{where } dV_{\rho k} = dV_{\varphi k} = 2\pi\rho_k L_z \Delta\rho \xi). \quad (3.52) \\ &= -2\pi\rho_k \xi L_z \Delta\rho (P_{conf,Nk}^V + P_{conf,T\varphi k}^V) \end{aligned}$$

A check will be the ‘‘volume balance’’: the overall volume change of bin k due to the perturbation (dV_{tk}) by rescaling the ρ -coordinates with a factor of $(1 + \xi)$ should equal the

summation of the volume changes contributed by the expansion purely in the ρ -direction ($dV_{\rho k}$) and the expansion purely in the φ -direction ($dV_{\varphi k}$) (See Appendix B for the checking).

The hydrostatic equilibrium in the cylinder, Eqn. (3.5), can be re-written as (for bin k):

$$P_{conf,T\varphi k}^V = P_{conf,Nk}^V + \rho_k \left. \frac{dP_{conf,Nk}^V}{d\rho} \right|_k + k_B T \rho_k \left. \frac{d\rho_{ad,k}}{d\rho} \right|_k, \quad (3.53)$$

where $\rho_{ad,k}$ is the number density of the adsorbate in bin k .

We now replace the configurational tangential pressure in Eqn. (3.52) using Eqn. (3.53) to obtain the equation for the configurational normal pressure component:

$$dF_{c,k} = -2\pi\rho_k \xi L_z \Delta\rho \left(2P_{conf,Nk}^V + \rho_k P'_{conf,Nk}{}^V + k_B T \rho_k \rho'_{ad,k} \right) \quad (3.54)$$

where $P'_{conf,Nk}{}^V = \left[P_{conf,Nk}^V / d\rho \right]_{\rho_k}$ and $\rho'_{ad,k} = [d\rho_{ad} / d\rho]_{\rho_k}$.

On the other hand, from Eqn. (3.38):

$$dF_{c,k} = -k_B T \lim_{\Delta V \rightarrow 0} \ln \langle e^{-\Delta U_k / k_B T} \rangle_0, \quad (3.55)$$

and we equate the right hand sides of Eqns. (3.54) and (3.55) (after manipulations) to obtain:

$$\rho_k P'_{conf,Nk}{}^V + 2P_{conf,Nk}^V = k_B T \lim_{\xi \rightarrow 0} \frac{\ln \langle e^{-\Delta U_k / k_B T} \rangle_0}{2\pi\rho_k \xi L_z \Delta\rho} - k_B T \rho_k \rho'_{ad,k}, \quad (3.56)$$

which can be rewritten in continuous form and is a linear first-order differential equation:

$$\rho P'_{conf,N}{}^V + 2P_{conf,N}^V = f(\rho) = k_B T \lim_{\xi \rightarrow 0} \frac{\ln \langle e^{-\Delta U(\rho) / k_B T} \rangle_0}{2\pi\rho \xi L_z \Delta\rho} - k_B T \rho \rho'_{ad}, \quad (3.57)$$

whose right hand side is a known function and can be obtained during the simulation. Due to the cylindrical symmetry, one constraint of Eqn. (3.57) would be the symmetric boundary at the center:

$$P'_{conf,N}(0) = 0. \quad (3.58)$$

However, in molecular simulation, a numerical instability may arise for the bin corresponding to the center line of the cylinder ($\rho = 0$), due to the very small volume of the bin, which causes poor statistics at the center. Alternatively, another constraint for the boundary at the wall could be considered, i.e., the configurational normal pressure evaluated at the inner radius of the pore equals the normal pressure acting on the wall (note that the kinetic contribution is zero because there is no adsorbate on the wall):

$$P'_{conf,N}(R) = P_{N,wall} \quad (3.59)$$

where $P_{N,wall}$ can be obtained during the simulation by summing up the forces of adsorbate molecules acting on the wall atoms, and divided by the surface area of the inner wall $2\pi RL_z$. But this boundary condition relies on the normal pressure calculated from the mechanical route.

It is straightforward to solve the first-order linear ordinary differential equation system defined by Eqns. (3.57) and (3.58) (See Appendix C). After adding the kinetic contribution, the total normal pressure and tangential pressure (by applying hydrostatic equilibrium) by the volume perturbation method are:

$$P'_N(\rho) = \frac{1}{\rho^2} \int_0^\rho \rho' (f_1(\rho') + 2\rho_{ad}(\rho')k_B T) d\rho', \quad (3.60)$$

$$P_{T\varphi}^V(\rho) = f_1(\rho) + 2\rho_{ad}(\rho)k_B T - P_N^V(\rho), \quad (3.61)$$

where

$$f_1(\rho) = \lim_{\xi \rightarrow 0} \frac{k_B T \ln \langle e^{-\Delta U_k / k_B T} \rangle_0}{2\pi L_z \xi \rho \Delta \rho}. \quad (3.62)$$

For the pressure tensor in a spherical pore, we can use a similar method to that described above to obtain equations from the thermodynamic route. The variables used are the usual spherical polar coordinates, (ρ, φ, θ) , and we divide the sphere into spherical shells (bins) of thickness (radial width) $\Delta\rho$, so that bin k has radii $(\rho_k - \Delta\rho/2)$ for the inner wall of the annulus, and $(\rho_k + \Delta\rho/2)$ for the outer wall before the perturbation, where k is the index of the bin. We perturb the volume by changing the pore radius from R to $(R + dR)$, keeping θ and φ fixed. Operationally the radial coordinates of particles in the system are scaled by a factor of $(1 + \xi)$ where $\xi = dR/R$. This causes the radius of bin k to change from ρ_k to $\rho_k(1 + \xi)$, and the bin width changes from $\Delta\rho$ to $(\Delta\rho + d(\Delta\rho)) = \Delta\rho(1 + \xi)$ where $d(\Delta\rho) = \xi\Delta\rho$. The length of the arc in the φ direction will increase from $l_{\varphi k}$ to $(l_{\varphi k} + dl_{\varphi k})$, and the length of the arc in the θ direction will increase from $l_{\theta k}$ to $(l_{\theta k} + dl_{\theta k})$, where (recall that while φ can vary from 0 to 2π , θ can only vary from 0 to π):

$$dl_{\varphi k} = 2\pi(\rho_k + d\rho_k) \sin \theta - 2\pi\rho_k \sin \theta = 2\pi d\rho_k \sin \theta = 2\pi\rho_k \xi \sin \theta, \quad (3.63)$$

$$dl_{\theta k} = \pi\rho_k(1 + \xi) - \pi\rho_k = \pi\rho_k \xi. \quad (3.64)$$

The change in the configurational Helmholtz energy, $F_{c,k}$, of bin k due to the volume perturbation will be the reversible work done in moving the boundaries against the normal and tangential pressures:

$$\begin{aligned}
dF_{c,k} &= dF_{c,\rho k} + dF_{c,\varphi k} + dF_{c,\theta k} \\
&= -P_{conf,Nk}^V dV_{\rho k} - P_{conf,T\varphi k}^V dV_{\varphi k} - P_{conf,T\theta k}^V dV_{\theta k} \\
&= -P_{conf,Nk}^V \mathcal{S}_{\rho k} d(\Delta\rho) - P_{conf,T\varphi k}^V \mathcal{S}_{\varphi k} dl_{\varphi k} - P_{conf,T\theta k}^V \mathcal{S}_{\theta k} dl_{\theta k}
\end{aligned} \tag{3.65}$$

The first term in Eqn. (3.65) is the normal pressure contribution and can be further written as:

$$dF_{c,\rho k} = -P_{conf,Nk}^V dV_{\rho k} = -P_{conf,Nk}^V (\mathcal{S}_{\rho k} d(\Delta\rho)) = -P_{conf,Nk}^V (4\pi\rho_k^2)(\Delta\rho\xi). \tag{3.66}$$

We now calculate the φ -contribution to the Helmholtz free energy (the second term in Eqn. (3.65)) due to the reversible work done in moving the boundaries toward the φ -direction. The surface area normal to φ is somewhat more complex as $dl_{\varphi k}$ in Eqn. (3.65) depends on θ , as well as ρ (Eqn. (3.63)). To determine this surface area we consider a plane (which is actually a constant φ -plane, Figure 3.5) which is normal to the xy -plane and passes through and is parallel to the z -axis (this cutting plane goes through the great circle of the sphere). Its intersection with bin k is an annular “band” (solid black band in right part of Figure 3.5).

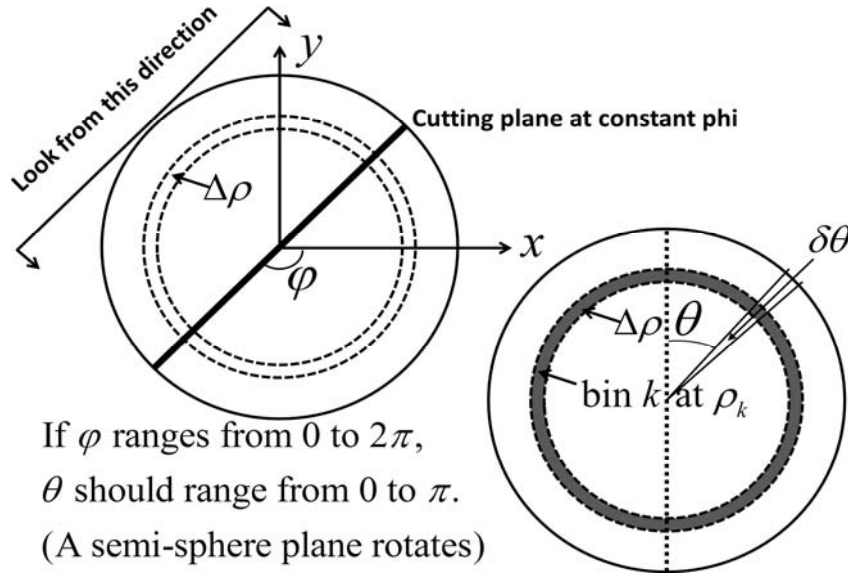


Figure 3.5 A plane at constant φ , normal to the φ direction and to the xy -plane. Left part: looking down on the xy -plane, the constant φ plane is seen end on as the solid black line. Right part: the plane of constant φ , showing bin k as the solid black circle; the tangential pressure $P_{T\varphi}$ acts normal to this plane.

We divide this band in the θ -direction into many infinitesimal angular elements, $\delta\theta$ (Figure 3.5), each of which has an area of

$$\delta S_{\varphi k} = 2\pi\rho_k\Delta\rho \times \frac{\delta\theta}{2\pi} = \rho_k\Delta\rho\delta\theta. \quad (3.67)$$

Thus, the free energy change in this element due to the expansion in the φ -direction is:

$$\delta dF_{c,\varphi k} = -P_{conf,T\varphi k}^V \delta S_{\varphi k} dl_{\varphi k} = -P_{conf,T\varphi k}^V (\rho_k\Delta\rho\delta\theta)(2\pi\rho_k\xi \sin\theta). \quad (3.68)$$

We now integrate over $\delta\theta$, noting that $P_{conf,T\varphi k}^V$ is independent of θ :

$$\begin{aligned}
dF_{c,\phi k} &= \int_0^\pi -P_{conf,T\phi k}^V (\rho_k \Delta\rho \delta\theta) (2\pi\rho_k \xi \sin\theta) \delta\theta \\
&= -P_{conf,T\phi k}^V 2\pi\rho_k^2 \Delta\rho \xi \int_0^\pi \sin\theta \delta\theta \\
&= -4\pi\rho_k^2 \Delta\rho \xi P_{c,T\phi k} \\
&= -P_{conf,T\phi k}^V dV_{\phi k} \quad (\text{where } dV_{\phi k} = 4\pi\rho_k^2 \Delta\rho \xi)
\end{aligned} \tag{3.69}$$

Concerning the third term in Eqn. (3.65), the calculation of free energy change due to the expansion in the θ -direction is also complex (see Figure 3.6). The change in surface area as θ goes from 0 to π , and the arc length change for a certain $\delta\theta$ element at angular coordinate θ (we can also divide the θ -direction into many infinitesimal part angular elements $\delta\theta$) are:

$$dS_{\theta k} = (2\pi\rho_k \sin\theta) \Delta\rho, \tag{3.70}$$

$$\delta dl_{\theta k} = \frac{\delta\theta}{\pi} \pi\rho_k \xi = \delta\theta\rho_k \xi. \tag{3.71}$$

Similarly to the second term in Eqn. (3.65),, the Helmholtz free energy is:

$$\begin{aligned}
dF_{c,\theta k} &= -P_{conf,T\theta k}^V \int_0^\pi dS_{\theta k} \delta dl_{\theta k} \\
&= -P_{conf,T\theta k}^V \int_0^\pi (2\pi\rho_k \Delta\rho \sin\theta) (\rho_k \xi \delta\theta) \\
&= -P_{conf,T\theta k}^V (4\pi\rho_k^2 \Delta\rho \xi) \\
&= -P_{conf,T\theta k}^V dV_{\theta k} \quad (\text{where } dV_{\theta k} = 4\pi\rho_k^2 \Delta\rho \xi)
\end{aligned} \tag{3.72}$$

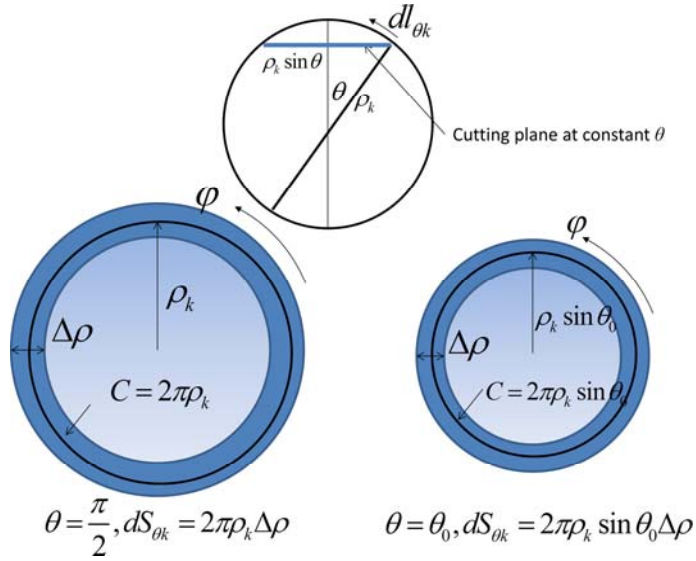


Figure 3.6 The shaded annuluses of the lower two parts show the surface area normal to the θ -direction ($dS_{\theta k}$) for different θ positions.

A check of Eqns. (3.66), (3.69) and (3.72) will be the “volume balance”: the total volume change of a bin k due to the perturbation (dV_{lk}) should equal to the summation of volume changes contributed by the expansion purely in the ρ -direction ($dV_{\rho k}$), the expansion purely in the φ -direction ($dV_{\varphi k}$), and the expansion purely in the θ -direction ($dV_{\theta k}$) (See Appendix B for confirmation of this check).

The hydrostatic equilibrium in the sphere, Eqn. (3.6), can be re-written as (for bin k , and because of the spherical symmetry the φ -component and θ -component of the tangential pressure are the same):

$$P_{conf, Tk}^V = P_{conf, Nk}^V + \frac{\rho_k}{2} \frac{dP_{conf, Nk}^V}{d\rho} \Big|_k + k_B T \frac{\rho_k}{2} \frac{d\rho_{ad, k}}{d\rho} \Big|_k. \quad (3.73)$$

Substitution of Eqns. (3.66), (3.69) and (3.72) into Eqn. (3.65), using the relationship between tangential and normal pressures expressed as Eqn. (3.73), gives:

$$\begin{aligned}
dF_{c,k} &= -4\pi\rho_k^2\Delta\rho\xi P_{conf,Nk}^V - 4\pi\rho_k^2\Delta\rho\xi P_{conf,Tk}^V - 4\pi\rho_k^2\Delta\rho\xi P_{conf,Tk}^V \\
&= -4\pi\rho_k^2\Delta\rho\xi \left(P_{conf,Nk}^V + 2P_{conf,Tk}^V \right) \\
&= -4\pi\rho_k^2\Delta\rho\xi \left[P_{conf,Nk}^V + 2 \left(P_{conf,Nk}^V + \frac{\rho_k}{2} P_{conf,Nk}^V + kT \frac{\rho_k}{2} \rho'_{ad,k} \right) \right], \\
&= -4\pi\rho_k^2\Delta\rho\xi \left[3P_{conf,Nk}^V + \rho_k P_{conf,Nk}^V + kT \rho_k \rho'_{ad,k} \right]
\end{aligned} \tag{3.74}$$

where $P_{conf,Nk}^V = \left[P_{conf,Nk}^V / d\rho \right]_{\rho_k}$, $\rho'_{ad,k} = \left[d\rho_{ad} / d\rho \right]_{\rho_k}$.

On the other hand, Eqn. (3.55) that we derived for the cylindrical pore from Eqn. (3.38) also applies to the spherical case. We can equate the right hand sides of Eqns. (3.55) and (3.74) to obtain (after manipulations):

$$\rho_k P_{conf,Nk}^V + 3P_{conf,Nk}^V = k_B T \lim_{\xi \rightarrow 0} \frac{\ln \langle e^{-\Delta U_k / k_B T} \rangle_0}{4\pi\rho_k^2 \xi \Delta\rho} - k_B T \rho_k \rho'_{ad,k}, \tag{3.75}$$

which can be re-written in continuous form, and is a linear first order differential equation:

$$\rho P_{conf,N}^V + 3P_{conf,N}^V = f(\rho) = k_B T \lim_{\xi \rightarrow 0} \frac{\ln \langle e^{-\Delta U(\rho) / k_B T} \rangle_0}{4\pi\rho^2 \xi \Delta\rho} - k_B T \rho \rho'_{ad}, \tag{3.76}$$

whose right-hand-side is a known function and can be obtained during the simulation. Due to the spherical symmetry, one possible constraint of Eqn. (3.76) could be a symmetric boundary condition at the center:

$$P_{conf,N}^V(0) = 0. \tag{3.77}$$

As for in the cylindrical pore, a numerical instability may arise for the bin corresponding to the center of the sphere ($\rho = 0$) in molecular simulation, due to the very small volume of the bin, which results in poor statistics. Hence, another constraint for the boundary at the wall should be considered. This constraint requires that the configurational normal pressure evaluated at the inner radius of the pore equals to the normal pressure acting on the wall (note that the kinetic contribution is zero because there is no adsorbate on the wall):

$$P_{conf,N}^V(R) = P_{N,wall} \quad (3.78)$$

where $P_{N,wall}$ can be obtained during the simulation by summing up the forces of adsorbate molecules acting on the wall atoms, and divided by the surface area of the inner wall $4\pi R^2$. However, this boundary condition relies on the normal pressure calculated from the mechanical route.

It is straightforward to solve the first-order linear ordinary differential equation system defined by Eqns. (3.76) and (3.77) (See Appendix C). After adding the kinetic contribution, the total normal pressure and tangential pressure (by applying hydrostatic equilibrium) by the volume perturbation method are:

$$P_N^V(\rho) = \frac{1}{\rho^3} \int_0^\rho \rho'^2 (f_2(\rho') + 3\rho_{ad}(\rho')k_B T) d\rho', \quad (3.79)$$

$$P_T^V(\rho) = \frac{1}{2} [f_2(\rho) + 3\rho_{ad}(\rho)k_B T - P_N^V(\rho)], \quad (3.80)$$

where

$$f_2(\rho) = \lim_{\xi \rightarrow 0} \frac{k_B T \ln \langle e^{-\Delta U_k/k_B T} \rangle_0}{4\pi\xi\rho^2\Delta\rho}. \quad (3.81)$$

For the spherical and cylindrical cases, the pressure tensor components have the general expressions as below:

$$\begin{aligned}
 P_N^V(\rho) &= \frac{1}{\rho^s} \int_0^\rho \rho'^{s-1} [f_{12} + s\rho_{ad}k_B T] d\rho' \\
 P_T^V(\rho) &= \frac{1}{s-1} ([f_{12}(\rho) + s\rho_{ad}(\rho)k_B T] - P_N(\rho)) \\
 \text{where } f_{12}(\rho) &= \lim_{\xi \rightarrow 0} \frac{k_B T \ln \langle e^{-\Delta U_k/k_B T} \rangle_0}{V_{k,0}\xi} \quad . \quad (3.82)
 \end{aligned}$$

$(V_{k,0}$ is the original volume of bin k ,
 and $s = 2$ or 3 for cylinder or sphere, respectively)

Now, energy must be assigned to each annulus bin k , i.e. $\Delta U_k = U_{kp} - U_{k0}$ in Eqns. (3.62) and (3.81). The energy assignment is non-unique, as in the slit pore (Sec. 3.3.1). In a similar way, we can adopt two choices which correspond to an IK-like definition (ij pair-wise energy is evenly assigned to the bins that are crossed by the straight line joining the centers of particles i and j) and a Harasima-like definition (ij pair-wise energy is assigned half to the bin where i is located and another half the bin where j is located), respectively.

3.4 Spatial Averaging of the Pressure Tensor

So far, we have discussed various ways to define/calculate the local value of the pressure tensor. It is also of interest to define an overall “effective” in-pore pressure. This effective pressure can be obtained by averaging the local pressure in various ways, depending on the physical meaning. In this section, we limit our discussion to the slit pore case. Due to the hydrostatic equilibrium, the normal pressure of adsorbate in a slit pore is a constant (see Eqn.

(3.4)), so it is not necessary to define an “average” or effective normal pressure. The constant normal pressure across the pore is the pressure acting on the adsorbate phase in the direction normal to the wall, and is also the pressure acting on the pore wall, which could cause the deformation of the porous material.

However, the tangential pressure in a slit pore is a function of z , the distance between the pore wall and the plane where the pressure is evaluated. Several ways of spatial averaging could be considered. As discussed by Tadmor and Miller in ref [77], the macroscopic field (some effective average) of a quantity such as stress tensor or pressure can be calculated by spatially averaging the microscopic quantity with a weighting factor, and due to the linearity the averaged macroscopic quantity satisfies the same balance equations as does the corresponding microscopic quantity [77]. The weighting factor should be normalized and can be arbitrarily chosen for the desired purposes or to result in different physical meaning. [77]

One natural idea is to average over the pore width weighted by the adsorbate density:

$$P_{T,avg,1} = \frac{\int P_T(z)\rho_{ad}(z)dV}{\int \rho_{ad}(z)dV} = \frac{\int_{-H/2}^{H/2} P_T(z)\rho_{ad}(z)A_{xy}dz}{\int_{-H/2}^{H/2} \rho_{ad}(z)A_{xy}dz} = \frac{\int_{-H/2}^{H/2} P_T(z)\rho_{ad}(z)dz}{\int_{-H/2}^{H/2} \rho_{ad}(z)dz}, \quad (3.83)$$

where H is the pore width. By this definition, $P_{T,avg,1}$ means that on average each adsorbate molecule in the pore is under a tangential pressure of $P_{T,avg,1}$. The advantage of this definition is that it excludes the pore volume where there are no adsorbate molecules but there is a finite pressure value due to the pair-wise interaction between particles. However, this definition gives different average values for different choices of the interal contour C_{ij} in Eqn.

(3.17) (e.g., the IK and Harasima definitions). As shown in Sec. 5.4.1, the density profile is well defined and will not change with the definition of the contour C_{ij} , whereas the tangential pressure profile varies with the definition of C_{ij} , which suggests that an adsorbate molecule located at a certain z -position is not necessarily under an operationally defined tangential pressure, $P_T(z)$, and thus the averaging weighted by the local density could be problematic.

An alternative way of averaging is to average without any weighting factor:

$$P_{T,avg,2} = \frac{\int P_T(z) dV}{\int dV} = \frac{\int_{-H/2}^{H/2} P_T(z) A_{xy} dz}{\int_{-H/2}^{H/2} A_{xy} dz} = \frac{1}{H} \int_{-H/2}^{H/2} P_T(z) dz . \quad (3.84)$$

By this definition, $P_{T,avg,2}$ means that if the adsorbate phase is considered as homogeneous or as a continuum, on average at any z -plane the pressure parallel to the wall is $P_{T,avg,2}$. The advantage of this definition is that the value of $P_{T,avg,2}$ corresponds to the overall in-pore tangential pressure (not locally calculated) calculated by the thermodynamic route:

$$\bar{P}_T^V = k_B T \lim_{\Delta A_{xy} \rightarrow 0} \frac{1}{L_z \Delta A_{xy}} \ln \left\langle \exp \left(\frac{-\Delta U}{k_B T} \right) \right\rangle_{0,N,T,L_z} + \rho_{ad} k_B T , \quad (3.85)$$

where ΔU is the change in the total (here total means in the whole pore instead of in a bin) configurational energy due to the perturbation in the xy -plane, and ρ_{ad} is the average in-pore density of adsorbate (the total number of adsorbate molecules divided by the pore volume). Because Eqn. (3.85) is well defined without any ambiguity of the “local” energy, this average $P_{T,avg,2}$ has the same value for all choices of contours C_{ij} by which the local tangential

pressure is calculated (see Sec. 5.4.1 for example). Another advantage is that $P_{T,avg,2}$ is related to the surfaces tension, which in the mechanical route is given by [78]:

$$\gamma = \int_{-H/2}^{+H/2} [P_N - P_T(z)] dz = P_N \int_{-H/2}^{+H/2} dz - \int_{-H/2}^{+H/2} P_T(z) dz = H(P_N - P_{T,avg,2}), \quad (3.86)$$

where γ is the surface tension.

CHAPTER 4

Molecular Simulation Methods

4.1 Statistical Thermodynamics and Molecular simulation

Statistical thermodynamics provides a mathematical recipe for predicting the thermodynamic (macroscopic) properties of a system by using the knowledge of its properties on a molecular (or atomic, which is interchangeable with molecular in this dissertation) level. Hence, statistical thermodynamics is a basis of molecular simulation. [79]

A system with a certain *macroscopic state* (e.g., a specified number of molecules, N , a specified volume, V , and a specified temperature, T , which refers to a canonical ensemble or NVT -ensemble) could be associated with an almost infinite number of *microscopic states*. The microscopic state of the system at any instant time can be specified by listing the position and momentum of all molecules in the system. Associated with each microscopic state is the total energy of the system (a sum of kinetic energy due to the molecular motion and potential energy, or configurational energy due to the intermolecular forces). For a specified total energy, there could be many microscopic states (or configurations of the molecules). Realistically, the system always fluctuates rapidly from one microscopic state to another, and the experimentally measured (macroscopic) properties of the system are actually the time averages of the microscopic properties. Statistical thermodynamics provides us with a statistical technique for taking these averages: a macroscopic property is the average of the

microscopic property over all possible microscopic states. [79] For example, the macroscopic pressure (at equilibrium) of a system can be obtained by taking the average of the pressures over a large number of microscopic states at equilibrium.

Molecular simulation is a technique used to generate a series of microscopic states that evolve according to the interactions between the molecules in the system and the previous microscopic state. Molecular Dynamics (MD) and Monte Carlo (MC) are two widely used methods of molecular simulation. In molecular dynamics, an initial configuration (the list of the positions and the momenta of all the molecules) is preset, and the total force (because of the interaction between molecules) acting on each molecule is calculated. Newton's equation of motion is solved for each molecule to obtain the updated position and momentum after a tiny time interval, i.e., a new state is obtained. As time evolves, this process is repeated and a series of microscopic states are generated. Thus, molecular dynamics is a *deterministic* method, whereas the Monte Carlo method is stochastic, and is discussed in Sec. 4.2.

4.2 Monte Carlo Method and Simulation of Adsorption

The first computer simulation of a molecular system used the Monte Carlo method [80]. The Monte Carlo simulation proceeds as follows: a series of molecular configurations (microscopic states) of a system are generated by making random changes (or moves, which is interchangeable in this dissertation) to the system (e.g., translational, rotational or vibrational movement of a randomly chosen molecule to a random position or angle, addition or deletion of a molecule at a random position, volume change of the system by rescaling the

coordinates of all the particles in the system, etc.). A Monte Carlo move involves two immediate subsequent steps: (1) a trial move, which proposes a random move as described above, and then (2) acceptance or rejection of the proposed trial move according to the pre-set criteria (e.g., usually the energy change, i.e., if after the move, the system goes towards a state with lower energy, the move is accepted, otherwise, the move will be accepted with a probability depending on the temperature, etc.). A Monte Carlo method generates states of low energy, and enables properties to be calculated accurately if carried out for an infinite number of moves. Practically, for a Monte Carlo simulation, one starts with an initial structure, then runs for many Monte Carlo moves to bring the system into equilibrium (equilibrium stage), and then attempts many more Monte Carlo moves during which the properties of the system (density, volume, energy, pressure, etc.) are sampled (production stage). [80]

Monte Carlo simulations can be applied to generate systems in various statistical mechanical *ensembles*. An ensemble is a collection of systems in identical macroscopic states which usually can be defined by three macroscopic state variables. For different ensembles, the acceptance probability for a Monte Carlo move varies.

The most natural ensemble for Monte Carlo simulation is canonical ensemble or *NVT*-ensemble, where all the generated systems (samples) are in the same/constant number of molecules, N , the same/constant volume, V , and the same/constant temperature, T . For this ensemble, the involved Monte Carlo moves include physical movement of the molecules,

such as translational displacement, rotation and bond vibration (the last two moves are only for non-spherical, multi-site molecules). After a trial move, the change in the configurational energy is calculated: if the change is negative (energy is decreased by the move), the move will be accepted; otherwise, the move will be accepted by a probability [81]:

$$p^{acc} = \exp(-\Delta U / k_B T), \quad (4.1)$$

where ΔU is the change in the configurational energy, and k_B is the Boltzmann constant. According to the Boltzmann law, the temperature of the system is fixed at T .

Beside the canonical ensemble, a common alternative is isothermal-isobaric ensemble or NPT -ensemble, where the volume of the system is allowed to fluctuate to obtain a constant pressure P . In addition to the moves that are involved in the NPT -ensemble Monte Carlo, there is a volume change for the NVT -ensemble Monte Carlo. The volume change aims to achieve the pre-set pressure of the system, and thus the acceptance probability for this move is [80]:

$$p^{acc} = \max\{1, \exp(-(\Delta U + P\Delta V) / k_B T + N\Delta \ln V)\}, \quad (4.2)$$

where ΔV is the volume change, ΔU is the change in the configurational energy due to the volume change, and $\Delta \ln V$ is the change in the logarithm of the volume. The volume change is practically obtained by rescaling the coordinates of the molecules and the boundaries by a factor. As a result, the pressure and the total configurational energy of the system are also changed (because the separation distances between molecules and thus their potential energy are changed).

Another important ensemble (widely used to study adsorption) is the Grand Canonical ensemble (or μVT -ensemble), in which the conserved properties are the chemical potential, μ , the volume of the system, V , and the temperature of the system, T . In addition to the moves that are involved in the NVT -ensemble Monte Carlo, there are addition and deletion of a molecule trials, since the grand canonical ensemble allows the total number of molecules to fluctuate. A constant chemical potential is maintained via the acceptance probabilities of molecule addition and deletion, which are given by [80]:

$$p_{add}^{acc} = \max\{1, \exp(-\Delta U / k_B T + \ln[zV / (N+1)])\} \quad (4.3)$$

$$\text{and } p_{del}^{acc} = \max\{1, \exp(-\Delta U / k_B T + \ln(N / zV))\}, \quad (4.4)$$

respectively, where z is the activity and is related to the chemical potential by

$$\mu = k_B T \ln(\Lambda^3 z) \quad (\text{where } \Lambda = \sqrt{h^2 / 2\pi m k_B T}). \quad (4.5)$$

Practically, an addition move is achieved by locating a new molecule at a randomly chosen position (within the volume of the system), and then accepting by a probability according to Eqn. (4.3). A deletion move is achieved by removing an existing molecule at random and then accepting by a probability according to Eqn. (4.4).

The Grand Canonical Monte Carlo (GCMC) method is especially useful to simulate adsorption in porous materials, since the number of molecules can be changed at constant chemical potential (or equivalently at the pressure of the bulk phase in equilibrium with the pore phase). A famous example of such simulation was the adsorption of a mixture of

methane and ethane onto a microporous graphite surface, done by Cracknell, Nicholson and Quirke, 1994 [82]. In this simulation, methane was modeled as a Lennard-Jones (LJ) spherical particle, while ethane was modeled as a molecule with two LJ sites connected with a bond of fixed length. The graphite pore is slit-shaped and the wall is composed of LJ spherical particles (carbon atoms). They calculated the selectivity of the pore for the two components (the ratio of the mole fractions in the pore to the ratio of the mole fraction in the bulk phase). The selectivity was obtained as a function of bulk phase pressure, which is related to the chemical potential assuming an ideal gas [80]:

$$P_{bulk} = k_B T \exp(\mu / k_B T) / \Lambda^3 . \quad (4.6)$$

For the non-ideal gas (at high pressure or low temperature), an appropriate *equation of state* (e.g. LJ Equation of State [83, 84]) could be applied to calculate the bulk phase pressure at certain chemical potential.

4.3 Semi-Grand Canonical Monte Carlo for System with Flexible Walls

Traditionally, the adsorption in porous materials is simulated by using GCMC as discussed in Sec. 4.2, where MC moves are performed only on the adsorbate molecules while the atoms in porous materials (wall atoms) are fixed in the space. The wall atoms only act as a source of external force field fixed in space, providing wall-adsorbate interaction. However, much experimental evidence shows that the adsorbate also imposes effects on the wall or the porous materials, causing pore deformation, change of wall structure, etc (as discussed in Sec. 2.4). Schoen et al., for the first time, proposed a Semi-Grand Canonical Monte Carlo

(SGCMC) method to simulate adsorption in a model of a flexible porous material [53, 85]. In the flexible pore model, each wall atom is either connected to an “equilibrium” or lattice position by a spring with an appropriate spring constant or bonded with its neighbors under a reactive force field, or any reasonable wall-wall interaction. By using SGCMC, the wall atoms are also allowed to move (but there is no insertion or deletion, and so the number of wall atoms are kept fixed) according to the metropolis Monte Carlo criteria. Meanwhile, the chemical potential of adsorbate and the temperature are kept to preset values, similar to the GCMC method. The SGCMC method involving flexibility of the porous materials is very useful for the adsorption in a carbon slit pore or activated carbon fibers, which are composed of multiple layers of graphene sheets. This is because the interaction between graphene sheets are mainly van der Waals (weak) interactions, and the wall deformation (corresponding to pore shrinkage or expansion) by adsorption would be appreciable. For cylindrical and spherical pores, the deformation would be less than for the slit pore, because if the deformation occurs, there must be changes in the chemical bond length (which involves much stronger forces than van der Waals interactions), not only the interlayer spacing, which only involves van der Waals interaction in the slit pore case.

CHAPTER 5

Pressure Enhancement in Slit Pores of Various Models

5.1 Introduction

With the aim of providing fundamental understanding of the apparently unconnected effects in confined nanophases discussed in Chapter 2, as a starting point, we study the pressure enhancement effects by calculating the pressure tensor components of argon (modeled as a spherical Lennard-Jones molecule) confined in carbon slit pores. Although the slit-pore model is a highly simplified approximation of the porous features found in many real materials [86], it has played an essential role in the development of theoretical approaches for characterizing porous materials [87]. In addition, it also provides a unified context for achieving a fundamental understanding of the impact of various confinement effects [1, 88] on adsorption [82], transport [89], chemical reaction [25, 90] and poromechanics [91]. The slit-pore model is also capable of making quantitative predictions of the adsorptive properties of ordered carbon materials, such as graphitizable carbon blacks [92, 93]. For the purposes of this study, it provides a well-established starting point for understanding pressure enhancement effects in confined systems in which Eqn. (3.14) may be readily evaluated.

By using the GCMC and SGCMC simulations (see Secs. 4.2 and 4.3), we examine the effects of the extent of confinement (pore width), temperature, and bulk phase pressure on the density and pressure profiles, and on the radial distribution function. We show that the

tangential pressure (parallel to the walls) is positive and reaches tens of thousands of bars locally at ambient bulk pressure, while the normal pressure can be positive or negative, depending on the pore width, and is of the order thousands of bars. We further find that the tangential pressure is sensitive to small changes in the bulk pressure, suggesting that it should be possible to control the tangential pressure over wide ranges in laboratory experiments.

5.2 Modeling Details

Argon is used as adsorbate in carbon slit pores. For argon-argon (adsorbate-adsorbate or *aa*) interaction, the Lennard-Jones (LJ) potential model (as shown in Eqn. (5.1)) and the BFW (Baker-Fisher-Watts) potential model (as shown in Eqn. (5.2)) [94] are used. In the LJ model, the parameters $\epsilon_{aa} / k_B = 119.8$ K and $\sigma_{aa} = 0.3405$ nm are taken from [95], and truncated at $r_c = 5\sigma$. For the BFW potential model the parameters ϵ_{BFW} , r_m , A_i , C_{2j} , and δ are taken from [96] and listed in Table 5.1. The interaction energy as a function of the separation distance r for the above two models are plotted in Figure 5.1.

$$u_{aa}(r_{ij}) = 4\epsilon_{aa}[(\sigma_{aa} / r_{ij})^{12} - (\sigma_{aa} / r_{ij})^6] \quad (5.1)$$

$$u_{aa}^{BFW}(r_{ij}) = \epsilon_{BFW} \left\{ \exp[\alpha(1 - r / r_m)] \sum_{i=0}^5 A_i (r / r_m - 1)^i - \sum_{j=3}^5 C_{2j} / [\delta + (r / r_m)^{2j}] \right\} \quad (5.2)$$

Table 5.1 The BFW parameters for argon [96]

ε_{BFW} / k_B (K)	142.095
r_m (nm)	0.37612
A_0	0.277 83
A_1	-4.504 31
A_2	-8.331 215
A_3	-25.2696
A_4	-102.0195
A_5	-113.25
C_6	1.107 27
C_8	0.169 713 25
C_{10}	0.013 611
α	12.5
δ	0.01

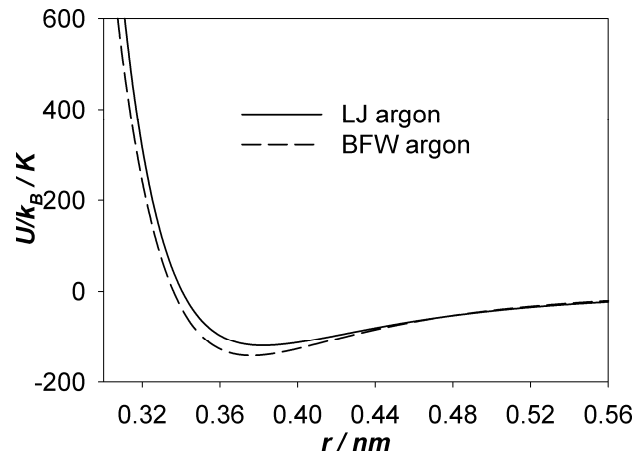


Figure 5.1 Intermolecular interaction potentials for argon for LJ and BFW models.

For the slit pore wall, the simplest model is Steele (10,4,3) structureless rigid infinite wall (Figure 5.2a), for which the adsorbate-carbon (aC) interaction is [97]:

$$u_{aC}(z) = 2\pi\varepsilon_{aC}\rho_w\Delta_w\sigma_{aC}^2 \left[\frac{2}{5} \left(\frac{\sigma_{aC}}{z} \right)^{10} - \left(\frac{\sigma_{aC}}{z} \right)^4 - \left(\frac{\sigma_{aC}^4}{3\Delta_w(z+0.61\Delta_w)^3} \right) \right] \quad (5.3)$$

where ε_{aC} and σ_{aC} are LJ parameters for adsorbate-carbon mixture, $\rho_w = 114 \text{ nm}^{-3}$ is the carbon atom density of the graphene wall, $\Delta_w = 0.335 \text{ nm}$ is the interlayer spacing between graphene sheets, and z is the distance between the center of mass of an adsorbate molecule to the carbon wall plane [97]. Periodic boundary conditions are applied in the x - and y -directions so that the slit pore is infinitely large in the xy -plane.

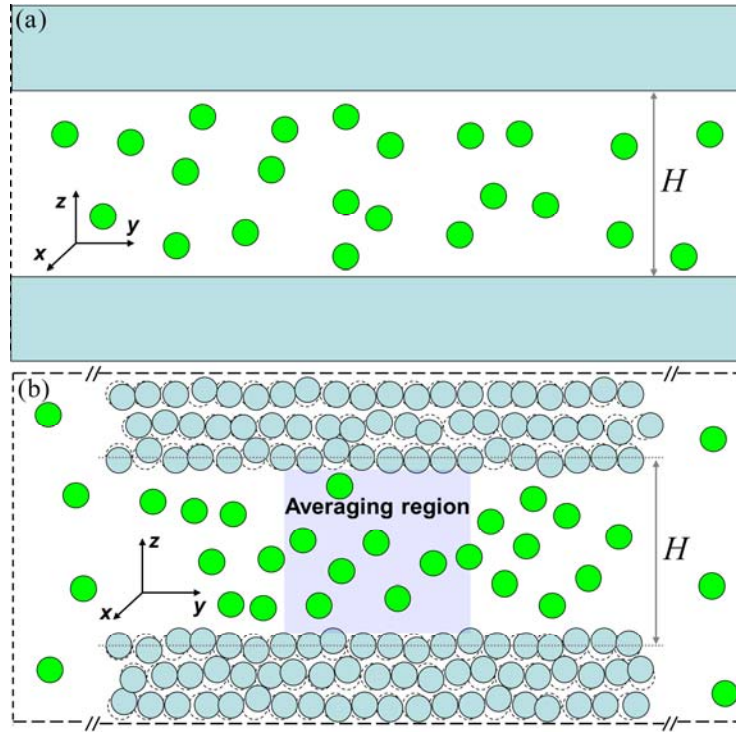


Figure 5.2 The simulation cells of (a) carbon slit pore with structureless wall and (b) carbon slit pore with atomistic wall. The green circles represent adsorbate argon molecules, and the blue circles and slabs represent wall atoms and carbon structureless walls, respectively. Carbon atoms are shown at reduced scale for clarity.

We also developed a realistic pore model with finite pore length and flexible and fully atomistic pore wall [98]. This model (shown in Figure 5.2b) is a slit-shaped pore with 3 layers of graphene in each wall. The pore is of finite length and so the confined phase is in direct physical contact with a bulk gas phase at both ends of the pore. The two walls lie parallel to the xy -plane, symmetric about $z = 0$. Carbon atoms are connected to their lattice positions by springs, with the value of the spring constant, k_s , matched to the AIREBO potential [99]. Carbon atoms in different layers interact via the LJ potential, where $\sigma_{CC} = 0.34$ nm and $\epsilon_{CC} / k_B = 28$ K. The lattice positions of the carbon atoms in the outermost layers are fixed in space, but the lattice planes of the surface and central graphene layers are permitted to move, thus allowing the effect of the confined nanophase on pore width and interlayer spacing of the pore wall to be studied. Periodic boundary conditions are applied in the x -direction only. In the y and z directions, hard wall boundary conditions are used.

Two sets of adsorbate-carbon interactive potentials for the realistic pore model are used to study the reason for the pressure enhancement effects. First, the adsorbate-carbon interaction is modeled with a normal LJ potential with the parameters mentioned above, and Lorentz-Berthelot combining rules:

$$\begin{aligned}\sigma_{aC} &= (\sigma_{aa} + \sigma_{CC}) / 2 \\ \epsilon_{aC} &= \sqrt{\epsilon_{aa}\epsilon_{CC}}\end{aligned}\quad (5.4)$$

Second, the WCA (Weeks-Chandler-Andersen) purely repulsive potential [100] is used for the adsorbate-carbon interaction, with the LJ parameters of carbon as the wall parameters:

$$u_{aC}^{WCA}(r_{ij}) = \begin{cases} 4\epsilon_{aC}[(\sigma_{aC}/r_{ij})^{12} - (\sigma_{aC}/r_{ij})^6] + \epsilon_{aC} & r_{ij} < 2^{1/6}\sigma_{fw} \\ 0 & r_{ij} \geq 2^{1/6}\sigma_{fw} \end{cases} \quad (5.5)$$

This potential model allows us to study whether the pressure enhancement arises from the adsorbate-carbon interaction or the geometric confinement effects.

5.3 Simulation Details

We perform argon adsorption in all the models mentioned above for different temperatures and bulk pressures. The slit pore width (when empty) in reduced units, $H_e^* = H_e / \sigma_{aa}$ varies from 2.0 to 8.0 (for BFW argon, the reduced unit is also obtained by scaling by LJ parameters for argon), and is defined as the distance between the wall planes (the simplest model with the Steele (10,4,3) potential), or the distance between the innermost graphene layers on the opposing wall surfaces, when at their equilibrium positions (the realistic model, when the pore is empty). We use (semi-) Grand Canonical Monte Carlo simulations at fixed volume V , temperature T , chemical potential of the confined adsorbate μ_a , and number of wall atoms N_w (the realistic model) to first bring the system to thermodynamic and mechanical equilibrium (equilibrium stage) for 10^8 Monte Carlo moves, and to subsequently calculate the average properties (production stage) for another 10^8 Monte Carlo moves. The MC moves include translational displacement of argon molecules, translational displacement of carbon atoms (for flexible pore only), insertion of argon molecules, and deletion of argon molecules, each of which shares the same probability. For the flexible pore, the displacement of the graphene sheets (along the z -axis) is attempted with an average frequency of 1 / 400 MC moves. The desired state variables (properties such as in-pore density, pressure tensor

component, etc.) are sampled every 4,000 MC moves (i.e., $\sim 25,000$ samples are taken to calculate the ensemble averages). In this study, the pressure is calculated, in general, by the mechanical route using the IK definition, but for the simplest Steele's (10,4,3) pore model, both the mechanical route and thermodynamic route are used and both the IK and Harasima definitions are used for comparison. Simulations are performed at the temperatures of 87.3 K (the normal boiling point of argon), 135 K (a bit lower than the critical point), and 300 K (room temperature, far above the critical point), a wide range of bulk pressures (determined by the chemical potential), and a variety of pore widths. The radial distribution function for adsorbate (argon) in the contact layer is also calculated to investigate the structure and the reason for the high pressure.

5.4 Results and Discussion

5.4.1 Argon in Steele (10,4,3) structureless rigid infinite walls

For the simplest case, the density and pressure of LJ argon confined in a Steele (10,4,3) structureless rigid infinite wall ($H_e^* = 3.0$) at 87.3 K are presented in Figure 5.3. The argon density and pressure profiles at 1 bar bulk pressure is shown in Figure 5.3a. The two peaks in the density profile indicate the well-known layering effect in confined systems. We find more argon layers in larger pores, and the inner layers ($\rho^* < 5$) are less dense than the layers in contact with the wall ($\rho^* > 7$) (see also Sec. 5.4.2 and Figure 5.5). Simulation snapshots show that the argon molecules in the contact layers are arranged as a face-centered cubic (fcc) structure, which only occurs at pressure higher than hundreds of bars for bulk argon at 87.3 K. The peak tangential pressure is located where the density peak occurs. The maximum

tangential pressure is enhanced by a factor of $\sim 19,000$ (by the IK definition) or $\sim 12,000$ (by the Harasima definition), and the normal pressure, which is a constant through the pore width, is negative and enhanced by a factor of 2,000. The normal pressure oscillates sensitively with pore width with an amplitude of 5,000 bar, and can be positive or negative (see also Chapter 8 for an extensive discussion on the normal pressure). In the central region of the pore (the vicinity of $z = 0$), where the density is zero (no argon molecules), the Harasima tangential pressure is exactly zero as expected, but the IK tangential pressure is negative, because the attractive interaction between argon layers contributes to the negative pressure at the planes sitting between the argon layers, that is, the central region. However, the integrals of both tangential pressures over the pore width (corresponding to the surface tension) are almost the same (0.1% difference). We also compare the pressures calculated by the thermodynamic route to those by the mechanical route, and find that the tangential pressure from the thermodynamic route agree perfectly with that from the mechanical route (Figure 5.3b), and that the normal pressure found by two routes is the same (-2204 bar). Furthermore, we investigate the accuracy and validity of the volume perturbation method (thermodynamic route) by calculating the normal pressure of argon adsorbed in carbon structureless pores (see Figure 5.4). We first vary the perturbation factor ζ , which should be small since the method will give accurate result as ζ approaches to the limit of zero. The normal pressure in a pore of $H_e^* = 3.0$ is calculated for a series of ζ , which approaches zero from both sides (positive and negative). As shown in Figure 5.4a, the limiting value of the normal pressure as ζ approaches zero is about -2204.7 bar, but the deviation is very small ($< 0.1\%$) even if ζ is as large as 5×10^{-5} . Therefore, this method is numerically stable for the value of ζ : one can obtain reliable

results and one does not have to choose ξ very carefully. The second examination is to compare the normal pressures calculated by the thermodynamic route with those by the mechanical route for various pore widths. As shown in Figure 5.4b, the normal pressures by both routes in all the pores under test agree quite well without appreciable difference. Therefore, the thermodynamic route and mechanical route give the same results for the pressure of adsorbate in slit pores.

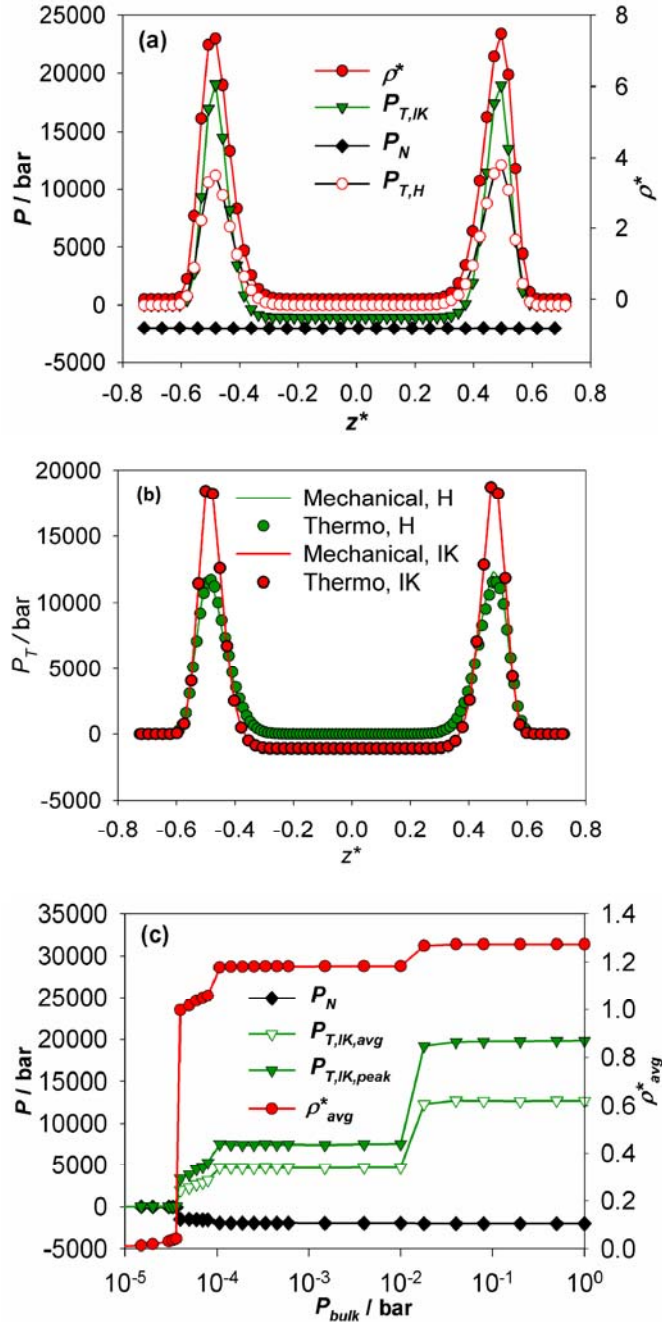


Figure 5.3 In a structureless rigid infinite pore of $H_e^* = 3.0$, at 87.3 K: (a) the density and pressure profiles at 1 bar bulk pressure; (b) the tangential pressure profiles from the mechanical and thermodynamic routes at 1 bar bulk pressure; (c) the average in-pore density and pressures of argon as a function of bulk pressure.

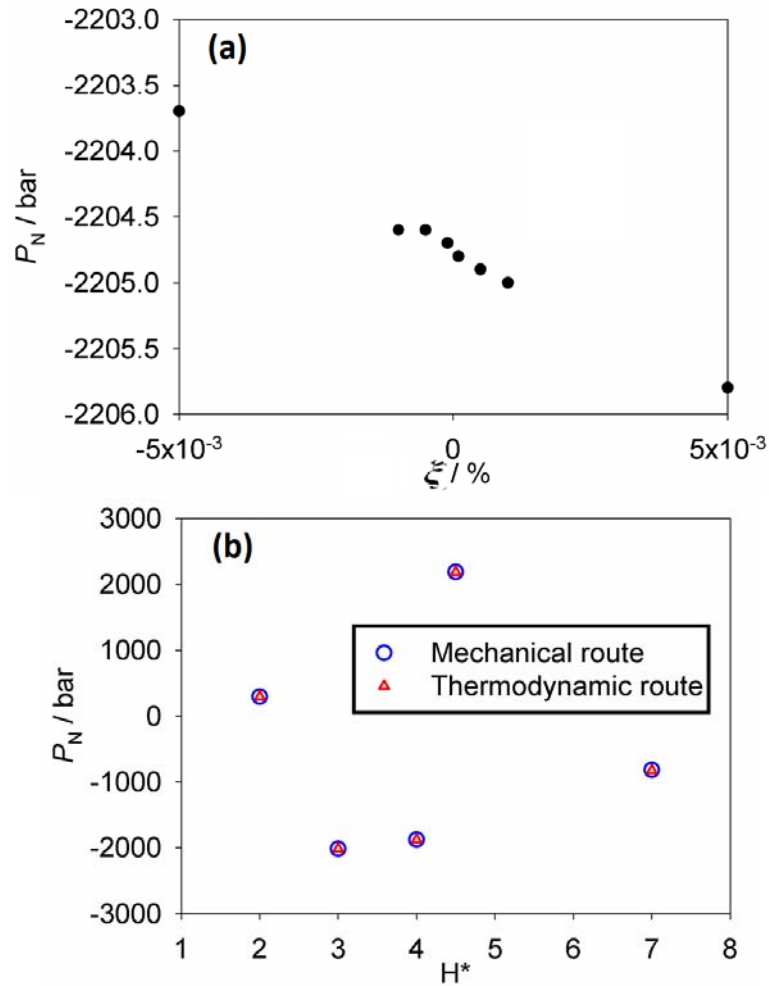


Figure 5.4 The normal pressures calculated by the thermodynamic route in a structureless rigid infinite pore at 87.3 K and 1 bar bulk pressure: (a) with various values of the perturbation parameter ζ , for $H_e^* = 3.0$, and (b) compared with those calculated from the mechanical route for various pore widths.

The averaged tangential pressure of argon confined in the carbon slit pore of $H_e^* = 3.0$ is calculated using the definitions discussed in Sec. 3.4. By using Eqn. (3.83), the average tangential pressure weighted by the density of adsorbate is calculated as 11,830 bar and 8,340

bar for IK and Harasima definitions, respectively. As expected (Sec. 3.4), the above averages are different for different choices of the contour C_{ij} in Eqn. (3.17). By using Eqn. (3.84), the average tangential pressure without weighting factor is calculated as 2,279 bar and 2,282 bar for the IK and Harasima definitions, respectively. As a reference, the overall thermodynamic in-pore tangential pressure calculated by the volume perturbation method by using Eqn. (3.85) is 2,269 bar. Therefore, as discussed in Sec. 3.4, the averaging of the tangential pressure without weighting factor yields the same value for different choices of the integral contour C_{ij} , and this value is equal to the overall thermodynamic tangential pressure ($< 0.5\%$ difference). The spatial averaging of the microscopic local pressure is a macroscopic quantity and can, in principle, be measured [77], whereas the microscopic local pressure contains the information of the peak value (especially for the contact layer), where the high-pressure phase forms and/or the high-pressure reaction occurs. The average weighted by the adsorbate density reflects the importance of the peak. It is actually the average pressure for the region where there are adsorbate layers. But it is not uniquely defined, and depends on the choice of the contour C_{ij} . Therefore, in this dissertation, we present the microscopic local pressure which show the pressure profile over the pore and can be averaged in various ways appropriate for different applications or purposes.

The effects of bulk pressure in a structureless rigid infinite pore are shown in Figure 5.3c for the pore of $H^* = 3.0$ at 87.3 K. Argon starts to be adsorbed at $P_{bulk} \sim 1 \times 10^{-5}$ bar, and at higher pressures two jumps in the density and $P_{T,IK,peak}$ correspond to phase transitions from a gas-like to a liquid-like phase (at $P_{bulk} \sim 5 \times 10^{-5}$ bar) and from the liquid-like to a fcc crystal

phase (at $P_{bulk} \sim 1 \times 10^{-4}$ bar). After the transition to the fcc crystal phase, there is another jump in the density and tangential pressure (at $P_{bulk} \sim 1 \times 10^{-2}$ bar), while the increases are continuously smooth for an atomistic flexible finite pore (Figure 5.8a). The additional jump phenomenon in an infinite pore with fixed periodic boundary conditions occurs probably because more argon cannot adsorb until the bulk pressure (chemical potential) is large enough to squeeze an additional molecule in the adsorbed layer. In contrast, for a pore of finite length, the in-pore molecular arrangement and intermolecular distance can change gradually according to the bulk pressure, since molecules can adsorb at the mouth and on the external surface of the pore. In addition to the maximum value, the weighted average tangential pressure averaged across the pore, $P_{T,avg} = \int P_T(z)\rho_{ad}(z)dz / \int \rho_{ad}(z)dz$, is also shown in Figure 5.3c. Both increase rapidly with P_{bulk} , following the increase in density, whereas P_N is only slightly affected. The pressure enhancement, $P_{T,IK,peak} / P_{bulk}$, is as large as 7 orders of magnitude at $P_{bulk} \sim 10^{-4}$ bar and is 4 orders of magnitude at $P_{bulk} \sim 1$ bar at 87.3 K.

5.4.2 Argon in realistic carbon slit pores with LJ interactive potential model

We next study the density and pressure of LJ argon confined in a more realistic pore model, having an atomistic flexible wall with finite length at 87.3 K. In Figure 5.5, we show the argon density and pressure profiles (of the averaging region, hereafter, unless specified) at 1 bar bulk pressure for several pore widths. The results are quite similar to the simplest model (Steele's (10,4,3) rigid wall with infinite length). The peak tangential pressure in this model (take $H_e^* = 3.0$ case for example) is higher than for the simpler model (30,000 bar compared

with 19,000 bar). A similar difference is also found for the peak value of density (8 compared with 6). This difference still arises from the nature of infinite pore with periodic boundary conditions, where the argon layer is not as dense as it should be at the same certain bulk pressure in an infinitely long pore, because a whole argon molecule cannot be accommodated inside the pore. The tangential pressure is then much lower because of the looser arrangement of argon. Hence, the pore with finite length gives more accurate results. The normal pressure in this model is also enhanced by a factor of ~ 1000 , in qualitative agreement with that for the simpler model, and the normal pressure depends on the pore widths: it could be positive ($H_e^* = 2.0$ and 4.5 , see Figure 5.5a and c) or negative ($H_e^* = 3.0$ and 7.0 , see Figure 5.5b and d). From Figure 5.5, it is also shown that the tangential pressure profile follows that of the density, with very high pressures of over 20,000 bar at the contact layer peaks for all pore widths. Specifically, for $H_e^* = 2.0$, only a single layer of argon can be accommodated, and the tangential pressure at the peak is approximately 60,000 bar.

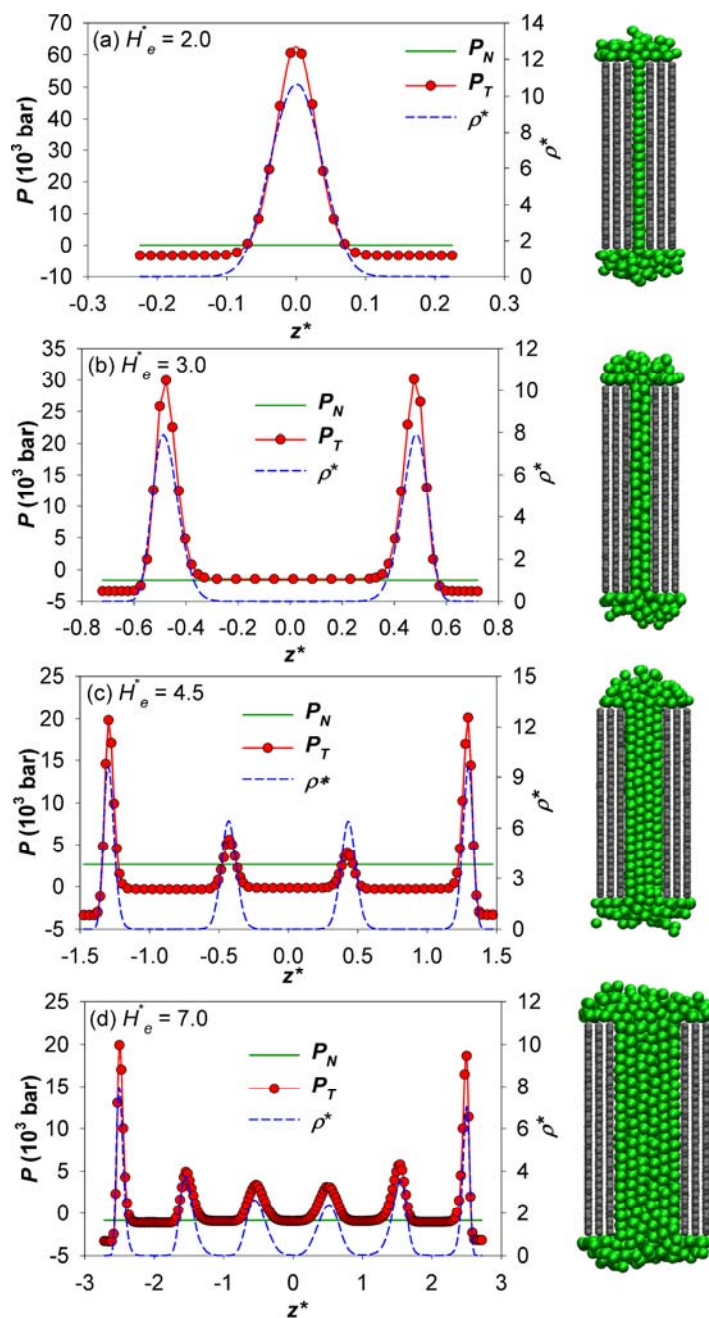


Figure 5.5 The density and pressure profiles and snapshots of argon adsorbed in the flexible finite atomistic carbon slit pore model at 87.3 K and 1 bar bulk pressure for pores of reduced widths of (a) 2.0, (b) 3.0, (c) 4.5 and (d) 7.0, respectively. Carbon atoms are shown at reduced scale for clarity.

The contribution of the kinetic and configuraitonal terms to the pressure profiles (see in Eqns. (3.15) and (3.16)) are shown in Figure 5.6 for $H_e^* = 3.0$ at 87.3K and 1 bar bulk pressure. In each case, the argon-argon and argon-carbon contributions of the configurational part of the pressure tensor profiles are shown separately.

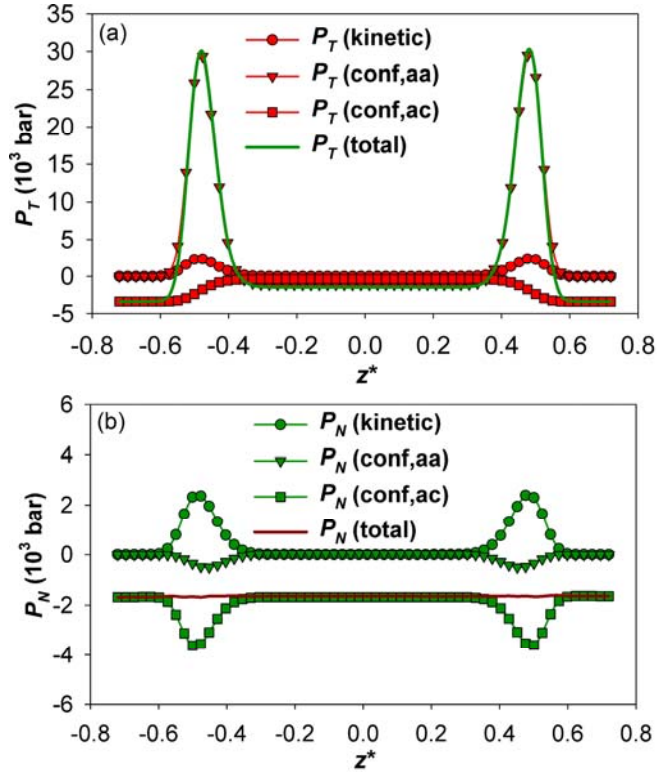


Figure 5.6 Decomposition of the (a) tangential and (b) normal pressure tensor profiles into the kinetic contribution and the argon-argon and argon-carbon configurational contributions for $H_e^* = 3.0$ at 87.3K and 1 bar bulk pressure in the flexible finite atomistic carbon slit pore.

As is evident from Figure 5.6a, the tangential pressure profile is strongly dominated by the configurational contribution arising from argon-argon interactions. This large, positive contribution that arises in the contact layers indicates the presence of strong repulsive forces

between argon molecules within the layer. However, the argon-carbon contribution is slightly negative and decreases to a value of about $-2,500$ bar in the contact layers due to attractive forces between the argon and carbon atoms. The argon-carbon contribution to the tangential pressure is roughly offset by the positive kinetic contribution at this temperature, which peaks at $\sim 2,500$ bar at the density maxima. The kinetic part of the normal pressure profile is the same as in the tangential pressure profile, again with a peak height of $\sim 2,500$ bar. However, both the argon-argon and argon-carbon configurational contributions are negative, which reflects the fact that the forces are attractive and that the system is in tension, rather than compression, along the normal direction. From Figure 5.5 and Figure 5.6b, it is shown that mechanical equilibrium is maintained, with constant P_N in each case, within the statistical uncertainty of the calculations.

The high in-pore tangential pressures arise from the confinement of the nanophase and the strong attraction between the carbon walls and argon molecules, which force the adsorbed phase into highly compressed layers. To demonstrate this, we calculated the radial distribution functions, $g(r)$, for the argon molecules in the contact layer, which gives the probability distribution of finding two argon molecules at a separation distance, r , within the same layer. The in-plane $g(r)$ for the contact layers of argon in the pore of $H_e^* = 3.0$ is shown in Figure 5.7a at 1 bar and 87.3 K (the boiling point of argon), and also at 3990 bar and 300 K (ambient temperature, and the pressure under which the in-pore density is similar to that at 87.3 K and 1 bar). For reference, $g(r)$ is also shown for bulk liquid argon at 87.3 K. The first peak in $g(r)$ corresponds to the most probable nearest neighbor distance in a given layer. At

both state conditions examined, this distance is found to be significantly smaller than in bulk liquid argon at 87.3 K, and is in the steeply rising repulsive region of the intermolecular pair force, as shown in Figure 5.7b. This large and positive repulsive force gives rise directly to the observed large tangential pressures. We note that for hard spheres against a hard wall, where attractive forces are absent, there is little or no enhancement of the tangential pressure [101] (we will also show the similar results in a WCA repulsive wall later in this section). Such compression has been previously reported for strongly attractive surfaces [102-104].

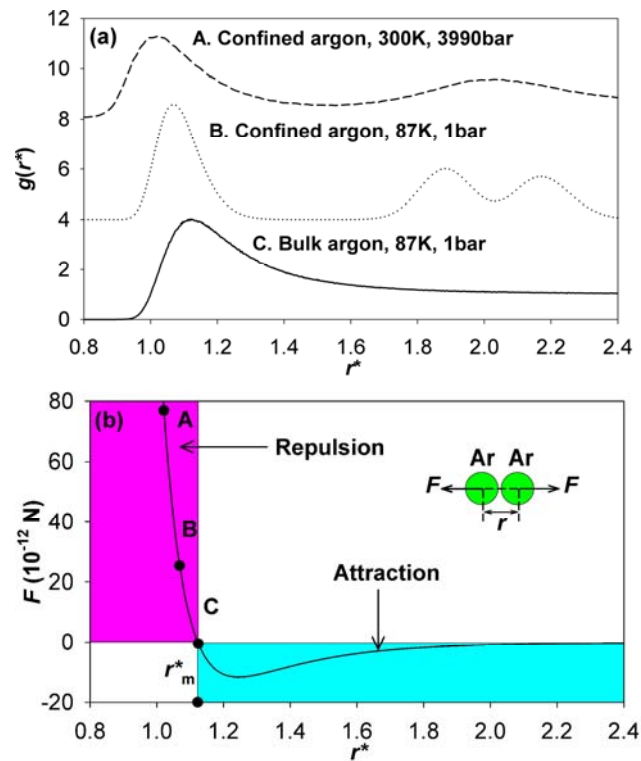


Figure 5.7 (a) Radial distribution function in the xy -plane for confined argon at 300 K and 3,990 bar bulk pressure (A, dashed line) and at 87.3 K and 1 bar bulk pressure (B, dotted line), and the isotropic radial distribution function for bulk argon at the boiling point, 87.3 K (C, solid line). (b) The intermolecular force between two argon molecules, F , with the most probable nearest neighbor separation distances shown for the three cases illustrated in (a).

It is of interest to note that this situation is the opposite of that observed in gas-liquid interfaces, where the most probable separation between neighboring molecules in the xy -plane is greater than that in the bulk liquid. Thus, in our MC simulations of the gas-liquid interface for Ar at its normal boiling point we find that the most probable Ar-Ar separation distance is $r^* = 1.17$, significantly greater than for bulk liquid argon ($r^* = 1.12$), so that the average pair force is negative (attractive), as it must be to produce a surface tension (see also [57]). The tangential pressure in this case is therefore negative, being approximately -80 bar near the center of the interface.

The effects of bulk pressure for the realistic model of $H_e^* = 3.0$ at various temperatures are shown in Figure 5.8. For the temperature 87.3 K, The bulk pressures at which argon starts to be adsorbed, transits from a gas-like to a liquid-like phase, and transits from the liquid-like to a fcc crystal phase are almost the same as those in the simplest model (Sec. 5.4.1 and Figure 5.3c). However, beyond these jumps, the isotherms in the realistic model are changing more smoothly than the simplest model. This phenomenon was also observed by a non-local density functional theory study of gas adsorption in finite and infinite carbon pores [105]. Therefore, the simplest model can qualitatively describe the pressure enhancement effects, but a realistic model gives more accurate results. As the temperature is increased, first to 135 K and then to 300 K, the nanophase capillary condensation transition vanishes (suggesting that these temperatures are above the pore critical temperature) and there is no evidence of a liquid-solid transition, as shown in Figure 5.8b and c. The kinetic contribution to the pressure tensor components becomes relatively more important at these higher temperatures, and this

reduces the pressure enhancement, $P_{T,peak} / P_{bulk}$, considerably, to about three orders and one order of magnitude at 135 K and 300 K, respectively. The normal pressure is insensitive to the bulk pressure after the pore is filled up (especially at low temperature), because the enhancement of the normal pressure depends directly on the compression in the normal direction and thus the pore width (see also Sec. 8.1).

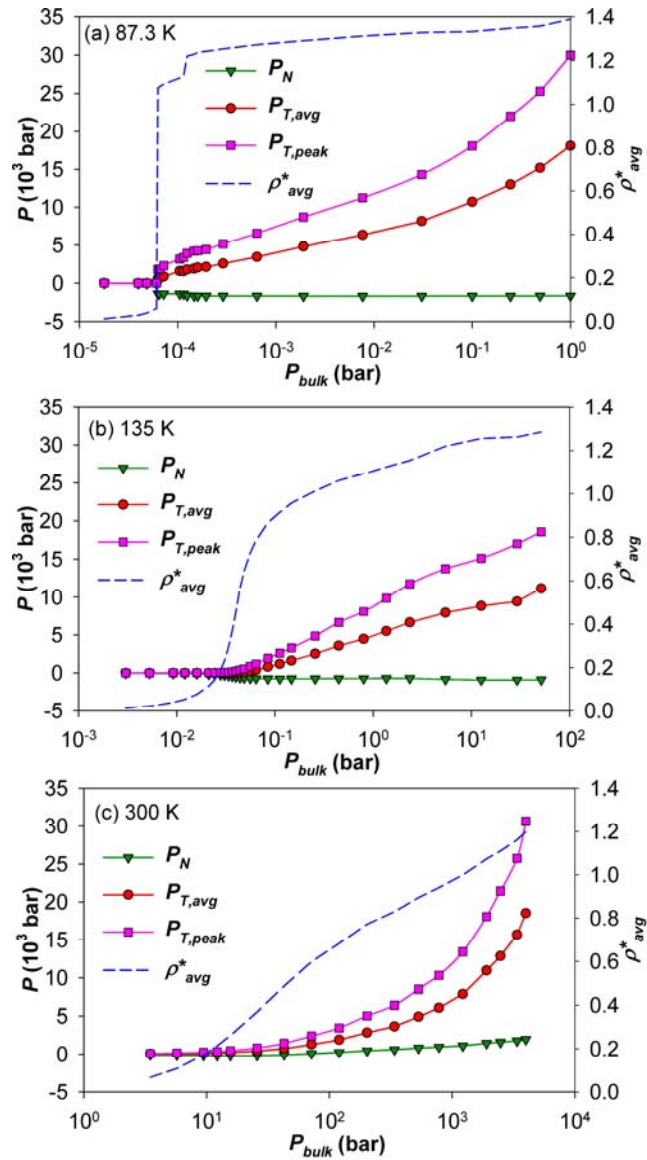


Figure 5.8 The average in-pore density and pressures of argon as a function of bulk pressure at (a) 87.3 K, (b) 135 K and (c) 300 K, respectively, for $H_e^* = 3.0$.

The realistic model also allows us to study edge effects (how the pressure tensor component changes as it goes to the mouth of the pore). We show in Figure 5.9 the pressures of LJ argon along the pore length at 87.3 K and 1 bar bulk pressure. Both normal and tangential pressures

are almost constant in the central part of the pore, and start to be less enhanced and approach to the bulk pressure when close to the pore mouth (~ 2.0 in reduced units away from the pore mouth).

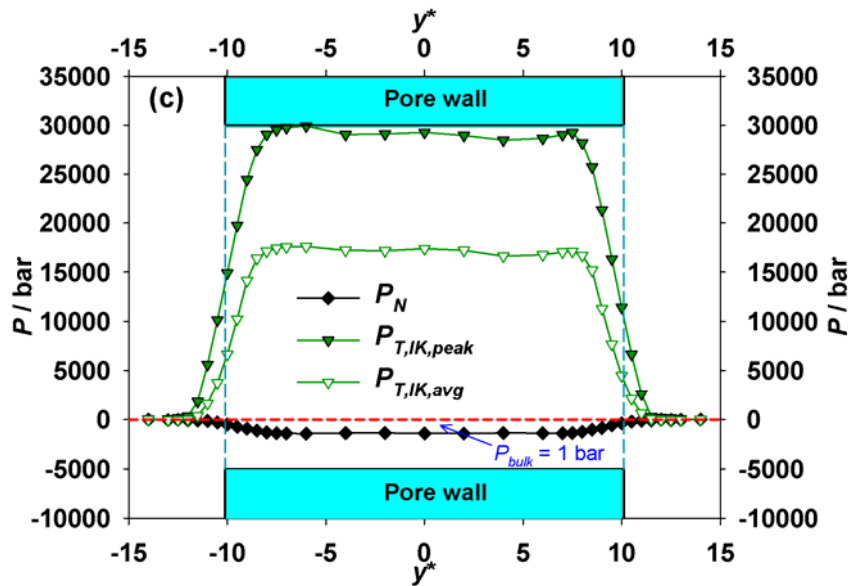


Figure 5.9 The pressure tensor components of LJ argon along the pore length at 87.3 K and 1 bar bulk pressure in an atomistic flexible finite pore of $H_e^* = 3.0$.

We also study argon with the BFW potential confined in the realistic pore model at 87.3 K and 1 bar bulk pressure. We compare the density and pressure profiles of LJ argon (Figure 5.10a) and BFW argon (Figure 5.10b) in a pore of $H_e^* = 4.5$. The average in-pore densities of the two cases are almost the same ($\sim 1\%$ difference), but the LJ argon exhibits higher peak values of local density in both contact layers and central layers than those of BFW argon, which means that the density peak of BFW argon is wider, and thus the layer of BFW argon is less perfect than for the LJ argon. This is probably because of the “softer” nature of the

BFW potential (Figure 5.1), that is, the BFW argon molecules in different layers have a higher probability of being closer to each other instead of standing in their own layers without any inter-intrusion. On the other hand, the tangential pressure of BFW argon is appreciably higher than for LJ argon in both contact layers ($\sim 23,000$ bar for BFW argon compared with $\sim 20,000$ bar for LJ argon) and central layers ($\sim 9,000$ bar for BFW argon compared with $\sim 5,000$ bar for LJ argon). This is probably because of the configurational contribution from the interlayer interaction of argon: for the BFW argon, which is softer, there is a higher probability to have argon molecules in different layers closer to each other compared with LJ argon, and this smaller separation distance gives rise to the repulsive contribution to the pressure tensor. Also note that for a pore of $H_e^* = 4.5$ where there are four argon layers, the interlayer spacing of argon is ~ 0.85 and smaller than the LJ diameter of argon, and thus the repulsive interaction of argon molecules in different layers is important. The normal pressure for the BFW argon ($\sim 2,120$ bar) is appreciably smaller than that for the LJ argon ($\sim 2,660$ bar), which is also a result of the softer nature of the BFW argon (with the same degree of compression in the normal direction, the repulsion between BFW argon is weaker than that for the LJ argon). However, generally LJ argon and BFW argon exhibit very similar layering and pressure enhancement phenomena quantitatively, and the LJ potential model is a satisfactory approximation and much more efficient in computation.

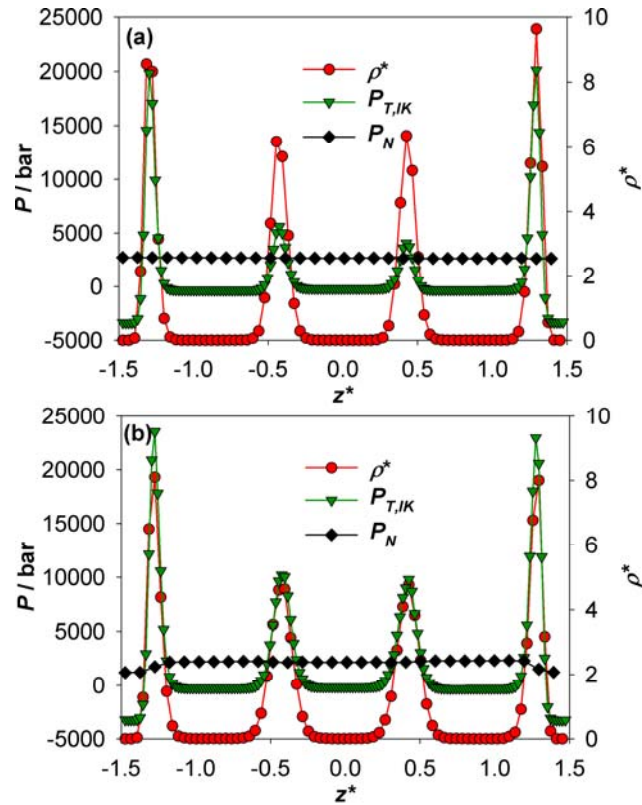


Figure 5.10 The density and pressure profiles of (a) LJ argon and (b) BFW argon in an atomistic flexible finite pore of $H_e^* = 4.5$, at 87.3 K and 1 bar bulk pressure.

5.4.3 Argon in realistic carbon slit pores with WCA interactive potential model

To find the reason for the highly enhanced tangential pressure in the argon layer in contact with the wall, we decomposed the tangential pressure, and found that the argon-argon configurational contribution is dominant (Sec. 5.4.2 and Figure 5.6a). The in-plane radial distribution function also showed that the separation distance between argon molecules is so small that the repulsive interaction is very strong (see also Figure 5.7), that is, the argon confined in the slit pore is highly compressed. To demonstrate that it is the strong attraction between the wall atoms and argon molecules that forces the adsorbed argon molecules to be

closely packed in the direction parallel to the wall (not because of the geometric confinement), we show in Figure 5.11 the density and pressure profiles in a WCA-repulsive wall, where there is no attractive interaction between argon and wall atoms. At 5 bar bulk pressure, the density, tangential and normal pressures are almost constant (homogeneous system) within statistical error. There is no layering, and the pressure is not enhanced (Figure 5.11a). At 200 bar bulk pressure, there is very weak layering phenomenon, and the pressure is enhanced by a factor as small as ~ 2.5 (Figure 5.11b). This test indicates that the geometric confinement itself does not compress the phase confined in the pore. Therefore, the compression of argon layer is a result of the attractive nature of the wall atoms.

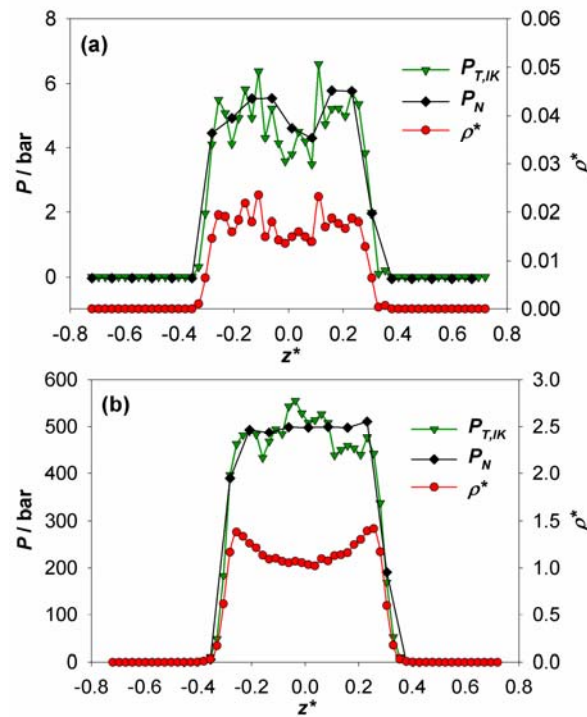


Figure 5.11 The density and pressure profiles of LJ argon in the atomistic flexible finite pore with a WCA-repulsive potential, at 87.3 K and bulk pressures of (a) 5 bar, and (b) 200 bar.

5.5 Conclusions

In summary, our calculations show that very high tangential and normal pressures are expected in carbon micropores and small mesopores. These high in-pore pressures provide a unifying explanation for a wide range of previously unconnected experimental observations, including the observation of high pressure phases and high pressure reactions in carbons, and could provide a route to connect the behavior of the confined phase to that of the bulk phase. Such a connection could prove useful as a guide to future experimental studies of high pressure phenomena in nanoporous carbons. This pressure enhancement effect arises from the strong attractive nature of the pore wall, and thus the adsorbate (especially for the molecules in contact with the wall) is strongly compressed which produces a strong repulsive force between adsorbate molecules (especially in the tangential direction). A further important finding is that relatively small changes in the bulk pressure (and to a lesser extent, the temperature) have a very large effect on the in-pore pressure. This sensitivity to the bulk phase pressure provides an explanation of the large effect of bulk pressure on the melting curve for confined phases that has been observed in molecular simulations [18, 106]. This also suggests that it should be possible to experimentally observe a range of high pressure phenomena by simply varying the bulk pressure. The average tangential pressure is calculated in various ways and yield different values. Each way of averaging has its own physical sense, so that the choice of the way of averaging depends on the purposes and applications.

CHAPTER 6

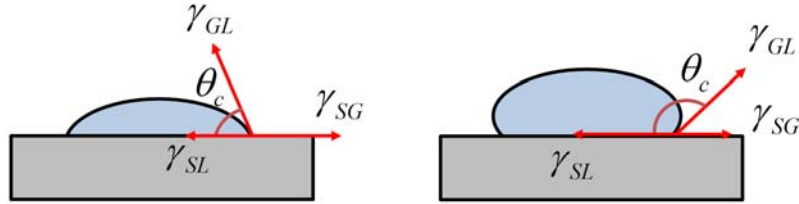
Effects of the Wetting Parameter on Adsorption and Pressure

6.1 Introduction

As discussed in Chapter 5, the adsorption behavior and the pressure enhancement are results of the attractive nature of the pore wall. Actually, the adsorption and thus the structure of confined adsorbate and the in-pore pressure are strongly related to the wettability of the adsorbate-wall system, i.e., the relative strength of the attraction between the adsorbate and the wall to the attraction among the adsorbate molecules themselves. In this Chapter, we introduce a *microscopic wetting parameter*, α_w , that is a measure of the adsorbate-wall (*aw*) relative to the adsorbate-adsorbate (*aa*) interaction, through a corresponding states analysis of the partition function. We report experimental measurements of the contact angle for a wide range of liquids (nonpolar, polar and H-bonded, metals) on three planar substrates, graphite, silica and mica. We show that these macroscale contact angle measurements are closely correlated with the microscopic wetting parameters for these systems. We then apply the microscopic wetting parameter concept to adsorbate nanophases in small pores. Using molecular simulation studies, we find that adsorption, capillary condensation, and pressure enhancement are all strongly dependent on α_w , and that it plays a key role in nano-scale behavior.

6.2 Nano-Scale Wetting and the Microscopic Wetting Parameter

At the macro-scale it is usual to discuss the degree to which a liquid wets a solid surface in terms of the contact angle, θ_c , and the surface tensions for the surfaces involved. These are related by a simple force balance, as shown by Young [107] (illustrated in Figure 6.1).



$$\text{Young's Equation: } \gamma_{SG} = \gamma_{SL} + \gamma_{GL} \cos \theta_c$$

Figure 6.1 Wetting of a solid surface by a liquid at the macro-scale, for strongly wetting (left) and weakly wetting (right) adsorbates. Arrows indicate the forces due to surface tensions for the solid (S), gas (G) and liquid (L) phases.

For sufficiently small nano-scale systems (e.g., a fluid wetting a nanoparticle or the walls of a nanopore), the surface tension concept breaks down because there is no longer a clearly defined interface separating two bulk phases [108]. Nevertheless, the degree to which one phase “likes” a solid substrate remains an important factor in determining the behavior of such nano-scale systems, and it would be useful to have a quantitative measure of this. The tendency to wet a solid substrate is the result of a competition between the interactions of fluid molecules with the substrate and the adsorbate-adsorbate interactions within the fluid itself (see Figure 6.2). This is true whether the system is a nanoscale or macroscopic one. Based on this idea, a dimensionless variable, named as the *microscopic wetting parameter*

(or simply the *wetting parameter*), α_w , measuring the adsorbate-wall (*aw*) relative to the adsorbate-adsorbate (*aa*) interaction, is defined quantitatively for a simple wall model as [109]:

$$\alpha_w = \rho_w \sigma_{aw}^2 \Delta_w \epsilon_{aw} / \epsilon_{aa}, \quad (6.1)$$

where ϵ and σ are the usual energy (well-depth) and molecular diameter parameters, respectively, ρ_w is the number density of the wall atoms, and Δ_w is the spacing between layers of the wall atoms (see the label on Figure 6.2). From Eqn. (6.1), the wetting parameter can be used to classify porous materials into “strongly attractive” ($\alpha_w > 1$), “weakly attractive” ($\alpha_w < 1$), or “intermediately attractive” ($\alpha_w \sim 1$). This dimensionless wetting parameter α_w arises from the corresponding states analysis discussed in the next section.

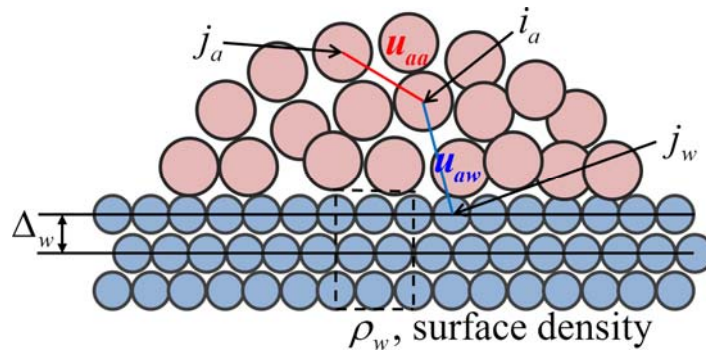


Figure 6.2 A schematic illustration of wetting on a molecular scale.

We name α_w the *wetting parameter* because the wettability (or quantitatively the contact angle, θ_c , as shown in Figure 6.1) of the adsorbate on the surface is closely related to the value of α_w as evidenced by experimental results provided by our collaborator, Professor

Śliwińska-Bartkowiak and coworkers. They measured the contact angles of various fluids (adsorbate) on graphite, silica and mica planar surfaces (systems with a wide range of α_w). The results are listed in Table 6.1, and the relationship between wetting parameter and contact angle is visualized in Figure 6.3. It is shown that the contact angle decreases almost exponentially with the increasing wetting parameter. This agrees with the physical meaning of the wetting parameter: the adsorbate-wall relative to the adsorbate-adsorbate interaction; for larger α_w , the adsorbate-wall interaction is stronger than the adsorbate-adsorbate interaction, and so the fluids tend to spread on the wall, which corresponds to a smaller contact angle.

Table 6.1 The wetting parameter and experimental contact angles of various liquids on graphite, silica and mica surfaces. The potential model parameters used to calculate the wetting parameters are taken from [8, 97, 110-112], and the detailed calculation can be found in Appendix D.

Substrate	Fluids	C ₆ H ₅ Br	CCl ₄	C ₆ H ₅ NO ₂	H ₂ O	Hg	OMCTS
Graphite	α_w	2.0782	1.9259	1.2623	0.4776	0.1221	3.3208
	θ_c / deg	15.76	17.34	23.61	71.32	142.4	9
Silica	α_w	1.284	1.1845	0.7764	0.2781	0.07127	2.1274
	θ_c / deg	24.45	19.12	--	44.59	141	10
Mica	α_w	2.351	2.1803	1.4289	0.5445	0.1391	3.7392
	θ_c / deg	34.3	23.6	--	38.5	138	9

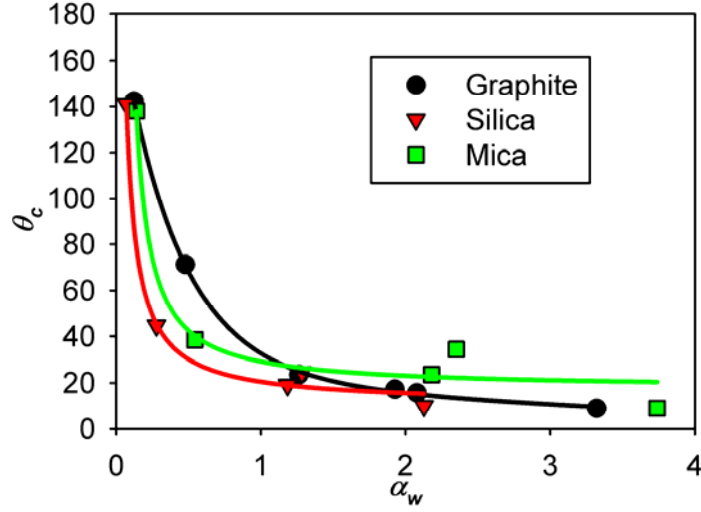


Figure 6.3 Experimental contact angles as a function of wetting parameters of various fluids on different substrates. The curves are a guide to the eye.

6.3 Corresponding States Analysis

We consider a system with a LJ adsorbate confined between Steele's (10,4,3) smooth walls (see Sec. 5.2 for definitions). The configurational partition function in the canonical ensemble $Q_{conf}(N, V, T)$ is given by

$$\begin{aligned}
 Q_{conf} &= \int_0^V d\mathbf{r}_i^N \exp\left(-\frac{U(\mathbf{r}_i^N)}{k_B T}\right) \\
 &= \int_0^V d\mathbf{r}_i^N \exp\left(-\frac{U_{aa}(\mathbf{r}_i^N)}{k_B T} - \frac{U_{aw}(\mathbf{r}_i^N)}{k_B T}\right) \\
 &= \int_0^V d\mathbf{r}_i^N \exp\left(-\frac{\varepsilon_{aa} f(\mathbf{r}_i^N)}{k_B T} - \frac{\varepsilon_{aw} \rho_w \Delta_w \sigma_{aC}^2 g(\mathbf{r}_i^N)}{k_B T}\right), \\
 &= \int_0^V d\mathbf{r}_i^N \exp\left(-\frac{1}{T^*} f(\mathbf{r}_i^N) - \frac{\alpha_w}{T^*} g(\mathbf{r}_i^N)\right)
 \end{aligned} \tag{6.2}$$

where T^* is the reduced temperature ($T^* = T / (\varepsilon_{aa}/k_B)$), and f and g are functions related to the adsorbate-adsorbate separation and adsorbate-wall separation, respectively and thus f accounts for the adsorbate-adsorbate interaction and g accounts for the adsorbate-wall interaction. Thus,

$$Q_{conf} = Q_{conf}(N, V^*, T^*, \alpha_w, \sigma_{aw} / \sigma_{aa}) = Q_{conf}(N, H^*, T^*, \alpha_w, \sigma_{aw} / \sigma_{aa}). \quad (6.3)$$

(Note that the reduced volume $V^* = V / \sigma_{aa}^3$ is related to the reduced pore width, $H^* = H / \sigma_{aa}$, for a porous system.)

At the freezing point, the chemical potential of the liquid phase equals to that of the solid phase [113]:

$$\mu_L(T_f) = \mu_S(T_f) \Rightarrow -k_B T_f \left(\frac{\partial \ln Q_L}{\partial N} \right)_{T,V} = -k_B T_f \left(\frac{\partial \ln Q_S}{\partial N} \right)_{T,V}. \quad (6.4)$$

Considering Eqns. (6.3) and (6.4), and the corresponding states principle (using reduced variables scaled by the adsorbate properties), the reduced freezing point of the adsorbate in the pore is

$$T_f^* = T_f^*(H^*, \alpha_w, \sigma_{aw} / \sigma_{aa}), \quad (6.5)$$

or a function of reduced pore width H^* , wetting parameter α_w , and size ratio of adsorbate molecules, σ_{aa} , to wall atoms, σ_{ww} . For the small adsorbate molecules (e.g., Ar, Hg, etc), the sizes of the molecules and the wall atoms are quite similar (~ 0.3 nm), and thus a good approximation is that the freezing point is only a function of reduced pore width and wetting parameter:

$$T_f^* = T_f^*(H^*, \alpha_w) \quad \text{for small adsorbate molecules.} \quad (6.6)$$

Similar results are true for the capillary condensation pressure:

$$P_c^* = P_c^*(H^*, \alpha_w, \sigma_{aw} / \sigma_{aa}) \approx P_c^*(H^*, \alpha_w) \quad (6.7)$$

6.4 Effects of the Wetting Parameter α_w on Capillary Condensation

6.4.1 Modeling and Simulation Details

The adsorption of argon in simple slit pores is performed by using the GCMC method. The argon-argon (adsorbate-adsorbate) interaction is modeled with a LJ potential with parameters of $\varepsilon_{aa} / k_B = 119.8$ K and $\sigma_{aa} = 0.3405$ nm [95] with a cut-off of $5\sigma_{aa}$, while the slit pore is composed of two parallel Steele's (10,4,3) structureless walls (adsorbate-wall potential is of the form shown in Eqn. (5.3)). Most of the parameters of this wall model are the same for Eqn. (5.3), but the well-depth ε_{aC} varies such that the wetting parameter of the adsorbate-wall system covers a range from 0.1 to 4.0. The separation distance between two parallel walls also varies to achieve the reduced pore width ($H^* = H / \sigma_{aa}$) in a range of 5 to 15 (for very small pores, $H^* < 5$, capillary condensation does not occur). The wall is made to be of infinite extent by applying periodic boundary conditions in the x - and y -directions, and the x - and y -dimensions of the simulation box is $15\sigma_{aa}$.

The adsorptions are performed at 87.3 K (the normal boiling point of argon at 1 bar bulk pressure, and so $T^* = 87.3\text{K} / 119.8 \text{ K} = 0.7287$) for a wide range of bulk pressures (chemical

potential). The capillary condensation pressure is carefully determined by running for a very fine grid of pressure points.

6.4.2 Results and Discussion

The capillary condensation pressure of argon as a function of the wetting parameter in different slit pores is shown in Figure 6.4. In general, the capillary condensation pressure P_c decreases with increasing wetting parameter α_w for all pore widths, which agrees with the fact that larger α_w means stronger attraction from the wall and so a lower chemical potential from the bulk is needed to condense the adsorbate. The condensation pressure decreases with decreasing pore width (holding the wetting parameter constant) because the adsorbate-wall interaction is relatively stronger relative to the adsorbate-adsorbate interaction in a smaller pore; this causes a decrease in the freezing point for smaller pores. For $\alpha_w < 0.85$, a weakly attractive wall, the adsorbate argon condenses at a pressure higher than the saturation pressure (*capillary evaporation*), suggesting that the wall provides even less attractive interaction compared with those for pure argon. For a large wetting parameter (e.g. $\alpha_w > 1.0$), the adsorbate condenses at pressures considerably lower than the saturation pressure (*capillary condensation*), suggesting a large attractive nature of the wall. These observations are true for all the pore widths. For very large pores (e.g. $H^* = 15$), the adsorbate in the pores forms a phase of very large volume, and thus the capillary condensation pressure is just slightly lower than the saturation pressure because the effect of the pore wall becomes smaller due to the larger separation distance between walls and adsorbate in the central part of the pore.

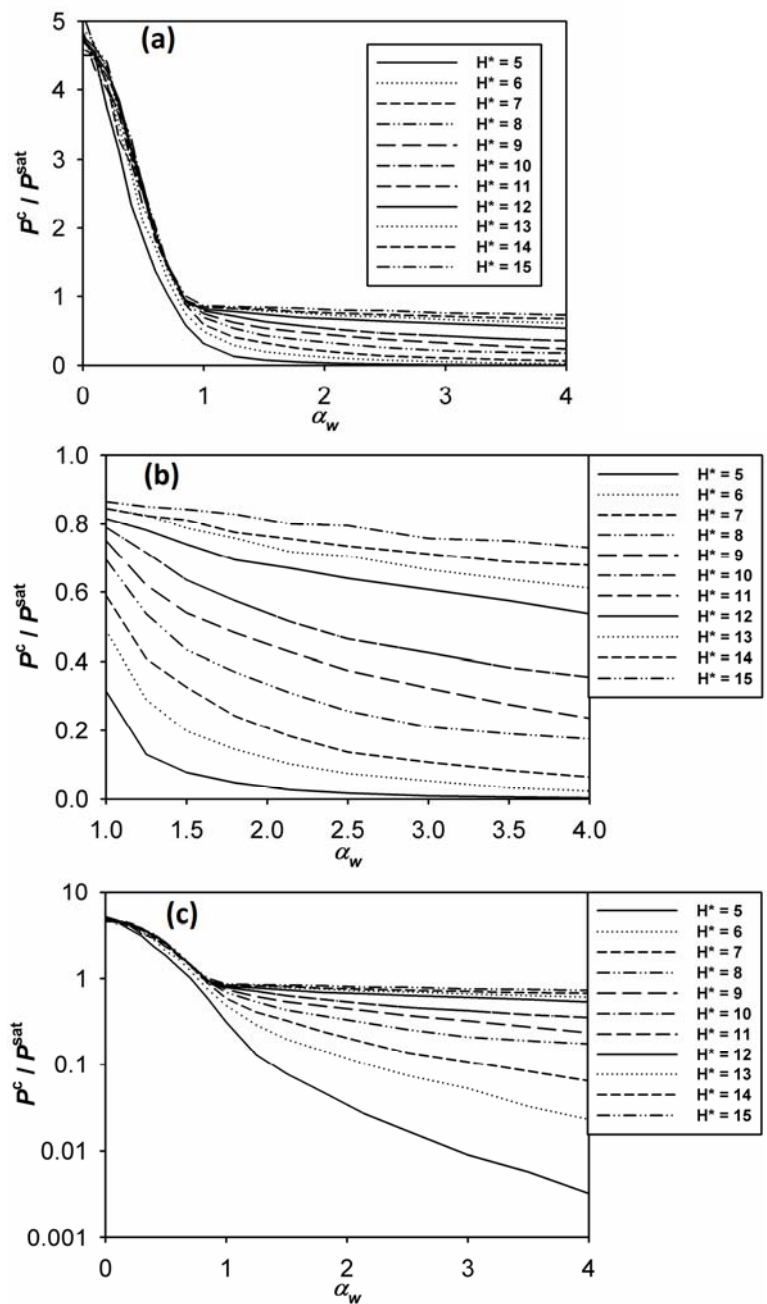


Figure 6.4 The capillary condensation pressure of argon as a function of wetting parameter in slit pores with various pore widths at 87.3 K. The three parts shows the same results but on different scales.

6.5 Effects of Wetting Parameter α_w on In-Pore Pressure

6.5.1 Modeling and Simulation Details

The adsorption of argon in a slit pore is performed using the GCMC method. The argon-argon (adsorbate-adsorbate) interaction is modeled with a LJ potential with parameters $\varepsilon_{aa} / k_B = 119.8$ K and $\sigma_{aa} = 0.3405$ nm [95] with a cut-off of $5\sigma_{aa}$, while the slit pore is composed of two parallel atomistic walls, each of which is composed of three graphene layers. Periodic boundary conditions are only applied to the x -direction. In each of the y -directions, there is a bulk phase in direct contact with the pore mouth (edge), which is similar to the realistic model described in Chapter 5 (Figure 5.2b), but the carbon atoms are fixed in space this time. The adsorbate-wall interaction is also a pure LJ potential, as described in Chapter 5, with Lorentz-Berthelot combining rules. The LJ well-depth ε_{aC} is varied, so that the wetting parameter of the adsorbate-wall system covers a range from 0.4 to 4.0. The separation distance between the two parallel walls is also varied to achieve some typical reduced pore widths ($H^* = H / \sigma_{aa}$) of 2.0, 3.0, 4.5 and 7.0. The adsorption is performed at 87.3 K and 1 bar bulk pressure (the normal boiling point of argon). The in-pore pressure is calculated using the IK definition with the mechanical route (see Sec. 3.2). We also calculate the in-pore density, normal pressure and tangential pressure along the isotherm (by varying the bulk pressure) for $H^* = 7.0$ with three typical wetting parameters which correspond to the argon-silica, argon-carbon and argon-mica systems.

6.5.2 Results and Discussion

The in-pore density, normal pressure and the peak value of tangential pressure as functions of the wetting parameter are shown in Figure 6.5 for the reduced pore widths of 2.0, 3.0, 4.5 and 7.0. For very small pores (e.g., $H^* = 2.0$), the effects of α_w on the tangential pressure and in-pore density are very strong (see Figure 6.5a). The in-pore density as well as the tangential pressure increases rapidly with increasing α_w . This large effect arises from the very small separation distance between the two parallel walls. For the pore of $H^* = 2.0$, only one layer of argon can be accommodated in the pore, and both walls impose strong interactions on this layer. Thus, as the value of α_w increases, the attractive interaction from the walls increases doubly, and the in-pore density as well as the tangential pressure increase rapidly and continuously compared to those in the larger pores (compare Figure 6.5a to Figure 6.5b, c, and d). The tangential pressure in this small pore could be as high as 180 000 bar for $\alpha_w = 4$. For a slightly larger pore of $H^* = 3.0$, two adsorbate layers can be accommodated, and the coupling of interactions from both walls to each adsorbate layer still exists but becomes much weaker. As a result, the in-pore density of the adsorbate is much smaller than that for $H^* = 2.0$, and the tangential pressure is about 80,000 bar for $\alpha_w = 4$. For even larger pores ($H^* = 4.5$ and 7.0), the walls have little effect on the adsorbate layer in contact with the opposite walls and so the increase of α_w increases the peak value of the tangential pressure (located at the contact layer) relatively slowly ($P_{T,peak} \sim 60,000$ bar for $\alpha_w = 4$ for both pore widths).

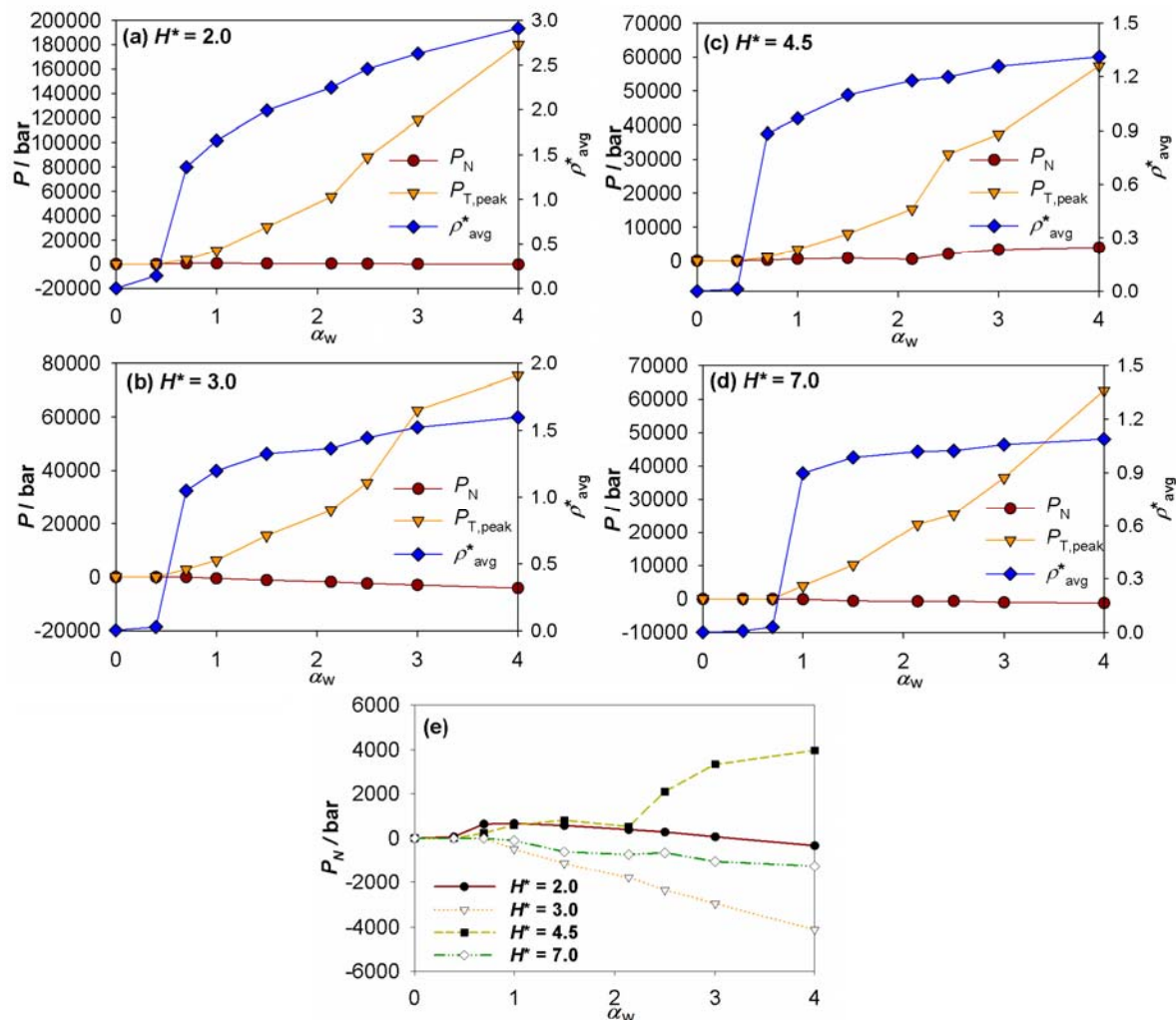


Figure 6.5 The in-pore density, the normal pressure and the peak value of the tangential pressure of argon as functions of the wetting parameter at 87.3 K and 1 bar bulk pressure for the reduced pore widths of (a) 2.0, (b) 3.0, (c) 4.5 and (d) 7.0. Part (e) shows the effects of wetting parameter on the normal pressure in an expanded scale.

The first and largest jump in the density of adsorbate corresponds to the phase transition from a gas-like phase to a condensed phase and is the starting point of pore filling. This also corresponds to where the pressure starts to be enhanced, as expected. It is seen in Figure 6.5 that for larger pores, a larger α_w is necessary for this transition (pore filling) to occur.

Moreover, the wetting parameter α_w plays a more interesting role for the intermediate pore width, e.g., $H^* = 4.5$. Theoretically, a pore of $H^* = 4.5$ could accommodate 3.5 complete layers of argon, and actually 4 layers are there. However, due to the smaller pore space, these 4 layers of argon in the pore of $H^* = 4$ are not as dense as in the pore of $H^* = 5$ where 4 complete layers of argon can be accommodated. As α_w increases, the attraction from the wall is strengthened until a point where the interaction is strong enough to compress the confined adsorbate and overcome the geometrical limitation. This point corresponds to the obvious jumps in both tangential and normal pressures at $\alpha_w \sim 2.2$ (see Figure 6.5c and e).

We show the effect of α_w on the normal pressure in Figure 6.5e. This effect strongly depends on the pore width, because the normal pressure and its changing range are very sensitive to the pore width (as discussed later in Sec. 8.3). In general, for the pore with an integer reduced pore width, the magnitude of the normal pressure changes smoothly with increasing α_w . For the intermediate pore width ($H^* = 4.5$), there is an obvious jump at $\alpha_w \sim 2.2$, corresponding to the completion of the confined argon layers due to the sufficiently strong attraction from the pore walls.

We also study the effects of α_w on the pressure of the adsorbate along the adsorption isotherm (see Figure 6.6). The in-pore density and the pressures of argon for the systems with three typical values of α_w : 1.2554 (as argon-silica system), 2.137 (as argon-carbon system), and 2.434 (as argon-mica system) are shown in Figure 6.6a, b and c, respectively (note: for these systems, α_w is calculated using the LJ parameters for argon, and the parameters listed in

Table D.1 of Appendix D for the three different walls). The in-pore density curves show that the pore starts to fill (the first and smooth step, corresponding to the filling of the argon layer in contact with the wall) at lower bulk pressure for higher α_w , and the capillary condensation (the second and sharp step, corresponding to the filling of the whole pore) also occurs at lower pressure for higher α_w , as expected. For the relatively weakly attractive wall ($\alpha_w = 1.2554$), the tangential pressure of the contact layer increases slowly during the stage of “contact layer filling” (from ~ 0 to 1,500 bar), followed by a big jump at capillary condensation. The maximum peak value of the tangential pressure (occurs for a completely filled pore) is $\sim 6,500$ bar for $\alpha_w = 1.2554$. For the strongly attractive walls ($\alpha_w = 2.137$ and 2.434), the tangential pressure increases very rapidly (from ~ 0 to $> 12,000$ bar) during this stage of “contact layer filling”, and is also followed by a jump, but not as significant as for small α_w , at capillary condensation. The maximum peak values of the tangential pressure (occur for completely filled pores) are $\sim 15,000$ bar and $\sim 22,000$ bar for $\alpha_w = 2.137$ and 2.434, respectively. The difference in the rate of the tangential pressure increase during the “contact layer filling” stage for different wetting parameters arises from the different strengths of attraction from the walls acting on the contact layer: for small α_w (but still attractive in nature, e.g., $\alpha_w \sim 1$), the attraction from the wall acting on the contact layer of adsorbate is weak, and as the bulk pressure increases, this weak attraction provides a very limited ability to compress the contact layer of adsorbate; thus the in-plane separation distance between the adsorbate molecules is not significantly decreased, which leads to a slow increase in the tangential pressure at the contact layer. The normal pressure is generally rather insensitive to the bulk pressure for all values of α_w , as discussed in Sec. 5.4.2 and this

section, except for a jump at capillary condensation, where a significant compression of argon in the normal direction occurs due to the filling of the central layers of adsorbate.

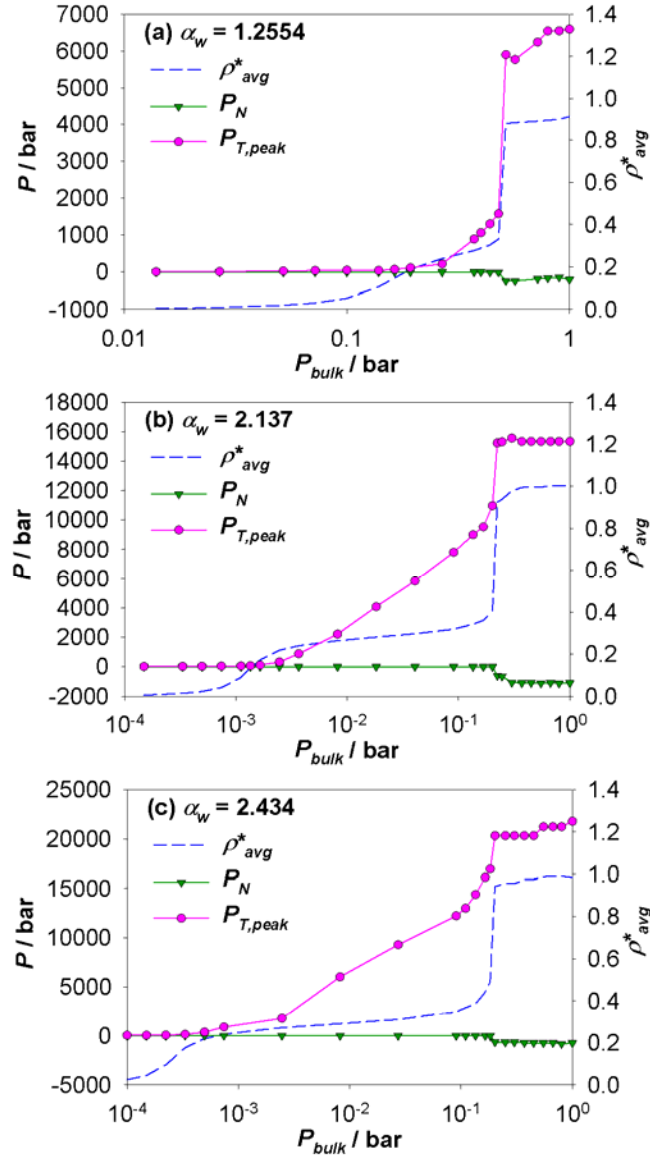


Figure 6.6 The in-pore density, the normal pressure and the peak value of the tangential pressure of argon in a carbon slit pore of $H^* = 7.0$ at 87.3 K as functions of bulk pressure for different wetting parameters of (a) 1.2554 (as argon-silica system), (b) 2.137 (as argon-carbon system), and (c) 2.434 (as argon-mica system).

6.6 An Example of a Non-Wetting Fluid: Mercury Intrusion in a Carbon Slit Pore

6.6.1 Introduction

In Chapter 5, we found that the pressure of argon confined in a carbon slit pore is significantly enhanced due to the attractive nature of the pore. In the previous sections of this chapter, we have shown that this enhancement is actually dependent on the wettability of the adsorbate-wall system, or quantitatively, on the wetting parameter α_w . For an argon-carbon system, our calculations show that it is a wetting system, with a strong attractive wall ($\alpha_w = 2.14$). It is natural to consider investigating the in-pore structure and pressure for a non-wetting system (e.g., mercury as the fluid and carbon as the substrate). In this section, we will show that for the Hg-C system, the in-pore pressure is weakly enhanced or even reduced, depending on the pore width.

6.6.2 Modeling and Simulation Details

The slit pore is composed of two opposing walls, each of which consists of three layers of graphene that lay parallel to the xy -plane. The pore is atomistic, of finite length, and the carbon atoms are fixed in space; for details of the model refer to Sec. 6.5.1 (see also Figure 6.7). The fluid (adsorbate) is LJ Hg, where $\sigma_{aa} = 0.3234$ nm and $\varepsilon_{aa} / k_B = 506$ K (obtained by reproducing the binding energy and equilibrium distance of the ab initio mercury potential [111]), and is truncated at $5\sigma_{aa}$. For the adsorbate-wall interaction, we also use the LJ potential between Hg and C atoms (aC) (where $\sigma_{aC} = 0.3321$ nm and $\varepsilon_{aC} / k_B = 14.7$ K, obtained by fitting the experimental contact angle of 152.5 deg for a Hg drop on carbon [111]). By using these parameters, the wetting parameter of the Hg-C system is calculated as

$\alpha_w = 0.1221$, suggesting a highly non-wetting system. The adsorption (intrusion) of Hg in carbon slit pores with various pore widths is performed by using GCMC method at 300 K (room temperature).

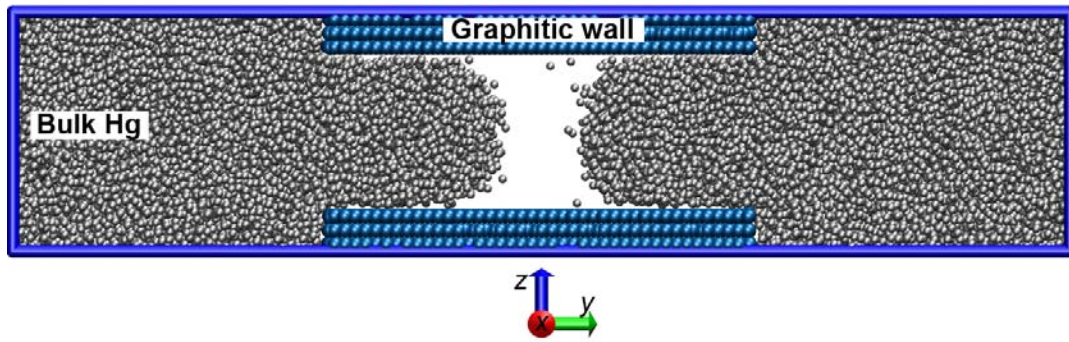


Figure 6.7 The snapshot of Hg intrusion in model carbon slit pore.

6.6.3 Results and Discussion

The bulk pressure is increased from 0 until the mercury intrudes into the pore. As observed in experiments [114] and molecular simulations [114-117], initially, at low pressure, there is a Hg vapor phase in the pore, and liquid Hg in the bulk phase. As the pressure increases to about 4000 bar, liquid Hg is forced into the pore, and eventually the pore is completely filled with Hg. This phenomenon is the opposite of the situation for the wetting adsorbate-wall system (e.g., Ar-C), where at low pressure the adsorbate condensed in the pore (in liquid or even crystal state) and is in equilibrium with the vapor phase in the bulk. The adsorbate in the bulk condenses into a liquid state as the pressure increases to about the saturation pressure of the adsorbate (sometimes the pressure is higher because of the supercooling phenomenon). In

this section, we show results for mercury confined in the carbon slit pores at 300 K and a bulk pressure of 4,080 bar (which seems to be the threshold pressure to achieve the Hg intrusion into the carbon pore).

The tangential and normal pressures of Hg confined in carbon slit pores with various pore widths are shown in Figure 6.8. In all the pores, the normal and average tangential pressures (spatial average without weighting factor, calculated by Eqn. (3.84)) are of the same order of the bulk pressure, i.e., the pressure is not significantly enhanced, and is even reduced in some cases. This is because the adsorbate-wall attraction is much weaker than the adsorbate-adsorbate attraction, and thus a bulk pressure that is high enough to condense the pure adsorbate phase (or even higher pressure depending on the nature of the wall) is required to condense the adsorbate inside the pore. Moreover, for some pore widths (e.g., $H^* = 4.0$ and 6.5, see Figure 6.8b and c), the tangential pressure at the central layer(s) of adsorbate is equal to or even higher than that for the contact layer of adsorbate, which is quite different from the wetting system, where the tangential pressure of the contact layer is significantly larger than that for the central layers (e.g., for argon in carbon, the tangential pressure of the contact layer could be $\sim 20,000$ bar compared with $\sim 5,000$ bar for the central layer, see Figure 5.5). This can be explained as follows: the non-wetting adsorbate does not “like” the pore wall, and they tend to stay together with the adsorbate molecules rather than go to the interface to be attracted by the wall atoms. As a result, the adsorbate molecules are more close-packed for the central layer, which is far away from the wall, than those in the contact layer. For small pores (e.g. $H^* = 3.0$, see Figure 6.8a), the average tangential pressure is lower than the

bulk pressure (e.g., 1,010 bar compared with 4,080 bar), suggesting a pressure reduction due to the weak attraction contribution from the pore wall, which is in contrast with the pressure enhancement for the wetting adsorbate-substrate system (e.g., Ar-C). For large pores (e.g., $H^* = 4.0$ and 6.5, see Figure 6.8b and c), the average tangential pressure approaches to the bulk pressure (3,140 bar and 3,700 bar compared with 4,080 bar), because in larger pores, the pressure reduction effect of walls on the confined adsorbate is much weaker.

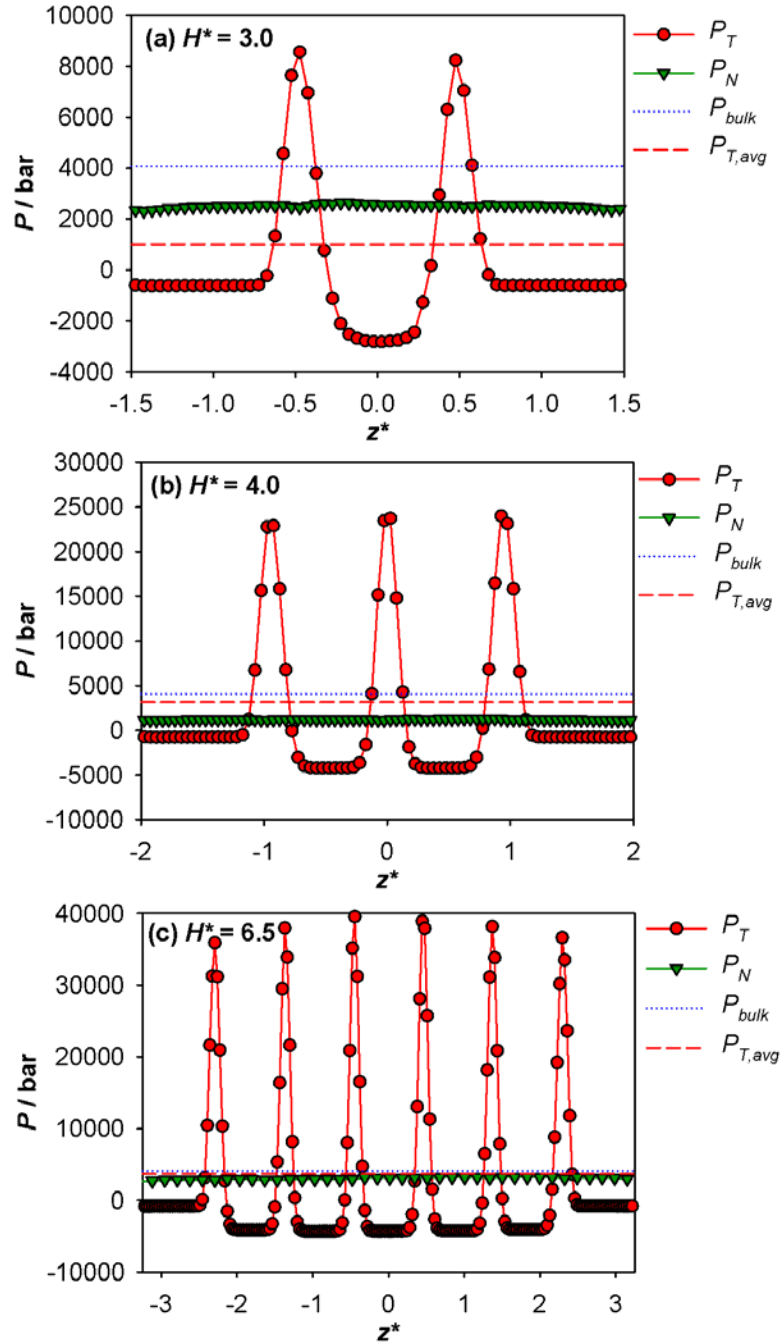


Figure 6.8 The pressure tensor profiles of Hg confined in the carbon slit pores of (a) $H^* = 3.0$, (b) $H^* = 4.0$, and (c) $H^* = 6.5$ at 300 K and 4,080 bar bulk pressure. The average tangential pressures (dashed lines) are calculated for the accessible pore width, and the values are (a) 1,010 bar, (b) 3,140 bar, and (c) 3,700 bar, respectively. The normal pressures are (a) 2,503 bar, (b) 1,195 bar, and (c) 3,039 bar, respectively.

We also study the effect of pore width on the normal and tangential pressures of Hg confined in carbon pores (shown in Figure 6.9). Both the normal pressure and the peak value of the tangential pressure are oscillating with increasing pore width. The amplitude of the oscillation in normal pressure does not change significantly. The oscillation is almost around the bulk pressure of 4,080 bar, and as the pore width increases, the normal pressure approaches the bulk pressure ($H^* > 7$). On the contrary, the oscillations in the peak value of the tangential pressure grow larger as pore width increases for the range of the studied H^* . This is because as the pore becomes larger, the effect of the pore wall becomes weaker, and the adsorbate in the pore is more likely to arrange in a more close-packed way, since the wall provides a weaker attraction than the adsorbate molecules do. The wall serves as a geometric constraint to force the layering of the adsorbate, and that is the reason why the local tangential pressure (peak value) is much higher than the bulk pressure: the in-plane separation distance between the Hg molecules in the same layer is smaller than that for the bulk liquid Hg. Another interesting finding for the oscillation in the peak value of the tangential pressure is that for a cycle (increment of 1.0 in H^*) there is a minimum between two local maximum values for the peak tangential pressure. This minimum occurs for the following reason: the increase in the pore width allows an additional layer of adsorbate to be accommodated, but due to lack of enough space in the z -dimension, all the layers are not completely filled with Hg molecules (compared with an ideally close-packed fcc structure), and thus the in-plane separation distance between the argon molecules is enlarged, resulting in a much lower tangential pressure.

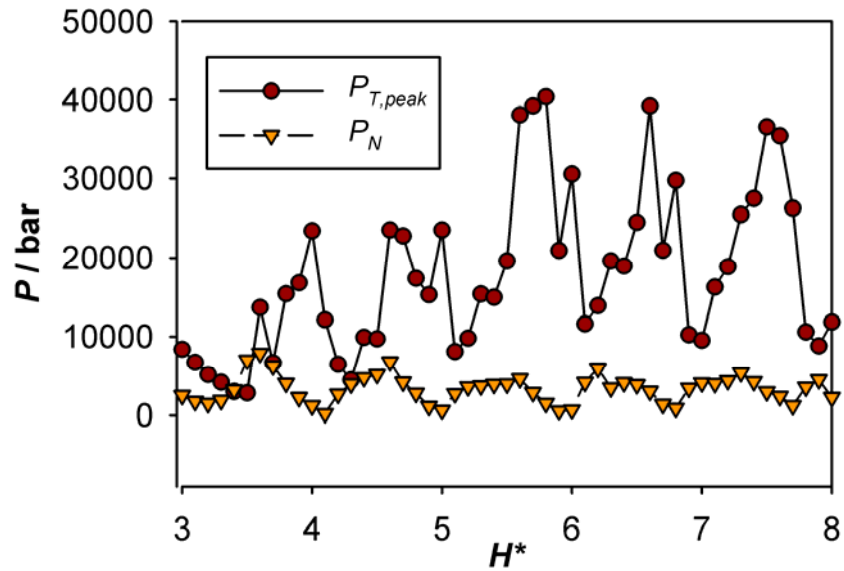


Figure 6.9 The normal pressure and peak value of tangential pressure of Hg confined in carbon slit pore as functions of pore width, at 300 K and 4,080 bar bulk pressure.

6.7 Conclusions

In conclusion, the wettability of an adsorbate-substrate system can be quantitatively represented by a microscopic wetting parameter α_w (which is closely related to the contact angle, a macroscopic measure of the wettability). The wetting parameter has large effects on the capillary condensation of an adsorbate in porous materials and on the in-pore structure, and thus on the in-pore pressure of the adsorbate. With large α_w (a wetting system), the capillary condensation occurs at low bulk pressure thanks to the strong attraction provided by the wall atoms, while for a system with small α_w , to condense the adsorbate, a pressure about or even higher than the bulk saturation pressure of the adsorbate is needed, to overcome or compensate for the weak attraction from the wall. The wetting parameter also plays a key

role on the in-pore structure of the adsorbate and thus on the in-pore pressure. For a system with large α_w , the adsorbate molecules tend to arrange themselves in a very close-packed array on the surface of the wall (i.e., they form a close-packed contact layer) due the strong attraction from the wall, and the tangential pressure peaks at these contact layers and is locally very large ($\sim 10^4$ bar, compared with the bulk pressure of ~ 1 bar). For a system with small α_w , the adsorbate molecules “dislike” the wall atoms, and a very high bulk pressure ($\sim 10^3$ bar) is required to force the adsorbate molecules to intrude into the pore. The tangential pressure of the contact layer is no longer the highest peak, but for most cases, it is comparable to, or even lower than, the tangential pressure in the central layers. The in-pore pressure of adsorbate for a non-wetting system is enhanced insignificantly or, in some cases, reduced, due to the disappearance of the reason for the pressure enhancement phenomenon (detailed discussion in Chapter 5). These findings confirm that the pressure enhancement arises from the strong attraction from the pore wall relative to the adsorbate-adsorbate attraction, and thus pressure enhancement is not always the case for adsorption in nanopores.

CHAPTER 7

Pressure of Fluids Confined in Spherical and Cylindrical Pores

7.1 Introduction

In previous chapters, we have shown and discussed the results for the pressure tensor components of adsorbate in slit pores. The slit pore model is simple but effective to catch some important features, and is a reasonable approximation to model the pores for many porous carbon materials (e.g., activated carbon fibers). In this chapter, we study the pressure tensor of adsorbate (LJ argon) confined in carbon pores of other simple geometries, namely ideal spherical and cylindrical pores, because many materials also contain spherical (e.g., hierarchical carbons and silica) and cylindrical (e.g., carbon nanotubes and mesoporous silicas) pores. We show that because of the curvature, the attractive force from the carbon wall is strengthened and the in-pore tangential pressure is more enhanced.

7.2 Modeling and Simulation Details

7.2.1 Cylindrical Carbon Pore Model

As shown in Figure 7.1a, the cylindrical pore model is based on a multi-walled carbon nanotube (MWCNT) which consists of three concentric carbon nanotubes. These three carbon nanotubes are constructed as follows: for the first (innermost) tube, the chirality parameters, (m,n) , of the carbon nanotube [118] and the number of unit cells, N_{uc} , are set to determine the diameter (D) and the length of the cylinder ($L_{z,wall}$), respectively. The diameter

of the cylindrical pore cannot be continuously or arbitrarily chosen, because of the nature of the carbon nanotube, i.e., the diameter of the cylindrical pore is a discrete value as listed in Table 7.1. For the second (central) and third (outermost) tubes, the values of (m,n) are chosen so that the interlayer spacing is very close to 0.335 nm, as in the graphite and the slit pore model. The numbers of unit cells are the same for all these tubes so that they are equal in length. In this study, we choose the number of unit cells to be 50, corresponding to $L_{z,\text{wall}} = 6.15$ nm (comparable with 6.8 nm as for the slit pore). To satisfy the hydrostatic equilibrium, similar to the slit pore case, the cylindrical pore is finite in length, and the length of the simulation box ($L_{z,\text{box}}$) is three times the pore length, so that there are two quasi-bulk phases, one in contact with each end of the cylindrical pore.

Table 7.1 The diameter of the carbon nanotube, D , as a function of the parameter (m,n) , and the length of the tube $L_{z,\text{wall}}$ as a function of the number of unit cells (N_{uc}).

(m,n)	D / nm	N_{uc}	$L_{z,\text{wall}} / \text{nm}$
(8,8)	1.085	20	2.4595
(10,10)	1.356	30	3.6893
(15,15)	2.034	40	4.9190
(20,20)	2.712	50	6.1488
(25,25)	3.390	60	7.3785
If $m = n$, $D = 0.1356 \text{ nm} \times m$		$L_{z,\text{wall}} = 0.12298 \text{ nm} \times N_{uc}$	

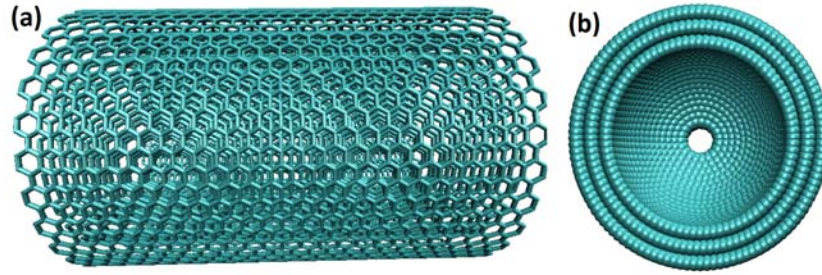


Figure 7.1 Snapshots of model carbon pores: (a) cylindrical carbon pore constructed from a multi-walled carbon nanotube, and (b) spherical carbon pores with a small opening. Carbon atoms are shown at reduced scale for clarity.

7.2.2 Spherical Carbon Pore Model

As shown in Figure 7.1b, the spherical pore is composed of three concentric spherical shells of carbon atoms. For a spherical pore with an inner diameter of D , the first (innermost) shell is constructed by surrounding a virtual spherical shell of diameter D with a shell of carbon atoms. The number of atoms in this shell is such that the areal number density of the carbon atoms is the same as that of a graphene layer (38.18 nm^{-2}). These carbon atoms are distributed evenly on the virtual spherical shell with their centers of mass located on the shell. The second (central) and third (outermost) shells are constructed similarly, where the diameter of the virtual spheres are taken to be $(D + 0.67 \text{ nm})$ and $(D + 1.34 \text{ nm})$, respectively. The values added to the diameter are such that the distances between the shells are the same as the interlayer spacing of carbon atoms in graphite (0.335 nm).

To satisfy hydrostatic equilibrium, a “channel” should be made to connect the inside of the pore to the outside. Hence, a cylinder whose diameter is 2.4 times the diameter of the

adsorbate molecule (a channel diameter ~ 0.82 nm for argon) is carved in the pore wall (see Figure 7.1b), so that the adsorbate molecule can go through the channel freely to reach hydrostatic equilibrium. The simulation box is a sphere with a diameter of $(D + 1.34 \text{ nm} + 3 \times \sigma_{aa})$ so that there could be at most three layers of adsorbate molecules outside the pore, which forms a quasi-bulk phase.

7.2.3 Simulation Details

The argon-argon (adsorbate-adsorbate, aa) and argon-carbon (adsorbate-carbon, aC) interactions are modeled with LJ potentials, with the parameters $\varepsilon_{aa} / k_B = 119.8$ K and $\sigma_{aa} = 0.3405$ nm [95] and $\sigma_{CC} = 0.34$ nm and $\varepsilon_{CC} / k_B = 28$ K [97]; the Lorentz-Berthelot combining rules are used for unlike pair parameters. The carbon atoms are fixed in space, because unlike the slit pore, the pore deformation will involve not only weak (van der Waals) interactions between graphene sheets, but also strong interactions due to covalent bonds between neighboring carbon atoms (the deformation of the pore will also stretch or compress the chemical bond), and thus the displacement of the carbon atoms is expected to be small. Therefore, in this study, there is no carbon-carbon interaction.

The GCMC simulations are carried out to perform argon adsorption in cylindrical and spherical carbon pores at 87.3 K and 1 bar bulk pressure for various pore diameters; the reduced pore diameter $D^* = D / \sigma_{aa}$ varies from 2 to 10. The simulations are run for 10^8 Monte Carlo moves to attain equilibrium, and a further 10^8 moves for the determination of the pressure. The pressure tensor components are sampled every 5000 configurations, and are

calculated by both the mechanical route and the thermodynamic route. For the cylindrical pore, the pressure is sampled only for the central part of the tube, away from the ends of the pore (a pore length of 2.0 nm, corresponding to ~ 6 diameters of an argon molecule), which is also called the averaging region similar to the definition for the slit pore case (see Sec. 5.2 and Figure 5.2b), to avoid edge effects. All cylindrical and spherical pores are divided into many small bins (with a thickness of ~ 0.02 nm) in the ρ -direction to calculate the local density and local pressure tensor components.

7.3 Results and Discussion

7.3.1 Pressures in Spherical Pores

We first show the density and pressure profiles of argon confined in spherical pores with various pore diameters of 2.4 nm, 3.2 nm, 4.0 nm and 4.8 nm (or reduced radii $R^* = R / \sigma_{aa} = 3.52, 4.70, 5.87$ and 7.05) at 87.3 K and 1 bar bulk pressure in Figure 7.2. The pressure tensor is calculated by the mechanical route (using Eqns. (3.29) and (3.34)). The results for the small vicinity of the pore center in some pores are omitted because of two reasons: first, the bin volume for this region is very small, which causes very poor statistics; second, the bin volume approaches zero, but the number of molecules (a molecule is regarded as a mass point without volume) is of finite value, which causes a mathematical limitation and an unphysical result. As shown in Figure 7.2a, b, c and d, the peaks of the tangential pressure profile follow those of the density profile in all pores (except for small pores, e.g., $D = 2.4$ nm, there are small deviations between the peaks of the two profiles), and the maximum tangential pressure occurs at the argon layer in contact with the pore wall (contact layer),

which is also found in the slit pore (see Sec. 5.4.2 and Figure 5.4). The values of the maximum tangential pressures, $P_{T,peak}$, in the pores of $D = 2.4$ nm, 3.2 nm, 4.0 nm and 4.8 nm are 26,500 bar, 26,100 bar, 26,200, and 21,200 bar, respectively. The tangential pressure at the contact layer in the spherical pore generally decreases with increasing pore diameter but with exceptions (e.g., $P_{T,peak}$ for $D = 3.2$ nm is slightly smaller than that for $D = 4.0$ nm). The general decreasing trend for the tangential pressure is because of the weaker interaction from the wall as the pore diameter increases. Moreover, the value of the diameter of a spherical pore geometrically influences the structure of the contact layer of argon (matching effect). This can be explained as follows: suppose a pore is of diameter D_c makes the contact layer of argon arrange in a “normal” fcc pattern with a comfortable separation distance between the argon molecules in that layer (without additional attraction or repulsion between them); a pore with a diameter slightly larger than D_c , but not large enough to accommodate additional argon molecules in the contact layer, arranges the argon molecules in the contact layer with a larger separation distance between them, which causes a smaller tangential pressure because of this less repulsive structure; on the contrary, a pore with a diameter slightly smaller than D_c , but not small enough to expel one or more argon molecules in the contact layer, further compresses the contact layer, which causes a larger tangential pressure because of the more repulsive structure. The scale of the normal pressure, P_N , is significantly smaller than that of the tangential pressure, and so the normal pressure is also shown separately with an expanded scale for all these pore diameters (Figure 7.2e). Unlike that of a slit pore (where $P_N =$ constant across the pore), the normal pressure in a spherical pore is no longer a constant, and is actually related to the tangential pressure (Eqn. (3.6)). We have checked that the normal

pressure and the tangential pressure calculated from the mechanical route (IK definition) satisfy Eqn. (3.6) derived from the condition of hydrostatic equilibrium for a spherical surface. The normal pressure in a spherical pore also exhibits positive peaks following the density profile, and the maximum peak occurs at the contact layer, except for small pores (e.g., $D = 2.4$ nm), with an order of magnitude of $\sim 1,000$ bar, suggesting that the argon molecules in a spherical pore experience a strong compression in the radial direction.

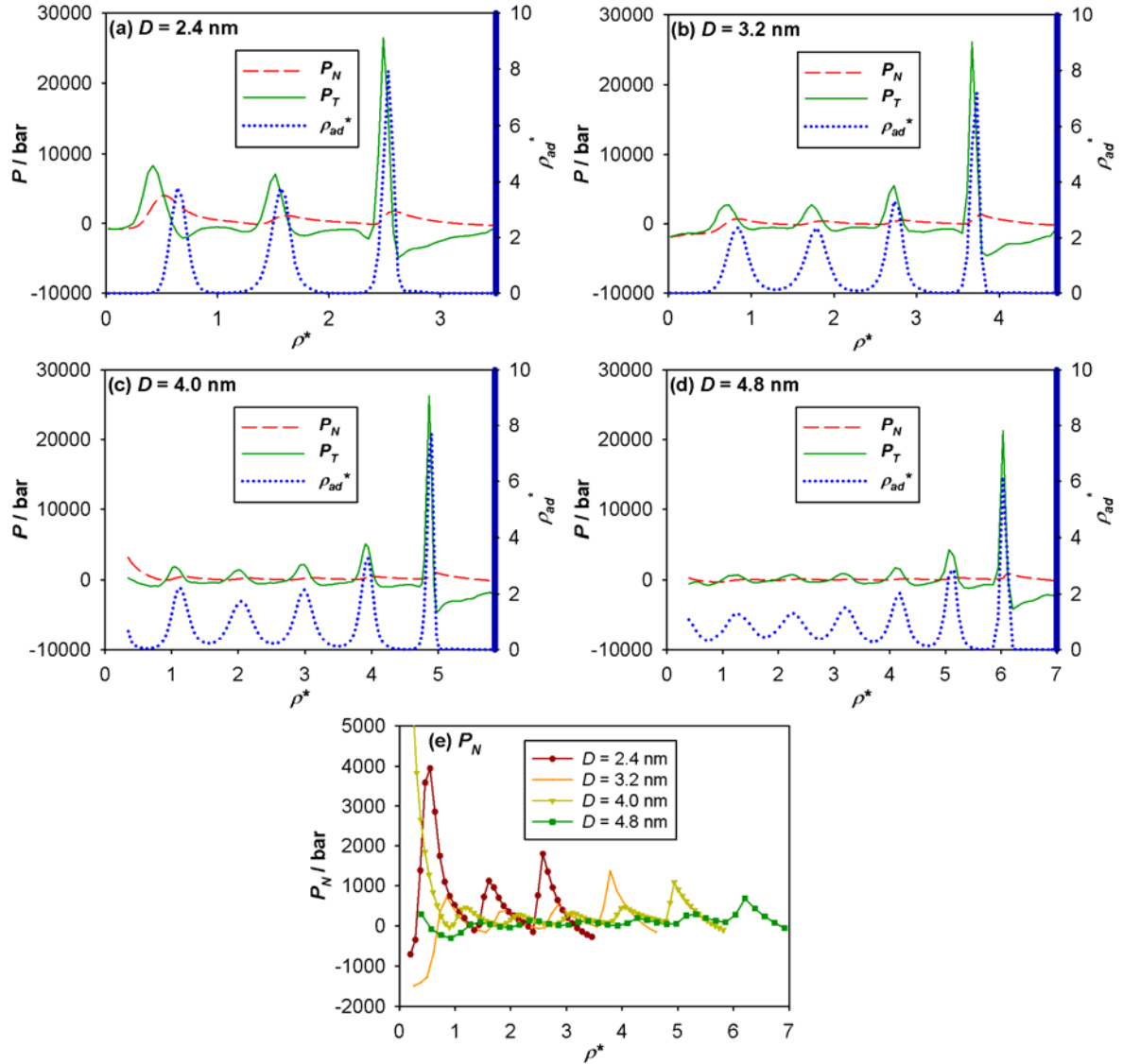


Figure 7.2 The density and pressure profiles (calculated by the mechanical route using the IK definition) of argon adsorbed in spherical carbon pores with various pore diameters of (a) 2.4 nm, (b) 3.2 nm, (c) 4.0 nm, and (d) 4.8 nm. The thick solid lines on the right vertical axes represent the positions of the pore walls. (e) The normal pressure is shown for the four pore diameters with an expanded vertical scale.

We also compare the pressure tensor components in a spherical pore ($D^* = 8.0$) calculated by the mechanical route (using the IK definition) with those calculated from the thermodynamic

route or the volume perturbation method (using an IK-like definition of energy assignment) for the spherical pore. As shown in Figure 7.3, the normal and the tangential pressure components calculated by the two routes agree with quite well. The small deviations may arise from the capillary wave effect for curved surfaces [73] (as we calculated, the leading capillary wave term of the pressure tensor in spherical pore is about $\sim 1\%$ of the total pressure), or from the numerical instability for such an inhomogeneous system (where there are sharp peaks in the density and pressure profiles and the discrete values of the derivatives in the equations for these peaks would be inaccurate), or from the statistical errors.

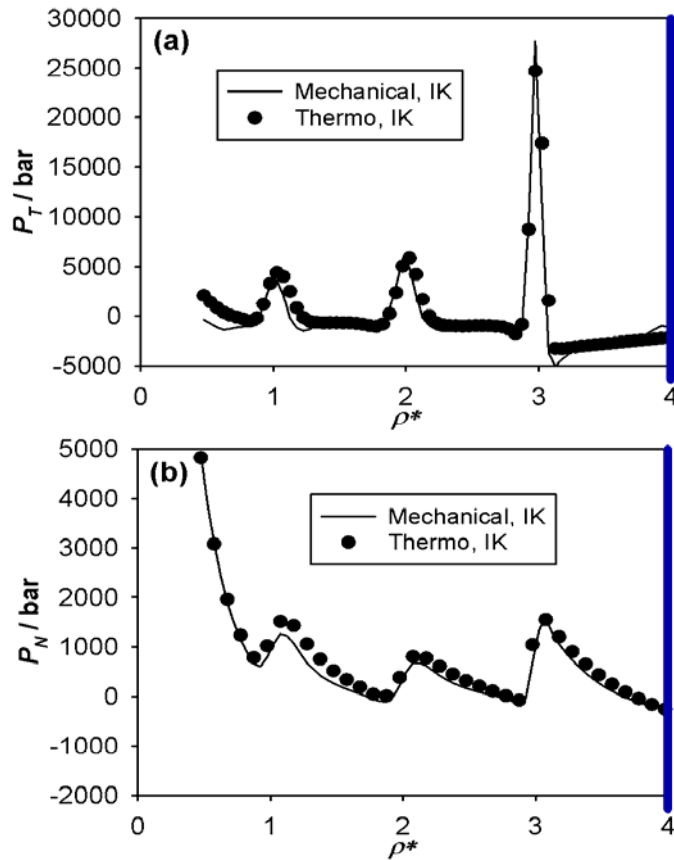


Figure 7.3 The (a) tangential and (b) normal pressure profiles (calculated by the mechanical and thermodynamic routes using the IK definition) of argon adsorbed in a spherical carbon pore ($D^* = 8.0$), at 87.3 K and 1 bar bulk pressure. The thick solid lines on the right vertical axes represent the positions of the pore walls.

7.3.2 Comparison of Pressures in Slit, Cylindrical and Spherical Pores

We compare the density and pressure profiles of argon confined in cylindrical and spherical pores ($D^* = 8.0$) with those in a slit pore ($H^* = 8.0$) of comparable pore size, as shown in Figure 7.4. The pressure tensor is calculated using IK definitions. As discussed above, the normal pressure in the slit pore is a constant (about -550 bar), while it oscillates following the density profile in the cylindrical and spherical pores with a peak value of 240 bar and 800

bar, respectively, for the contact layer. The peak value of the tangential pressure (for the cylindrical pore, we use $P_{T\phi}$) at the contact layer in the cylindrical and spherical pores is appreciably larger than that in the slit pore (18,800 bar for the cylindrical pore and 27,700 bar for the spherical pore compared with 18,100 bar for the slit pore), which agrees with the higher adsorbate density of the contact layer in the cylindrical and spherical pores than for the slit pore (7.6 for the cylindrical pore and 7.7 for the spherical pore compared with 7.2 for the slit pore, in reduced density). The higher density and tangential pressure in cylindrical and spherical pores arise from a more compressed adsorbate structure in the contact layer, which is a result of the wall curvature and thus stronger attraction from the pore wall. For a cylindrical pore of $D^* = 8.0$, the other tangential pressure component, P_{Tz} , shows a qualitatively similar behavior to $P_{T\phi}$ but with lower peaks for argon layers, for example, at the contact layer $P_{Tz} \sim 14,000$ bar. This is smaller than the peak value of $P_{T\phi}$ because the wall is not curved in the z -direction; this further illustrates the fact that the wall curvature enhances the compression of the adsorbate phase, and thus the tangential pressure $P_{T\phi}$. Since the curvature of a cylindrical pore wall is only in one-dimension, this enhancement effect is weaker for a cylindrical pore than that for a spherical pore, whose curvature is in two dimensions. The radial distribution functions, $g(r)$, for the contact layers confined in the slit, cylindrical and spherical pores (with the same reduced pore size of 8.0) were calculated, showing that the contact layer in the spherical pore is the most compressed, followed by the cylindrical pore, and then the slit pore (see Figure 7.5).

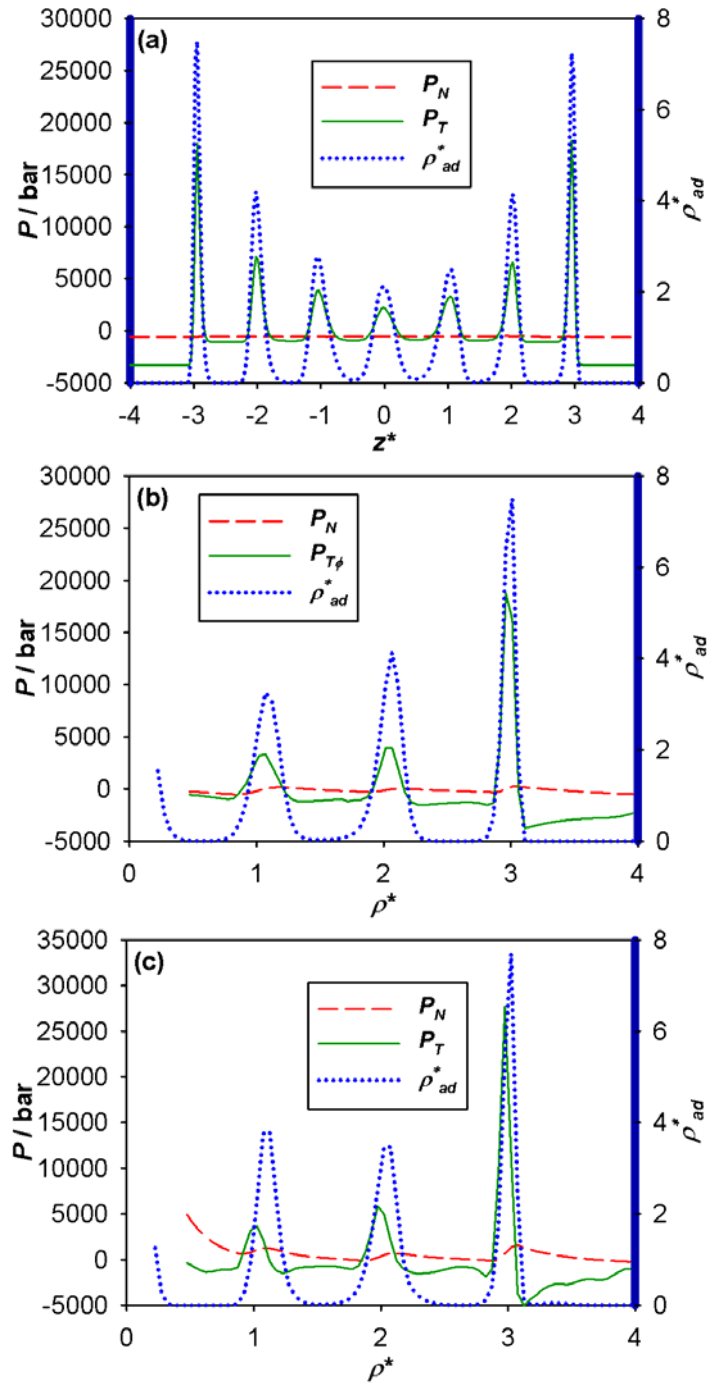


Figure 7.4 The density and pressure profiles (calculated by using the IK definition) of argon adsorbed in (a) slit ($H^* = 8.0$), (b) cylindrical ($D^* = 8.0$) and (c) spherical ($D^* = 8.0$) carbon pores, at 87.3 K and 1 bar bulk pressure. The thick solid lines on the vertical axes represent the positions of the pore walls.

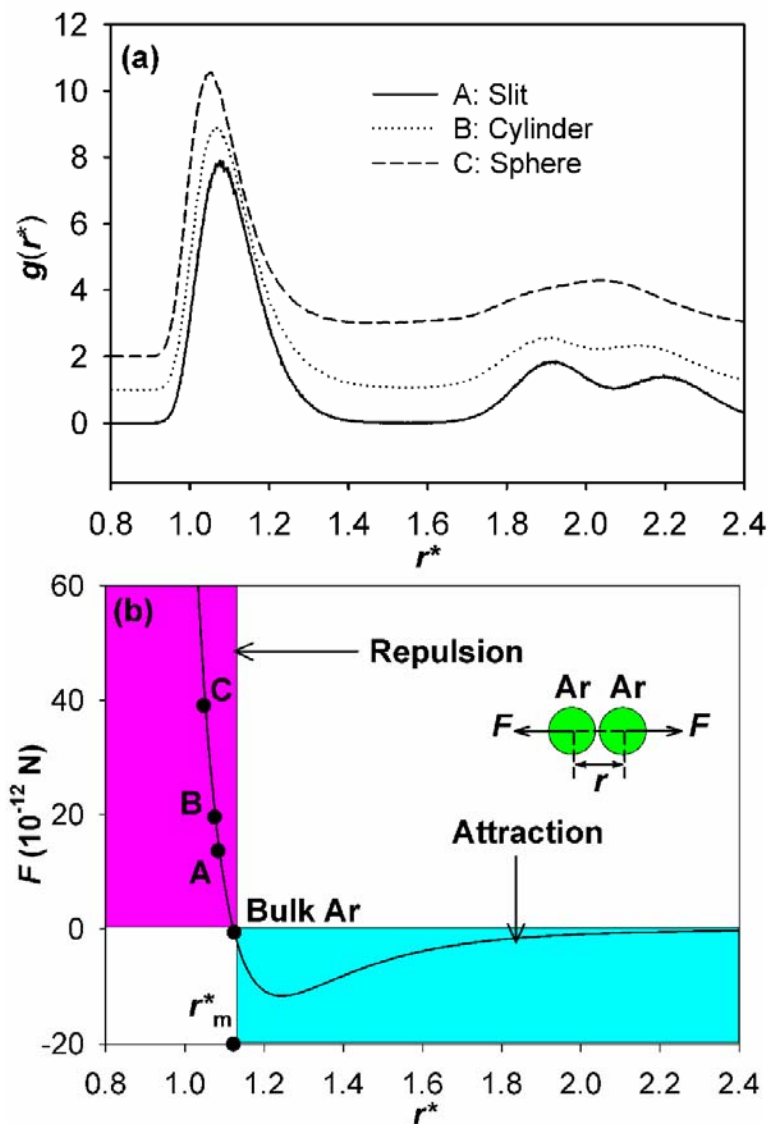


Figure 7.5 (a) Radial distribution function for the contact layer of argon at 87.3 K and 1 bar bulk pressure confined in the slit (A, solid line, $H^* = 8.0$), cylindrical (B, dotted line, $D^* = 8.0$), and spherical (C, dashed line, $D^* = 8.0$) carbon pores. (b) The intermolecular pair force between two argon atoms, F , with the most probable nearest neighbor separation distances shown for the three cases illustrated in (a). The most probable separation distance for bulk argon at 87 K and 1 bar bulk pressure is also shown.

7.3.3 Effects of Bulk Pressure for Various Pore geometries

The effects of bulk pressure in the cylindrical and spherical pore were also investigated (shown in Figure 7.6). We show the adsorption isotherms of LJ argon in slit, cylindrical and spherical carbon pores of the same reduced pore size of 8.0 at 87.3 K (Figure 7.6a). Because of the wall curvature and the consequent strong attraction, argon starts to be adsorbed in the spherical pore at a bulk pressure much lower than in the cylindrical and slit pores. The second-stage pore-filling pressure (indicated by the second jump of the isotherm) for the spherical pore is also much lower than that for the slit pore (~ 0.01 bar compared with ~ 0.25 bar). The overall in-pore density of argon when the pore is fully filled is largest for the spherical pore, suggesting that the attraction from the wall of the spherical pore compresses the adsorbate phase more than for the cylindrical and slit pores. The effect of bulk pressure on the in-pore tangential and normal pressures for argon adsorption in the spherical carbon pore ($D^* = 8.0$) at 87.3 K is shown in Figure 7.6b. At very low bulk pressure ($< 2 \times 10^{-5}$ bar), the tangential pressure is negative with a value as large as several thousand bars, suggesting a highly attractive adsorbate-wall interaction. As the bulk pressure increases further the tangential pressure becomes positive, and increases rapidly with bulk pressure: as the bulk pressure is increased from 2×10^{-5} bar to 1 bar, the in-pore tangential pressure increases from $-3,000$ bar to $+30,000$ bar. This indicates that it should be possible to explore a wide range of in-pore pressures in experiments by tuning the bulk pressure over a small range in a spherical pore (similar to that in the slit pore, but with a stronger effect). The average normal pressure is negative and increases in magnitude with increasing bulk pressure until the second-stage pore-filling (also named the capillary condensation for a slit pore), where a maximum

negative normal pressure occurs. This suggests that the argon layers adsorbed in the pore attract each other, and they attract the carbon layer of the wall as well, due to a low density of adsorbate in the normal (radial) direction. After the capillary condensation, the normal pressure increases from negative to positive with increasing bulk pressure and thus the increasing adsorbate density due to the pore filling. At a bulk pressure of ~ 0.4 bar, the normal pressure starts to be positive, indicating that the argon layers repel each other and that they tend to expand the pore. The normal pressures acting on the wall of cylindrical and spherical shapes are discussed in Sec. 8.4 (see also Figure 8.5).

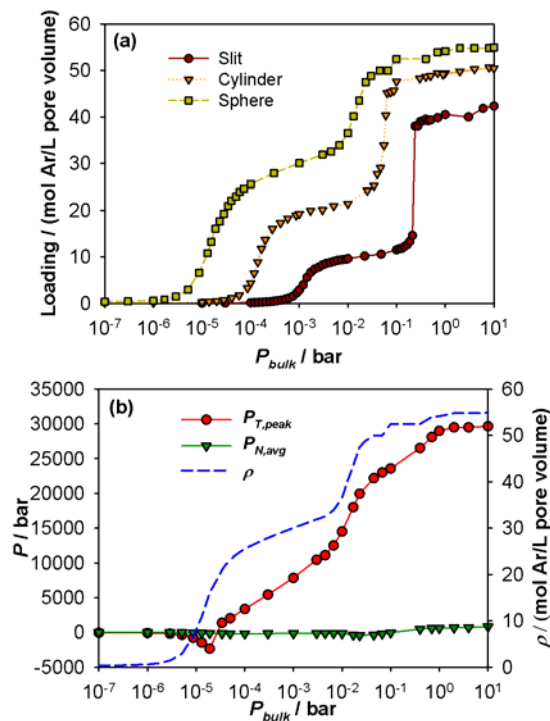


Figure 7.6 (a) The adsorption isotherms of argon in slit ($H^* = 8.0$), cylindrical ($D^* = 8.0$) and spherical ($D^* = 8.0$) carbon pores at 87.3 K. (b) The peak value of the tangential pressure and the average normal pressure as functions of bulk pressure for argon confined in a spherical carbon pore ($D^* = 8.0$) at 87.3 K.

7.4 Conclusions

The pressure tensor components of LJ argon adsorbed in carbon pores of different simple geometries: i.e., ideal slit, spherical and cylindrical pores are studied and compared. We find that the pore geometry has large effects on the adsorption isotherm, the structure of the confined phase and the in-pore pressure of the adsorbate. Depending on the wall curvature, the attraction from the carbon wall acting on the contact layer of adsorbate is strengthened, and thus the confined phase is more compressed, which results in a more enhanced tangential pressure, especially at the contact layer. For the same reason, pore fillings occur at lower pressure in a spherical pore than in a slit or cylindrical pore of the same size. Moreover, our new framework to calculate pressure tensor components based on the thermodynamic route (or volume perturbation method) works well for the pressure in a spherical pore.

CHAPTER 8

Normal Pressure Acting on the Wall and Pore Deformation

8.1 Introduction

The normal pressure of adsorbate acting on the pore wall is of great interest because this normal component can be measured experimentally, directly or indirectly (as discussed in Chapter 2), and this component is directly responsible for the deformation of the porous materials. In this chapter, the results of the normal pressure acting on the wall are presented for fluids (e.g. argon, water and carbon tetrachloride) adsorbed in carbon materials having pores of different geometries (slit, cylindrical, and spherical).

8.2 Argon Adsorbed in Carbon Slit Pore and Pore Deformation

8.2.1 Modeling Details

To study the normal pressure of argon acting on the wall of the carbon slit pore and the pore deformation in response to the adsorption, a flexible pore model is used. A rectangular simulation cell comprised of a slit-shaped carbon pore, symmetric about $z = 0$ is shown in Figure 8.1. Opposing walls of the slit-pore each consists of three layers of graphene that lay parallel to the xy -plane. During the simulations, the positions of the outermost graphene layers are kept fixed in space, but the two innermost graphene layers in each pore wall are permitted to move (which is regarded as the “primary flexibility”), thus allowing the effect of the confined nanophase on the pore width and interlayer spacing to be studied. The

dimensions of the simulation cell were $L_{x,box} \times L_{y,box} \times L_{z,box} = L_{x,wall} \times (3 \times L_{y,wall}) \times (H_e + 5 \times d_{002,e})$, where $L_{x,wall} \times L_{y,wall} = 3.408 \text{ nm} \times 6.8866 \text{ nm}$ are the dimensions of the graphene layers. Here, H_e is the width of the pore when empty, defined as the distance between the innermost graphene layers on the opposing wall surfaces, when at their equilibrium positions (the actual pore width with adsorbate is denoted H). The values for the graphene interlayer spacing when empty at equilibrium, $d_{002,e} = 0.3395 \text{ nm}$ and 0.3438 nm at 87.3 K and 300 K , respectively, are obtained by running an initial set of simulations for an empty pore. Carbon atoms in a given graphene layer were arranged on a hexagonal lattice, with a C-C bond length of 0.142 nm . The atoms in all layers are connected to their lattice positions by a harmonic potential, with a spring constant, $k_s = 18.1 \text{ N/m}$, which is obtained by matching to the AIREBO potential of Stuart and coworkers for carbon [99]. That means that a “secondary flexibility” is applied to allow the individual carbon atoms to move around their lattice positions which are moving according to the primary flexibility. The reduced empty pore width, $H_e^* = H_e / \sigma_{aa}$ (where σ_{aa} is the diameter of the adsorbate molecule) varies from 2.0 to 8.0 with a 0.1 increment so as to study the effects of pore width.

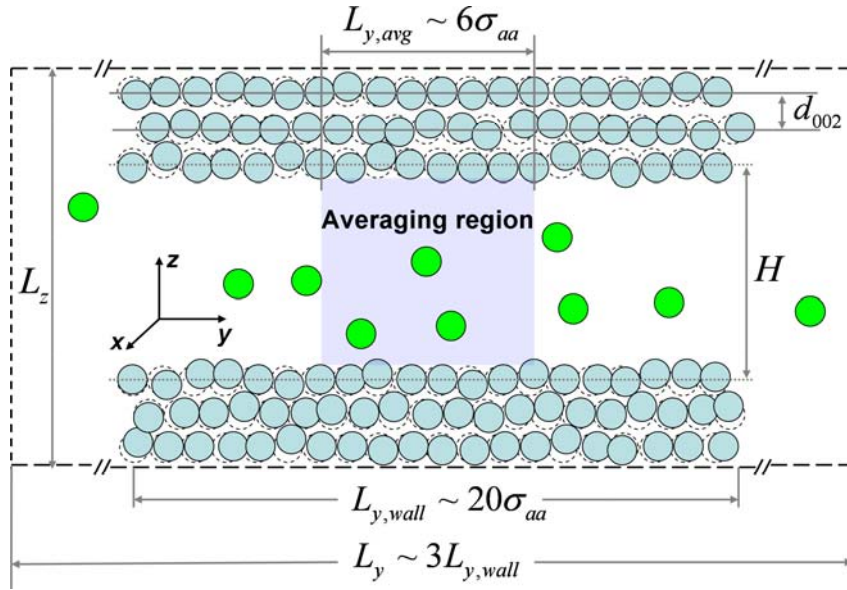


Figure 8.1 The simulation cell of our flexible model for the carbon slit pore. The dark (green in color) circles represent adsorbate argon molecules, and the light (blue in color) circles represent carbon atoms. Dashed circles represent the equilibrium position of carbons atoms. Carbon atoms are shown at reduced scale for clarity.

Interactions between carbon atoms (carbon-carbon or CC) in different graphene layers were modeled using the Lennard-Jones (LJ) potential with Steele's parameters [97], $\epsilon_{CC} / k_B = 28$ K and $\sigma_{CC} = 0.34$ nm. Argon-argon (adsorbate-adsorbate, or aa) and argon-carbon interactions (aC) are also modeled using the LJ potential. The LJ parameters used for argon [95], $\epsilon_{aa} / k_B = 119.8$ K and $\sigma_{aa} = 0.3405$ nm, are widely used and have been shown to accurately predict the vapor-liquid equilibrium envelope [119]. Parameters for the argon-carbon interactions are estimated using the usual Lorentz-Berthelot combining rules (Eqn. (5.4)). All LJ interactions are truncated at $r_c = 5\sigma_{ij}$ and intermolecular distances are evaluated according to the minimum image convention. Periodic boundary conditions are applied in the x -direction, and hard-wall boundary conditions are used for the y and z directions, so that the

pore is of finite length and the adsorbate in the pore phase is in direct contact with the bulk phase, which satisfies the hydrostatic equilibrium condition.

8.2.2 Simulation Details

The semi-grand Canonical Monte Carlo (SGCMC) method is used to perform argon adsorption in the model described in Sec. 8.2.1. The bulk phase pressure in equilibrium with the pore phase is 1 bar for a temperature of 87.3 K, and the pressure is 3,990 bar for a temperature of 300.0 K (this high bulk pressure is needed for this temperature to achieve a comparable in-pore density as for the 87.3 K case) for all the pore widths. Each simulation is composed of two stages: the equilibrium stage which brings the system from the preset initial state (an empty pore) into equilibrium; and the production stage in which the ensemble averages of desired state variables (in-pore density, pressure tensor components of adsorbate, actual pore width, interlayer spacing of graphene sheets, etc) are accumulated. In the equilibrium stage, 10^8 MC moves are performed using the SGCMC method, where translational displacement of argon molecules, translational displacement of carbon atoms, insertion of argon molecules, and deletion of argon molecules share 1 / 4 of the total moves, respectively. The displacement of the graphene sheets (along the z -axis) is attempted with an average frequency of 1 / 400 MC moves. In the production stage, another 10^8 MC moves are performed (in exactly the same way as the equilibrium stage) and the desired state variables are sampled every 4,000 MC moves (i.e., $\sim 25,000$ samples are taken to calculate the ensemble averages). In this study, the normal pressure is calculated by the mechanical route

using the IK definition, but it is exactly the same as that obtained by the Harasima definition, and is a constant due to the hydrostatic equilibrium (Sec. 3.2).

8.2.3 Results and Discussion

The normal pressure of adsorbate (argon) is a constant across the pore for a given pore width and thus this value is also equal to the normal pressure acting on the wall. This normal pressure usually oscillates between positive and negative as the empty pore width, H_e^* , increases due to oscillations in the average density of the adsorbate, as shown in Figure 8.2. For example, for a pore width of $H_e^* = 2.0$ only two layers of argon can be accommodated, and further increases in H_e^* only increases the distance between the two layers, which causes the average density and the normal pressure to decrease, and places the adsorbate inside the pore in a state of tension. However, at $H_e^* = 2.4$ the pore becomes wide enough to accommodate the formation of an additional layer of argon, which results in a rapid increase in density and compression of the fluid in the normal direction. The density peaks at $H_e^* = 2.5$ when this additional layer is completely filled, and further increase in pore width leads to another increase in interlayer distance and decrease in density and normal pressure, until another additional layer of argon can start to form. Such oscillations in the normal pressure, P_N , are well known and are observed in surface force measurements [4, 5] as well as in simulations and theoretical calculations [39]. It is worth noting that at a temperature as high as 300.0 K, due to the large kinetic contribution (see Eqn. (3.15)), the normal pressure is almost always positive, except for very small pores ($H_e^* < 2.4$), where the configurational adsorbate-carbon contribution is very large.

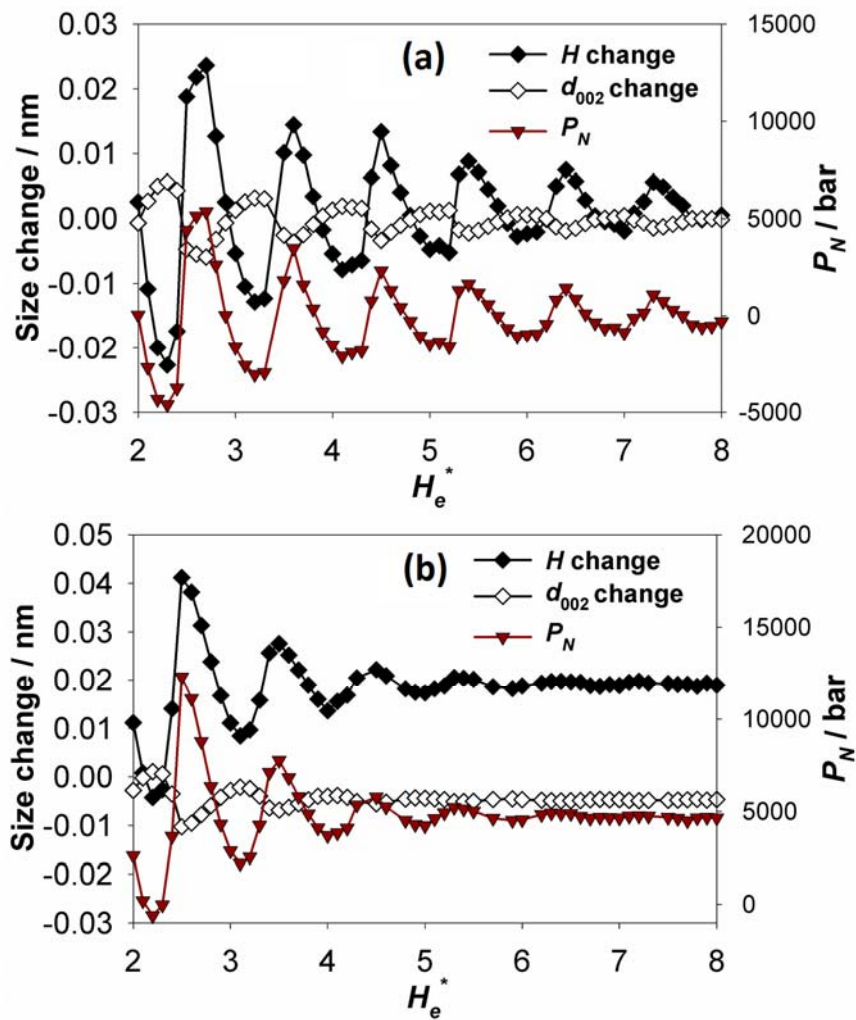


Figure 8.2 The normal pressures of argon adsorbed in carbon slit pores and the corresponding pore deformation for various pore widths at (a) 87.3 K and 1 bar bulk pressure and (b) 300.0 K and 3990 bar bulk pressure.

Positive and negative values of the normal pressure, respectively, result in an expansion or contraction of the pore in the direction normal to the wall, as illustrated in Figure 8.2. For smaller pore widths, changes in the pore width and interlayer spacing of graphene sheets are

approximately in the range ± 0.025 and ± 0.005 nm, respectively. As the pore width increases, these changes decay due to the decreased effects of the pore wall and the consequent decrease of the normal pressure. At 300.0 K, this decay becomes much quicker: for $H_e^* > 5.0$, the pore deformation, in agreement with the normal pressure, is almost constant. This is also because the kinetic contribution is much more important at high temperatures and the interaction from the pore wall becomes relatively weaker.

8.3 Carbon Tetrachloride and Water Adsorbed in Activated Carbon Fibers

8.3.1 Experimental

The experiments have been done by our collaborator Professor Śliwiska-Bartkowiak's Group (Adam Mickiewicz University, Poland). They have used X-ray diffraction to study two types of isotropic pitch-based activated carbon fiber (ACF) samples supplied by Ad'all Company, Japan, A10 and A20, with average pore widths of 0.85 nm and 1.40 nm, respectively (Note: the pore widths of the ACF samples were determined by our collaborator, Professor Katsumi Kaneko's Group, Chiba University, Japan). The structures of empty ACF samples and the structures of ACF loaded with water and carbon tetrachloride (ACF-H₂O and ACF-CCl₄) systems were studied at 300 K using monochromatic X-ray diffraction MoK α ($\lambda = 0.071069$ nm) over a wide range of wave vectors (4.30 to 153.10 nm⁻¹). Further details of the sample preparation and experimental method are given in [120]. From experiments, we determine the interlayer spacing of the graphene sheets for the unloaded A10 and A20, and for those loaded with water and carbon tetrachloride.

8.3.2 Modeling Details

A simple carbon slit pore model can be used to simulate the adsorption of fluids in ACFs, because ACFs are composed of many grains of slit pore structure, as shown in Figure 8.3a. In this study, the rigid, infinite carbon slit pore model is used, because the normal pressure is not sensitive to the flexibility of the pore. The simulation cell is shown in Figure 8.3b. The pore walls consist of three graphene layers lying in the xy -plane of dimension $L_{x,box} = 4.26$ nm, $L_{y,box} = 4.18$ nm. Periodic boundary conditions are applied in the x - and y -directions parallel to the pore walls, so that the pore is infinite in length in these directions, while being of fixed width, H . The carbon atoms are fixed at their lattice positions, so that the system volume is fixed. The normal pressure is a constant due to the hydrostatic equilibrium in a slit pore. As shown by Henderson [64], the constancy of the chemical potential in the pore, maintained in GCMC simulations for a system of constant volume, guarantees that hydrodynamic equilibrium is satisfied.

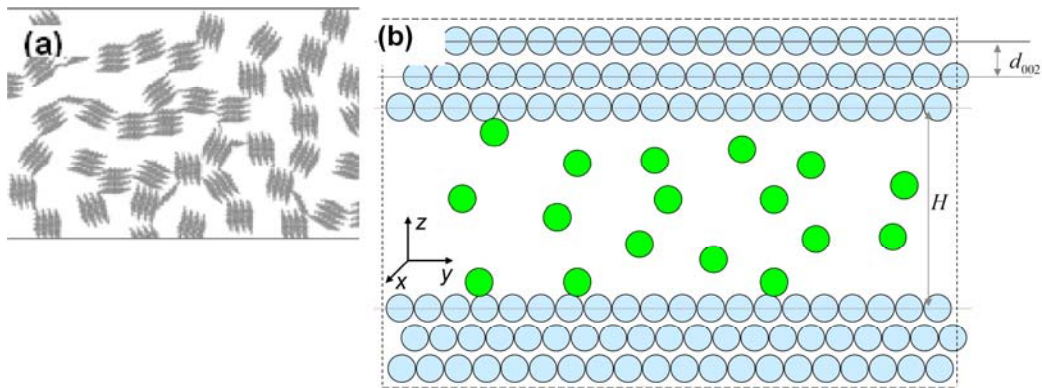


Figure 8.3 The schetimatic illustration of (a) ACFs and (b) an ACF model for molecular simulation.

Carbon tetrachloride is modeled as a single-site LJ molecule, whose LJ parameters (aa) are taken from Arstila et al., [121] $\epsilon_{aa} / k_B = 322.7$ K and $\sigma_{aa} = 0.5947$ nm, while those for carbon are taken from [97], $\epsilon_{CC} / k_B = 28$ K and $\sigma_{CC} = 0.34$ nm. Parameters for the adsorbate-carbon interactions (aC) are calculated from the Lorentz-Berthelot combining rules (Eqn. (5.4)). All LJ interactions are truncated at $r_c = 5\sigma$.

Water-water interactions are modeled using the extended simple-point-charge (SPC/E) pair potential [122]. This model consists of a LJ potential centred on the O atom, with parameters $\epsilon_{aa} / k_B = 78.2$ K and $\sigma_{aa} = 0.31656$ nm, and three point charges, one of $-0.8476e$ on the O and one of $+0.4238e$ on each of the H atoms. The SPC/E model accounts for the direct electrostatic interactions and includes a polarization correction. The water interaction with the carbon walls consists of two terms, a LJ interaction between the O atom and the C atoms, and a two-body induction interaction. Parameters for the LJ oxygen-carbon interactions are calculated using the Lorentz-Berthelot combining rules. The electric field, \mathbf{E}_j , acting on a carbon atom j due to the charges on the O and H atoms of the water molecules also leads to polarization of the carbon atom and an induction interaction U_j , given by:

$$U_j = -\int_0^{E_j} d\mathbf{E}_j \cdot \boldsymbol{\mu}_j = -\int_0^{E_j} d\mathbf{E}_j \cdot \alpha \mathbf{E}_j \quad (8.1)$$

where $\alpha = 1.958 \times 10^{-40}$ C m² V⁻¹ is the isotropic polarizability of a carbon atom [123], j is the index of the carbon atoms, and \mathbf{E}_j and $\boldsymbol{\mu}_j$ are the vector electric field and dipole acting on the j -th carbon atom due to the charges on all the water molecules. Long-range interactions

are cut off at 2 nm. As reported by Perera et al. [124], simple truncation of the SPC/E potential at a cut-off of at least 1.2 nm produces results very similar to the results where Ewald sums are used to treat long-range Coulomb effects.

According to the intermolecular potential model, the normal pressure of the confined water phase can be decomposed into a kinetic part, an adsorbate-adsorbate configurational part (dispersion and Coulombic contributions), and an adsorbate-carbon configurational part (dispersion and induction contributions):

$$P_N = P_{N,kin} + P_{N,aa,disp} + P_{N,aa,coul} + P_{N,aC,disp} + P_{N,aC,ind} \cdot \quad (8.2)$$

For confined carbon tetrachloride, the Coulombic (*aa,coul*) and induction (*aC,ind*) terms are absent.

8.3.3 Simulation Details

The GCMC simulations are carried out for intermolecular potentials chosen to model carbon tetrachloride and water in slit-shaped carbon pores with various pore widths at 300 K and 1 bar bulk pressure. The simulations are carried out for 10^8 Monte Carlo moves to attain equilibrium, and a further 10^8 moves for the determination of the pressure. The normal pressure is sampled every 5,000 configurations via volume perturbations (thermodynamic route) according to Eqn. (3.45). The final values of P_N are the result of averaging over 20000 samples in the unperturbed system of volume V . For each sampling step, a series of “perturbed” systems are constructed by rescaling the z -coordinates of all the atoms by $(1+\zeta)$, where $\zeta \ll 1$, and then the thermodynamic normal pressure is calculated by using Eqn. (3.45),

taking the limiting value as the volume change (only in the z -direction) goes to zero. A series of ζ values ($\pm 10^{-5}$, $\pm 10^{-6}$, $\pm 10^{-7}$) are used to calculate the limiting value of P_N as ζ goes to zero.

8.3.4 Results and Discussion

The normal pressures of carbon tetrachloride and water adsorbed in slit carbon pores at 300 K and 1 bar bulk pressure are shown in Figure 8.4. For LJ carbon tetrachloride, the normal pressure oscillates from positive to negative with amplitude of a few thousands of bars, as is the case for argon at low temperature (Sec. 8.2.3, Figure 8.2). For water, the oscillating normal pressure is always positive except for very small pores ($H < 0.82$ nm), which is expected from the strong non-wetting behavior for water on carbon. Such oscillating behavior of the normal pressure has been observed for water on mica surfaces in surface force apparatus experiments [42] (see also Figure 2.2b, for the part of $H < 2$ nm).

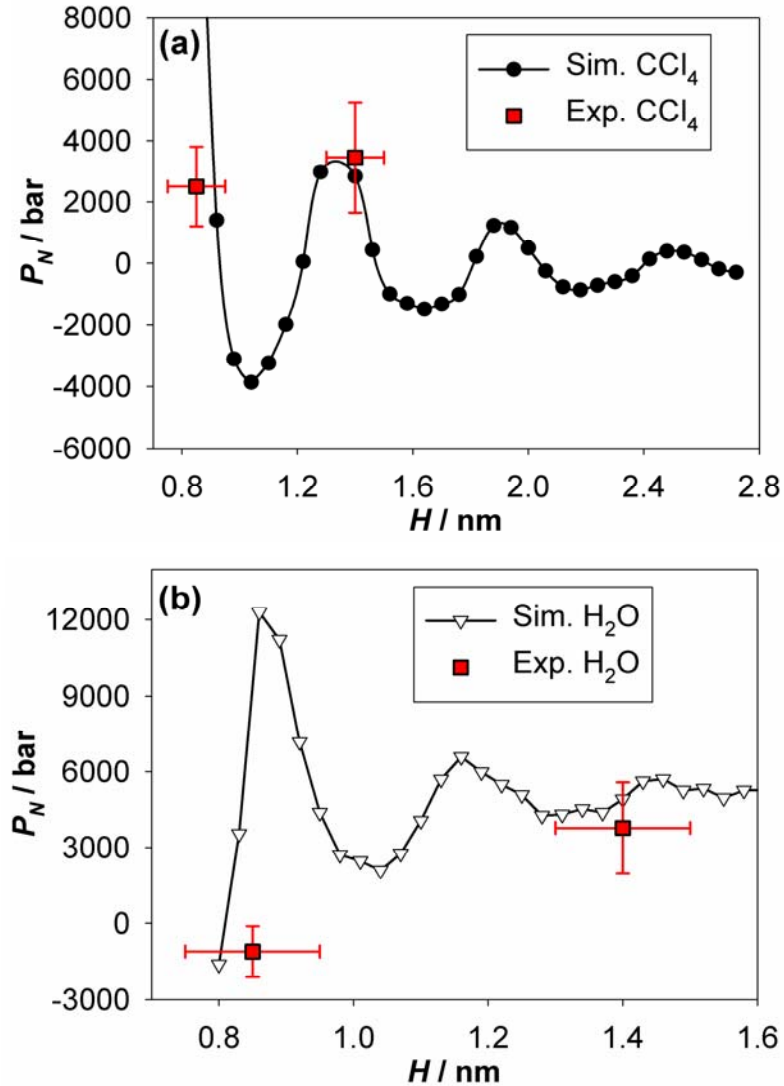


Figure 8.4 The normal pressure of (a) carbon tetrachloride and (b) water as a function of the pore widths of carbon slit pores at 300 K and 1 bar bulk pressure. The experimental data are included for carbon tetrachloride and water adsorbed in ACF ($H = 0.85$ nm and 1.4 nm).

The X-ray diffraction experiments measure the deformation of ACF due to adsorption of carbon tetrachloride and water (performed by Professor Śliwińska-Bartkowiak's group). These can be used to estimate the normal pressure on the pore walls. From the X-ray

scattering, we find that the average pore widths are 0.85 nm and 1.4 nm for A10 and A20, respectively and that the interlayer spacings between carbon graphene sheets are 0.364 and 0.378 nm, respectively, before adsorption. After loading with carbon tetrachloride and water at 300 K and 1 bar bulk pressure, the interlayer spacings of the graphene sheets are changed for A10 and A20. These changes are shown in Table 8.1. Using Young's equation $P_N = -\sigma_N = -E_T (\Delta d_{002} / d_{002})$, the normal pressure of the adsorbate on the wall can be roughly estimated, provided that the transverse compressive modulus, E_T , is known. Here Δd_{002} is the change in the interlayer spacing (d_{002}) of graphene sheets due to adsorption. The transverse compressive modulus E_T for these pitch-based fibers has been estimated to be ~ 2.9 GPa, with an uncertainty of $\sim 50\%$ [120]. With this value of E_T , Young's equation predicts experimental normal pressures for carbon tetrachloride of +1,912 bar and +3,452 bar, and for water, -1,115 bar and +3,683 bar for A10 and A20, respectively. The negative normal pressure for water in A10 indicates that the pore wall is attracted by the adsorbate, and the interlayer spacing of graphene sheets is increased. These experimental pressures are also included in Figure 8.4.

Table 8.1 The interlayer spacings (d_{002}) of graphene sheets in ACF samples with the pores empty and loaded with adsorbates.

Samples	Pore width H/nm	d_{002}/nm		
		Unloaded	with H_2O	with CCl_4
A10	0.85	0.364	0.378	0.340
A20	1.40	0.378	0.330	0.333

8.4 Argon Adsorbed in Cylindrical and Spherical Pores

To investigate the effects of pore geometry on the adsorption and normal pressure of the confined adsorbate, argon (a simple LJ fluid) adsorption and its normal pressure acting on the pore wall are studied in cylindrical and spherical carbon pores.

8.4.1 Modeling and Simulation Details

For the cylindrical pore, as shown in Figure 7.1a, the pore walls consist of three layers of carbon nanotubes (multiwall carbon nanotube). The interlayer spacing of the tubes is fixed to 0.335 nm. The chirality parameters are varied to construct the carbon nanotube with different diameter D (defined as the distance between the center of mass of carbon atoms on opposite sides of the pore). The length of the tube (z -dimension) is fixed to 6.15 nm, while the z -dimension of the simulation box is three times larger than that. Hard wall boundaries are applied in the z -direction, so that the pore is of finite length and the fluid confined in the pore is in direct contact with the bulk phase. For the spherical pore, as shown in Figure 7.1b, the pore walls consist of three layers of spherical carbon shells. The interlayer spacing of the shells is fixed to 0.335 nm. For each wall layer, a certain number of the carbon atoms are evenly distributed on the spherical shell, so that the areal density of the carbon atoms is the same as that in a graphene sheet. A hole with a size of two argon diameters (~ 0.8 nm) is artificially carved into each layer of the wall, so that the fluid confined in the pore is in direct contact with the bulk phase. In both models, hydrostatic equilibrium is satisfied. The argon-argon (adsorbate-adsorbate) and argon-carbon (adsorbate-carbon) interactions are modeled as purely LJ potentials, as described in Sec. 8.2.1. The carbon atoms are fixed in space, because

in contrast to the slit pore, the pore deformation will involve not only the weak (van der Waals) interaction between graphene sheets but also the covalent bonds between neighboring carbon atoms (the deformation of the pore will also stretch or compress the chemical bond), and thus the displacement of the carbon atoms is expected to be small. Therefore, in this study, there is no carbon-carbon interaction. The GCMC simulations are carried out to perform argon adsorption in the cylindrical and spherical carbon pores at 87.3 K and 1 bar bulk pressure for various pore diameters (the reduced pore diameter D^* varies from 2 to 10 adsorbate diameters). The simulations are carried out over for 10^8 Monte Carlo moves to attain equilibrium, and a further 10^8 moves for the determination of the pressure. The normal pressure of argon acting on the wall is sampled every 5,000 moves.

8.4.2 Results and Discussion

The normal pressures of LJ argon adsorbed in cylindrical and spherical carbon pores at 87 K and 1 bar bulk pressure are shown in Figure 8.5. The oscillation in the normal pressure with increasing pore size is observed for all three geometries (including for the slit pore, as shown in Figure 8.2). In cylindrical and spherical pores, the oscillation of the normal pressure is more complicated (Figure 8.5) compared with that in the slit pores, where the oscillations are regular in their behavior, with approximately constant wavelength and monotonically decreasing amplitude as pore width increases (Figure 8.2). In cylindrical and spherical pores P_N shows smaller amplitude of oscillation (less than 2,000 bars) than for the slit pore ($\sim 5,000$ bar), and more interestingly, unless the pore is small ($D^* < 5$) the normal pressure is always negative. The complication in the shape of the oscillation in P_N for cylindrical and

spherical pores is due to additional factors arising from the curvature of the pore walls. As the pore diameter is increased, oscillations in average density will occur as new adsorbed layers form as for the slit pore case, but superimposed on this is the fact that different layers can include different numbers of molecules, and this number depends on how far the layer is located from the center of the pore.

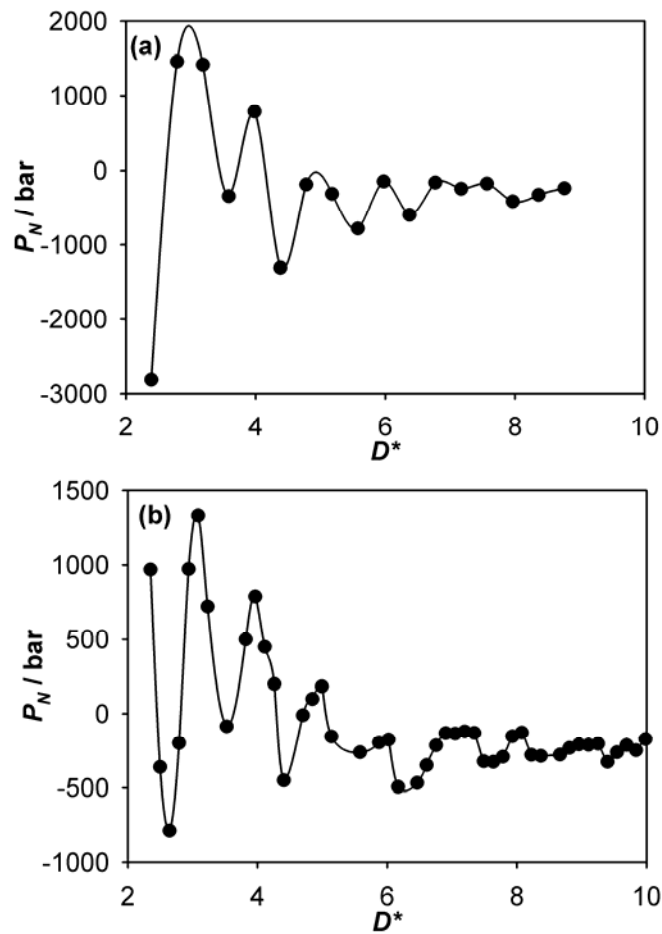


Figure 8.5 The normal pressure of adsorbed LJ argon acting on the wall of (a) cylindrical and (b) spherical carbon pores, at 87.3 K and 1 bar bulk pressure, for various pore widths.

8.5 Conclusions

The normal pressure of adsorbate acting on the pore wall oscillates with increasing pore width. This oscillation is a result of the in-pore density or number of adsorbate layers that could be accommodated in a certain pore width and their interlayer spacing. The amplitude of the oscillation in the normal pressure decreases with increasing pore width, in general. At higher temperatures this amplitude decreases faster than that at lower temperatures. The normal pressure and its oscillation causes the deformation of the pore structure, either enlarging the pore (positive normal pressure) or shrinking the pore (negative normal pressure), accordingly, in agreement with experimental results.

CHAPTER 9

Effects of Wall Roughness on Pressure in Slit Pore

9.1 Introduction

In addition to the study in carbon pores, the pressure tensor of adsorbate (LJ argon) in silica pores is investigated under collaboration with Dr. Benoit Coasne (University of Montpellier II, France). Compared with the carbon wall, the silica wall is less dense (in terms of wall atoms), weaker in attraction, and atomically rough on the surface. In this chapter, we first present the results of pressure and density profiles in the silica pores, which show that the pressure enhancement effect is significantly reduced in the silica pore compared with that in the carbon pores. We also examine simulation snapshots as well as the radial distribution function for the adsorbate layer in contact with the pore wall, which suggests that the reason of this reduction is the wall roughness (geometrical reason rather than the energetic reason). We then systematically study the effects of roughness on the adsorption isotherm and the in-pore pressure in the carbon slit pores.

9.2 Reduced Pressure Enhancement in the Silica Slit Pore

We artificially carve the β -cristobalite silica into a slit-shaped pore, and remove the unsaturated Si atoms as well as the free oxygen atoms on the carved surface. We saturate the dangling oxygen atoms (those that only have one bond with Si atoms) by adding H atoms to neutralize the system. The system is then randomized slightly. The model is now an atomistic

silica pore with a finite length of 6.8 nm, and the bulk phase is in contact with each end of the pore as shown in Figure 9.1.

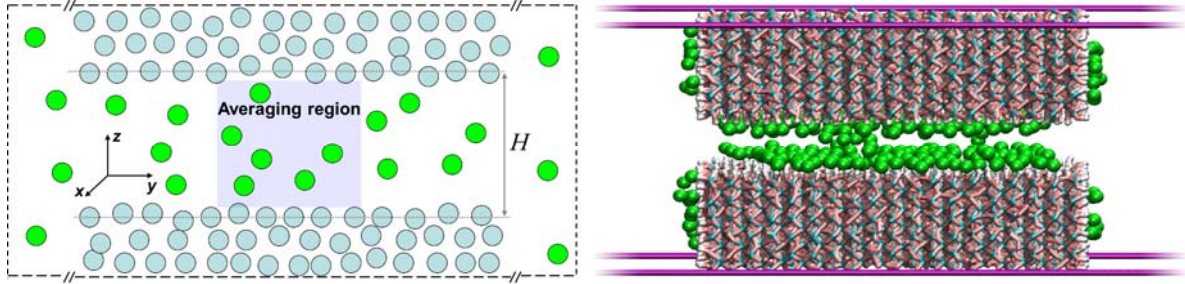


Figure 9.1 Simulation cell of silica slit pore. The green circles represent adsorbate argon molecules. Atoms in silica are covalently bonded and less dense than those in carbon wall.

Unlike the realistic carbon slit pore model described in Sec. 5.2, all the atoms of the silica wall are fixed in the space during the simulation, because the atoms in silica are connected by covalent bonds which are much stronger than the interaction between graphene layers and thus makes the silica wall much more difficult to deform. The argon-silica interaction is modeled by PN-TrAZ [125]:

$$u_i = \sum_{j \in \{O, Si, H\}} \left[A_{ij} e^{-b_{ij} r_{ij}} - \sum_{n=3}^5 f_{2n} \frac{C_{2n,ij}}{r_{ij}^{2n}} \right] - \frac{\alpha_i E_i^2}{2}, \quad (9.1)$$

where

$$f_{2n} = 1 - \sum_{k=0}^{2n} \frac{(b_{ij} r_{ij})^k}{k!} e^{-b_{ij} r_{ij}}. \quad (9.2)$$

and u_i is the potential energy of adsorbate molecule (rare gas atom) i with the silica substrate, silica, α_i is the polarizability of molecule i , E_i is the electric field acting on the molecule i , and other symbols are model parameters whose values are listed in Table 9.1 [126]:

Table 9.1 Model parameters for PN-TrAZ potential (in atomic units, $E_h = 3.1578 \times 10^5$ K, $a_0 = 0.529177$ Å) [126].

	Ar-O	Ar-Si	Ar-H
$C_6/E_h a_0^6$	50.15	18.79	13.49
$C_8/E_h a_0^8$	966	261	291.3
$C_{10}/E_h a_0^{10}$	221	--	--
A/E_h	711.6	1422	20.98
B/a_0^{-1}	2.045	2.090	2.009
Polarizability $\alpha_{Ar} = 11.075 a_0^3$	$q_O = -1 e$	Partial Charges $q_{Si} = +2 e$	$q_H = +0.5 e$

We use the GCMC method to perform argon adsorption. As before, the simulations are run for 10^8 Monte Carlo moves to attain equilibrium, and a further 10^8 moves for the determination of the pressure. The pressure tensor components for the averaging region are sampled every 5,000 moves.

The density and pressure profiles of argon adsorbed in a slit silica pore ($H^* = 3.0$) at 87.3 K, 1 bar bulk pressure are shown in Figure 9.2a. The normal pressure is constant, as expected. However, the tangential pressure of argon in the silica pore is significantly lower than that in the carbon pore, at the same bulk condition ($\sim 2,000$ bar compared with 20,000 \sim 30,000 bar

for the local peak value), i.e., the pressure enhancement effect in the silica pore is significantly reduced compared with the carbon pore. We also note that, different from the case in the carbon pore of the same width (Sec. 5.4.2 and Figure 5.5b), there are five layers of argon molecules adsorbed in the slit silica pore with $H^* = 3.0$ as shown from the density profile (Figure 9.2a), but the density is appreciably smaller than in the carbon pore (~ 2.5 compared with ~ 8). By looking at the z -coordinates of the contact layer of argon and the wall atoms, we see that the contact layer is located at the plane where there are also wall atoms. This results from the fact that the silica wall surface is “atomically rough”, so that the adsorbate can be “embedded” into the wall (Figure 9.3a). The radial distribution function shows that at the argon layers, there are strong peaks located at a separation distance larger than 1.49 in reduced unit (Figure 9.2c), which gives rise to an attractive interaction between fluid-fluid molecules, and results in a negative fluid-fluid configurational contribution to the tangential pressure (Figure 9.2b) at the planes where there are argon layers.

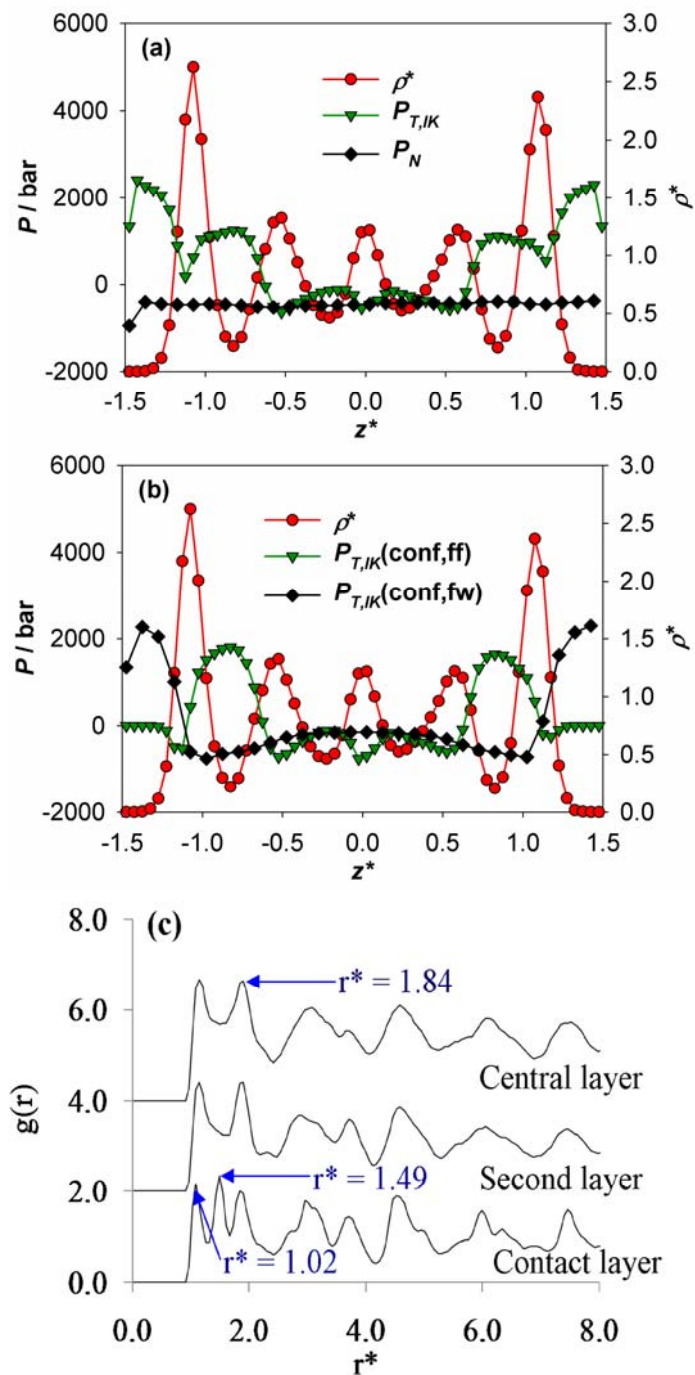


Figure 9.2 (a) The density and pressure profiles of argon in the atomistic fixed silica pore model with finite length ($H^* = 3.0$) at 87.3 K and 1 bar bulk pressure, (b) the individual contributions of tangential pressure, and (c) the radial distribution function of the different argon layers.

In the silica pore (actually any pore with a rough surface), the separation distance between the neighboring argon molecules in the contact layer is dominated by the geometric effect: as adsorption starts, the adsorbate molecule tends to be accommodated on the wall surface or the “hole” of a rough surface where attractive interaction is the strongest (Figure 9.3a), instead of being as closely packed as on a smooth surface or atomistic surface with a very high surface density (e.g., smooth wall model or atomistic graphene, see Figure 9.3b). Thus, the distance between neighboring adsorbate molecules on a rough surface strongly depends on the geometric arrangement of the surface atoms. The arrangement of the adsorbate in the contact layer also influences the arrangement of the second layer of adsorbate (the second layer of adsorbate could also be embedded partly in the contact layer); this holds true for all the following adsorbate layers as adsorption continues. Since the adsorbate layers are partly embedded with each other, their interlayer spacing is unsurprisingly smaller than the effective diameter of the adsorbate molecule, which is the reason why there can be five layers of argon in a silica pore of $H^* = 3.0$ with a lower density peak.

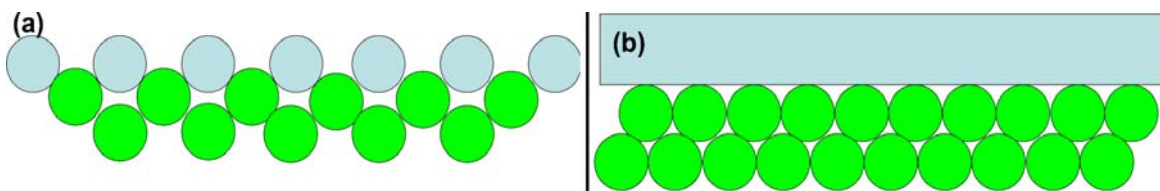


Figure 9.3 Schematic representations of adsorbate molecules accommodated on (a) a rough surface (e.g. surface of a silica pore) and (b) a smooth surface or an atomistic surface with high atomic density (e.g. graphene surface). Dark circles (green in color) represent adsorbate molecules, and light circles or slab (light blue in color) represent wall surfaces.

9.3 Effects of Wall Roughness on Adsorption Isotherm and In-Pore Pressure

As discussed in Sec. 9.2, the surface roughness significantly reduces the pressure enhancement effect in the silica pore. In light of this finding, the effects of roughness of carbon slit pores are also studied, since many carbon porous materials are amorphous rather than perfectly crystalline [86], which will cause roughness on the inner surface of the pores.

9.3.1 Models and Simulation Details

We construct the wall with a roughness model based on a model of an atomistic carbon slit pore with finite length, composed of two parallel walls, each of which is three layers of graphene sheets. The pore is centered at the origin and the walls are normal to the z -direction. The wall is of finite length in the y -direction (Periodic boundary conditions are only applied in the x -directions). Roughness is imitated by basing the z -coordinates of the carbon atoms of inner-layer graphene (wall surface) on their y -coordinates through the relationship (a model proposed by Jagiello, 2012 [127]):

$$z = \pm[H/2 + A_w \cos(2\pi y / \lambda_w)], \quad (9.3)$$

such that a cosine wave (where the amplitude is A_w , the wave length is λ_w , and $H/2$ is half of the pore width) is applied to the wall surface, while the other graphene layers are kept planar. We can also set $A_w = 0$ to generate an atomically smooth wall (provided carbon atoms are very closely packed in the graphene layer). A sketch of the rough wall is shown in Figure 9.4. A variety of amplitudes A_w and wave lengths λ_w are chosen so as to investigate the effects of roughness. The models under study are labeled to show the roughness amplitude A_w and wave lengths λ_w as described in Table 9.2. The first six models listed in Table 9.2 (with wave

lengths smaller or comparable to 1 nm) are constructed to study the sensitivity of in-pore structure and pressure of adsorbate to “fine” roughness (such as on a silica surface, or surface covered with a large amount of functional groups), while the last two models in Table 9.2 (with wave lengths of 3 nm and 4 nm) are constructed according to the DFT calculations, where the wave length of a more realistic graphene sheet is found to be 3 ~ 4 nm, as shown in Figure 9.5 [128, 129].

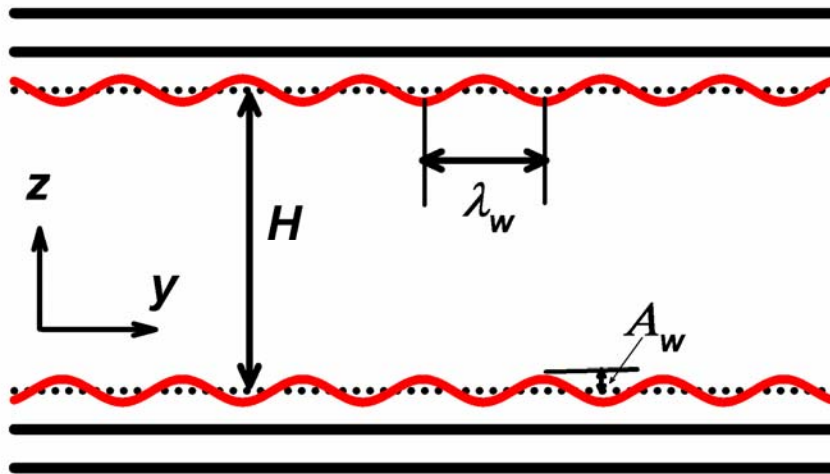


Figure 9.4 The schematic model of a rough pore. The thick solid lines represent the planar layer of graphene, and the red solid curves represent the rough wall surface, while the dotted lines show the average z -position of the rough wall layer.

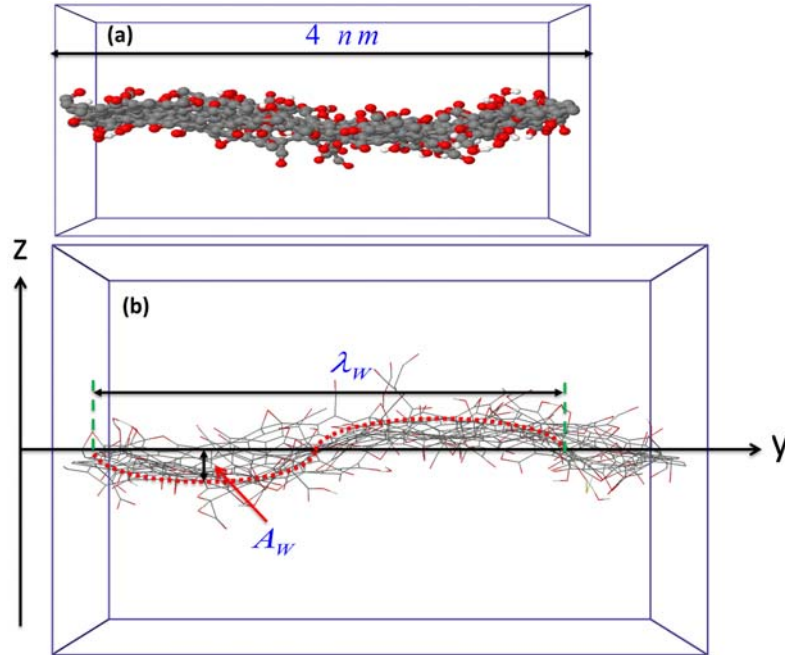


Figure 9.5 A functionalized graphene with 30% coverage of defects including hydroxyl, epoxy, carboxyl, vacancies, and Stone-Wales, obtained by the DFT calculation: (a) the snapshots and (b) fitted by a sine wave curve. [129]

Table 9.2 The model parameters for pores of various roughnesses.

Model ID	Pore width	Finite pore	A_w	λ_w
FLAT	$8 \sigma_{aa}$	Yes	0	∞
A10W08	$8 \sigma_{aa}$	Yes	0.10 nm	0.861 nm
A13W08	$8 \sigma_{aa}$	Yes	0.13 nm	0.861 nm
A07W08	$8 \sigma_{aa}$	Yes	0.07 nm	0.861 nm
A10W06	$8 \sigma_{aa}$	Yes	0.10 nm	0.615 nm
A10W11	$8 \sigma_{aa}$	Yes	0.10 nm	1.107 nm
A10W30	$8 \sigma_{aa}$	Yes	0.10 nm	3.0 nm
A10W40	$8 \sigma_{aa}$	Yes	0.10 nm	4.0 nm

The adsorbate is argon, and the adsorbate-adsorbate interaction and the adsorbate-carbon interaction are modeled with LJ potentials as described in Sec. 7.2.3. We perform argon adsorption in models with different wall roughnesses at 87.3 K. The slit pore width is fixed to 8.0 in reduced units (2.724 nm), and is defined as the distance between the average position of the centers of mass of carbons in the opposing walls of the inner surfaces. We use GCMC simulations to first bring the system to thermodynamic and mechanical equilibrium, and to subsequently calculate the average properties.

9.3.2 Results and Discussion

We first show the effects of fine roughness on argon adsorption isotherms in Figure 9.6. For all models, the capillary condensation occurs at similar bulk pressures (~ 0.3 bar, see the big jump in Figure 9.6a), suggesting that the capillary condensation pressure is dominated by the pore width and insensitive to the pore wall roughness. On the contrary, the adsorption isotherm at low pressures is very sensitive to the roughness (see the part of Figure 9.6a where $P_{bulk} < 0.1$ bar as well as Figure 9.6b). In the smooth wall, there is a clear jump followed by a platform corresponding to the filling of the close-packed argon layer in contact with the wall (contact layer). For the pores with rough walls, this jump is smoothed into a steadily increasing curve depending on the nature of the roughness (which actually forms micropores). These smoothed isotherms in pores with rough wall were also found by Jagiello and Olivier [127].

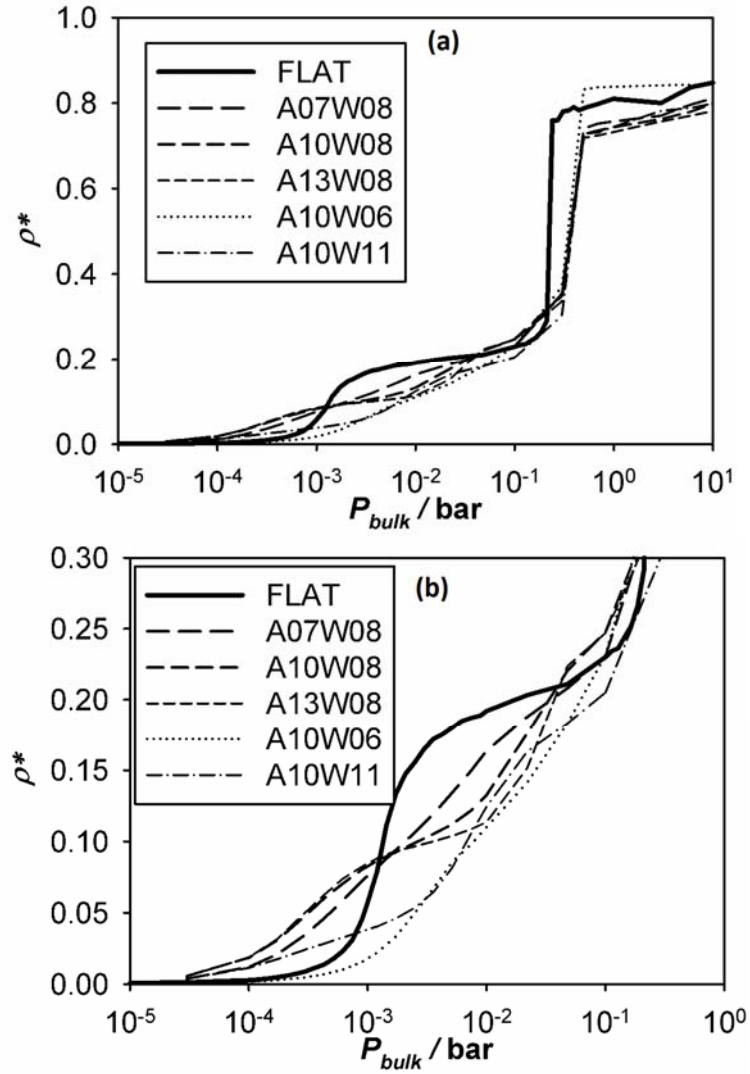


Figure 9.6 The adsorption isotherms of argon in carbon slit pore models with various roughness at 87.3 K (a) on a full pressure scale and (b) for low pressures.

We next examine the density and pressure profiles and the structure of argon confined in several models as shown in Figure 9.7. Note that for all models, the reduced pore width is 8.0, which can accommodate 7 complete layers of argon molecules in a geometrical sense. This is true for the pore with smooth walls, which is evidenced by the 7 peaks in the density profile,

and is visualized from a snapshot of this system (Figure 9.7a). The contact layers of argon in the pore with smooth walls show very high and narrow peaks in the density profile (with a maximum of > 7 in reduced unit), suggesting a very close-packed structure. The tangential pressure profile in the pore with smooth wall follows the density profile because this highly enhanced tangential pressure is a result of the adsorbate compression in the tangential direction. Unlike these phenomena found in the pore with smooth walls, the contact layers of argon on rough walls are far away from an ideal close-packed plane, which is evidenced by the split peaks for the contact layers in the density profiles and by the reduction of peak values to ~ 3 (Figure 9.7b, c and d). This is because the argon molecules prefer to fill in the vacancies produced by roughness to form a “loose” argon layer. This then causes the loose argon layer itself to produce new vacancies for later argon molecules to fill in (similar to the illustration in Figure 9.3a). The snapshots in Figure 9.7b and c also show this: one argon molecule is filled in each wave trough and two argon molecules are filled in the vacancy produced by the argon molecules closest to the wall. It is also shown that if the amplitude of the roughness is larger (for the same wave length), this effect is stronger: in Figure 9.7b, $A_w = 1.0$ nm, and only the density peaks for the contact layer split, while in Figure 9.7c, $A_w = 1.3$ nm, the first and second inner layers also split. As a result of this splitting, the local tangential pressure (peak at 1,000 \sim 2,000 bar) is not enhanced as significantly as in the pore with smooth walls (peak at \sim 20,000 bar), and can even be negative in some cases, because the separation distance of argon molecules in the tangential direction is relatively large because of this geometrical arrangement. For the pore roughness with larger wavelengths (Figure 9.7d, where $\lambda_w = 1.107$ nm compared with 0.861 nm for Figure 9.7b and c), this

splitting effect becomes smaller, because the argon molecules have enough space to arrange to form a curved continuous layer rather than to fill in the small vacancy in a discrete manner. Thus, the density profile in Figure 9.7d only shows a very small peak accompanied by a wide main peak for the contact layer, and the effect on the inner layers is inappreciable. As a result, the tangential pressure profile follows the density profile and does not deviate considerably from that of the smooth wall model with its peak value of 6,000 bar, which is much larger than for the pore roughness with smaller λ_w . We recall that for the planar surface, because of the hydrostatic equilibrium, the normal pressure should be a constant (Eqn. (3.4)), which holds true for pores with smooth walls (Figure 9.7a). For pores with rough walls, the confined argon is not arranged in a layering pattern, especially for the region close to the pore wall. As a result, the normal pressure is no longer a constant. The normal pressure deviates from a constant value according to the effects of roughness: for the pore with “rougher” walls (large A_w and/or small λ_w), the non-constant region for the normal pressure is thicker (Figure 9.7b and c), while for the smoother wall with larger λ_w , the normal pressure is almost a constant for most of the pore region.

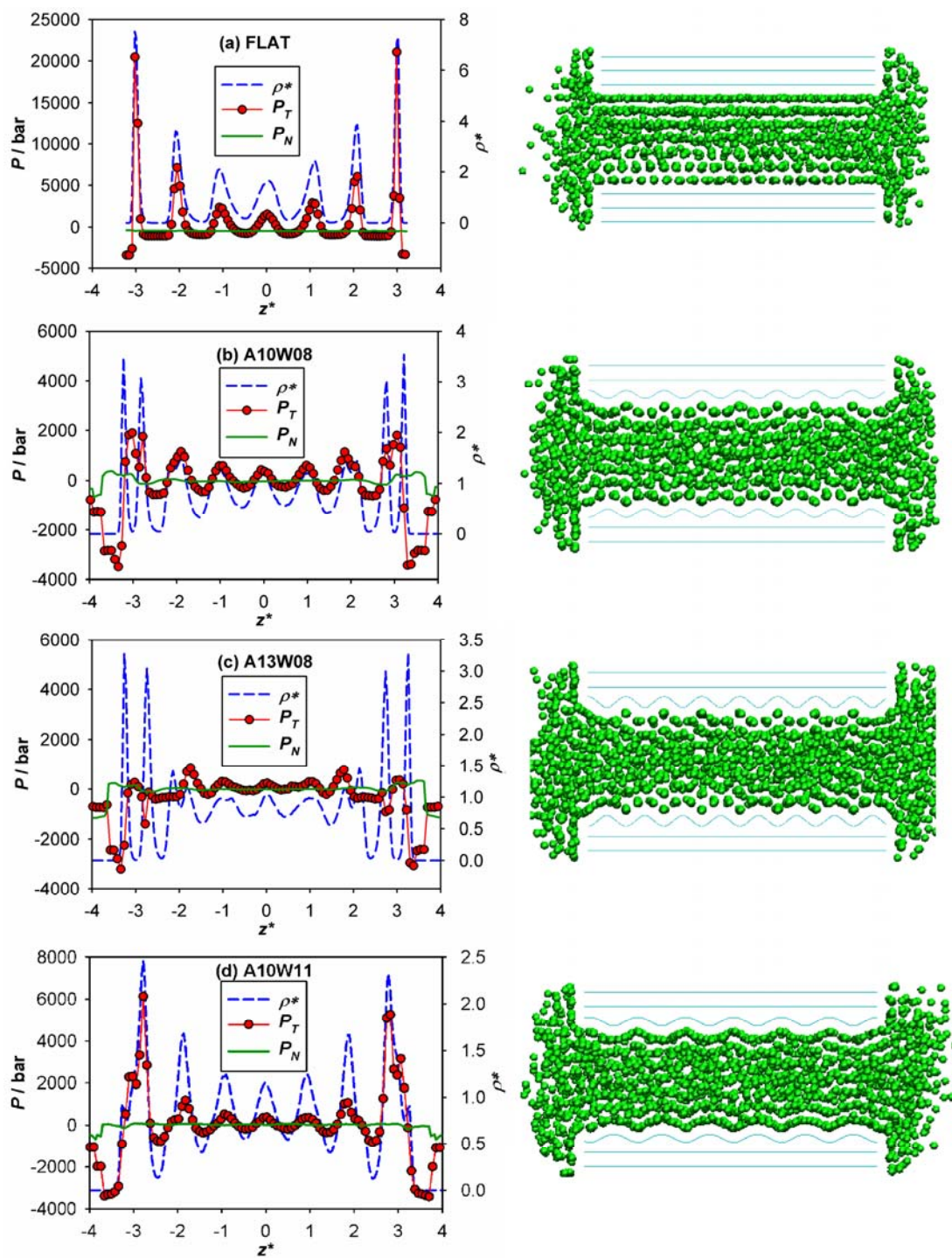


Figure 9.7 The density and pressure profiles (left) and snapshots (right) of argon adsorbed in carbon pore models with various roughness at 87.3 K and 1 bar bulk pressure.

We studied the effect of bulk pressure on the peak value of the tangential pressure of argon confined in the pore with varying wall roughness (see Figure 9.8). For the pore with smooth walls, the tangential pressure increases much more rapidly with increasing bulk pressure, because for the smooth wall, with increasing bulk pressure, the argon in the contact layer is continuously compressed in the tangential direction which causes a rapid increase in the tangential pressure. But for the pore with rough walls, because of the geometric blockage from the wall roughness, additional argon molecules are not easy to insert with the increasing bulk pressure. Moreover, as shown in Figure 9.7c, sometimes the peak value of the tangential pressure occurs at the inner layer, depending on the nature of the roughness, thus the maximum of this peak value could not be very large, because of lack of a strong attraction from the wall, which is the reason for the significantly enhanced tangential pressure.

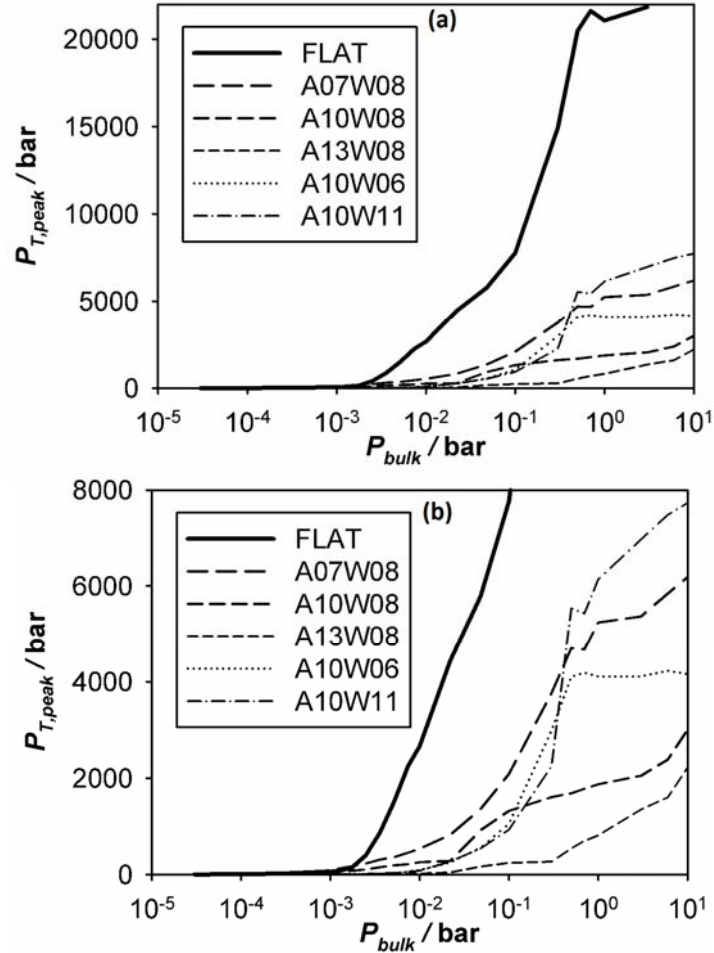


Figure 9.8 The peak value of tangential pressure of argon along the isotherm in carbon slit pore models with varying wall roughness at 87.3 K (a) on a full pressure scale and (b) with expanded vertical scale.

Because of the non-planar nature of the walls the normal pressure is no longer a constant, and so we average the normal pressure over the accessible pore width (using the definition provided by Eqn. (3.84)). This average normal pressure was also studied as a function of bulk pressure for the pores with rough walls at 87.3 K (see Figure 9.9). For all the pore models (including the smooth wall), the normal pressure exhibits a minimum with a negative value

right after capillary condensation, and then increases to positive values as the bulk pressure increases. The magnitude of the minimum of the normal pressure is greatest for the smooth wall, suggesting a very strong attraction between the wall and the confined adsorbate due to the incomplete pore filling at this bulk pressure. For pores with rough walls this attraction is much weaker (-200 bar for rough walls compared with -400 bar for the smooth wall), because with roughness, the degree of pore filling is higher, since the adsorbate molecules can fill in the roughness-produced micropore, and thus there are more adsorbate layers which push the normal pressure towards the repulsive (positive) region leading to a weaker attraction (less negative value). After capillary condensation, as the bulk pressure continues to increase, the normal pressure for the pore with smooth walls increases more rapidly than for those with rough walls, because the adsorbate layers for the former can be more close-packed (almost ideal fcc planes), and thus the total repulsive interaction between these layers is stronger than those in the pores with rough walls, where the roughness prevents the adsorbate layers from being very close-packed. One exception is for the A10W06 model, where the wave length of the roughness is as small as 0.615 nm. At the capillary condensation pressure, the in-pore normal pressure is as large (but negative in value) as for the pore with the smooth wall, and then it generally decreases slightly with increasing bulk pressure. The strong attraction in the A10W06 model, similar to that in the smooth wall model, is most likely because of the very small wave length, which coincidentally matches the adsorbate structure and makes the latter become similar to that in the smooth wall model at the capillary condensation pressure. But as the bulk pressure increases, the adsorbate in the smooth wall model can be compressed to make the interaction become repulsive, while the

adsorbate in the A10W06 model cannot follow this behavior due to the geometrical blockage from the roughness.

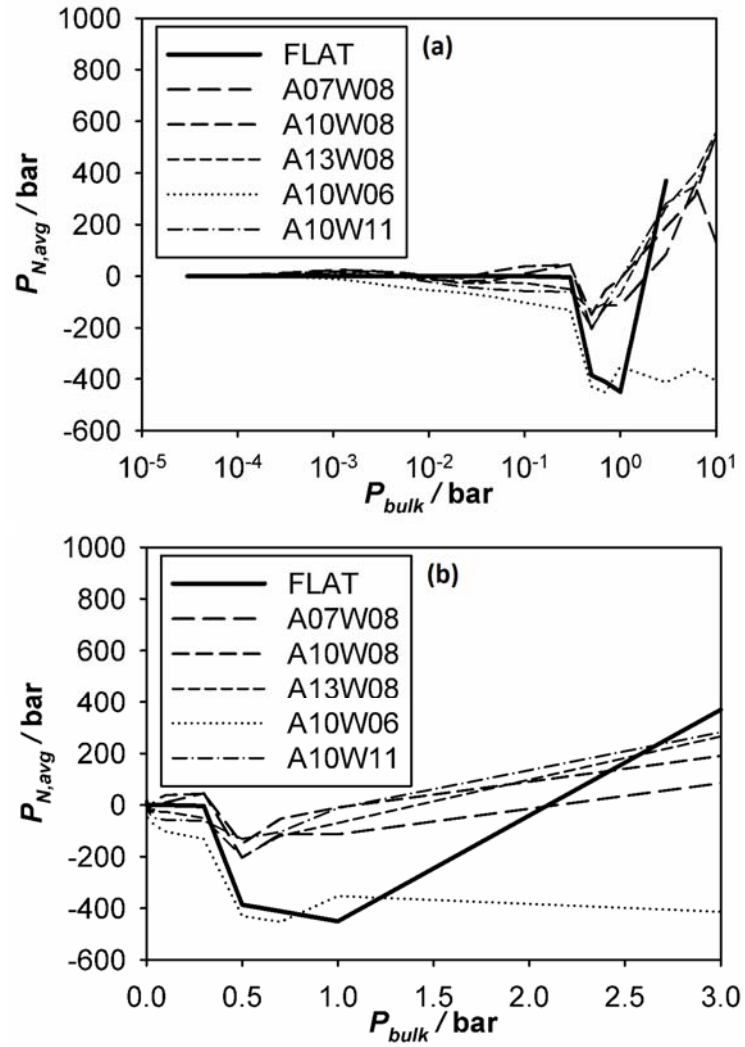


Figure 9.9 The average normal pressure of argon along the isotherm in carbon slit pore models with varying roughness at 87.3 K (a) on a log scale and (b) on a linear scale for the bulk pressure (horizontal axis).

Finally, we show in Figure 9.10 the density and pressure profiles of argon confined in models with larger wave length of the roughness ($\lambda_w = 3.0$ nm for A10W30 model and $\lambda_w = 4.0$ nm for A10W40 model) and compare them with those for the smooth wall model. As for the pores with smaller λ_w , the peaks of density profile split for the contact layers (in both A10W30 and A10W40 models) as well as the inner layers (obvious in A10W30) suggesting the split of argon layers due to the constraint by the wall roughness. It also suggests that the extent of the split (the relative height of the peaks in density profile and how many argon layers are affected to be split) is dominated by the match of the roughness with the adsorbate arrangement rather than just simply the values of λ_w and A_w . But in general as λ_w increases, the effect of wall roughness on the adsorbate structure and thus the in-pore pressure becomes weaker (the peak value of the tangential pressure in these models are 5,000 ~ 8,000 bar compared with 1,000 ~ 5,000 bar for those with $\lambda_w < 1$ nm). The normal pressures in A10W30 and A10W40 models are larger than that in the smooth wall model mainly because in these pores, more argon layers can be accommodated (a result of roughness) while the density of each argon layer is not significantly lower than that for the smooth wall model (a result of large wave length). However, the relationship between the roughness and the in-pore pressure components is complex, and the dominant factor is the match between the geometrical nature of the roughness and the adsorbate structure, rather than simply the values of the characteristic variables of the roughness model.

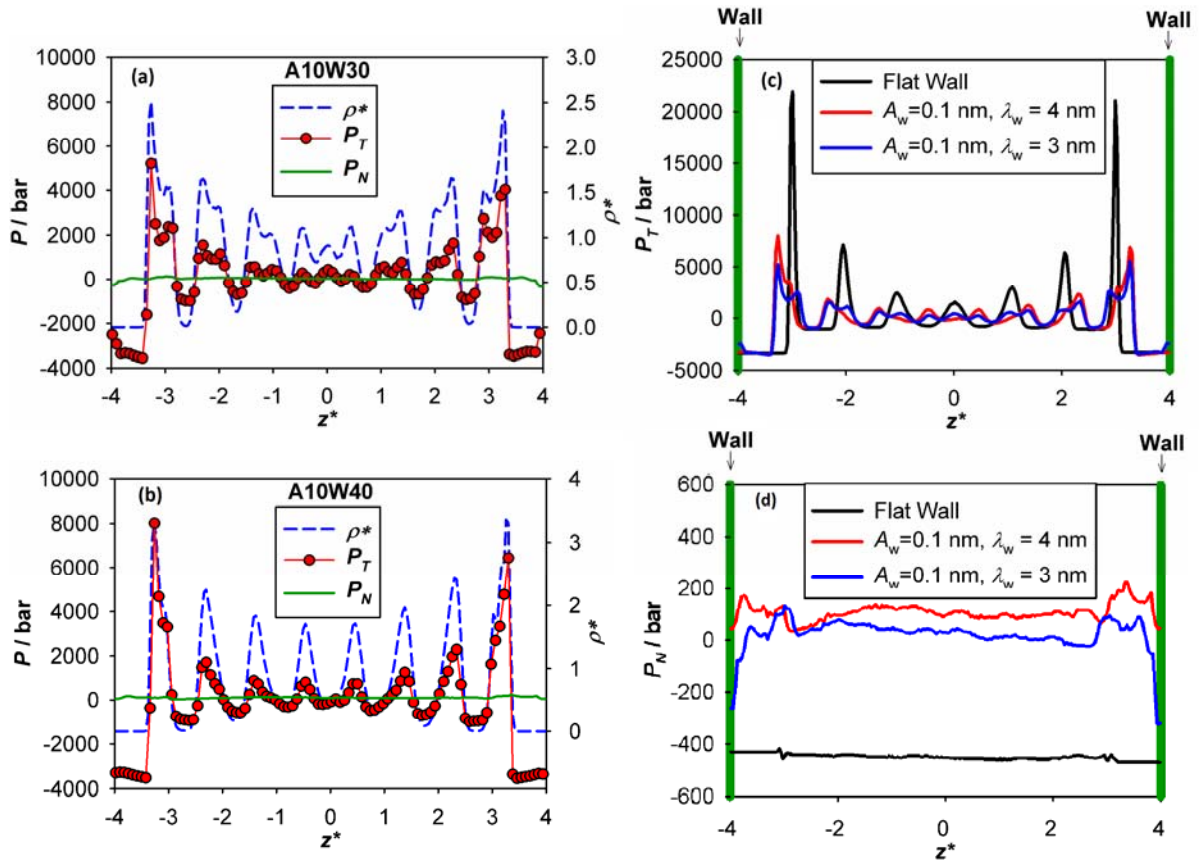


Figure 9.10 The density and pressure profiles of argon confined in carbon slit pores with rough walls of (a) $\lambda_w = 3.0$ nm and (b) $\lambda_w = 4.0$ nm. The comparisons for the (c) tangential and (d) normal pressure components with those in the pore with smooth wall are also shown.

9.4 Conclusions

The roughness of the pore walls imposes very strong effects on the structure of the confined adsorbate and thus on the in-pore pressure. Generally speaking, the roughness on the wall surface prevents the adsorbate layer in contact with the wall from arranging into a very close-packed structure, which probably also produces the roughness of the adsorbate and prevents the inner layer in contact with this “contact layer” from being closely packed. As a result, the

peak value of the tangential pressure in the pore with rough walls is not as large as that in a similar pore with smooth walls. The normal pressure in these pores is no longer constant across the pore width since the adsorbate molecules are not arranged in a quasi-planar way due to the geometric constraint imposed by the wall roughness. The magnitude of the normal pressure for a certain pore width with rough walls is also different from that in a pore with smooth walls, which is a result of the match between the wall roughness and the structure of the confined adsorbate.

CHAPTER 10

Conclusions and Perspectives

10.1 Conclusions

In this dissertation, we use the GCMC and SGCMC methods to perform simulations of adsorption of various fluids (mainly LJ argon, but also LJ Hg, LJ CCl₄, LJ and SPC/E water) in various micro-/nano-pore models (carbon slit, cylindrical and spherical pores with and without flexibility, with different potential models and different wetting parameters, and silica slit pore with PN-TrAZ potential). The pressure tensor components of the adsorbate confined in pores are calculated by both the mechanical and thermodynamic routes. For the mechanical route, due to the ambiguity of the integral contour, the Irving-Kirkwood and Harasima definitions are chosen. For the thermodynamic route, due to the ambiguity of the “local energy”, we develop two definitions of the energy assignment corresponding to the Irving-Kirkwood and Harasima definitions in the mechanical route, respectively. We also develop a new framework of the volume perturbation method (based on the thermodynamic route) to calculate the pressure tensor components in the cylindrical and spherical pores.

Using the above methods, we systematically study the pressure tensor and the pressure enhancement effect in micro-/nano-porous materials as well as the physical reason for this large effect. Our findings can be summarized as follows:

- (a) The pressure of fluids confined in the micro-/nano-pores (an inhomogeneous system) is a second-order tensor rather than a scalar as for a homogeneous system. The tangential (parallel to the pore wall) and the normal (perpendicular to the pore wall) components of the pressure tensor are generally different in magnitude and even in sign, depending on the effects of confinement in these directions.
- (b) The attractive nature of the pore wall, or more precisely, the nature of the adsorbate-wall interaction, plays an important role in the structure of the confined phase (especially the adsorbate layer in contact with the pore wall), and thus the in-pore pressure tensor, especially the tangential component at the contact layer.
- (c) For the adsorbate-wall wetting system, the tangential pressure is significantly enhanced (e.g., by a factor of $10^4 \sim 10^6$ for argon adsorbed in carbon pores). This enhancement effect arises from the strong attraction from the wall, which compensates for the repulsive interaction between the adsorbate molecules and thus compresses the adsorbate phase. The wall imposes this effect most strongly on the contact layer of the adsorbate, and thus the tangential pressure at the contact layer is enhanced most significantly.
- (d) For the adsorbate-wall non-wetting system, the tangential pressure is slightly enhanced (e.g., by a factor of < 10 for mercury adsorbed in carbon pores). For the non-wetting system, the attraction from the wall is weak (even weaker than the attraction between the adsorbate molecules), and thus the wall does not help to compress the adsorbate phase. A

very large bulk pressure is needed (e.g., ~ 4000 bar for mercury in a carbon pore) to push the adsorbate to intrude into the pore, and the adsorbate layer in the central region of the pore is equally or even more compressed (by the bulk pressure) than the contact layer, where the weaker attraction from the wall decreases the degree of the compression.

- (e) The normal pressure of the confined phase depends on its compression in the normal direction, and thus depends on the pore size, or more precisely, the match between the pore size and the adsorbate layer arrangement in the normal direction. As a result, the normal pressure exhibits an oscillation between positive and negative values with increasing pore size.
- (f) The normal pressure of adsorbate acting on the wall is also enhanced (by a factor of 10^3), but the value can be positive or negative depending on the pore size. This large normal pressure also causes deformation of the porous material: a positive normal pressure (strong repulsive force) expands the pore, while a negative normal pressure (strong attractive force) contracts the pore.
- (g) In the cylindrical and spherical pores (wetting system), the pressure enhancement effect is stronger than that in the slit pore of the same size. Because of the curvature of the walls, the attraction from the wall is enhanced due to more wall atoms interacting strongly with the adsorbate phase, and thus the adsorbate in the cylindrical and spherical pores are more compressed, which results in a larger tangential pressure at the contact layer.

- (h) The roughness of the pore wall, in general, decreases the pressure enhancement effect (for the wetting system), because the roughness prevents the contact layer of adsorbate from arranging into a very close-packed structure due to the steric hindrance effect, which probably also produces roughness of the adsorbate layers and prevents the inner layer in contact with this “contact layer” from being closely packed. As a result, the tangential pressure at the contact layer of adsorbate confined in a pore with rough walls is not as large as that in a similar pore with smooth walls.
- (i) The pressure tensor (specifically, the tangential pressure component in a slit pore) calculated from the mechanical route by using the Irving-Kirkwood definition is different from that by using the Harasima definition, due to the different physical meanings of the two definitions. However, integral of the tangential pressure and its average over the pore width are the same for both definitions.
- (j) The pressure tensor components calculated from the mechanical route (with the Irving-Kirkwood choice of the integral contour) agree well with those calculated from the thermodynamic route (with the Irving-Kirkwood-like definition of local energy).
- (k) The pressure tensor components can be averaged in various ways, providing different information. The choice of the ways of averaging depends on the purpose and applications. The local pressures, although not experimentally measurable at present, are also interesting because they contain the information of maximum values and the

information at any position (e.g., the region close to the pore walls, where the high-pressure phenomena usually occur), and they can be used to calculate any average pressures suitable for various applications.

10.2 Recommendations for Future Studies

There is still abundant possible work to do to further the studies of pressure enhancement effects in the micro-/nano-porous materials:

- (a) Phase diagrams (e.g., *PVT*-diagram) can be studied for fluids confined in the pores in terms of the in-pore pressure, rather than the bulk phase pressure that is in equilibrium with the pore phase, and the in-pore diagram can be compared with the diagram for the bulk fluid. This comparison can also provide some ideas to define an “effective” in-pore pressure specifically for the phase transition (since now, the in-pore pressure is only locally defined and is ambiguous in value depending on the choice of the integral contour in the equation or the energy assignment).
- (b) Besides grand canonical (or semi-grand canonical) ensemble, the isothermal-isobaric ensemble (N, P_{bulk}, T) simulation method can be used. By allowing a change in the volume, the deformation of the porous materials due to the in-pore normal pressure can be studied in a more realistic manner, and the bulk pressure can be determined directly. It could also overcome the simulation limitations for very dense system (water or

mercury as fluids), where the addition and deletion of adsorbate molecules are very ineffective.

- (c) Deformations in the spherical and cylindrical porous materials due to adsorption (although they are expected to be very small) can be studied by applying a reactive force field to the wall atoms. Moreover, more realistic models for the spherical and cylindrical pores can be constructed, such as hierarchical carbons, bundles of multi-walled carbon nanotubes, and SBA-15.
- (d) Mercury intrusion can be further studied by using (N, P_{bulk}, T) -ensemble (as mentioned in item (b)) and in silica cylindrical pores such as MCM-41 or SBA-15 which are more common materials for the Hg-intrusion experiments.[130]
- (e) The pressure of adsorbate in a more realistic pore model can be studied by applying more complex roughness of the pore wall. For example, besides geometrical roughness, an “energetic roughness” (energetic inhomogeneity) can be applied: the geometric roughness arises mainly from the functional groups, which have different sizes and energy well-depth from the base carbon atoms, and thus different LJ parameters representing these functional groups (more computationally efficient than adding actual functional groups) can be assigned to part of the model carbon atoms to construct a more physical pore wall in the geometric and energetic senses.

(f) It would be of great interest to study the influence of confinement and the in-pore pressure tensor components on chemical reactions, particularly reactions that are favored by high pressure, either through improved yield (reactions leading to a reduction in the number of moles) or improved kinetics or mechanism.

REFERENCES

- [1] K.E. Gubbins, Y.C. Liu, J.D. Moore, J.C. Palmer, The Role of Molecular Modeling in Confined Systems: Impact and Prospects, *Phys. Chem. Chem. Phys.*, 13 (2011) 58-85.
- [2] C. Alba-Simionesco, B. Coasne, G. Dosseh, G. Dudziak, K.E. Gubbins, R. Radhakrishnan, M. Sliwinska-Bartkowiak, Effects of Confinement on Freezing and Melting, *J. Phys. Condens. Matter*, 18 (2006) R15-R68.
- [3] Y. Fujiwara, K. Nishikawa, T. Iijima, K. Kaneko, Simulation of Small-Angle X-Ray-Scattering Behavior of Activated Carbon-Fibers Adsorbing Water, *J. Chem. Soc., Faraday Trans.*, 87 (1991) 2763-2768.
- [4] J. Klein, E. Kumacheva, Confinement-Induced Phase-Transitions in Simple Liquids, *Science*, 269 (1995) 816-819.
- [5] J. Klein, E. Kumacheva, Simple Liquids Confined to Molecularly Thin Layers. I. Confinement-Induced Liquid-to-Solid Phase Transitions, *J. Chem. Phys.*, 108 (1998) 6996-7009.
- [6] E. Kumacheva, J. Klein, Simple Liquids Confined to Molecularly Thin Layers. II. Shear and Frictional Behavior of Solidified Films, *J. Chem. Phys.*, 108 (1998) 7010-7022.
- [7] H.W. Hu, G.A. Carson, S. Granick, Relaxation-Time of Confined Liquids under Shear, *Phys. Rev. Lett.*, 66 (1991) 2758-2761.
- [8] S.T. Cui, C. McCabe, P.T. Cummings, H.D. Cochran, Molecular Dynamics Study of the Nano-Rheology of n-dodecane Confined between Planar Surfaces, *J. Chem. Phys.*, 118 (2003) 8941-8944.
- [9] D. Takaiwa, I. Hatano, K. Koga, H. Tanaka, Phase Diagram of Water in Carbon Nanotubes, *Proceedings of the National Academy of Sciences of the United States of America*, 105 (2008) 39-43.
- [10] K. Matsuda, T. Hibi, H. Kadowaki, H. Kataura, Y. Maniwa, Water Dynamics inside Single-Wall Carbon Nanotubes: NMR Observations, *Physical Review B*, 74 (2006) 073415.

- [11] M. Śliwinska-Bartkowiak, M. Jazdzewska, L.L. Huang, K.E. Gubbins, Melting Behavior of Water in Cylindrical Pores: Carbon Nanotubes and Silica Glasses, *Phys. Chem. Chem. Phys.*, 10 (2008) 4909-4919.
- [12] Water Structure and Behavior, <http://ergodic.ugr.es/termo/lecciones/water1.html>, in, London South Bank University.
- [13] K. Urita, Y. Shiga, T. Fujimori, T. Iiyama, Y. Hattori, H. Kanoh, T. Ohba, H. Tanaka, M. Yudasaka, S. Iijima, I. Moriguchi, F. Okino, M. Endo, K. Kaneko, Confinement in Carbon Nanospace-Induced Production of KI Nanocrystals of High-Pressure Phase, *Journal of American Chemical Society*, 133 (2011) 10344-10347.
- [14] K. Asami, T. Suzuki, T. Mori, High-Pressure Optical-Adsorption and X-Ray-Diffraction Studies in RBI and KI Approaching The Metallization Transition, *Physical Review B*, 28 (1983) 3529-3533.
- [15] S. Hashimoto, T. Fujimori, H. Tanaka, K. Urita, T. Ohba, H. Kanoh, T. Itoh, M. Asai, H. Sakamoto, S. Niimura, M. Endo, F. Rodriguez-Reinoso, K. Kaneko, Anomaly of CH₄ Molecular Assembly Confined in Single-Wall Carbon Nanohorn Spaces, *J. Am. Chem. Soc.*, 133 (2011) 2022-2024.
- [16] T. Iiyama, K. Nishikawa, T. Suzuki, T. Otowa, M. Hijiriyama, Y. Nojima, K. Kaneko, Molecular Assembly Structure of CCl₄ in Graphitic Nanospaces, *J. Phys. Chem. B*, 101 (1997) 3037-3042.
- [17] B. Coasne, C. Alba-Simionesco, F. Audonnet, G. Dosseh, K.E. Gubbins, Adsorption, Structure and Dynamics of Benzene in Ordered and Disordered Porous Carbons, *Phys. Chem. Chem. Phys.*, 13 (2011) 3748-3757.
- [18] B. Coasne, J. Czwartos, M. Sliwinska-Bartkowiak, K.E. Gubbins, Effect of Pressure on the Freezing of Pure Fluids and Mixtures Confined in Nanopores, *J. Phys. Chem. B*, 113 (2009) 13874-13881.
- [19] B. Coasne, J. Czwartos, M. Sliwinska-Bartkowiak, K.E. Gubbins, Freezing of Mixtures Confined in Silica Nanopores: Experiment and Molecular Simulation, *J. Chem. Phys.*, 133 (2010) 084701.
- [20] H. Kanda, M. Miyahara, Sublimation Phenomena of Lennard-Jones Fluids in Slit Nanopores, *J. Chem. Phys.*, 126 (2007) 054703.

- [21] H. Kanda, M. Miyahara, K. Higashitani, Solidification of Lennard-Jones Fluid in Cylindrical Nanopores and its Geometrical Hindrance Effect: A Monte Carlo Study, *Langmuir*, 16 (2000) 8529-8535.
- [22] H. Kanda, M. Miyahara, K. Higashitani, Triple Point of Lennard-Jones Fluid in Slit Nanopore: Solidification of Critical Condensate, *J. Chem. Phys.*, 120 (2004) 6173-6179.
- [23] K. Kaneko, N. Fukuzaki, K. Kakei, T. Suzuki, S. Ozeki, Enhancement of NO Dimerization by Micropore Fields of Activated Carbon-Fibers, *Langmuir*, 5 (1989) 960-965.
- [24] O. Byl, P. Kondratyuk, J.T. Yates, Adsorption and Dimerization of NO inside Single-Walled Carbon Nanotubes - An Infrared Spectroscopic Study, *J. Phys. Chem. B*, 107 (2003) 4277-4279.
- [25] C.H. Turner, J.K. Johnson, K.E. Gubbins, Effect of Confinement on Chemical Reaction Equilibria: The Reactions $2\text{NO} \leftrightarrow (\text{NO})_2$ and $\text{N}_2 + 3\text{H}_2 \leftrightarrow 2\text{NH}_3$ in Carbon Micropores, *J. Chem. Phys.*, 114 (2001) 1851-1859.
- [26] J. Imai, M. Souma, S. Ozeki, T. Suzuki, K. Kaneko, Reaction of Dimerized NO_x ($x = 1$ OR 2) with SO_2 in a Restricted Slit-Shaped Micropore Space, *J. Phys. Chem.*, 95 (1991) 9955-9960.
- [27] S.F. Agnew, B.I. Swanson, L.H. Jones, R.L. Mills, Disproportionation of Nitric-Oxide at High-Pressure, *J. Phys. Chem.*, 89 (1985) 1678-1682.
- [28] T.P. Melia, Decomposition of Nitric Oxide at Elevated Pressures, *Journal of Inorganic & Nuclear Chemistry*, 27 (1965) 95.
- [29] T. Yamamoto, D.A. Tryk, K. Hashimoto, A. Fujishima, M. Okawa, Electrochemical Reduction of CO_2 in the Micropores of Activated Carbon Fibers, *Journal of the Electrochemical Society*, 147 (2000) 3393-3400.
- [30] M. Azuma, K. Hashimoto, M. Hiramoto, M. Watanabe, T. Sakata, Carbon-Dioxide Reduction at Low-Temperature on Various Metal-Electrodes, *Journal of Electroanalytical Chemistry*, 260 (1989) 441-445.
- [31] M. Azuma, K. Hashimoto, M. Hiramoto, M. Watanabe, T. Sakata, Electrochemical Reduction of Carbon-Dioxide on Various Metal-Electrodes in Low-Temperature

Aqueous KHCO_3 Media, *Journal of the Electrochemical Society*, 137 (1990) 1772-1778.

- [32] H. Noda, S. Ikeda, Y. Oda, K. Imai, M. Maeda, K. Ito, Electrochemical Reduction of Carbon-Dioxide at Various Metal-Electrodes in Aqueous Potassium Hydrogen Carbonate Solution, *Bulletin of the Chemical Society of Japan*, 63 (1990) 2459-2462.
- [33] K. Hara, A. Kudo, T. Sakata, Electrochemical Reduction of High-Pressure Carbon-Dioxide on Fe Electrode at Large Current-Density, *Journal of Electroanalytical Chemistry*, 386 (1995) 257-260.
- [34] K. Hara, A. Kudo, T. Sakata, M. Watanabe, High-Efficiency Electrochemical Reduction of Carbon-Dioxide under High-Pressure on a Gas-Diffusion Electrode Containing Pt Catalysts, *Journal of the Electrochemical Society*, 142 (1995) L57-L59.
- [35] K. Hara, A. Tsuneto, A. Kudo, T. Sakata, Electrochemical Reduction of CO_2 on a Cu Electrode under High-Pressure - Factors that Determine the Product Selectivity, *Journal of the Electrochemical Society*, 141 (1994) 2097-2103.
- [36] Y. Nishi, T. Suzuki, K. Kaneko, Ambient Temperature Reduction of NO to N_2 in Ru-Tailored Carbon Subnanospace, *J. Phys. Chem. B*, 101 (1997) 1938-1939.
- [37] J.L. Parker, H.K. Christenson, B.W. Ninham, Device for Measuring the Force and Separation between 2 Surfaces down to Molecular Separations, *Review of Scientific Instruments*, 60 (1989) 3135-3138.
- [38] H.K. Christenson, Phase Behavior in Confinement Studied with a Surface Force Apparatus, *J. Dispersion Sci. Technol.*, 27 (2006) 617-624.
- [39] P.B. Balbuena, D. Berry, K.E. Gubbins, Solvation Pressures for Simple Fluids in Micropores, *J. Phys. Chem.*, 97 (1993) 937-943.
- [40] E. Perret, K. Nygard, D.K. Satapathy, T.E. Balmer, O. Bunk, M. Heuberger, J.F. van der Veen, Molecular Liquid under Nanometre Confinement: Density Profiles Underlying Oscillatory Forces, *Journal of Physics-Condensed Matter*, 22 (2010) 235102.
- [41] J.N. Israelachvili, G.E. Adams, Measurement of Forces between 2 Mica Surfaces in Aqueous Electrolyte Solutions in Range 0 - 100 nm, *Journal of the Chemical Society-Faraday Transactions I*, 74 (1978) 975.

- [42] U. Raviv, P. Laurat, J. Klein, Time Dependence of Forces between Mica Surfaces in Water and its Relation to the Release of Surface Ions, *J. Chem. Phys.*, 116 (2002) 5167-5172.
- [43] K. Kaneko, T. Suzuki, Y. Fujiwara, K. Nishikawa, Dynamic Micropore Structures of Micrographitic Carbons during Adsorption, *Characterization of Porous Solids II*, pp. 389-398, 1991.
- [44] J.W. McBain, J.L. Porter, R.F. Sessions, The Nature of the Sorption of Water by Charcoal, *J. Am. Chem. Soc.*, 55 (1933) 2294-2304.
- [45] J.R. Dacey, M.J.B. Evans, Volume Changes in Saran Charcoal Caused by Adsorption of Water, Methanol and Benzene Vapours, *Carbon*, 9 (1971) 579.
- [46] T. Suzuki, K. Kaneko, Structural Change of Activated Carbon Fibers with Desorption by InSitu X-Ray Diffraction, *Carbon*, 26 (1988) 744-745.
- [47] K. Kaneko, Y. Fujiwara, K. Nishikawa, The Micropore Swelling of Activated Carbon-Fibers with Water-Adsorption Studied by Use of InSitu Small-Angle X-Ray-Scattering, *J. Colloid Interface Sci.*, 127 (1989) 298-299.
- [48] C. Mellot-Draznieks, C. Serre, S. Surble, N. Audebrand, G. Ferey, Very Large Swelling in Hybrid Frameworks: A Combined Computational and Powder Diffraction study, *J. Am. Chem. Soc.*, 127 (2005) 16273-16278.
- [49] T. Loiseau, C. Serre, C. Huguenard, G. Fink, F. Taulelle, M. Henry, T. Bataille, G. Ferey, A Rationale for the Large Breathing of the Porous Aluminum Terephthalate (MIL-53) upon Hydration, *Chem.-Eur. J.*, 10 (2004) 1373-1382.
- [50] C. Serre, S. Bourrelly, A. Vimont, N.A. Ramsahye, G. Maurin, P.L. Llewellyn, M. Daturi, Y. Filinchuk, O. Leynaud, P. Barnes, G. Ferey, An Explanation for the Very Large Breathing Effect of a Metal-Organic Framework during CO₂ Adsorption, *Adv. Mater.*, 19 (2007) 2246.
- [51] F. Millange, C. Serre, G. Ferey, Synthesis, Structure Determination and Properties of MIL-53as and MIL-53ht: The First Cr-III Hybrid Inorganic-Organic Microporous Solids: Cr-III(OH).{O₂C-C₆H₄-CO₂}.{HO₂C-C₆H₄-CO₂H}_x, *Chem. Commun.*, (2002) 822-823.

- [52] A.V. Neimark, F.X. Coudert, A. Boutin, A.H. Fuchs, Stress-Based Model for the Breathing of Metal-Organic Frameworks, *J. Phys. Chem. Lett.*, 1 (2010) 445-449.
- [53] G. Gunther, J. Prass, O. Paris, M. Schoen, Novel Insights into Nanopore Deformation Caused by Capillary Condensation, *Phys. Rev. Lett.*, 101 (2008) 086104.
- [54] P. Kowalczyk, S. Furmaniak, P.A. Gauden, A.P. Terzyk, Carbon Dioxide Adsorption-Induced Deformation of Microporous Carbons, *Journal of Physical Chemistry C*, 114 (2010) 5126-5133.
- [55] D.D. Do, D. Nicholson, H.D. Do, Effects of Adsorbent Deformation on the Adsorption of Gases in Slitlike Graphitic Pores: A computer Simulation Study, *Journal of Physical Chemistry C*, 112 (2008) 14075-14089.
- [56] J.P.R.B. Walton, D.J. Tildesley, J.S. Rowlinson, J.R. Henderson, The Pressure Tensor at the Planar Surface of a Liquid, *Mol. Phys.*, 48 (1983) 1357-1368.
- [57] D.J. Lee, M.M. Telo Da gama, K.E. Gubbins, The Vapor-Liquid Interface for a Lennard-Jones Model of Argon Krypton Mixtures, *Mol. Phys.*, 53 (1984) 1113-1130.
- [58] Y.J. Lei, Y.S. Leng, Force Oscillation and Phase Transition of Simple Fluids under Confinement, *Phys. Rev. E.*, 82 (2010) 040501.
- [59] Y. Hamada, K. Koga, H. Tanaka, Phase Behavior and Fluid-Solid Surface Tension of Argon in Slit Pores and Carbon Nanotubes, *Physica A-Statistical Mechanics and Its Applications*, 388 (2009) 2289-2298.
- [60] K. Van Workum, J.J. de Pablo, Local Elastic Constants in Thin Films of An fcc Crystal, *Phys. Rev. E.*, 67 (2003) 031601.
- [61] R.J.M. Pellenq, J.M. Caillol, A. Delville, Electrostatic Attraction between Two Charged Surfaces: A (N,V,T) Monte Carlo Simulation, *J. Phys. Chem. B*, 101 (1997) 8584-8594.
- [62] N. Giovambattista, P.J. Rossky, P.G. Debenedetti, Phase Transitions Induced by Nanoconfinement in Liquid Water, *Phys. Rev. Lett.*, 102 (2009) 050603.
- [63] C.G. Gray, K.E. Gubbins, C.G. Joslin, *Theory of Molecular Fluids. 2. Applications*, Sec. 8.3, Oxford University Press, Oxford, 2011.

- [64] J.R. Henderson, Potential-Distribution Theorem Mechanical Stability and Kirkwood Integral-Equation, *Mol. Phys.*, 48 (1983) 715-717.
- [65] P. Schofield, J.R. Henderson, Statistical-Mechanics of Inhomogeneous Fluids, *Proc. R. Soc. Lond.*, 379 (1982) 231-246.
- [66] J.H. Irving, J.G. Kirkwood, The Statistical Mechanical Theory of Transport Processes .4. The Equations of Hydrodynamics, *J. Chem. Phys.*, 18 (1950) 817-829.
- [67] G.J. Tjatjopoulos, J.A. Mann, The Pressure Tensor of an Inhomogeneous Fluid - Transformation of the Irving-Kirkwood Formula, *Mol. Phys.*, 60 (1987) 1425-1432.
- [68] J.D. Jackson, *Classical Electrodynamics*, John Wiley, 1975.
- [69] A. Harasima, Molecular Theory of Surface Tension, *Adv. Chem. Phys.*, 1 (1958) 203-237.
- [70] E.M. Blokhuis, D. Bedeaux, Pressure Tensor of a Spherical Interface, *J. Chem. Phys.*, 97 (1992) 3576-3586.
- [71] B. Hafskjold, T. Ikeshoji, Microscopic Pressure Tensor for Hard-sphere Fluids, *Phys. Rev. E.*, 66 (2002) 011203.
- [72] A. Ghoufi, F. Goujon, V. Lachet, P. Malfreyt, Surface Tension of Water and Acid Gases from Monte Carlo Simulations, *J. Chem. Phys.*, 128 (2008) 154716.
- [73] J.G. Sampayo, A. Malijevsky, E.A. Muller, E. de Miguel, G. Jackson, Communications: Evidence for the Role of Fluctuations in the Thermodynamics of Nanoscale Drops and the Implications in Computations of the Surface Tension, *J. Chem. Phys.*, 132 (2010) 141101.
- [74] E. de Miguel, G. Jackson, Detailed Examination of the Calculation of the Pressure in Simulations of Systems with Discontinuous Interactions from the Mechanical and Thermodynamic Perspectives, *Mol. Phys.*, 104 (2006) 3717-3734.
- [75] J.S. Rowlinson, B. Widom, *Molecular Theory of Capillarity*, Clarendon Press, Oxford, 1982.
- [76] A.J.C. Ladd, L.V. Woodcock, Interfacial and Coexistence Properties of Lennard-Jones System at Triple Point, *Mol. Phys.*, 36 (1978) 611-619.

- [77] E.B. Tadmor, R.E. Miller, *Modeling Materials: Continuum, Atomistic and Multiscale Techniques*, Sec. 8.2.5, Cambridge University Press, Cambridge, 2011.
- [78] C.G. Gray, K.E. Gubbins, C.G. Joslin, *Theory of Molecular Fluids. 2. Applications*, Sec. 8.2.5, Oxford University Press, Oxford, 2011.
- [79] C.K. Hall, *Thermo*, Chapter 10 Introduction to Statistical Thermodynamics, Unpublished Textbook.
- [80] A.R. Leach, *Molecular Modeling: Principles and Applications*, Chapter 7, Longman, Harlow, 1996.
- [81] M.P. Allen, D.J. Tildesley, *Computer Simulation of Liquids*, Oxford Science Publications, Bristol, 1987.
- [82] R.F. Cracknell, D. Nicholson, N. Quirke, A Grand-Canonical Monte-Carlo Study of Lennard-Jones Mixtures in Slit Shaped Pores, *Mol. Phys.*, 80 (1993) 885-897.
- [83] J.J. Nicolas, K.E. Gubbins, W.B. Streett, D.J. Tildesley, Equation of State for the Lennard-Jones Fluid, *Mol. Phys.*, 37 (1979) 1429-1454.
- [84] J.K. Johnson, J.A. Zollweg, K.E. Gubbins, The Lennard-Jones Equation of State Revisited, *Mol. Phys.*, 78 (1993) 591-618.
- [85] G. Gunther, M. Schoen, Sorption Strain as a Packing Phenomenon, *Phys. Chem. Chem. Phys.*, 11 (2009) 9082-9092.
- [86] J.C. Palmer, J.D. Moore, J.K. Brennan, K.E. Gubbins, Simulating Local Adsorption Isotherms in Structurally Complex Porous Materials: A Direct Assessment of the Slit Pore Model, *J. Phys. Chem. Lett.*, 2 (2011) 165-169.
- [87] P.I. Ravikovitch, A. Vishnyakov, R. Russo, A.V. Neimark, Unified Approach to Pore Size Characterization of Microporous Carbonaceous Materials from N₂, Ar, and CO₂ Adsorption Isotherms, *Langmuir*, 16 (2000) 2311-2320.
- [88] L.D. Gelb, K.E. Gubbins, R. Radhakrishnan, M. Sliwinska-Bartkowiak, Phase Separation in Confined Systems, *Rep. Prog. Phys.*, 62 (1999) 1573-1659.

- [89] Q. Cai, A. Buts, N.A. Seaton, M.J. Biggs, A Pore Network Model for Diffusion in Nanoporous Carbons: Validation by Molecular Dynamics Simulation, *Chem. Eng. Sci.*, 63 (2008) 3319-3327.
- [90] C.H. Turner, J.K. Brennan, M. Lisal, W.R. Smith, J.K. Johnson, K.E. Gubbins, Simulation of Chemical Reaction Equilibria by the Reaction Ensemble Monte Carlo Method: A Review, *Mol. Simul.*, 34 (2008) 119-146.
- [91] K. Yang, X.C. Lu, Y.Z. Lin, A.V. Neimark, Deformation of Coal Induced by Methane Adsorption at Geological Conditions, *Energ. Fuel*, 24 (2010) 5955-5964.
- [92] D.D. Do, H.D. Do, Effects of Potential Models on the Adsorption of Ethane and Ethylene on Graphitized Thermal Carbon Black. Study of Two-Dimensional Critical Temperature and Isothermic Heat versus Loading, *Langmuir*, 20 (2004) 10889-10899.
- [93] D.D. Do, H.D. Do, Evaluation of 1-Site and 5-Site Models of Methane on its Adsorption on Graphite and in Graphitic Slit Pores, *J. Phys. Chem. B*, 109 (2005) 19288-19295.
- [94] J.A. Barker, R.A. Fisher, R.O. Watts, Liquid Argon - Monte Carlo and Molecular Dynamics Calculations, *Mol. Phys.*, 21 (1971) 657.
- [95] C.R. Fuselier, J.C. Raich, N.S. Gillis, Equilibrium-Configurations of Commensurate Adsorbed Monolayers - Argon on Graphite, *Surf. Sci.*, 92 (1980) 667-680.
- [96] M.J. McGrath, J.N. Ghogomu, N.T. Tsona, J.I. Siepmann, B. Chen, I. Napari, H. Vehkamäki, Vapor-Liquid Nucleation of Argon: Exploration of Various Intermolecular Potentials, *J. Chem. Phys.*, 133 (2010) 084106.
- [97] W.A. Steele, Physical Interaction of Gases with Crystalline Solids .1. Gas-Solid Energies and Properties of Isolated Adsorbed Atoms, *Surf. Sci.*, 36 (1973) 317-352.
- [98] Y. Long, J.C. Palmer, B. Coasne, M. Śliwinska-Bartkowiak, K.E. Gubbins, Pressure Enhancement in Carbon Nanopores: A Major Confinement Effect, *Phys. Chem. Chem. Phys.*, 13 (2011) 17163-17170.
- [99] S.J. Stuart, A.B. Tutein, J.A. Harrison, A Reactive Potential for Hydrocarbons with Intermolecular Interactions, *J. Chem. Phys.*, 112 (2000) 6472-6486.
- [100] J.D. Weeks, D. Chandler, H.C. Andersen, Role of Repulsive Forces in Determining Equilibrium Structure of Simple Liquids, *J. Chem. Phys.*, 54 (1971) 5237.

- [101] J.R. Henderson, F. Van Swol, On the Interface between a Fluid and a Planar Wall - Theory and Simulations of a Hard-Sphere Fluid at a Hard-Wall, *Mol. Phys.*, 51 (1984) 991-1010.
- [102] G.L. Aranovich, M.D. Donohue, Adsorption Compression: An Important New Aspect of Adsorption Behavior and Capillarity, *Langmuir*, 19 (2003) 2722-2735.
- [103] G.L. Aranovich, M.D. Donohue, The Role of Adsorption Compression in Nanocapillarity, *J. Colloid Interface Sci.*, 292 (2005) 202-209.
- [104] T.E. Wetzel, J.S. Erickson, P.S. Donohue, C.L. Charniak, G.L. Aranovich, M.D. Donohue, Monte Carlo Simulations on the Effect of Substrate Geometry on Adsorption and Compression, *J. Chem. Phys.*, 120 (2004) 11765-11774.
- [105] J. Jagiello, J.P. Olivier, A Simple Two-Dimensional NLDFT Model of Gas Adsorption in Finite Carbon Pores. Application to Pore Structure Analysis, *Journal of Physical Chemistry C*, 113 (2009) 19382-19385.
- [106] M. Miyahara, H. Kanda, M. Shibao, K. Higashitani, Solid-Liquid Phase Transition of Lennard-Jones Fluid in Slit Pores under Tensile Condition, *J. Chem. Phys.*, 112 (2000) 9909-9916.
- [107] T. Young, An Essay on the Cohesion of Fluids, *Philosophical Transactions. Royal Society London*, 95 (1805) 65-87.
- [108] C.G. Gray, K.E. Gubbins, C.G. Joslin, *Theory of Molecular Fluids. 2. Applications*, pp. 733-734, 914-916, Oxford University Press, Oxford, 2011.
- [109] R. Radhakrishnan, K.E. Gubbins, M. Sliwinska-Bartkowiak, Effect of the Fluid-Wall Interaction on Freezing of Confined Fluids: Toward the Development of a Global Phase Diagram, *J. Chem. Phys.*, 112 (2000) 11048-11057.
- [110] K.G. Ayappa, R.K. Mishra, Freezing of Fluids Confined between Mica Surfaces, *J. Phys. Chem. B*, 111 (2007) 14299-14310.
- [111] J.Y. Chen, A. Kutana, C.P. Collier, K.P. Giapis, Electrowetting in Carbon Nanotubes, *Science*, 310 (2005) 1480-1483.
- [112] R. Radhakrishnan, K.E. Gubbins, M. Sliwinska-Bartkowiak, Global Phase Diagrams for Freezing in Porous Media, *J. Chem. Phys.*, 116 (2002) 1147-1155.

- [113] T.M. Reed, K.E. Gubbins, *Applied Statistical Mechanics*, p. 48, McGraw-Hill, 1973.
- [114] F. Porcheron, M. Thommes, R. Ahmad, P.A. Monson, Mercury Porosimetry in Mesoporous Glasses: A Comparison of Experiments with Results from a Molecular Model, *Langmuir*, 23 (2007) 3372-3380.
- [115] B. Coasne, A. Galarneau, F. Di Renzo, R.J.M. Pellenq, Intrusion and Retraction of Fluids in Nanopores: Effect of Morphological Heterogeneity, *Journal of Physical Chemistry C*, 113 (2009) 1953-1962.
- [116] F. Porcheron, P.A. Monson, Modeling Mercury Porosimetry Using Statistical Mechanics, *Langmuir*, 20 (2004) 6482-6489.
- [117] H.J. Woo, F. Porcheron, P.A. Monson, Modeling Desorption of Fluids from Disordered Mesoporous Materials, *Langmuir*, 20 (2004) 4743-4747.
- [118] N. Hamada, S.-i. Sawada, A. Oshiyama, New One-Dimensional Conductors: Graphitic Microtubules, *Phys. Rev. Lett.*, 68 (1992) 1579-1581.
- [119] D.D. Do, L. Herrera, C.Y. Fan, A. Wongkoblap, D. Nicholson, The Role of Accessibility in the Characterization of Porous Solids and their Adsorption Properties, *Adsorption*, 16 (2010) 3-15.
- [120] M. Śliwiska-Bartkowiak, H. Drozdowski, M. Kempinski, M. Jazdzewska, Y. Long, J.C. Palmer, K.E. Gubbins, Structural Analysis of Water and Carbon Tetrachloride Adsorbed in Activated Carbon Fibres, *Phys. Chem. Chem. Phys.*, 14 (2012) 7145-7153.
- [121] H. Arstila, O.V. Vasilev, M. Kulmala, The Role of the Attractive Potential of a Droplet in Unary and Binary Steady State Nucleation, *J. Chem. Phys.*, 107 (1997) 544-549.
- [122] H.J.C. Berendsen, J.R. Grigera, T.P. Straatsma, The Missing Term in Effective Pair Potentials, *J. Phys. Chem.*, 91 (1987) 6269-6271.
- [123] T.M. Miller, B. Bederson, *Advances in Atomic and Molecular Physics*, p. 1, Academic, London, 1977.
- [124] L. Perera, U. Essmann, M.L. Berkowitz, Effect of the Treatment of Long-Range Forces on the Dynamics of Ions in Aqueous-Solutions, *J. Chem. Phys.*, 102 (1995) 450-456.

- [125] R.J.M. Pellenq, D. Nicholson, Intermolecular Potential Function for the Physical Adsorption of Rare-Gases in Silicalite, *J. Phys. Chem.*, 98 (1994) 13339-13349.
- [126] R.J.M. Pellenq, P.E. Levitz, Capillary Condensation in a Disordered Mesoporous Medium: A Grand Canonical Monte Carlo Study, *Mol. Phys.*, 100 (2002) 2059-2077.
- [127] J. Jagiello, J.P. Olivier, Gas Adsorption between Curved Graphene Pore Walls of Porous Carbons, in: E. Maginn (Ed.) *Foundations of Molecular Modeling and Simulation*, Mt. Hood, OR, USA, 2012.
- [128] L.L. Huang, Computational Study of Toxic Gas Removal by Reactive Adsorption, Ph.D. Dissertation, Ch5, in: *Chemical and Biomolecular Engineering*, North Carolina State University, Raleigh, 2012.
- [129] L.L. Huang, DFT Results of Functionalized Graphene, Private Communication, in: Y. Long (Ed.), 2012.
- [130] W.L. Jorgensen, J. Chandrasekhar, J.D. Madura, R.W. Impey, M.L. Klein, Comparison of Simple Potential Functions for Simulating Liquid Water, *J. Chem. Phys.*, 79 (1983) 926-935.

APPENDICES

Appendix A

Derivations for Hydrostatic Equilibrium in Slit, Cylindrical and Spherical Pores

In the absence of external fields, the condition for the hydrostatic equilibrium is (recall Eqn. (3.3) or see proof in [C.G. Gray, K.E. Gubbins, C.G. Joslin, Theory of Molecular Fluids. 2. Applications, pp. 929-932, Oxford University Press, Oxford, 2011]):

$$\nabla \cdot \mathbf{P}(\mathbf{r}) = 0, \quad (\text{A.1})$$

which comes from the requirement that at equilibrium there cannot be net flow of momentum. $\mathbf{P}(\mathbf{r})$ is a second-order tensor with elements $P_{\alpha\beta}(\mathbf{r})$ that give the force per unit area in the β -direction acting on a surface element normal to the α -direction at point \mathbf{r} . When the system is at equilibrium (no stresses) the off-diagonal elements will be zero, so there will then be three non-zero elements (P_{xx} , P_{yy} and P_{zz} for Cartesian coordinate system). The condition of hydrostatic equilibrium usually provides a relation between some of these components, depending on the geometry of the system.

A.1 Condition of Hydrostatic Equilibrium for a Planar Interface (in a Slit Pore)

We consider a planar surface or slit pore with the surface lying in the xy -plane and with the z -axis normal to the surface. The system has axial symmetry about the z -axis and translational symmetry in the xy -plane, so that $P_{xx} = P_{yy} = P_T$, the tangential pressure (parallel to the surface) and $P_{zz} = P_N$, the pressure normal to the wall. Eqn. (A.1) becomes:

$$\nabla \cdot \mathbf{P} = \left[\mathbf{e}_x \frac{\partial}{\partial x} + \mathbf{e}_y \frac{\partial}{\partial y} + \mathbf{e}_z \frac{\partial}{\partial z} \right] \cdot \left[\mathbf{e}_x \mathbf{e}_x P_{xx} + \mathbf{e}_y \mathbf{e}_y P_{yy} + \mathbf{e}_z \mathbf{e}_z P_{zz} \right] = 0. \quad (\text{A.2})$$

Recalling that

$$[\mathbf{e}_i \cdot \mathbf{e}_j \mathbf{e}_k] = \delta_{ij} \mathbf{e}_k, \quad (\text{A.3})$$

Eqn. (A.2) gives

$$\nabla \cdot \mathbf{P} = \left[\mathbf{e}_x \frac{\partial P_{xx}}{\partial x} + \mathbf{e}_y \frac{\partial P_{yy}}{\partial y} + \mathbf{e}_z \frac{\partial P_{zz}}{\partial z} \right] = 0. \quad (\text{A.4})$$

Thus, each of these three terms in Eqn. (A.4) must vanish, i.e.

$$\begin{aligned} \frac{\partial P_{xx}}{\partial x} = \frac{\partial P_{yy}}{\partial y} = \frac{\partial P_T}{\partial x} = \frac{\partial P_T}{\partial y} = 0 \\ \frac{\partial P_{zz}}{\partial z} = \frac{\partial P_N}{\partial z} = 0 \end{aligned} \quad (\text{A.5})$$

From Eqn. (A.5) P_T will be independent of x and y (but will depend on z), while P_N will be independent of z . P_N will also be independent of x and y due to the symmetry of the system, assumed to be infinitely large in the x - and y -dimensions, i.e., P_N will be a constant in pore for the planar case. For the confined fluids, P_N will not be simply equal to the pressure of the bulk fluid in equilibrium with the pore phase due to the intermolecular forces from the pore walls.

A.2 Condition of Hydrostatic Equilibrium for A Cylindrical Interface

Any point A in the cylinder is given in terms of $A(\rho, \phi, z)$ coordinates, where z is the direction along the axis of the cylinder and ρ is the radial distance from the center of the pore (Figure 3.1b). The cylindrical coordinates are related to the Cartesian coordinates as follows:

$$\begin{cases} x = \rho \cos \varphi \\ y = \rho \sin \varphi \\ z = z \end{cases} \quad (\text{A.6})$$

For the cylindrical geometry, Eqn. (A.1) gives

$$\nabla \cdot \mathbf{P} = \left[\mathbf{e}_\rho \frac{\partial}{\partial \rho} + \mathbf{e}_\varphi \frac{1}{\rho} \frac{\partial}{\partial \varphi} + \mathbf{e}_z \frac{\partial}{\partial z} \right] \cdot \left[\mathbf{e}_\rho \mathbf{e}_\rho P_{\rho\rho} + \mathbf{e}_\varphi \mathbf{e}_\varphi P_{\varphi\varphi} + \mathbf{e}_z \mathbf{e}_z P_{zz} \right]. \quad (\text{A.7})$$

There are 9 terms if Eqn. (A.7) is expanded. To evaluate these 9 terms, we recall Eqn. (A.3)

and

$$\begin{cases} \mathbf{e}_\rho = (\cos \varphi) \mathbf{e}_x + (\sin \varphi) \mathbf{e}_y + (0) \mathbf{e}_z \\ \mathbf{e}_\varphi = (-\sin \varphi) \mathbf{e}_x + (\cos \varphi) \mathbf{e}_y + (0) \mathbf{e}_z \\ \mathbf{e}_z = (0) \mathbf{e}_x + (0) \mathbf{e}_y + (1) \mathbf{e}_z = \mathbf{e}_z \end{cases} \quad (\text{A.8})$$

and the following relationships (easy to derived from Eqn. (A.8)):

$$\begin{aligned} \frac{\partial}{\partial \rho} \mathbf{e}_\rho &= 0; & \frac{\partial}{\partial \rho} \mathbf{e}_\varphi &= 0; & \frac{\partial}{\partial \rho} \mathbf{e}_z &= 0 \\ \frac{\partial}{\partial \varphi} \mathbf{e}_\rho &= (-\sin \varphi) \mathbf{e}_x + (\cos \varphi) \mathbf{e}_y = \mathbf{e}_\varphi; & \frac{\partial}{\partial \varphi} \mathbf{e}_\varphi &= -\mathbf{e}_\rho; & \frac{\partial}{\partial \varphi} \mathbf{e}_z &= 0. \\ \frac{\partial}{\partial z} \mathbf{e}_\rho &= 0; & \frac{\partial}{\partial z} \mathbf{e}_\varphi &= 0; & \frac{\partial}{\partial z} \mathbf{e}_z &= 0; \end{aligned} \quad (\text{A.9})$$

By using Eqns. (A.3) (A.8) and (A.9), we can now write out the 9 terms resulting from Eqn.

(A.7) one by one as follows:

$$(1) \left[\mathbf{e}_\rho \frac{\partial}{\partial \rho} \cdot \mathbf{e}_\rho \mathbf{e}_\rho P_{\rho\rho} \right] = [\mathbf{e}_\rho \cdot \mathbf{e}_\rho \mathbf{e}_\rho] \frac{\partial}{\partial \rho} P_{\rho\rho} = \frac{\partial P_{\rho\rho}}{\partial \rho} \mathbf{e}_\rho,$$

$$(2) \left[\mathbf{e}_\rho \frac{\partial}{\partial \rho} \cdot \mathbf{e}_\varphi \mathbf{e}_\varphi P_{\varphi\varphi} \right] = [\mathbf{e}_\rho \cdot \mathbf{e}_\varphi \mathbf{e}_\varphi] \frac{\partial}{\partial \rho} P_{\varphi\varphi} = 0,$$

$$(3) \left[\mathbf{e}_\rho \frac{\partial}{\partial \rho} \cdot \mathbf{e}_z \mathbf{e}_z P_{zz} \right] = [\mathbf{e}_\rho \cdot \mathbf{e}_z \mathbf{e}_z] \frac{\partial}{\partial \rho} P_{zz} = 0,$$

$$(4) \left[\mathbf{e}_\varphi \frac{1}{\rho} \frac{\partial}{\partial \varphi} \cdot \mathbf{e}_\rho \mathbf{e}_\rho P_{\rho\rho} \right] = \frac{P_{\rho\rho}}{\rho} \left[\mathbf{e}_\varphi \frac{\partial}{\partial \varphi} \cdot (\mathbf{e}_\rho \mathbf{e}_\rho) \right] = \frac{P_{\rho\rho}}{\rho} \left[\mathbf{e}_\varphi \cdot \frac{\partial}{\partial \varphi} (\mathbf{e}_\rho \mathbf{e}_\rho) \right]$$

$$= \frac{P_{\rho\rho}}{\rho} \left[\mathbf{e}_\varphi \cdot \frac{\partial \mathbf{e}_\rho}{\partial \varphi} \mathbf{e}_\rho + \mathbf{e}_\varphi \cdot \mathbf{e}_\rho \frac{\partial \mathbf{e}_\rho}{\partial \varphi} \right] = \frac{P_{\rho\rho}}{\rho} [\mathbf{e}_\varphi \cdot \mathbf{e}_\varphi \mathbf{e}_\rho + \mathbf{e}_\varphi \cdot \mathbf{e}_\rho \mathbf{e}_\varphi],$$

$$= \frac{P_{\rho\rho}}{\rho} [\mathbf{e}_\rho + 0] = \frac{P_{\rho\rho}}{\rho} \mathbf{e}_\rho$$

$$(5) \left[\mathbf{e}_\varphi \frac{1}{\rho} \frac{\partial}{\partial \varphi} \cdot \mathbf{e}_\varphi \mathbf{e}_\varphi P_{\varphi\varphi} \right] = \frac{1}{\rho} \left[\mathbf{e}_\varphi \cdot \frac{\partial}{\partial \varphi} (\mathbf{e}_\varphi \mathbf{e}_\varphi P_{\varphi\varphi}) \right] = \frac{1}{\rho} \left[\mathbf{e}_\varphi \cdot \frac{\partial}{\partial \varphi} (\mathbf{e}_\varphi \mathbf{e}_\varphi P_{\varphi\varphi}) \right]$$

$$= \frac{1}{\rho} \left[\mathbf{e}_\varphi \cdot \frac{\partial \mathbf{e}_\varphi}{\partial \varphi} \mathbf{e}_\varphi + \mathbf{e}_\varphi \cdot \mathbf{e}_\varphi \frac{\partial (\mathbf{e}_\varphi P_{\varphi\varphi})}{\partial \varphi} \right] = \frac{1}{\rho} \left[\mathbf{e}_\varphi \cdot (-\mathbf{e}_\rho) \mathbf{e}_\varphi + \mathbf{e}_\varphi \cdot \mathbf{e}_\varphi \frac{\partial (\mathbf{e}_\varphi P_{\varphi\varphi})}{\partial \varphi} \right]$$

$$= \frac{1}{\rho} \left[0 + \mathbf{e}_\varphi \cdot \mathbf{e}_\varphi \left(\mathbf{e}_\varphi \frac{\partial P_{\varphi\varphi}}{\partial \varphi} + P_{\varphi\varphi} \frac{\partial \mathbf{e}_\varphi}{\partial \varphi} \right) \right]$$

$$= \frac{1}{\rho} \mathbf{e}_\varphi \cdot \left(\mathbf{e}_\varphi \mathbf{e}_\varphi \frac{\partial P_{\varphi\varphi}}{\partial \varphi} \right) + \frac{P_{\varphi\varphi}}{\rho} \mathbf{e}_\varphi \cdot \mathbf{e}_\varphi (-\mathbf{e}_\rho) = \frac{1}{\rho} \frac{\partial P_{\varphi\varphi}}{\partial \varphi} \mathbf{e}_\varphi - \frac{P_{\varphi\varphi}}{\rho} \mathbf{e}_\rho$$

$$(6) \left[\mathbf{e}_\varphi \frac{1}{\rho} \frac{\partial}{\partial \varphi} \cdot \mathbf{e}_z \mathbf{e}_z P_{zz} \right] = [\mathbf{e}_\varphi \cdot \mathbf{e}_z \mathbf{e}_z] \frac{1}{\rho} \frac{\partial}{\partial \varphi} P_{zz} = 0,$$

$$(7) \left[\mathbf{e}_z \frac{\partial}{\partial z} \cdot \mathbf{e}_\rho \mathbf{e}_\rho P_{\rho\rho} \right] = [\mathbf{e}_z \cdot \mathbf{e}_\rho \mathbf{e}_\rho] \frac{\partial}{\partial z} P_{\rho\rho} = 0,$$

$$(8) \left[\mathbf{e}_z \frac{\partial}{\partial z} \cdot \mathbf{e}_\varphi \mathbf{e}_\varphi P_{\varphi\varphi} \right] = [\mathbf{e}_z \cdot \mathbf{e}_\varphi \mathbf{e}_\varphi] \frac{\partial}{\partial z} P_{\varphi\varphi} = 0,$$

$$(9) \left[\mathbf{e}_z \frac{\partial}{\partial z} \cdot \mathbf{e}_z \mathbf{e}_z P_{zz} \right] = [\mathbf{e}_z \cdot \mathbf{e}_z \mathbf{e}_z] \frac{\partial}{\partial z} P_{zz} = \frac{\partial P_{zz}}{\partial z} \mathbf{e}_z.$$

By summing up all \mathbf{e}_ρ terms and set them to zero, all \mathbf{e}_φ terms and set them to zero, etc.:

$$\frac{\partial P_{\rho\rho}}{\partial \rho} + \frac{1}{\rho} [P_{\rho\rho} - P_{\varphi\varphi}] = \frac{1}{\rho} \frac{\partial}{\partial \rho} (\rho P_{\rho\rho}) - \frac{P_{\varphi\varphi}}{\rho} = 0, \quad (\text{A.10})$$

$$\frac{1}{\rho} \frac{\partial P_{\varphi\varphi}}{\partial \varphi} = 0, \quad (\text{A.11})$$

$$\frac{\partial P_{zz}}{\partial z} = 0. \quad (\text{A.12})$$

which can be rewritten as:

$$\frac{\partial}{\partial \rho} (\rho P_N) - P_{T\varphi} = 0, \quad (\text{A.13})$$

$$\frac{\partial P_{T\varphi}}{\partial \varphi} = 0, \quad (\text{A.14})$$

$$\frac{\partial P_{Tz}}{\partial z} = 0, \quad (\text{A.15})$$

where $P_N = P_{\rho\rho}$ is the pressure normal to the wall, $P_{\phi\phi} = P_{T\phi}$ is the tangential pressure parallel to the wall in the ϕ -direction, and $P_{zz} = P_{Tz}$ is the tangential pressure in the z -direction, parallel to the wall. Thus P_N will vary with ρ , but $P_{T\phi}$ will be independent of ϕ and P_{Tz} will be independent of z . $P_{T\phi}$ can, presumably, vary with ρ and z , and P_{Tz} may vary with ρ and ϕ .

Eqns. (A.13), (A.14) and (A.15) agree with Eqns. (J), (K), and (L) of Table (A.7-2) on page 834 of [R.B. Bird, W.E. Stewart and E.N. Lightfoot, “Transport Phenomena”, 2nd edition, John Wiley & Sons (2007)], where the authors write down the expression for $\nabla \cdot \boldsymbol{\tau}$, where $\boldsymbol{\tau}$ is some arbitrary second order tensor.

Finally, we note that if the pore wall is a cylinder whose central axis is the z -axis of the coordinate system, by symmetry of a infinitely long cylinder, the local pressure tensor does not depend on ϕ or z , i.e., $\mathbf{P} = \mathbf{P}(\rho)$. Then the Eqns. (A.13), (A.14) and (A.15) can be simplified as:

$$P_{T\phi}(\rho) = P_N(\rho) + \rho \frac{dP_N(\rho)}{d\rho}, \quad (\text{A.16})$$

$$P_{T\phi} = P_{T\phi}(\rho), \quad (\text{A.17})$$

$$P_{Tz} = P_{Tz}(\rho). \quad (\text{A.18})$$

A.3 Condition of Hydrostatic Equilibrium for A Spherical Interface

Any point A in the sphere is given in terms of $A(\rho, \theta, \varphi)$ coordinates, where ρ is the radial distance from the center of the sphere, and θ and φ are the polar and azimuthal angles (Figure 3.1c). The spherical coordinates are related to the Cartesian coordinates as follows:

$$\begin{aligned} x &= \rho \cos \varphi \sin \theta \\ y &= \rho \sin \varphi \sin \theta . \\ z &= \rho \cos \theta \end{aligned} \quad (\text{A.19})$$

For the spherical geometry, Eqn. (A.1) gives

$$\nabla \cdot \mathbf{P} = \left[\mathbf{e}_\rho \frac{\partial}{\partial \rho} + \mathbf{e}_\theta \frac{1}{\rho} \frac{\partial}{\partial \theta} + \mathbf{e}_\varphi \frac{1}{\rho \sin \theta} \frac{\partial}{\partial \varphi} \right] \cdot \left[\mathbf{e}_\rho \mathbf{e}_\rho P_{\rho\rho} + \mathbf{e}_\theta \mathbf{e}_\theta P_{\theta\theta} + \mathbf{e}_\varphi \mathbf{e}_\varphi P_{\varphi\varphi} \right]. \quad (\text{A.20})$$

There are 9 terms if Eqn (A.20) is expanded. To evaluate these 9 terms, we recall Eqn. (A.3) and

$$\begin{cases} \mathbf{e}_\rho = (\sin \theta \cos \varphi) \mathbf{e}_x + (\sin \theta \sin \varphi) \mathbf{e}_y + (\cos \theta) \mathbf{e}_z \\ \mathbf{e}_\theta = (\cos \theta \cos \varphi) \mathbf{e}_x + (\cos \theta \sin \varphi) \mathbf{e}_y + (-\sin \theta) \mathbf{e}_z , \\ \mathbf{e}_\varphi = (-\sin \varphi) \mathbf{e}_x + (\cos \varphi) \mathbf{e}_y + (0) \mathbf{e}_z \end{cases} \quad (\text{A.21})$$

and the following relationships (easy to derived from Eqn. (A.21)):

$$\begin{aligned}
\frac{\partial}{\partial \rho} \mathbf{e}_\rho &= 0; & \frac{\partial}{\partial \rho} \mathbf{e}_\theta &= 0; & \frac{\partial}{\partial \rho} \mathbf{e}_\varphi &= 0 \\
\frac{\partial}{\partial \theta} \mathbf{e}_\theta &= (-\sin \theta \cos \varphi) \mathbf{e}_x + (-\sin \theta \sin \varphi) \mathbf{e}_y + (-\cos \theta) \mathbf{e}_z = -\mathbf{e}_\rho \\
\frac{\partial}{\partial \theta} \mathbf{e}_\varphi &= 0 \\
\frac{\partial}{\partial \theta} \mathbf{e}_\rho &= (\cos \theta \cos \varphi) \mathbf{e}_x + (\cos \theta \sin \varphi) \mathbf{e}_y + (-\sin \theta) \mathbf{e}_z = \mathbf{e}_\theta \quad . \quad (\text{A.22}) \\
\frac{\partial}{\partial \varphi} \mathbf{e}_\rho &= (-\sin \theta \sin \varphi) \mathbf{e}_x + (\sin \theta \cos \varphi) \mathbf{e}_y \\
\frac{\partial}{\partial \varphi} \mathbf{e}_\theta &= (-\cos \theta \sin \varphi) \mathbf{e}_x + (\cos \theta \cos \varphi) \mathbf{e}_y \\
\frac{\partial}{\partial \varphi} \mathbf{e}_\varphi &= (-\cos \varphi) \mathbf{e}_x + (-\sin \varphi) \mathbf{e}_y
\end{aligned}$$

By using Eqns. (A.3) (A.21) and (A.22), we can now write out the 9 terms resulting from Eqn. (A.20). See Example A.7.2, p. 838-39 of [R.B. Bird, W.E. Stewart and E.N. Lightfoot, “Transport Phenomena”, 2nd edition, John Wiley & Sons (2007)], where the authors work out the ρ -component. Summing up the terms involved in the ρ -, θ - and φ -components, and setting each of these equal to zero gives (see Eqns. (J), (K), and (L) of Table (A.7-3) on page 836 of [R.B. Bird, W.E. Stewart and E.N. Lightfoot, “Transport Phenomena”, 2nd edition, John Wiley & Sons (2007)]):

$$\frac{1}{\rho^2} \frac{\partial}{\partial \rho} (\rho^2 P_N) - \frac{P_{T\theta} + P_{T\varphi}}{\rho} = 0, \quad (\text{A.23})$$

$$\frac{1}{\rho \sin \theta} \frac{\partial}{\partial \theta} (P_{T\theta} \sin \theta) - \frac{P_{T\varphi} \cot \theta}{\rho} = 0, \quad (\text{A.24})$$

$$\frac{1}{\rho \sin \theta} \frac{\partial P_{T\varphi}}{\partial \varphi} = 0. \quad (\text{A.25})$$

From symmetry considerations (see Figure 3.1c), $P_{T\theta}$ must be independent of θ , so that Eqn. (A.24) becomes:

$$\frac{P_{T\theta} \cos \theta}{\rho \sin \theta} - \frac{P_{T\varphi} \cot \theta}{\rho} = 0, \quad (\text{A.24a})$$

and thus:

$$P_{T\theta} = P_{T\varphi}. \quad (\text{A.24b})$$

Moreover, from Eqn. (A.25) it follows that $P_{T\varphi}$ must be independent of the azimuthal angle φ . Thus, $P_{T\theta} = P_{\theta\theta} = P_{T\varphi} = P_{\varphi\varphi}$, and this pressure component will be independent of both θ and φ , but will depend on ρ .

Eqn. (A.23) provides a useful relationship between the normal and tangential components of the pressure tensor:

$$P_T = \frac{1}{2\rho} \frac{\partial}{\partial \rho} (\rho^2 P_N), \quad (\text{A.26})$$

or its alternative form:

$$P_T(\rho) = P_N(\rho) + \frac{\rho}{2} \frac{dP_N(\rho)}{d\rho}. \quad (\text{A.27})$$

Appendix B

Volume Balance Examinations for the Volume Perturbation Method

B.1 Perturbation in A Cylindrical Pore

In a cylindrical pore case, suppose the system is perturbed by scaling the radial coordinates of all the particles in the system by a factor of $(1 + \xi)$, while keeping z - and φ -coordinates fixed. The overall volume change of bin k due to this perturbation, dV_{tk} , can be calculated as the difference between the bin volume of the perturbed system, V'_{tk} , and that of the reference (unperturbed) system, $V_{tk,0}$:

$$\begin{aligned} V_{tk,0} &= \pi \left(\rho_k + \frac{\Delta\rho}{2} \right)^2 L_z - \pi \left(\rho_k - \frac{\Delta\rho}{2} \right)^2 L_z \\ &= \pi L_z \left[\left(\rho_k + \frac{\Delta\rho}{2} \right)^2 - \left(\rho_k - \frac{\Delta\rho}{2} \right)^2 \right] , \\ &= \pi L_z (2\rho_k \Delta\rho) \\ &= 2\rho_k \Delta\rho \pi L_z \end{aligned}$$

$$\begin{aligned} V'_{tk} &= \pi \left[\left(\rho_k + \frac{\Delta\rho}{2} \right) (1 + \xi) \right]^2 L_z - \pi \left[\left(\rho_k - \frac{\Delta\rho}{2} \right) (1 + \xi) \right]^2 L_z \\ &= (1 + \xi)^2 V_{tk,0} , \\ &= 2\rho_k \Delta\rho \pi L_z (1 + \xi)^2 \end{aligned}$$

$$dV_{tk} = V'_{tk} - V_{tk,0} = [(1 + \xi)^2 - 1](2\rho_k \Delta\rho \pi L_z) = (2\xi + \xi^2)2\rho_k \Delta\rho \pi L_z \sim 4\pi\rho_k L_z \Delta\rho \xi + O(\xi^2) .$$

On the other hand, From Eqn. (3.52):

$$dV_{\rho k} = dV_{\varphi k} = 2\pi\rho_k L_z \Delta\rho \xi \Rightarrow dV_{\rho k} + dV_{\varphi k} = 4\pi\rho_k L_z \Delta\rho \xi .$$

Therefore, for the leading term the volume balance is satisfied (for small ξ):

$$dV_{tk} = dV_{\rho k} + dV_{\varphi k} = 4\pi\rho_k L_z \Delta\rho \xi$$

B.2 Perturbation in A Spherical Pore

In a spherical pore case, suppose the system is perturbed by scaling the radial coordinates of all the particles in the system by a factor of $(1 + \xi)$, while keeping φ - and θ -coordinates fixed.

The overall volume change of bin k due to this perturbation, dV_{tk} , can be calculated as the difference between the bin volume of the perturbed system, V'_{tk} , and that of the reference (unperturbed) system, $V_{tk,0}$:

$$\begin{aligned} V_{tk,0} &= \frac{4\pi}{3} \left(\rho_k + \frac{\Delta\rho}{2} \right)^3 - \frac{4\pi}{3} \left(\rho_k - \frac{\Delta\rho}{2} \right)^3 \\ &= \frac{4\pi}{3} \left[\left(\rho_k + \frac{\Delta\rho}{2} \right)^3 - \left(\rho_k - \frac{\Delta\rho}{2} \right)^3 \right] \quad (\text{note: } a^3 - b^3 = (a-b)(a^2 + b^2 + ab)) \\ &= \frac{4\pi}{3} \Delta\rho \left[\left(\rho_k + \frac{\Delta\rho}{2} \right)^2 + \left(\rho_k - \frac{\Delta\rho}{2} \right)^2 + \left(\rho_k + \frac{\Delta\rho}{2} \right) \left(\rho_k - \frac{\Delta\rho}{2} \right) \right] \\ &= \frac{4\pi\Delta\rho}{3} \left[2\rho_k^2 + \frac{(\Delta\rho)^2}{2} + \rho_k^2 - \frac{(\Delta\rho)^2}{4} \right] \\ &= \frac{4\pi\Delta\rho}{3} \left[3\rho_k^2 + \frac{(\Delta\rho)^2}{4} \right] \end{aligned}$$

$$\begin{aligned} V'_{tk} &= \frac{4\pi}{3} \left[\left(\rho_k + \frac{\Delta\rho}{2} \right) (1 + \xi) \right]^3 - \frac{4\pi}{3} \left[\left(\rho_k - \frac{\Delta\rho}{2} \right) (1 + \xi) \right]^3 \\ &= (1 + \xi)^3 V_{tk,0} \\ &= \frac{4\pi\Delta\rho}{3} \left[3\rho_k^2 + \frac{(\Delta\rho)^2}{4} \right] (1 + \xi)^3 \end{aligned}$$

$$\begin{aligned}
dV_{tk} &= [(1+\xi)^3 - 1]V_{tk,0} \\
&= (3+3\xi+\xi^2)\xi V_{tk,0} \\
&= (3+3\xi+\xi^2)\xi \frac{4\pi\Delta\rho}{3} \left[3\rho_k^2 + \frac{(\Delta\rho)^2}{4} \right] \\
&\sim 12\pi\rho_k^2\Delta\rho\xi + O(\xi^2) + O(\Delta\rho^3)
\end{aligned}$$

On the other hand, from Eqns. (3.66), (3.69) and (3.72):

$$dV_{\rho k} = dV_{\phi k} = dV_{\theta k} = 4\pi\rho_k^2\Delta\rho\xi \Rightarrow dV_{\rho k} + dV_{\phi k} + dV_{\theta k} = 12\pi\rho_k^2\Delta\rho\xi .$$

Therefore, for the leading term the volume balance is satisfied (for small ξ and small $\Delta\rho/\rho$):

$$dV_{tk} = dV_{\rho k} + dV_{\phi k} + dV_{\theta k} = 12\pi\rho_k^2\Delta\rho\xi$$

Appendix C

Solution of Ordinary Differential Equations Arising from Volume Perturbation Method

In Sec. 3.3.2, we present a new framework to calculate the normal and tangential pressures of adsorbate confined in cylindrical and spherical pores by the thermodynamic route (or the volume perturbation method). In the process, we have to solve an ordinary differential equation (ODE) with a constraint. The ODE system is defined by Eqns. (3.57) and (3.58) (or (3.59)) for the cylindrical case and Eqns. (3.76) and (3.77) (or (3.78)) for the spherical case, respectively.

These two ODE systems can be written as a unified form:

$$\rho P'_{conf,N} + s P_{conf,N} = f(\rho) = k_B T \lim_{\xi \rightarrow 0} \frac{\ln \langle e^{-\Delta U(\rho)/k_B T} \rangle_0}{V_{k,0} \xi} - k_B T \rho \rho'_{ad}, \quad (C.1)$$

$$\text{s.t. : } P'_{conf,N}(0) = 0, \quad (C.2a)$$

$$\text{or s.t. : } P_{conf,N}(R) = P_{N,wall}, \quad (C.2b)$$

where $s = 2$ for the cylindrical case and $s = 3$ for the spherical case, and $V_{k,0}$ is the volume of bin k of the reference (unperturbed) system. For a first-order ODE, only one constraint is required, thus, either Eqn. (C.2a) or Eqn. (C.2b) will be used depending on what information we could obtain and the numerical stability.

Eqn. (C.1) is a first-order inhomogeneous linear ODE, which can be solved as follows:

Assume $y_h(\rho)$ is the solution to the homogenous part of Eqn. (C.1), i.e.,

$$\rho \frac{dy_h}{d\rho} + sy_h = 0, \quad (\text{C.3})$$

and solving for $y_h(\rho)$ by separating the variables in ODE (C.3) gives:

$$y_h = \frac{c_1}{\rho^s}, \quad (\text{C.4})$$

where c_1 is a integral constant. Thus the solution to the inhomogeneous ODE (C.1) should be in the form of:

$$P_{conf,N}^V = \frac{u(\rho)}{\rho^s}. \quad (\text{C.5})$$

To find the undetermined function $u(\rho)$, we substitute Eqn. (C.5) into Eqn. (C.1):

$$\rho \frac{d}{d\rho} \left(\frac{u}{\rho^s} \right) + \frac{su}{\rho^s} = f(\rho), \quad (\text{C.6})$$

or (after expansions and simplifications):

$$\frac{du}{d\rho} = \rho^{s-1} f(\rho) \Rightarrow \int_{u_0}^u du' = \int_{\rho_0}^{\rho} \rho'^{s-1} f(\rho') d\rho'. \quad (\text{C.7})$$

If the symmetric boundary condition of Eqn. (C.2a) is chosen to apply, then we let $\rho_0 = 0$, and $u_0 = u(\rho_0) = 0$, because as ρ_0 approaches to 0, $u_0 = [\rho_0^s P_{conf,N}^V(\rho_0)] = 0$, provided $P_{conf,N}^V(0)$ should be a finite value. Thus, we have:

$$\int_0^u du' = u = \int_0^{\rho} \rho'^{s-1} f(\rho') d\rho' \Rightarrow P_{conf,N}^V = \frac{u(\rho)}{\rho^s} = \frac{1}{\rho^s} \int_0^{\rho} \rho'^{s-1} f(\rho') d\rho'. \quad (\text{C.8})$$

Alternatively, if the constraint condition of the normal pressure acting at the wall (Eqn. (C.2b)) is applied, it can be rewritten for $u(\rho)$ using the relationship in Eqn. (C.5):

$$P_{conf,N}^V(R) = \frac{u(R)}{R^s} = P_{N,wall} \Rightarrow u(R) = R^s P_{N,wall}. \quad (C.9)$$

Integrating Eqn. (C.7) with the constraint condition of Eqn. (C.8), we obtain:

$$\int_{u(R)}^u du = \int_R^\rho \rho'^{s-1} f(\rho') d\rho' \Rightarrow u(\rho) = R^s P_{N,wall} + \int_R^\rho \rho'^{s-1} f(\rho') d\rho'. \quad (C.10)$$

Therefore,

$$P_{conf,N}^V = \frac{u(\rho)}{\rho^s} = \frac{1}{\rho^s} \left(R^s P_{N,wall} + \int_R^\rho \rho'^{s-1} f(\rho') d\rho' \right). \quad (C.11)$$

where (for both Eqns. (C.8) and (C.11))

$$f(\rho) = k_B T \lim_{\xi \rightarrow 0} \frac{\ln \langle e^{-\Delta U(\rho)/k_B T} \rangle_0}{V_{k,0} \xi} - k_B T \rho \rho'_{ad} = f_{12}(\rho) - k_B T \rho \rho'_{ad}, \quad (C.12)$$

and

$$f_{12}(\rho) = k_B T \lim_{\xi \rightarrow 0} \frac{\ln \langle e^{-\Delta U(\rho)/k_B T} \rangle_0}{V_{k,0} \xi}. \quad (C.13)$$

Eqns. (C.8) and (C.11) are the solutions of the configurational normal pressure with two different constraint conditions.

To simplify the answer, we calculate the integrals in Eqns. (C.8) and (C.11) with substitution of Eqn. (C.12):

$$\begin{aligned}
\int_{\rho_0}^{\rho} f \rho'^{s-1} d\rho' &= \int_{\rho_0}^{\rho} \rho'^{s-1} [f_{12}(\rho') - k_B T \rho' \frac{d\rho_{ad}}{d\rho'}] d\rho' \quad (\rho_0 = 0 \text{ for (C.8) or } R \text{ for (C.11)}) \\
&= \int_{\rho_0}^{\rho} \rho'^{s-1} f_{12}(\rho') d\rho' - \int_{\rho_0}^{\rho} \rho'^{s-1} k_B T \rho' \frac{d\rho_{ad}}{d\rho'} d\rho' \\
&= \int_{\rho_0}^{\rho} \rho'^{s-1} f_{12}(\rho') d\rho' - k_B T \int_{\rho_0}^{\rho} \rho'^s d\rho_{ad} \\
&= \int_{\rho_0}^{\rho} \rho'^{s-1} f_{12}(\rho') d\rho' - k_B T \left[\rho_{ad} \rho'^s \Big|_{\rho_0}^{\rho} - \int_{\rho_0}^{\rho} \rho_{ad} d(\rho'^s) \right] \quad , \quad (C.13) \\
&= \int_{\rho_0}^{\rho} \rho'^{s-1} f_{12}(\rho') d\rho' - k_B T \left[\rho^s \rho_{ad}(\rho) - s \int_{\rho_0}^{\rho} \rho'^{s-1} \rho_{ad} d\rho' \right] (\rho^s \rho_{ad} \Big|_{\rho_0} = 0) \\
&= \int_{\rho_0}^{\rho} \rho'^{s-1} f_{12}(\rho') d\rho' - k_B T \rho^s \rho_{ad}(\rho) + s k_B T \int_{\rho_0}^{\rho} \rho'^{s-1} \rho_{ad} d\rho' \\
&= \int_{\rho_0}^{\rho} \rho'^{s-1} [f_{12}(\rho') + s \rho_{ad} k_B T] d\rho' - \rho^s \rho_{ad}(\rho) k_B T
\end{aligned}$$

and thus the solutions Eqns. (C.8) and (C.10) become:

$$P_{conf,N}^V = \frac{1}{\rho^s} \int_0^{\rho} \rho'^{s-1} [f_{12}(\rho') + s \rho_{ad}(\rho') k_B T] d\rho' - \rho_{ad}(\rho) k_B T \quad , \quad (C8.a)$$

$$P_{conf,N}^V = \frac{1}{\rho^s} \left(R^s P_{N,wall} + \int_R^{\rho} \rho'^{s-1} [f_{12}(\rho') + s \rho_{ad}(\rho') k_B T] d\rho' \right) - \rho_{ad}(\rho) k_B T \quad , \quad (C.10a)$$

and thus:

$$P_N^V = P_{conf,N}^V + P_{kin} (= \rho_{ad}(\rho) k_B T) = \frac{1}{\rho^s} \int_0^{\rho} \rho'^{s-1} [f_{12}(\rho') + s \rho_{ad}(\rho') k_B T] d\rho' \quad , \quad (C14a)$$

$$P_N^V = P_{conf,N}^V + P_{kin} (= \rho_{ad}(\rho) k_B T) = \frac{1}{\rho^s} \left(R^s P_{N,wall} + \int_R^{\rho} \rho'^{s-1} [f_{12} + s \rho_{ad} k_B T] d\rho' \right) \quad , \quad (C.14b)$$

for the constraint conditions of Eqns. (C.2a) and (C.2b), respectively.

Note: applying either of the constraint condition Eqn. (C.2a) or Eqn. (C.2b) will cause a problem of numerical instability in practice. To apply Eqns. (C.2a), the constraint is defined at $\rho = 0$, and practically, in this region (the vicinity of the pore center) the bin width is very small, so that the statistics are very poor; to apply Eqns. (C.2b), as shown, the solution is Eqn. (C.14b) with a factor of $1/\rho^s$ multiplied by a finite value, which approaches to an unphysical infinity as ρ approaches to 0 (the pore center).

The tangential pressure can be calculated either from the condition of hydrostatic equilibrium or the relationship with the normal pressure provided by Eqn. (3.52) for the cylindrical pore or Eqn. (3.74) for the spherical pore.

We derive here the equation for the cylindrical pore case, and then a similar process can be done for the spherical case. From Eqn. (3.52) (as well as Eqn. (3.55)), we have:

$$dF_{c,k} = -2\pi\rho_k \xi L_z \Delta\rho (P_{conf,Nk}^V + P_{conf,T\phi k}^V) = -k_B T \lim_{\xi \rightarrow 0} \ln \langle e^{-\Delta U_k/k_B T} \rangle_0, \quad (C.15)$$

and thus, if written in a continuous form:

$$P_{conf,T\phi}^V = k_B T \lim_{\xi \rightarrow 0} \frac{\ln \langle e^{-\Delta U(\rho)/k_B T} \rangle_0}{2\pi\rho L_z \Delta\rho \xi} - P_{conf,N}^V. \quad (C.16)$$

By using Eqns. (C.13) and (C.16), we can get the total tangential pressure:

$$\begin{aligned}
P_{T\varphi}^V &= P_{conf,T\varphi}^V + P_{kin} = k_B T \lim_{\xi \rightarrow 0} \frac{\ln \langle e^{-\Delta U(\rho)/k_B T} \rangle_0}{2\pi\rho L_z \Delta\rho\xi} - P_{conf,N}^V + \rho_{ad} k_B T \\
&= k_B T \lim_{\xi \rightarrow 0} \frac{\ln \langle e^{-\Delta U(\rho)/k_B T} \rangle_0}{2\pi\rho L_z \Delta\rho\xi} - (P_{conf,N}^V + \rho_{ad} k_B T) + 2\rho_{ad} k_B T \quad . \quad (C.17) \\
&= f_{12} - P_N^V + 2\rho_{ad} k_B T
\end{aligned}$$

For the spherical pore case, from Eqns. (3.74) and (3.55), we have:

$$dF_{c,k} = -4\pi\rho_k^2 \Delta\rho\xi \left(P_{conf,Nk}^V + 2P_{conf,Tk}^V \right) = -k_B T \lim_{\xi \rightarrow 0} \ln \langle e^{-\Delta U_k/k_B T} \rangle_0, \quad (C.18)$$

and thus, if written in a continuous form:

$$P_{conf,T}^V = \frac{1}{2} \left[k_B T \lim_{\xi \rightarrow 0} \frac{\ln \langle e^{-\Delta U(\rho)/k_B T} \rangle_0}{4\pi\rho^2 \Delta\rho\xi} - P_{conf,N}^V \right]. \quad (C.19)$$

By using Eqns. (C.13) and (C.19), we can get the total tangential pressure:

$$\begin{aligned}
P_T^V &= P_{conf,T}^V + P_{kin} = \frac{1}{2} \left[k_B T \lim_{\xi \rightarrow 0} \frac{\ln \langle e^{-\Delta U(\rho)/k_B T} \rangle_0}{4\pi\rho^2 \Delta\rho\xi} - P_{conf,N}^V \right] + \rho_{ad} k_B T \\
&= \frac{1}{2} \left[k_B T \lim_{\xi \rightarrow 0} \frac{\ln \langle e^{-\Delta U(\rho)/k_B T} \rangle_0}{4\pi\rho^2 \Delta\rho\xi} - (P_{conf,N}^V + \rho_{ad} k_B T) + 3\rho_{ad} k_B T \right] \quad . \quad (C.21) \\
&= \frac{1}{2} \left[f_{12} - P_N^V + 3\rho_{ad} k_B T \right]
\end{aligned}$$

Appendix D

Calculations of Wetting Parameters for Various Adsorbate-Substrate Systems

The wetting parameter, α_w , for a certain adsorbate-substrate system is calculated from the mathematical definition of α_w (Eqn. (6.1)):

$$\alpha_w = \rho_w \sigma_{aw}^2 \Delta_w \varepsilon_{aw} / \varepsilon_{aa}, \quad (6.1)$$

where ε and σ are the usual energy (well-depth) and molecular diameter parameters, ρ_w is the number density of the wall atoms, and Δ_w is the spacing between layers of the wall atoms.

The interaction parameters (σ_{aw} , ε_{aa} and ε_{aw}) are obtained in the following way:

For the spherical LJ molecules (e.g., Ar, CCl₄ and OMCTS in this dissertation), the adsorbate-adsorbate interaction potential model can be expressed as:

$$u_{aa} = 4\varepsilon_{aa}^{disp} \left[\left(\frac{\sigma_{aa}}{r} \right)^{12} - \left(\frac{\sigma_{aa}}{r} \right)^6 \right], \quad (D.1)$$

where σ_{aa} and ε_{aa}^{disp} are the normal LJ parameters for the adsorbate. The parameters used to calculate α_w are:

$$\begin{aligned} \varepsilon_{aa} &= \varepsilon_{aa}^{disp} \\ \sigma_{aw} &= (\sigma_{aa} + \sigma_{ww}) / 2. \\ \varepsilon_{aw} &= \sqrt{\varepsilon_{aa}^{disp} \varepsilon_{ww}} \end{aligned} \quad (D.2)$$

For the dipolar fluids (C_6H_5Br and $C_6H_5NO_2$ in this dissertation), the adsorbate-adsorbate interaction can be modeled as a Stockmayer potential: [J. O. Hirshfelder, C. F. Curtiss, and B. Bird, Molecular Theory of Gases and Liquids, Wiley, New York, 1964]

$$u_{aa} = 4\epsilon_{aa}^{disp} \left[\left(\frac{\sigma_{aa}}{r} \right)^{12} - \left(\frac{\sigma_{aa}}{r} \right)^6 \right] - \frac{k_e \mu_1 \mu_2}{r^3} (2 \cos \theta_1 \cos \theta_2 - \sin \theta_1 \sin \theta_2 \cos \phi), \quad (D3)$$

which is composed of an overlap and dispersive contribution (the first term on the right-hand-side) and a dipolar contribution (the second term on the right-hand-side). On the other hand, by fitting simulation data to the experimental freezing points of these dipolar fluids, the adsorbate-adsorbate interaction can be modeled as a LJ potential with an “effective” energy well-depth:

$$u_{aa} = 4\epsilon_{aa}^{eff} \left[\left(\frac{\sigma_{aa}}{r} \right)^{12} - \left(\frac{\sigma_{aa}}{r} \right)^6 \right]. \quad (D.4)$$

To calculate α_w for these dipolar fluids, the parameters can be obtained by:

$$\begin{aligned} \epsilon_{aa} &= \epsilon_{aa}^{eff} \\ \sigma_{aw} &= (\sigma_{aa} + \sigma_{ww}) / 2. \\ \epsilon_{aw} &= \sqrt{\epsilon_{aa}^{disp} \epsilon_{ww}} \end{aligned} \quad (D.5)$$

(Note: the dispersive well-depth of the adsorbate-adsorbate interaction in the Stockmayer potential is used to calculate the cross-interactive aw well-depth; here we neglect any electrostatic or induction contribution to the adsorbate-wall interaction)

For the fluids with H-bonding, specifically, H₂O in this dissertation, the adsorbate-adsorbate interaction can be modeled as the TIP4P potential [W.L. Jorgensen, J. Chandrasekhar, J.D. Madura, R.W. Impey, M.L. Klein, J. Chem. Phys., 79 (1983) 926-935] which is composed of a LJ dispersive contribution plus a columbic electrical term:

$$u_{aa} = 4\epsilon_{aa}^{disp} \left[\left(\frac{\sigma_{aa}}{r} \right)^{12} - \left(\frac{\sigma_{aa}}{r} \right)^6 \right] + \sum_i \frac{k_e q_i q_j}{r_{ij}}. \quad (\text{D.6})$$

On the other hand, by fitting simulation data to the experimental freezing point of H₂O, the adsorbate-adsorbate interaction can be modeled as a LJ potential with an “effective” energy well-depth as shown by Eqn. (D.4). Similar to the dipolar fluids, the parameters used to calculate α_w for H₂O can be obtained by Eqn. (D.5).

For Hg, the effective LJ parameters (σ_{aa} and ϵ_{aa}^{eff}) for modeling adsorbate-adsorbate interaction are found by fitting binding energy and equilibrium distance of the *ab initio* Hg potential. The *aa* parameter used for modeling adsorbate-wall interaction (ϵ_{aa}^w) are obtained by simulating the wetting of a graphite surface by a mercury drop and fitting to the experimental contact angle. To calculate α_w for these dipolar fluids, the parameters can be obtained by:

$$\begin{aligned} \epsilon_{aa} &= \epsilon_{aa}^{eff} \\ \sigma_{aw} &= (\sigma_{aa} + \sigma_{ww}) / 2. \\ \epsilon_{aw} &= \sqrt{\epsilon_{aa}^w \epsilon_{ww}} \end{aligned} \quad (\text{D.7})$$

The parameters of various walls and fluids are listed in Tables D.1 and D.2, respectively.

Table D.1 The parameters of various walls used to calculate the wetting parameter.

	ρ_w / nm^{-3}	Δ_w / nm	σ_{ww} / nm	$\varepsilon_{ww}/k_B / \text{K}$
Graphite ¹	114.0	0.335	0.34	28
Silica ²	44.2	0.220	0.27	230
Mica ³	25.4	0.287	0.35	940

¹ W.A. Steele, Surf. Sci., 36 (1973) 317-352

² R. Radhakrishnan, K.E. Gubbins, M. Sliwinska-Bartkowiak, J. Chem. Phys., 116 (2002) 1147-1155

³ S.T. Cui, C. McCabe, P.T. Cummings, H.D. Cochran, J. Chem. Phys., 118 (2003) 8941-8944

Table D.2 The parameters of various fluids used to calculate the wetting parameter.

	σ_{aa} / nm	$\varepsilon_{aa}^{eff}/k_B / \text{K}$	$\varepsilon_{aa}^{disp}/k_B / \text{K}$
CCl ₄ ¹	0.514	366	366
OMCTS ²	0.77	351.36	351.36
C ₆ H ₅ Br ³	0.538	351.2	351.2
C ₆ H ₅ NO ₂ ¹	0.514	425	212
H ₂ O ¹	0.3154	401	77.9
Hg ⁴	0.3234	506	(ε_{aa}^w) 7.7175

¹ R. Radhakrishnan, K.E. Gubbins, M. Sliwinska-Bartkowiak, J. Chem. Phys., 116 (2002) 1147-1155

² K.G. Ayappa, R.K. Mishra, J. Phys. Chem. B, 111 (2007) 14299-14310

³ Fitted from the experimental measurements of viscosity provided by Sliwinska-Bartkowiak

⁴ J.Y. Chen, A. Kutana, C.P. Collier, K.P. Giapis, Science, 310 (2005) 1480-1483.

Appendix E

List of Important Symbols

A	Surface area
A_ρ	Surface area of a spherical shell with radius ρ
A_w	Amplitude of the cosine wave for the roughness of the pore wall
ΔA_{xy}	Change in the xy -surface area due to the perturbation in x - and/or y -dimensions
C_{0i}	An arbitrary contour from the center of mass of particle i to an arbitrary point \mathbf{r}_0 in the fluid
C_{ij}	An arbitrary contour from the center of mass of particle i to the center of mass of particle j
D	Inner diameter of a cylindrical or spherical pore
$d_{002}, d_{002,e}$	Interlayer spacing of the graphene sheets of the pore wall and interlayer spacing without loading adsorbate, respectively
E_T	Transverse Young's modulus
$\mathbf{e}_\rho, \mathbf{e}_\varphi, \mathbf{e}_\theta$	Unit vectors in respective directions of a spherical system
$\mathbf{e}_x, \mathbf{e}_y, \mathbf{e}_z$	Unit vectors in respective directions of a Cartesian system
F, F_c	Total and configurational Helmholtz free energies, respectively
ΔF_c	Change in the configurational Helmholtz free energy due to the

	small change in the volume (volume perturbation)
$\Delta F_{c1}, \Delta F_{c2}, \Delta F_{c3}$	Leading term and two capillary wave terms of the change in the configurational Helmholtz free energy, respectively
$dF_{c,k}$	Change in the configurational Helmholtz free energy of bin k
$dF_{c,\rho k}, dF_{c,\varphi k}, dF_{c,\theta k}$	Change in the configurational Helmholtz free energy of bin k due to the volume perturbation contributions in respective directions
$g(r)$	Radial distribution function
H, H_e	Pore width and pore width without loading adsorbate
i, j	Indices for particles (molecules or atoms), usually used as subscripts
j^α	Rate of change of the α -component of the linear momentum density
k	Index for the bin, into a series of which the pore is divided
k_s	Spring constant of a carbon atom connecting with its lattice position
k_B	Boltzmann constant, $1.38065 \times 10^{-23} \text{ J K}^{-1}$
$\tilde{\ell}(\mathbf{r}_i, \mathbf{r}_j)$	A point on the contour connecting particles i and j
l, l_φ, l_θ	ρ -, φ - and θ -components of vector $\tilde{\ell}$ in spherical system, respectively
l_k	Circumference of bin k in the φ -direction for a cylindrical system
$l_{\varphi k}, l_{\theta k}$	Circumferences of bin k in the φ - and θ -directions for a spherical system, respectively
L_z	Length in the z -direction

$L_{z,wall}$	Length of the pore wall (in the z -direction)
$L_{x,box}, L_{y,box}, L_{z,box}$	Lengths of simulation box in the x -, y - and z -directions, respectively
N	Number of particles
N_{uc}	Number of unit cells (for carbon nanotube)
\mathbf{P}	Pressure tensor (second-order)
$P_{\alpha\beta}$	Pressure tensor component acting in the β -direction on a surface normal to the α -direction
P_{xx}, P_{yy}, P_{zz}	Diagonal elements of the pressure tensor in the Cartesian coordinate system
$P_{\rho\rho}, P_{\varphi\varphi}, P_{zz}$	Diagonal elements of the pressure tensor in the cylindrical coordinate system
$P_{\rho\rho}, P_{\varphi\varphi}, P_{\theta\theta}$	Diagonal elements of the pressure tensor in the spherical coordinate system
P_T	Pressure tensor component parallel to the pore wall, or the tangential pressure
P_N	Pressure tensor component perpendicular to the pore wall, or the normal pressure
$P_{Tz}, P_{T\varphi}$	Tangential pressures in z - and φ -directions of a cylindrical system, respectively
$\mathbf{P}_{kin}, \mathbf{P}_{conf}$	Kinetic and configurational contributions of a pressure tensor, respectively
$P_{T,IK}, P_{N,IK}$	Tangential and normal pressures obtained by the mechanical route

	with Irving-Kirkwood definition
$\mathbf{P}_{conf,IK}$	Configurational contribution of the pressure tensor obtained by the mechanical route with Irving-Kirkwood definition
$P_{conf,N,IK}, P_{conf,T,IK}$	Configurational contributions of the normal and tangential pressures obtained by the mechanical route with Irving-Kirkwood definition
$P_{T,H}$	Tangential pressure obtained by the mechanical route with Harasima definition
P^V	Thermodynamic pressure or the average pressure obtained by the volume perturbation method
P_{conf}^V	Configurational contribution of the pressure obtained by the thermodynamic route (i.e., volume perturbation method)
$P_{conf,\alpha\alpha}^V$	Configurational contribution of the α -pressure tensor component obtained by the volume perturbation method
$P_{conf,N}^V$	Configurational contribution of the normal pressure obtained by the volume perturbation method
$P_{conf,zz}^V$	Configurational contribution of the z -pressure tensor component obtained by the volume perturbation method
$P_{conf,T}^V$	Configurational contribution of the tangential pressure obtained by the volume perturbation method
$P_{conf,Tz}^V$	Configurational contribution of the z -tangential pressure obtained by the volume perturbation method in the cylindrical system

$P_{conf,Nk}^V$	Configurational contribution of the normal pressure obtained by the volume perturbation method evaluated at bin k
$P_{conf,T\phi k}^V, P_{conf,T\theta k}^V$	Configurational contributions of the ϕ - and θ -tangential pressures obtained by the volume perturbation method evaluated at bin k
$P_{N,wall}$	Normal pressure of adsorbate acting on the pore wall
P	Scalar pressure
P_{bulk}	Bulk pressure
$P_{T,IK,peak}$	Peak value of the tangential pressure calculated by the mechanical route using IK definition
$P_{T,avg}$	Average tangential pressure over the pore width
$P_{T,peak}$	Peak value of the tangential pressure
P_c	Capillary condensation pressure
p^{acc}	Probability of accepting a Monte Carlo trial move
p_i	Momentum of molecule i
Q_{conf}	Configurational partition function
R	Inner radius of a cylindrical or spherical pore
\mathbf{r}	Position vector
$\mathbf{r}_i, \mathbf{r}_j$	Position vector of particles i and j , respectively
\mathbf{r}_{ij}	$\mathbf{r}_j - \mathbf{r}_i$

r_{ij}	Distance between particles i and j
r_c	Interaction cut-off distance (beyond which the interaction is zero)
S_{Nk}	Surface area that the normal pressure acts on
$S_{\phi k}, S_{\theta k}$	Surface areas that the ϕ - and θ -tangential pressures act on, respectively
t	Time
T	Temperature
T_f	Freezing temperature
u	Pairwise interactive potential (usually a function of the distance between two interacting particles)
$U(\mathbf{r}^N \boldsymbol{\omega}^N)$	Total internal potential energy, as a function of molecule configuration (including positions and orientations)
$V(\mathbf{r}^N)$	Total external force field, as a function of molecule positions
V	Volume of the system
ΔV	Change in the volume, usually refers to a small change
v	External force field (a function of position in space)
$dV_{\rho k}, dV_{\phi k}, dV_{\theta k}$	Volume changes of bin k due to the contributions in respective directions
$V_{k,0}$	Unperturbed volume of bin k in a cylindrical or spherical system
(x, y, z)	Cartesian coordinates

δz	Width of bin, into which the silt pore is divided in the z -direction
α, β	Directions in space (can be x, y, z, ρ, φ or θ)
α_w	Microscopic wetting parameter
$\delta(x)$	Dirac Delta function
Δ	Width of bin, into which a spherical or cylindrical pore is divided in the ρ -direction
Δ_w	Interlayer spacing between the layers of wall atoms
ε	Lennard-Jones parameter of energy well-depth. Subscripts aa, ww, aw, CC, aC indicate the interaction between adsorbate-adsorbate, wall-wall, adsorbate-wall, carbon-carbon, and adsorbate-carbon, respectively
λ_w	Wave length of the cosine wave for the roughness of the pore wall
μ, μ_a	Chemical potential and chemical potential of adsorbate, respectively
$\theta(x)$	Heaviside unit step function
θ_c	Contact angle
ρ_{ad}	Number density of the adsorbate (a function of spatial position)
ρ_w	Number density of the wall atoms
(ρ, φ, z)	Cylindrical coordinates
(ρ, φ, θ)	Spherical coordinates
$\Delta\rho$	Width of bin, into which the spherical and cylindrical pore is

divided in the ρ -direction

σ

Stress tensor (a function of time and spatial position)

$\sigma^{\alpha\beta}, \sigma_{kin}^{\alpha\beta}, \sigma_{conf}^{\alpha\beta}$

Stress tensor component acting in the β -direction on a surface normal to the α -direction, and its kinetic and configurational contributions, respectively

σ

Lennard-Jones parameter of molecule size. Subscripts aa, ww, aw, CC, aC indicate the interaction between adsorbate-adsorbate, wall-wall, adsorbate-wall, carbon-carbon, and adsorbate-carbon, respectively

ξ

A small number related to the volume perturbation method